Abstract

The Orenada Zone 4 deposit is an Archean orogenic gold deposit situated southeast of Val d'Or, Québec in the southeastern Abitibi Greenstone Belt. It is located directly within the Cadillac-Larder-Lake Deformation Zone. Mineralization is hosted within a volcanoclastic horizon of the Cadillac Group where two distinct facies were defined. Both facies underwent a pervasive sericite-chlorite-carbonate±albite alteration assemblage that predates gold mineralization. Gold is associated with two generation of auriferous quartz-carbonate-tourmaline veins and within fractures of corroded arsenopyrite grains, located proximal to the vein walls. A LA-ICP-MS study determined that neither textural type of arsenopyrite displayed refractory gold. Therefore, gold was not remobilized from arsenopyrite but instead, likely precipitated during formation of the quartz-carbonate veins. Gold precipitation is likely related to electrochemistry gold deportment where As-rich fractures within the corroded arsenopyrite acted as p-type conductors which attract the gold particles for precipitation.

Keywords

Arsenopyrite, quartz-carbonate veins, gold, Abitibi, tourmaline, n-p conductors

Summary for Lay Audience

The Orenada Zone 4 deposit is an Archean orogenic gold deposit situated southeast of Val d'Or, Québec in the southeastern Abitibi Greenstone Belt. The Abitibi greenstone belt is a structurally controlled region, widely recognized for gold production where it produces 81% of the gold in Canada. The Orenada deposit is associated with one of these gold producing structures, the Cadillac-Larder-Lake Deformation Zone where, mineralization is hosted within a felsic rock unit of the Cadillac Group rocks. Two distinct rock types have been identified, one is quartz rich and the other feldspar rich. Geochemical results determined that both rock types underwent the same pervasive alteration that predates gold mineralization. Mineralization is associated with two generations of quartz-carbonate-tourmaline veins and arsenopyrite, an arsenic-rich sulfide mineral that is associated gold within the selected study area. . However, there are two different textures of arsenopyrite however, gold is only observed within fractures of large deformed grains observed proximal to vein emplacement. Both textures display zonations of differing arsenic and sulphur concentrations. In the literature, mineralization associated with arsenopyrite exists commonly as refractory gold, where gold cations are trapped within the arsenopyrite mineral structure. However, chemical analyses of arsenopyrite in this study determined that neither textural type contains refractory gold. Therefore, the gold likely precipitated during the formation of the quartz-carbonate veins. It is proposed that gold was deposited by an electrochemical reaction where, arsenic-rich fractures within the arsenopyrite act as electron recipients which attract the gold particles.After examining all the visible gold particles within the investigated arsenopyrite grains, 86% of gold grains are observed within arsenic-rich regions, which supports the electrochemical deposition hypothesis. There is a lack of published articles on non-refractory gold associated with arsenopyrite, thus this thesis makes a very important contribution that can be applied to examining other arsenopyrite-rich gold deposits and used as a guideline for similar deposits within the Abitibi and on a global scale.

Acknowledgements

I would like to thank everyone who helped in the development and completion of this project. Firstly, I would like to thank my supervisor Dr. Robert Linnen for developing this project, for helping me through stressful times and for always believing in me. I would like to sincerely thank Alexandria Minerals Corp. specifically Philippe Berthelot for providing me with employment and for the support for sample collection. I would also like to thank Marc Beauchamp for helping with my EMPA data and, Dr. Iain Samson and J.C Barrette for helping me with LA-ICP-MS measurements and data reduction. Lastly, I would like to thank my family and friends for supporting me through this project, I wouldn't have been able to complete it without their constant support.

Table of Contents

Abstract ii

Keywords iii

Summary for Lay Audience iv

Acknowledgements v

Table of Contents vi

List of Abbreviations viii

List of Figures ix

List of Tables xiii

Chapter 1 1

1 Introduction 1

1.1 The Geology of the Superior Province 1

1.2 Regional Geology of the Abitibi Greenstone Belt 4

1.3 Deformation and Metamorphism 14

1.4 Gold Mineralization 16

1.5 The Orenada Deposit 17

1.6 Background information of arsenopyrite 21

1.7 Project Objectives 23

1.8 References 24

Chapter 2 32

2 Integrated Paper 32

2.1 Introduction 32

2.1.1 Regional Geology 34
2.1.2 Deposit Geology 38
2.2 Analytical Methods 47
2.3 Results 50
2.3.1 Petrography 50
2.3.2 Alteration 54
2.3.3 Ore Mineralogy 57
2.3.4 Whole Rock Lithogeochemistry 64
2.3.5 Arsenopyrite chemistry 83
2.4 Discussion 91
2.4.1 Timing of mineralization 92
2.4.2 Arsenopyrite 94
2.4.3 Gold deportment 99
2.5 Conclusions 103
2.5.1 Recommendations for future work 105
2.6 References 106
Appendix A : Drill hole sample locations……... 112
Appendix B : Thin section petrography……..... 115
Appendix C : Lithogeochemistry…… 143
Appendix D : Mass Balance results……..... 153
Appendix E : EMPA Data……. 156
Appendix F: LA-ICP-MS Data…….……. 200
Curriculum Vitae ……...214

List of Abbreviations

Asp=arsenopyrite

Qtz=quartz

Cb=carbonate

Tm= tourmaline

Fld=feldspar

Ser=sericite

Chl=chlorite

QV=Quartz volcanoclastic

FV=Feldspar volcanoclastic

PDDZ= Porcupine Destor Deformation Zone

CLLDZ= Cadillac Larder Lake Deformation Zone

PF= Parfouru fault

NVZ= Northern Volcanic zone

SVZ= Southern volcanic zone

EMPA = Electron microprobe analyses

BSE= Back-scatter electron

WDS= Wavelength dispersive spectrometers

EDS= Electron dispersive spectrometers

LA-ICP-MS = Laser ablation inductively coupled plasma mass spectrometry

List of Figures

Figure 1-1. Map of the Superior province divided into the 19 Subprovinces. Taken from Système d'information Géominière du Québec (SIGÉOM) 2

Figure 1-2. Abitibi greenstone belt showing the distribution of major deformation zones. Adapted from Dubé and Gosselin (2007) and Poulsen et al., (2000). 5

Figure 1-3. The main lithological units and major fault/deformation zones of the southern Abitibi and the Pontiac Subprovince of the Quebec side. Map adapted from Daigneault et al., 2002. 10

Figure 1-4. Deposition model for the Pontiac Group sediments and the southern Abitibi sediments and volcanics. Image taken from Davis, (2002) 13

Figure 2-1. Stratigraphic chart of the Rouyn, Malartic and Val d'Or areas with the relevant isotopic ages. Stratigraphic relationships are based on Dimroth et al., (1982), Mueller et al., (1996), Pilote et al., (1999), Davis, (2002), Scott et al., (2002) 35

Figure 2-2. Geological map of the southern Abitibi, Val d'Or area with the main lithological units. Adapted from Bedeaux et al., 2017..... 37

Figure 2-3. Plan view section of the Orenada deposit 40

Figure 2-4. Cross section of mineralized zone in Orenada Zone 4 deposit. Image taken from Alexandria Minerals Corp 2018 NI-43-101 Technical report. 41

Figure 2-5. Drill core samples of the Cadillac volcanoclastic rocks. 42

Figure 2-6. Drill core samples of the four different quartz (Qz)-carbonate (Cb) veins observed at the Orenada Zone 4 deposit 46

Figure 2-7. Photomicrographs of the QV ground mass with main penetrative foliation S_1 crenulated by S_2 foliation..... 51

Figure 2-8. Photomicrographs of quartz porphyroclasts with pre-kinematic textures..... 52

Figure 2-9. Photomicrographs of feldspar porphyroclasts with pre-kinematic textures 53

Figure 2-10. Photomicrographs of QV groundmass 54

Figure 2-11. Photomicrograph of albitization and chloritization of the FV groundmass. 55

Figure 2-12. Photomicrographs of tourmaline alteration. 56

Figure 2-13. Cross polarized photomicrographs of quartz-carbonate veins. 58

Figure 2-14. Reflected and transmitted light photomicrographs of arsenopyrite textures 60

Figure 2-15. Transmitted light photomicrographs of secondary sulphide minerals 62

Figure 2-16. Photomicrographs of free gold in V3A quartz±carbonate veins 63

Figure 2-17. Transmitted light photomicrographs of gold filling in fractures and pits of anhedral arsenopyrite grains 63

Figure 2-18. Tectonic classification of mafic igneous rocks (Cabanis and Lecolle, 1989) 65

Figure 2-19. REE Spider diagram normalized to chondrite (McDonough and Sun, 1995) 66

Figure 2-20. Box and whisker diagrams showing primary whole-rock lithogeochemical variations for major oxide group elements 67

Figure 2-21. Box and whisker diagrams showing primary whole-rock lithogeochemical variations for Au, As, S and B 69

Figure 2-22. As-S-Au-B graph of altered QV and FV samples 70

Figure 2-23. General Element Ratio (GER) diagram illustrating an alteration trend of Na and K from whole rock analyses 71

Figure 2-24. Immobile element binary plot of Zr vs. TiO_2 for all samples 75

Figure 2-25. Mass change binary plots which display alteration FV altered samples. Plots are defined as: A) SiO_2 % vs. K_2O %, B) FeO + MgO % vs. K_2O %, and C) CaO + Na_2O % vs. FeO + MgO %. 78

Figure 2-26. Mass and Percent change binary plots which display alteration of FV altered samples related to arsenopyrite, tourmaline and gold mineralization..... 79

Figure 2-27. Box and whisker plots representing mass and percent changes for the major oxide elements of the altered samples of FV rocks 80

Figure 2-28. Box and whisker plots representing mass and percent change for the four main elements associated with gold mineralization (Au, As, B, S)..... 82

Figure 2-29. EMPA back scatter electron (BSE) images of arsenopyrite grains with spot analysis points adjacent to their corresponding line plots of Fe, As and S..... 84

Figure 2-30. Binary As-S graph of all EMPA data points (n=174) from 14 arsenopyrite grains..85

Figure 2-31. WDS images of arsenopyrite grains with cobalt (Co) zonation..... 86

Figure 2-32. BSE images of arsenopyrite with ICP-MS traverses (red line) with accompanying signal intensity displayed in time (sec) by counts/second 89

Figure 2-33. Box and whisker plots representing the variation of trace elements measured by LA-ICP-MS for anhedral, subhedral and euhedral arsenopyrite grains 91

Figure 2-34. Paragenetic sequence for the timing of mineralization related to rock type, alteration, sulphidation, fabric and veins. 92

Figure 2-35. Box-and whisker plots of Co (ppm) concentrations in EMPA Spot data of euhedral/subhedral and anhedral/corroded arsenopyrite grains..... 95

Figure 2-36. Binary Au (ppm) vs. Co (ppm) plot from LA-ICP-MS results of both euhedral/subhedral and anhedral/corroded arsenopyrite grains..... 98

Figure 2-37. Corroded arsenopyrite grain with visible gold within a fracture. Visible gold is observed in light As-rich region of the grain. 103

List of Tables

Table 1-1. Lithotectonic assemblages of the southern Abitibi Subprovince (Ontario) and their corresponding isotopic ages, rock types and volcanic chemical affinity. Data compiled from Ayer et al. 2002, Ayer et al. 2005, Thurston et al., 2008 and Monecke et al., 2018. 7

Table 1-2. Lithotectonic groups of the southern Abitibi Subprovince (Quebec) and their corresponding isotopic age ranges, rock types and volcanic chemical affinity. Data compiled from Mortensen, 1993; Pilote et al., 1999; Davis, 2002; Ayer et al. 2005, Thurston et al., 2008; Pilote et al., 2015a; Bedeaux et al., 2017) 8

Table 1-3. Summary of the 2015-2017 drilling programs conducted at Orenada Zone 2 & 4 modified after Carrier et al., 2018..... 19

Table 2-1. Characteristics and structural timing of quartz carbonate veins found at the Orenada zone 4 deposit 44

Table 2-2. The average detection limit for each element (ppm) measured by Electron microprobe analysis (EMPA)..... 49

Table 2-3. The average detection limit of each isotopic element (ppm) measured by Laser Ablation Induced Coupled Spectrometry (LA-ICP-MS)..... 50

Table 2-4. Paragenetic sequence of QV and FV rock types 64

Table 2-5. Mean, median, maximum and minimum values of elements for segments of LA-ICP-MS traverses of different arsenopyrite textures..... 90

Table 2-6. Average Co (ppm) values for the different electron microprobe (EMPA) spot analysis for all location of both arsenopyrite textures..... 96

Chapter 1

1 Introduction

1.1 The Geology of the Superior Province

The Superior Province (Figure 1-1), which is the core of the Canadian shield, is an Archean craton that spans approximately 1,400,00 km^2 from Quebec, to Manitoba and is mostly Archean in age ranging from 3.1-2.6 Ga, with the exception of some Proterozoic and Phanerozoic rocks (Card, 1990). The northeastern region of the Superior Province is divided into two large terranes (the Hudson Bay Terrane and the Arnaud River Terrane), which highlight the evolution of the Archean crust. The Hudson Bay Terrane in the south-west shows evidence of Eoarchean crust (<3600 Ma), being some of the oldest rocks on Earth (Simard et al., 2008).

The Superior Province used to be more extensive, however, it is now surrounded and truncated by Proterozoic orogens likely caused from several collision and accretionary events (2720-2680Ma; Percival et al., 2006) between Archean-aged proto-continental terranes (Card, 1990; Percival et al., 2012) that occurred between 2680 and 2600 Ma (Percival et al., 2012). The northern, western and south-eastern boundaries of the Superior Province are tectonic, marked by thrust and strike-slip faults. The southern and north-eastern boundaries are unconformably overlain/over thrusted by Paleoproterozoic sequences (Card, 1990, Card and Poulsen, 1998).

The Superior Province can be further divided into 19 subprovinces where four different types lithologies are predominant: metasedimentary, metamorphic, volcano-plutonic and plutonic (Card, 1990) (Figure 1-1). Most of the Subprovinces are linear and are bounded by subparallel boundary faults. Subprovinces typically trend east-west in the south, west-northwest in the northwest and northwest in the northeast (Percival, 2007). More than half of the Superior Province, 740,000 km^2, is located in Quebec, where Subprovince are divided into two major zones, the southern zone and the northern zone. The southern zone is comprised of alternating linear east-west trending metasedimentary Subprovince (Pontiac, Nemiscau and Opinaca), volcano-plutonic (Abitibi, Opatica and La Grande) and metamorphic (Ashuanipi) Subprovinces. The Minto Subprovince makes up the northern zone, which is mostly plutonic in origin. The

Minto block is further divided into 6 domains (the Inukjuak domain, the Tikkerutuk domain, the Lake Minto domain, the Goudalie domain, the Utalik domain and the Douglas Harbour domain) defined by the basis of lithology, isotopic age constraints, structural trends and magmatic intensities (Percival et al., 2007).

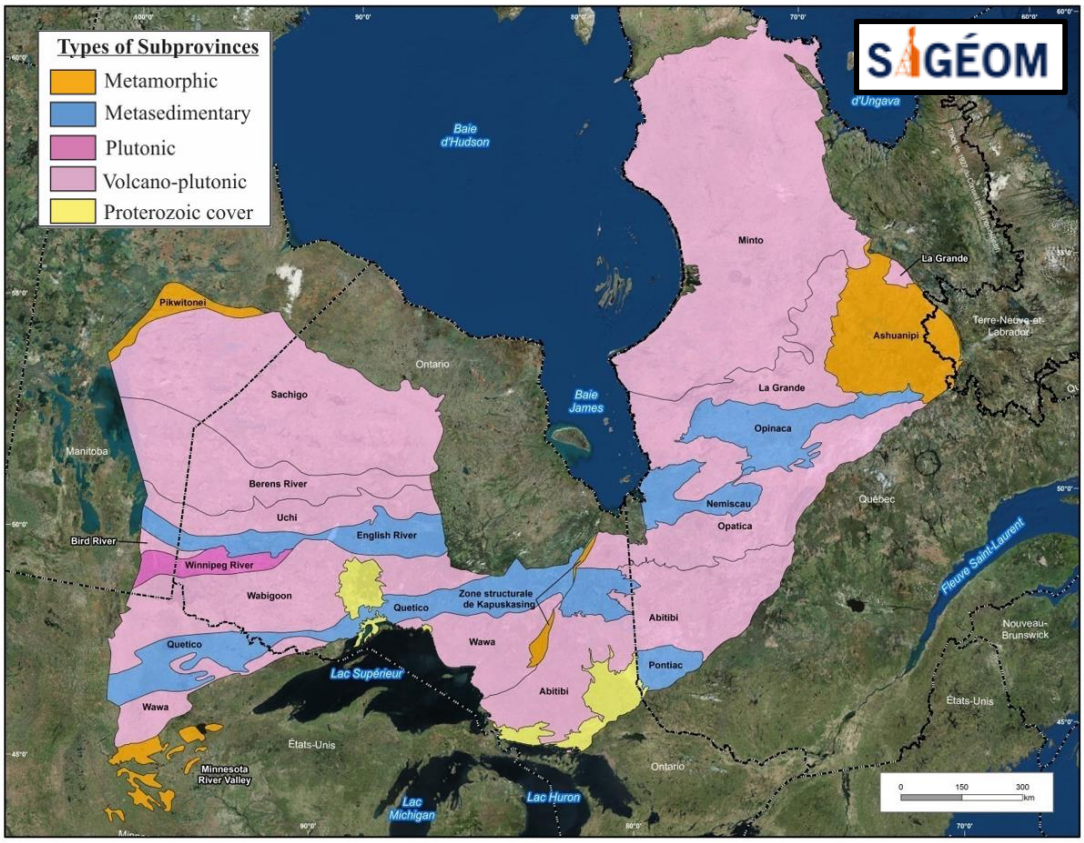

Figure 1-1. The Superior province divided into the 19 Subprovinces. Taken from Système d'information Géominière du Québec (SIGÉOM)

The Superior Province contains numerous mineral deposits and is home to many world-class deposits of different styles. Many of the mineral deposits are Archean in age however there are also a large number of non-Archean mineral occurrences, some of these include: Ni-Cu mineralized mafic sills within the lower Huronion strata, uranium mineralization in basal Huronion strata, the silver-rich veins and sills of the Paleoproterozoic Cobalt deposit, the Ni-PGE deposits of the Sudbury Intrusive complex assumed to be generated by a meteorite impact

at about 1.85Ga (Davis, 2008), and kimberlite clusters of Proterozoic and Mesozoic ages (Heaman and Kjarsgaard, 2000ke; Percival, 2007; Davis, 2008).

In terms of Archean-aged mineral deposits, most deposits are related to the many tectonic, plutonic and orogenic events within the geologic history of the Superior Province. Volcanogenic massive sulphide (VMS) deposits in the province have been interpreted to reflect a north to south younging and are associated with high temperature magmatism from rifted arc, back-arc and plume arc environments in continental or oceanic settings (Hannington et al., 1999a; Percival, 2007). A world-class example is the Kidd Creek deposit situated in western part of the Abitibi Subprovince where Hannington et al. (1999), reported >138.7 million tons with an average grade of 2.35 percent Cu, 6.5 percent Zn, 0.23 percent pb and 89g/t Ag. Magmatic Cu-Ni-PGE deposits within the Superior Province occur in various settings like Kambalda-type komatiitic deposits within the Abitibi Subprovince or, intrusion-hosted deposit like those associated with sanukitoid rocks (Entwine Lake) or mantle derived gabbro (Big Trout Lake) (Percival, 2007). Fractionated pegmatites are wide-spread within the Superior Province and contain rare element mineralization (Li, Cs, Rb, Be, Ta, Nb, Ga, Tl, and Ge; Breaks et al., 2005) usually along faults within volcanic-plutonic terranes or, along the margins of metasedimentary terranes (Percival, 2007). The pegmatites represent the youngest Neoarchean event (2.66 to 2.64 Ga; Corkery et al., 1992; Percival, 2007).

The Superior Province is particularly rich in gold, and the province contributes 86% of the gold production in Canada (Dubé and Gosselin, 2007). Most of these gold deposits are classified as orogenic gold deposits, were formed during collisional orogeny and subsequent faulting where, the formation of gold mineralization is associated with the movement along these faults and later through fluid flow along the fault pathways (Robert and Poulsen, 1997; Dubé and Gosselin, 2007, Percival, 2007). These deposits are strongly related to fault and shear zones however, host rock type and alteration play an important part in the formation of the deposits (Dubé and Gosselin, 2007). Gold deposits in the Superior province reflect a southward younging where gold showings in the north (Red Lake camp, Stull Lake) report ages around 2.72 Ga whereas in the southeast (Abitibi terrane) younger ages of around 2.68 Ga are reported (Dubé and Gosselin,

2007; Wong et al., 1991). This is consistent with the idea that gold mineralization may have occurred in multiple phases (Dubé et al., 2004; Percival, 2007).

1.2 Regional Geology of the Abitibi Greenstone Belt

When referencing gold production in the Superior Province the Abitibi Subprovince, the southernmost Subprovince of the Superior Province, is a highly recognized powerhouse for gold where the Subprovince produces more than 4500t of Au hosted in lode gold, intrusion and Au-rich VMS deposits (Dubé and Gosselin, 2007; Monecke et al., 2018). However, most of the gold deposits within the Abitibi are considered to be orogenic gold deposits, also termed mesothermal and lode (Dubé and Gosselin, 2007). The Abitibi is home to many gold camps (Kirkland Lake, Timmins, Val-d'Or, etc. Dubé and Gosselin, 2007) which are associated with large crustal scale east-west trending fault zones, also referred to as deformation zones (Robert, 1989; Neumayr et al., 2000). North-south trending faults are also observed within the Abitibi however these faults generally occur along the borders of large plutonic bodies, like the Bourlamaque Pluton (Card, 1990).

The Abitibi Subprovince is bound by the Opatica Subprovince to the north, the Kapuskasing structure to the west, the Pontiac Subprovince to the southeast and the Grenville Tectonic Front to the south (Figure 1-1). In general, the Abitibi Subprovince consists of metavolcanic, metasedimentary, and intrusive rocks that have been metamorphosed to variable grades. The Abitibi Subprovince contains the Abitibi greenstone belt (Figure 1-2), which is 700km east to west, 350km north to south, that occurs in the southeastern part of the Abitibi Subprovince of Ontario and the southwestern part of Quebec (Monecke et al., 2018). The greenstone belt is comprised of sequences of folded volcanic and sedimentary rocks with various intrusive bodies (Monecke et al., 2018). A number of unconformities and disconformities are also observed throughout the subprovince, usually observed within the metasedimentary rock assemblages.

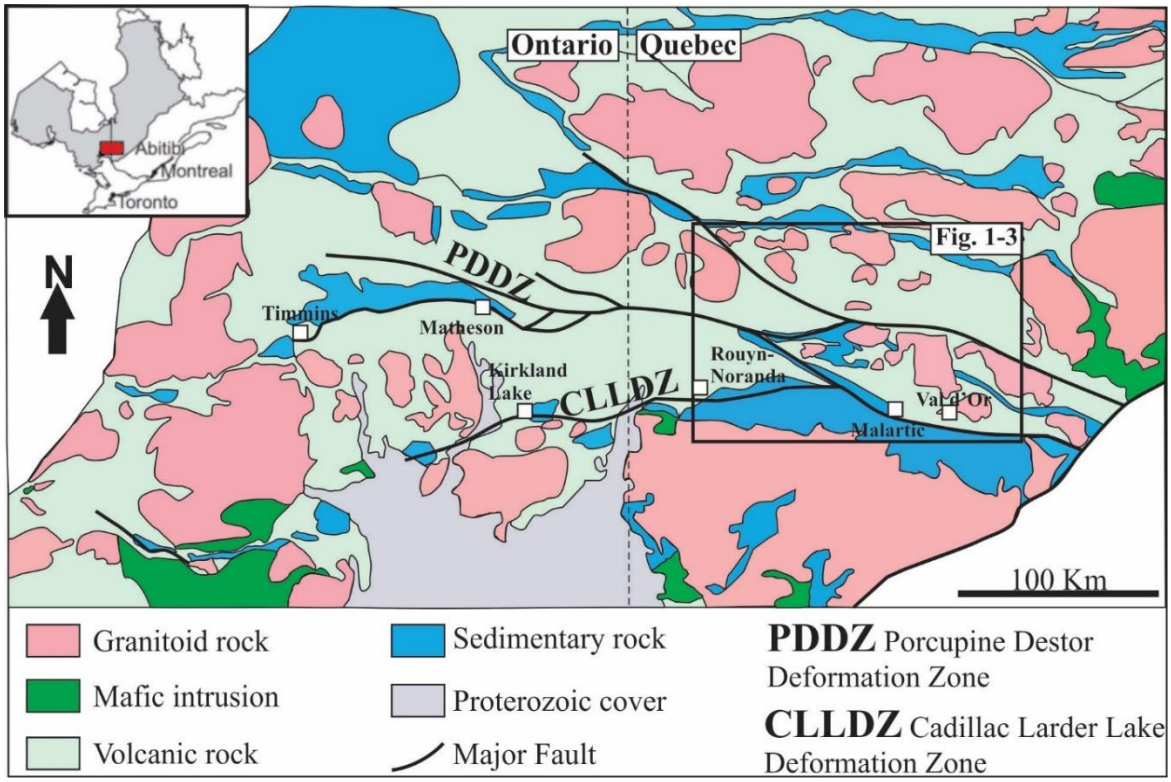

Figure 1-2. Abitibi greenstone belt showing the distribution of major deformation zones. Adapted from Dubé and Gosselin (2007) and Poulsen et al., (2000).

The formation of the Abitibi Subprovince was once thought to have formed from the merger of allochthonous terranes (Corfu et al., 1993). However, Ayer et al., (2002) proposed that the Abitibi Subprovince is instead a series of autochthonous layers which were deposited by in-situ volcanic and sedimentary events. This theory is supported by the observation that key assemblages are laterally extensive across the greenstone belt (Ayer et al., 2002). An example supporting autochthonous construction in the Abitibi has been made by Thurston et al., (2008), who interpreted that the deposition of sedimentary units between volcanic units in fact represents periods of slow or discontinuous deposition between active volcanism. Although assemblages are assumed to be laterally extensive, no complete stratigraphic succession of known lithologies is observed. This is likely due to the irregular distribution of volcanics and sediments during synvolcanic deformation events (Ayer et al., 2002). Due to intense folding and thrusting it is

possible that deformation may have been heterogeneous throughout the subprovince (Ayer et al., 2002).

The Abitibi Subprovince can be further divided into two sections, the Northern volcanic zone (NVZ) and the southern volcanic zone (SVZ). The two zones are interpreted to represent two volcanic arcs which are now separated by the Destor-Porcupine Deformation Zone (PDDZ; Chown et al., 1992; Mueller et al., 1996, Daigneault et al., 2002). The arc development commenced with the NVZ (2730-2705 M) followed by the SVZ (2705-2700 Ma) (Chown et al., 1992; Mueller et al., 1996; Daigneault et al., 2002). Arc development was followed by NVZ-SVZ arc-arc collision, which was characterized by transpression and thrusting between 2700-2690 Ma. Lastly, terrane docking, and strike slip tectonics followed (2690-2680 Ma) (Chown et al., 1992; Mueller et al., 1996; Daigneault et al., 2002). The NVZ is interpreted as an intact arc segment composed of two volcanic cycles which, according to Chown et al., (1992), are interpreted as volcanic edifices which formed on the Archean ocean floor. The SVZ is composed of packages of ultramafic to felsic volcanics and sedimentary rocks units that trend east-west and dip strongly to the north (Card, 1990; Chown et al., 1992; Pilote et al., 1999; Dimroth et al., 1982 Pilote et al., 2015). The main rock units of the SVZ are intruded by several plutonic bodies of varied granitic compositions (Chown et al., 2002). Metamorphic grades in the SVZ ranges from sub-greenschist to amphibolite facies (Dimroth et al., 1983b; Imreh, 1984).

In general, the Abitibi Subprovince can be divided into eight major assemblages, two of which are metasedimentary and six are lithotectonic. They are, from oldest to youngest, the Pacaud Assemblage, the Deloro Assemblage, the Stroughton-Roquemaure Assemblage, the Kidd-Munro Assemblage, the Tisdale Assemblage, the Blake-River Assemblage, the Porcupine Assemblage and the Timiskaming Assemblage. The lithologies and isotopic ages of each Assemblage are presented in Table 1-1. Broadly, volcanism extends from about 2750 to 2696 Ma concluding with the deposition of the Blake River Assemblage. The volcanism was followed by the deposition of two sedimentary sequences. The first is the Porcupine Assemblage (2690-2685 Ma) which is defined by a period of marine sedimentation with the addition of calc-alkaline volcanics (Corfu, 1993; Ayer et al., 2002). The second is the Timiskaming Assemblage (2676-

2670 Ma) which is defined by a period of terrestrial sedimentation with periods of alkaline volcanism (Corfu, 1993; Ayer et al., 2002).

Table 1-1. Lithotectonic assemblages of the southern Abitibi Subprovince (Ontario) and their corresponding isotopic ages, rock types and volcanic chemical affinity. Data compiled from Ayer et al. 2002, Ayer et al. 2005, Thurston et al., 2008 and Monecke et al., 2018.

Assemblage	**Related ages (Ma)**	**Rock types**	**Volcanic chemical Affinity**
Timiskaming	2676-2670	Polymictic conglomerate, with distinct jasper clasts, sandstone; mafic to intermediate volcanics.	Alkalic to calc-alkalic
Porcupine	2690-2685	Turbiditic sediments (argillite to wacke), minor conglomerates and localized banded iron formations.	Calc-alkaline
Blake River	2703-2698	Mafic to felsic volcanics	Tholeiitic basalt to calc-alkalic basalts and andesites
Tisdale	2710-2703	Ultramafic, mafic and felsic volcanics with minor iron formations	Komatiitic, tholeiitic basalts and calc-alkalic volcanics
Kidd-Munro	2719-2711	Ultramafic, mafic and felsic volcanics with minor iron formations	Tholeiitic to komatiitic, and calc-alkaline volcanics.
Stroughton-Roquemaure	2723-2720	Ultramafic, mafic and local felsic volcanics.	Komatiitic, magnesium and iron rich tholeiitic basalts and calc-alkalic volcanics
Deloro	2730-2724	Mafic, intermediate and felsic volcanics capped by a regionally extensive banded iron formation.	Calc-alkaline with minor tholeiites
Pacaud	2750-2735	Ultramafic, mafic and felsic volcanics with minor iron formations	Komatiitic, tholeiitic and calc-alkalic

The above assemblages are largely defined from sequences of the Abitibi Subprovince in Ontario and most of them do not directly correlate to the rocks in Quebec. However, some of the groups

referred to on the Quebec side directly correspond to isotopic ages and rock types of the Ontario assemblages. The Quebec groups and their corresponding rock types, formations and isotopic ages will be discussed below.

The south-eastern part of the Abitibi Subprovince in Quebec is situated in the SVZ where four main lithotectonic groups are defined. These groups are, from oldest to youngest: the Malartic Group, the Louvicourt Group, the Cadillac Group and the Timinskaming Group. Details of the ages, rock types, chemical volcanic affinity and related formations are listed in Table 1-2 and their distributions are presented in Figure 1-3.

Table 1-2. Lithotectonic groups of the southern Abitibi Subprovince (Quebec) and their corresponding isotopic age ranges, rock types and volcanic chemical affinity. Data compiled from Mortensen, 1993; Pilote et al., 1999; Davis, 2002; Ayer et al., 2005, Thurston et al., 2008; Pilote et al., 2015a; Bedeaux et al., 2017; Bedeaux et al., 2018)

Group	Formations	Related ages (Ma)	Rock types	Volcanic chemical Affinity
Timiskaming	-	2677-2672	Polymictic conglomerate, with distinct jasper clasts, sandstone; mafic to intermediate volcanics.	Alkalic to calc-alkalic
Piche*	-	2680	Mafic to ultramafic, sheared volcanics	-
Pontiac*	-	2685	greywacke, siltstone, mudstone, monomictic conglomerate	-
Kewagama	-	2686-2684	Turbidites, greywackes, mudstones and minor conglomerate and banded iron formations	-
Cadillac*	-	2687	Turbidites, greywackes, mudstones and minor conglomerate and banded iron formations	-

Blake River	-	2703-2698	Mafic basaltic flows and, basaltic to andesitic volcanics	Tholeiitic to calc-alkali
Louvicourt*	1. Héva* 2. Val d'Or	2704-2699	Mafic flows and pillow basalts, andesitic volcaniclastics	Calc-alkalic to tholeiitic
Malartic	1. Jacola 2. Dubuisson 3. Lamotte-Vassan	2714-2704	Ultramafic komatiitic flows and basaltic to andesitic volcanics	Komatiitic, tholeiitic and calc-alkalic

*units observed at the Orenada Zone 4 deposit

Two main volcanic segments make up the SVZ. The first, is the Blake River Group (2703-2698 Ma), which is considered an oceanic arc island made up of tholeiitic basalts overlain by calc-alkaline mafic to felsic volcanics (Dimroth et al., 1982; Mortensen, 1993; Daigneault et al., 2002). The second, the Malartic Group (2714-2701 Ma) also referred to as the Malartic composite block is considered a collage of different tectonic domains (Dimroth et al., 1982; Desrochers et al., 1993; Scott et al., 2002).

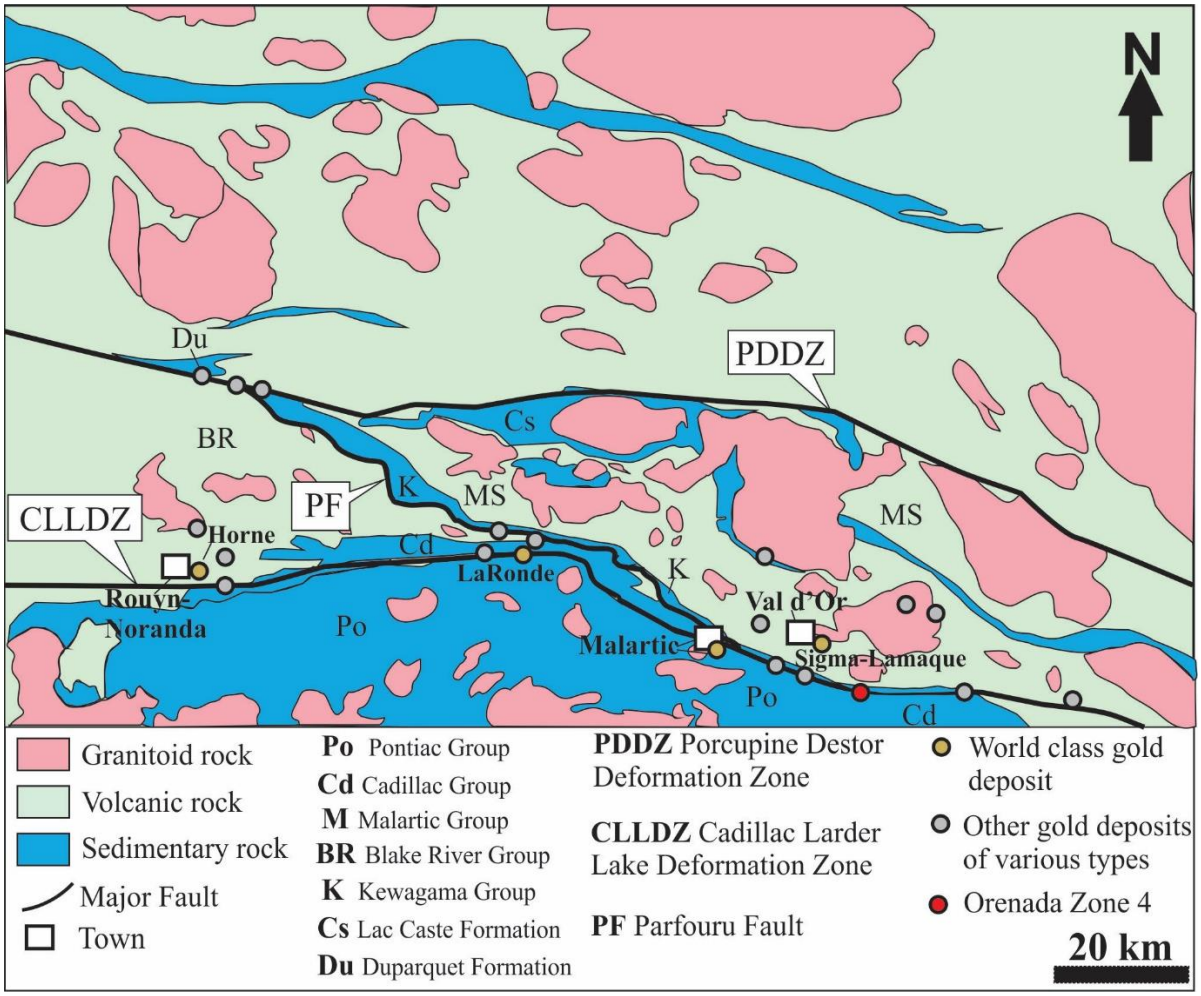

Figure 1-3. The main lithological units and major fault/deformation zones of the southern Abitibi and the Pontiac Subprovince of the Quebec side. Map adapted from Daigneault et al., 2002.

The eastern Malartic segment is divided into two main Groups: The Malartic Group and the Louvicourt Group. These groups represent both subduction and plume generated volcanism (Daigneault et al., 2002; Scott et al., 2002). The Malartic Group (2714–2703 Ma) is composed of komatiitic flows, and basaltic to andesitic volcanic rocks which are interpreted to reflect a deep ocean-floor volcanic environment (Dimroth et al., 1982; Scott et al., 2002; Bedeaux et al., 2018). It is composed, from oldest to youngest of the La Motte–Vassan Formation (2714±2 Ma), the

Dubuisson Formation (2708±2 Ma), and the Jacola Formation (2706±2 Ma). The Louvicourt Group (2704-2699 Ma) is composed of massive to pillowed mafic flows and felsic volcanoclastic horizons that conformably overly the Malartic Group. This Group represents a transition towards arc volcanism (Scott et al., 2002). The Louvicourt Group is made up of the Val d'Or Formation (2704±2 Ma), which is synchronous with the Jacola Formation, and the Héva Formation (2702 ±1 Ma). Both formations are intruded by diorite and gabbro dykes and sills (Pilote et al., 1999; Zhou and LaFrance, 2017).

Many synorogenic (2700-2687 Ma; Daigneault et al., 2002) flysch-type sedimentary assemblages are observed on the margins of the outline the Malartic Group. Two of these include, the Cadillac Group and the Kewagama Group. The Cadillac Group (2686±2 Ma) overlies the Louvicourt Group and consists of sedimentary rocks, dominantly turbidites, greywackes, mudstones and minor sequences of conglomerate and banded iron formations as well as some volcanoclastic rock units (Davis, 2002; Bedeaux et al., 2018). The Kewagama Group (2684 Ma) is a turbiditic sedimentary basin which straddles the Parfouru Fault, that separates the Malartic Group to the east and the Blake River Group to the west (Dimroth et al., 1982; Daigneault et al., 2002).

The Pontiac Group (2685 Ma) is located south of the CLLDZ (Figure 1-3) within the Pontiac Subprovince. It consists of greywacke, siltstone, mudstone, rare monomictic conglomerate layers and ultramafic to felsic intrusions (Dimroth et al., 1982; Davis, 2002; Perrouty et al., 2017). U-Pb detrital zircon ages show that deposition of the Pontiac basin is coeval with the turbiditic Cadillac sediments (Davis, 2002). The formation of the Pontiac Subprovince is interpreted to have formed from the collision of either a foreland accretionary wedge or, an exotic terrane with the Abitibi Subprovince. It then likely developed as a sedimentary basin adjacent to the Abitibi Subprovince (Davis, 2002). Davis, (2002) reported that the deposition of the sediments in the Pontiac group are coeval with the Cadillac and Kewagama sediments in the southern Abitibi Subprovince.

Davis, (2002) proposed a model for the formation and deposition of the Pontiac Group sediments and the sedimentary and volcanic rocks of the numerous southern Abitibi groups. At around 2685 Ma the environment was one of oceanic crust subduction and uplift of an extinct 2700Ma arc. Compression of the back-arc results in the deposition of locally-derived sediments in a back-arc basin (Abitibi). Over time the arc completely eroded, which resulted in arc sedimentation (Pontiac) (Figure 1-4A). Major fold-thrust events occur between 2685 and 2680 Ma that caused the back-arc complex and its sediments to be folded and burial of the arc sediments (Figure 1-4B). Between 2680 and 2670 strike-slip movement continued along a decollement at the base of the arc sediments (Pontiac), which was followed by high-angle thrust faults that cut through both the folded back-arc rocks and the buried arc sediments. The exposed parts of the tectonically layered crust were eroded, which included slivers of the Abitibi metavolcanic and metasedimentary units. Lastly, the strike-slip movement along the faults resulted in the deposition of late alluvial lacustrine sedimentary basins such as those filled by the Timiskaming and Duparquet groups (Figure 1-4C).

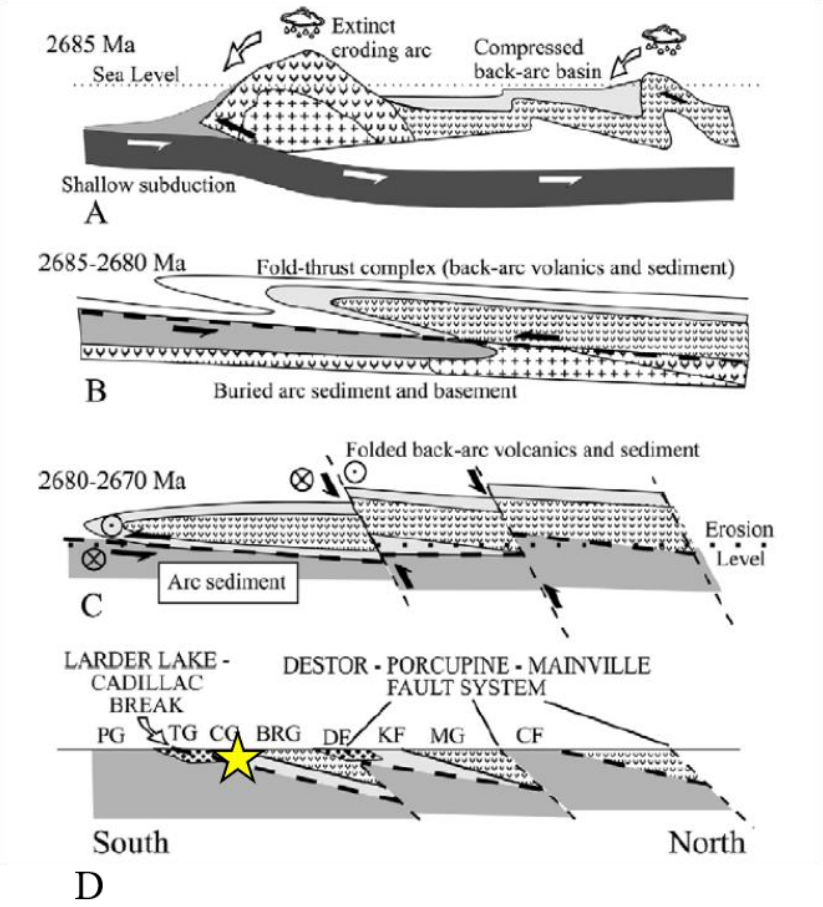

Figure 1-4. Deposition model for the Pontiac Group sediments and the southern Abitibi sediments and volcanics. Image taken from Davis, (2002). The star indicates the presumed setting of the Orenada deposit

The Piché Group, observed south of the Cadillac Group and north of the Pontiac Group, is a <2 km thick band of highly strained ultramafic to mafic volcanic rocks that is interpreted to represent the CLLDZ (Dimroth et al., 1982; Simard et al., 2013; Bedeaux et al., 2018). This group is composed of tholeiitic basalts, komatiites (talc schists), porphyritic andesites and calc-alkaline tuffs that are crosscut by felsic to mafic dykes and sills (Dimroth et al., 1982; Imreh, 1984; Simard et al., 2013). However, in some regions the Piché Group is absent, and the Cadillac Group is in contact with the Pontiac Group.

The rocks in the Val d'Or area are intruded by several late granitoid plutons, dykes and sills. Most notably in the area of the present study, is the East Sullivan pluton (2684±1 Ma) a felsic alkaline pluton that intruded the Val d'Or and Héva formations (Lavoie, 2003).

1.3 Deformation and Metamorphism

The Abitibi Subprovince has a complex structural history with many different deformation events. Some of these events overprint each other making the timing of the different deformation events hard to define. Orogenic gold mineralization in the Abitibi Subprovince is related to two major east-west trending regional strike-slip faults (also referred to as deformation zones), which both span over 200 km E-W in both Ontario and Quebec. They are, the Porcupine-Destor Deformation Zone (PDDZ) and the Cadillac-Larder-Lake Deformation Zone (CLLDZ) (Figure 1-3). Most gold deposits in the Abitibi are scattered along these first order deformation zones and their 2nd and 3rd order offsets (Neumayr et al., 2000).

The PDDZ and the CLLDZ both display numerous styles of deformation and are interpreted to be long-lived structures with complex histories. For this reason, both deformation zones are interpreted to be polyphase with continuous reactivation along strike (Daigneault et al., 2002). Ductile deformation along the CLLDZ is thought to have begun slightly after the PDDZ, post 2675 Ma. A change from left-lateral to right-lateral strain was also constrained from dating to have occurred at around 2669 Ma (Bateman et al., 2008).

The SE-tending Parfouru fault (PF) lies between the PDDZ and the CLLDZ (Figure 1-3). The PF does not crosscut either major E-W trending deformation zone, but it is associated with the turbiditic Kewagama basin (2684 Ma; Davis, 1991), which links both major deformation zones (Daigneault et al., 2002). It is interpreted that because the PF and Kewagama basin separate the Malartic and Blake River volcanic assemblages, that they must have been active during volcanism and sedimentation (Daigneault et al., 2002). The PF represents an early fracture system that developed during the NVZ–SVZ accretion and, was continuously reactivated during the ongoing Abitibi Subprovince tectonism. Numerous phases of gold mineralization in the region are strongly associated with the continued reactivation along the CLLDZ, where gold-rich

fluids were mobilized along the fault zone (Daigneault et al., 2002; Ayer et al., 2005; Bleeker, 2012). It is important to note, that although the PDDZ and the CLLDZ span portions of Ontario and Quebec, each region along the deformation zones has different deformational events. In this chapter only the deformational events on the Quebec side associated with the CLLDZ are discussed.

Many authors (Dimroth et al., 1983; Daigneault et al., 2002; Scott et al., 2002; Neumayr et al., 2000, 2002; Lafrance, 2015; Bedeaux et al., 2017, Perrouty et al., 2017, etc.) refer to different deformation events by different numerical values however, this report will follow the deformation events defined by Robert (1989, 1990) which is specifically focused on the Val d'Or area.

Deformation is characterized by two main ductile deformation events (D1 and D2), which are considered to be multiphase. Brittle structures related to a late deformation event (D3) are developed locally.

D1 is defined as an early, pre-metamorphic, ductile, north-south shortening event that is characterized by an E-trending, subvertical, penetrative schistosity (S_1), accompanied with a steeply east-plunging stretching lineation and tight isoclinal folds (F1) (Robert, 1989). During D1, the rocks experienced northerly directed shortening and a subvertical stretching, which Robert, (1989) credits to locally derived dip-slip movements and synchronous dextral transcurrent shearing. This D1 event is responsible for most of the structural framework of the Abitibi and represents deformation in the area which occurred over a long period of time. S_1 may have overprinted fabrics of previous deformational events thus, erasing evidence of past events (Bedeaux et al., 2017).

D2 is defined as a NE-SW shortening event that caused regional, dextral strike-slip faulting along the CLLDZ. D2 is most notably characterized by the development of shallowly plunging, meter-to-kilometer-scale asymmetric Z-shaped F2 folds (Figure 1-4B). F2 folds are spatially associated with several gold deposits along the CLLDZ. D2 is responsible for NE-SW steeply

dipping foliation S2, which crenulated S1 and is best developed in the F2 fold hinges. Structures associated with D2 are locally overprinted by late dextral strike-slip reactivation along the CLLDZ. The D2 event was continued until 2682 Ma, which is constrained by detrital zircon ages of the sedimentary rocks bounded by the Malartic segment (Davis, 1991).

Metamorphism within the south-eastern Abitibi (Val d'Or, Cadillac, Malartic, etc.) occurred between 2680 to 2643 Ma and reached lower-greenschist to greenschist facies (Powell et al., 1995). Upper-greenschist to lower amphibolite facies metamorphism is only observed at the borders of large batholiths (Corfu, 1993; Bateman et al., 2008). By contrast, the neighboring Pontiac Subprovince has been metamorphosed to amphibolite facies (Daigneault et al., 2002), thus there is a strong contrast in metamorphic grades of the two subprovinces. The juxtaposition of metamorphic grades across the CLLDZ is interpreted to reflect a structural displacement of 5 to 7 km. This displacement is attributed to both extensional and vertical components of movement along the CLLDZ (Daigneault et al., 2002; Neumayr et al., 2002).

1.4 Gold Mineralization

The exploration for gold within the southern Abitibi, more specifically the Val d'Or region, has a complex history. Prospectors began exploring the region since 1910 when it became obvious that a large crustal scale fault first observed in the Kirkland Lake area (now referred to as the Cadillac Larder lake Fault) continued into Quebec, through the Cadillac township (Gourd, 1983). Between 1910 and 1921 there was a surge in gold prospecting with that led to the discovery of several deposits, including the Beattie, Siscoe and Sullivan deposits. It wasn't until 1923 when Robert Clark discovered a large gold vein in the district of Bourlamque thus, sparking the discovery of the Lamaque deposit. The Lamaque mine is a one of the most renowned gold mines within the Southern Abitibi and within Canada. The Lamaque mine was opened in 1935 and by the end of 1937 the mill increased operations to 1000 tonnes per day. The very rich deposit was exploited from 1935 to 1985 and produced over 4.5 million ounces of gold.

Gold occurrences are spatially associated with the crustal scale CLLDZ along second and third order structures however, gold within the main first order fault is rare and extremely localized

(Kerrich, 1989; Robert et al., 1990; Neumayr et al., 2000). The CLLDZ is considered to be the main conduit for gold-bearing hydrothermal fluids in the Val d'Or camp which, is interpreted by the spatial relationship between the fault zones, and hydrothermal alteration found within the camp (Robert et al., 1990; Neumayr et al., 2000).

Two main generations of gold have been reported within the Val d'Or area. The oldest mineralization was emplaced pre- to syn-D2 and the ore bodies are highly strained by the D2 asymmetric Z-shaped folds. An example of this is at the Orion deposit, where gold was initially emplaced during D1, but was later remobilized during D2 (Trudeau and Raymond, 1992). Another example is the upper portion of the Kiena mine where the ore zone is located in the hinge zone of an asymmetric D2 fold (Morasse, 1998).

The second generation is interpreted as a younger, late- to post-D2 mineralization event where deposits did not experience much deformation after gold emplacement (Couture et al., 1994). This young event is defined by shear-hosted quartz-carbonate-tourmaline±scheelite veins that were emplaced as subhorizontal extension veins (Couture et al., 1994). These veins have been reported to crosscut all rock types except Proterozoic dykes (Couture et al., 1994; Robert and Brown, 1986). An example is at the Sigma deposit where mineralization is hosted in quartz-tourmaline veins where microstructural textures illustrate that the gold deposition post-dates metamorphism and deformation (Robert and Brown, 1986). Rutile associated with mineralization have been dated by the U-Pb method as 2599±9 Ma at the Sigma deposit and 2593±5 Ma at the Lamaque mine (Jemielita et al., 1990; Wong et al., 1991).

1.5 The Orenada Deposit

The Orenada property is situated 8 km south-east of the city of Val d'Or, Quebec within the historical Val d'Or gold camp of the Abitibi greenstone belt. There are 5 zones of mineralization located on the property, however the focus of this research is Zones 4 and 2**.** Both zones share the same lithological units, vein types, alteration assemblages and style of sulphide mineralization. Therefore, both zones will now be referred to as simply the Orenada deposit unless each zone is specifically mentioned.

The Orenada deposit has a long history within the Val d'Or mining camp. Gold mineralization was first discovered on the Orenada property in 1933 by Quebec Gold Belt Mines Ltd, by prospecting an outcrop near the present Zone 2 gold showing. It wasn't until 1939 that the Zone 4 gold occurrence was discovered by a magnetic anomaly detected in an overburden covered area (Robert et al., 1990). Between 1939 to 1975 only limited drilling and exploration was undertaken on the Zone 4 deposit including three brief drilling campaigns and six different geophysical surveys (Robert et al., 1990; Beauregard and Gaudreault, 2008). In 1980 the soaring price of gold provoked new owners, Brominco Inc., to start a major drill program with the objective of outlining reserves for an open pit deposit. The drilling resulted in defining an estimated reserves at 263,393 tonnes with a grade of 2.7g/t Au which lead to the excavation of a small open pit. Mining extracted 16,071 tonnes of bulk sample which was processed however, only 26.8 kg of gold (1.4 g/t Au, average grade) and 3 kg of silver were recovered. The low recovery caused the closure of the small open pit. In 1983, Aur Resources Inc. acquired controlling interest of the Orenada deposit from Brominco and fully reinterpreted the existing drill data during which they presumably identified an unnoticed extension of the mineralized body. In 1984, a drill program tested their theory, which resulted in the definition of new reserves down plunge of Zone 4 totalling 598,214 tonnes at 5.5 g/t Au to a vertical depth of 260 m (Robert et al., 1990; Beauregard and Gaudreault, 2008). In 1985 Brominco merged with Aur Resources Inc. and embarked on an underground exploration drilling program with, a 275 m shaft, 1,100 m lateral development work on two levels and, 19,200 m of definition drilling. Underground exploration ceased in 1987 because the program revealed that the auriferous veins were strongly folded with a complex geometry that was not readily agreeable to underground mining (Robert et al., 1990). However, underground exploration defined a large low-grade reserve at 195,357 tonnes at 1.7 g/t Au. Aur Resources continued a brief drilling program and geophysical surveys of Zone 4 however, in 2007 the deposit was acquired by Alexandria Minerals Corp. Alexandria conducted small drill programs in 2007 and 2008 however, their most extensive drilling campaigns were conducted from 2015 to 2017, where drill holes were planned to intercept interpreted veins and structural features (Savard et al., 2018). The details from each

year's drill program are listed in Table 1-3. In 2019 the entire Orenada property was acquired by O3 mining.

Table 1-3. Summary of the 2015-2017 drilling programs conducted at Orenada Zone 2 & 4 modified after Savard et al., 2018

Program	Number of drill holes	Meters drilled	Location	Purpose of drill project
2015	3	844	Zone 4	• To test the new geological model of auriferous high-grade, flat-dipping veins
2016	11	4,018	Zone 2 & 4	• To continue to test the new geologic model of the flat-dipping veins • To aid the characterization of vein types • To test the areas between zone 2 and 4
2017	157	41,550	Zone 2 & 4	<u>Winter-Spring 2017</u> • To extend the known strike of the auriferous veins in Zone 4 • To provide infill drilling around the historic open pit area <u>Summer-Fall 2017</u> • To infill drilling in known mineralization areas • To test the western extension of gold bearing structures • To test the area between zone 2 and 4 • To extend the mineralization in zone 2 along strike in both the east and west directions

The Orenada deposit has a number of features that are consistent with the classification as an orogenic gold deposit, similar to the other deposits in the Val d'Or gold camp. These include, deformed and metamorphosed host rocks, the presence of quartz-carbonate-tourmaline veins and, a spatial association with a transpressional structure (Groves et al., 1998; McCuaig and Kerrich, 1998; Simard et al., 2013). That said, the Orenada deposit is unlike most of the other orogenic gold deposits in the region because it is located directly within the first order, crustal scale, CLLDZ, the mineralization is hosted within a volcanoclastic horizon within the Cadillac Group

sediments (not the typical Piché Group host) and, mineralization is linked to arsenopyrite sulphidation. This style of mineralization is rare in the Val d'Or camp and therefore poorly understood.

The lithological units observed at the Orenada deposits are, from north to south described below:

A diorite intrusion/sill is observed at the southern edge of the volcanic Héva Formation within the Malartic Group. The diorite is quartz rich and has local chlorite and biotite alteration. The intensity of foliation in the diorite increases towards the contact to the Cadillac Group sediments (Latulippe, 1976).

The Cadillac Group sediments consist of interlayered medium-grained siltstone and fine-grained greywacke that are foliated and locally are chloritized. A fine-grained graphitic argillite horizon is observed towards the lower contact of the sediments. This graphitic horizon is intersected by many drill holes on the property and consists of 5-10% pyrite and pyrrhotite veinlets. A volcanoclastic horizon that is interlayered with the Cadillac sediments occurs within the Cadillac Group. This volcanoclastic horizon is the main host of mineralization.

The Piché Group metavolcanics lie south of the Cadillac volcanoclastic horizon and consists of a talc-chlorite-sericite-carbonate schist, which is highly foliated and strained. Moderate deformation is observed by a penetrative chlorite-rich schistosity and thin carbonate veinlets. The volcanic rocks of the Piché Group outline the CLLDZ (Dimroth et al., 1982; Bedeaux et al., 2017).

Robert et al., (1990) and Neumayr et al., (2002) previously examined the Orenada deposit and reported that mineralization is linked to quartz-carbonate-tourmaline veins observed primarily in the Cadillac volcanoclastic horizon and, euhedral to subhedral arsenopyrite grains observed in the visibly altered wall-rock. In the present study two types of quartz-carbonate-tourmaline veins along with an early and late generation of barren quartz-carbonate veins were identified. Robert et al., (1990) importantly noted that only a small proportion of the gold actually occurs in the quartz-carbonate-tourmaline veins and instead, most of the gold is associated with arsenopyrite

as blebs or in fractures within the arsenopyrites. The present study will evaluate if the observations of Robert et al., (1990) that two different textures of arsenopyrite, each with different chemical characteristics also applies to the most recent drill holes. A more in-depth description of the veins and the arsenopyrite is discussed in section 2.3.5.

1.6 Background information of arsenopyrite

Arsenopyrite (FeAsS) is the most common arsenic mineral and it is locally associated with gold mineralization. Along with pyrite, arsenopyrite is the preferential host for submicroscopic gold (refractory) which is strongly correlated to arsenic-rich minerals such as arsenopyrite and arsenian-pyrite (Chryssoulis et al., 2005). Examples of arsenopyrite rich mineralization in the literature are limited, however, for most of the arsenopyrite-gold associations, the gold is refractory and is present as submicroscopic nano-particles or, was once trapped in the arsenopyrite crystal lattice as has subsequently been remobilized to form free gold. Submicroscopic gold can be incorporated into the crystal lattice of arsenopyrite and arsenian-pyrite at sub-greenschist to lower greenschist facies temperatures. However, arsenopyrite recrystallization, during which gold can be remobilized, can continue through upper greenschist to amphibolite facies temperature during burial and deformation (Vaughan and Kyin, 2004).

Many Archean greenstone-hosted gold deposits in Western Australia (Exhibition, Coolgardie, Paddington, etc.) display high concentrations of refractory gold in arsenopyrite, where timing and grain size of the arsenopyrites play a role in gold mineralization. Vaughan and Kyin (2004) concluded that gold concentrations in arsenopyrite at these deposits are inversely correlated to grain size where fine-grained arsenopyrite have higher Au (ppm) concentrations. These fine grains are associated with late deformation where fluids are interpreted to have been gold-rich. A similar relationship was observed at the Lapa mine in the Val d'Or region, where fine-grained arsenopyrite (0-25 μm) have an average Au concentration of 602 ppm (Simard et al., 2013). These features are considered to be evidence for metamorphic recrystallization (Vaughan and Kyin, 2004; Simard et al., 2013).

Commonly, arsenopyrite-bearing deposits display multiple stages of gold mineralization and both refractory gold in arsenopyrite and as free gold associated with quartz±carbonate veins are present. For example, the Obuasi deposit in Ashanti Ghana is the largest gold deposit in west Africa. It contains both refractory gold in arsenopyrite and arsenian-pyrite and free gold in quartz veins (Fougerouse et al., 2013). The same is observed at the Giant and Con deposits in Yellowknife where free gold is observed in late quartz-carbonate veins and, as refractory gold as sub-microscopic gold particles in As-enriched rims of zoned arsenopyrite (Coleman, 1957; Armstrong, 1997; Siddorn, 2011). Grains may contain up to 5600 ppm Au within As-rich portions (Armstrong, 1997). Lastly, the Casa Berardi deposit, northwest of Val d'Or has been described as a metasedimentary-hosted deposit that contains both volcanogenic massive sulfide and orogenic styles of gold mineralization (Archambault-Giroux et al., 2019). The ore is dominated by free gold, but some refractory gold is also present. However little work on this deposit has been published and it cannot be used for a comparison in this study.

Despite the examples given above, sulphidation in greenstone hosted gold deposits are dominated by pyrite where arsenopyrite, if observed, is typically a secondary ore mineral (Dubé and Gosselin, 2007). Furthermore, most of the research conducted on arsenopyrite from lode gold deposits have been concerned with refractory mineralization. This is especially true for the gold deposits within the southern Abitibi. Because of this, there is a knowledge gap associated with arsenopyrite and free gold deposition. An investigation of the Orenada deposit offers an excellent opportunity to fill this gap. Sulphidation at Orenada is dominated by arsenopyrite and, mineralization is observed as free gold, features that are rare at other orogenic gold deposits. The chemical and physical controls of arsenopyrite will be studied in relation to mineralization to evaluate if they are associated with gold deposition and what role they play in gold deportment. This study can then be used as a blueprint for similar deposits within the Abitibi and within greenstone terranes with similar mineralization styles.

1.7 Project Objectives

The Orenada Zone 4 deposit is unlike most other deposits in the Abitibi because of its structural position, host lithology and association with arsenopyrite. Because the Orenada deposit is atypical, the controls of mineralization are poorly constrained. To understand the controls of mineralization and the deportment of gold, petrographic and geochemical studies were undertaken that focused on alteration, sulphidation and vein emplacement. Two main topics were investigated.

The first topic, is to understand the mineral alteration in the volcanoclastic unit and whether alteration is associated with gold. Alteration minerals consist of tourmaline, muscovite/sericite, chlorite, albite and carbonates. Altered and least altered volcanoclastic samples were examined via petrography and mass balance through whole rock lithogeochemical analyses. Understanding the distribution of alteration is important because whole rock chemical changes related to alteration have the potential to indicate the presence of additional mineralized zones.

The second topic, is to characterize the main controls of the gold mineralization associated with arsenopyrite sulphidation and veining. The characterization involves identifying the characteristics of gold mineralization, its relative timing, whether gold mineralization is preferential to a certain style of arsenopyrite and/or vein types and, the relative distribution of mineralization throughout the deposit. To understand the association between mineralization and sulphidation, arsenopyrite grains from spatially different locations of the deposit were analyzed by: (1) Electron Microprobe Analysis (EMPA) on the different textural styles of arsenopyrite to distinguish differences in their major-element compositions and their association with the different styles of gold mineralization; (2) Laser Ablation Inductively Coupled Plasma Mass Spectrometry (LA-ICP-MS) line traverses on the different textural styles of arsenopyrite to evaluate the gold contents in both types, i.e., whether refractory gold is present.

1.8 References

Archambault-Giroux, J., De Los Rios, H., Blier, A., Roy, P., and McDonald, D. 2019. NI 43-101 Technical Report on the Casa Berardi Mine, Northwestern Québec, Canada.

Armstrong, J.P. 1997. Variations in silicate and sulfide mineral chemistry be- tween free-milling "metallic" and refractory "invisible" gold ores, Con mine, Yellowknife, N.W.T. University of Western Ontario.

Ayer, J., Amelin, Y., Corfu, F., Kamo, S., Ketchum, J., Kwok, K., and Trowell, N. 2002. Evolution of the southern Abitibi greenstone belt based on U-Pb geochronology: Autochthonous volcanic construction followed by plutonism, regional deformation and sedimentation. Precambrian Research, **115**: 63–95.

Ayer, J., Thurston, P.C., Bateman, R., Dubé, B., Gibson, H.L., Hamilton, M.A., Hathway, B., Hocker, S.M., Houlé, M., Hudak, G.J., Ispolatov, V., Lafrance, B., Lesher, C.M., MacDonald, P.J., Péloquin, A.S., Piercey, S.J., Reed, L.E., and Thompson, P.H. 2005. Overview of results from the Greenstone Architecture Project: Discover Abitibi Initiative. *In* Ontario Geological Survey.

Bateman, R., Ayer, J.A., and Dubé, B. 2008. The Timmins-Porcupine Gold Camp, Ontario: Anatomy of an Archean Greenstone Belt and Ontogeny of Gold Mineralization. Economic Geology, **103**: 1285–1308.

Beauregard, A.-J., and Gaudreault, D. 2008. NI 43-101 Technical Report on the Cadillac Break properties, Province of Quebec, Canada. Prepared by Geological Groupe – Conseil for Alexandria Minerals Corporation.

Bedeaux, P., Mathieu, L., Pilote, P., Rafini, S., and Daigneault, R. 2018. Origin of the Piché structural complex and implications for the early evolution of the archean crustal-scale Cadillac – Larder lake fault zone, Canada. Canadian Journal of Earth Sciences, **55**: 905–922.

Bedeaux, P., Pilote, P., Daigneault, R., and Rafini, S. 2017. Synthesis of the structural evolution and associated gold mineralization of the Cadillac Fault, Abitibi, Canada. Ore Geology Reviews, **82**: 49–69.

Bleeker, W. 2012. Targeted Geoscience Initiative 4. Lode Gold Deposits in Ancient Deformed and Metamorphosed Terranes: The Role of Extension in the Formation of Timiskaming Basins and Large Gold Deposits, Abitibi Greenstone Belt—A Discussion. Summary of Field Work.

Card, K.D. 1990. A review of the Superior Province of the Canadian Shield, a product of Archean accretion. Precambrian Research, **48**: 99–156.

Card, K.D., and Poulsen, K.H. 1998. Geology and mineral deposits of the Superior Province of the Canadian Shield. Geology of the Precambrian Superior and Grenville Provinces and Precambrian Fossils in North America (Lucas, S. and St-Onge, M.R., co-ordinators). Geological Survey of Canada,: 15–232.

Chown, E.H., N'Dah, E., and Mueller, W.U. 2000. The relation between iron-formation and low temperature hydrothermal alteration in an Archean volcanic environment. Precambrian Research, **101**: 263–275.

Chryssoulis, S.L., and McMullen, J. 2016. Mineralogical Investigation of Gold Ores. *In* Gold Ore Processing, Project Development and Operations, 2nd edition. *Edited by* M.D. Adams. Elsevier B.V. pp. 57–93.

Coleman, L.C. 1957. Mineralogy of the giant yellowknife gold mine, yellowknife, N.W.T. Economic Geology, **52**: 400–425.

Corfu, F. 1993. The Evolution of the Southern Abitibi Greenstone Belt in Light of Precise U-Pb Geochronology. Economic Geology, **88**: 1323–1340.

Corkery, M.., Davis, D.W., and Lenton, P.G. 1992. Geochronological constraints on the

development of the Cross Lake Greenstone Belt. Canadian Journal of Earth Sciences, **29**: 2171–2185.

Couture, J.F., Pilote, P., Machado, N., and Desrochers, J.P. 1994. Timing of gold mineralization in the Val-d'Or district, southern Abitibi Belt: evidence for two distinct mineralizing events. Economic Geology, **89**: 1542–1551

Daigneault, R., Mueller, W.U., and Chown, E.H. 2002. Oblique Archean subduction: Accretion and exhumation of an oceanic arc during dextral transpression, Southern Volcanic Zone, Abitibi Subprovince Canada. Precambrian Research, **115**: 261–290.

Davis, D.W. 1991. Ages constraints on deposition and provenance of Archean sediments in the southern Abitibi and Pontiac Subprovinces from U–Pb analysis of detrital zircons. In LITHOPROBE: Abitibi-Grenville Transect Workshop. Lithoprobe, Report 25,: 147–150. The University of British Columbia, Vancouver, B.C.

Davis, D.W. 2002. U-Pb geochronology of Archean metasedimentary rocks in the Pontiac and Abitibi subprovinces, Quebec, constraints on timing, provenance and regional tectonics. Precambrian Research, **115**: 97–117.

Davis, D.W. 2008. Sub-million-year age resolution of Precambrian igneous events by thermal extraction-thermal ionization mass spectrometer Pb dating of zircon: Application to crystallization of the Sudbury impact melt sheet. Geology, **36**: 383–386.

Desrochers, J.-P., Hubert, C., Ludden, J.N., and Pilote, P. 1993. Accretion of Archean oceanic plateau fragments in the Abitibi greenstone belt, Canada. Geology, **21**: 451–454.

Dimroth, E., Imreh, L., Goulet, N., and Rocheleau, M. 1983. Evolution of the south-central segment of the Archean Abitibi Belt, Québec. Part II: tectonic evolution and geomechanical model. Canadian Journal of Earth Sciences, **20**: 1355–1373.

Dimroth, E., Imreh, L., Rocheleau, M., and Goulet, N. 1982. Evolution of the south-central part

of the Archean Abitibi belt, Quebec. Part I: stratigraphy and paleogeographic model. Canadian Journal of Earth Sciences, **19**: 1729–1758.

Dubé, B., and Gosselin, P. 2007. Greenstone-hosted quartz-carbonate vein deposits, in Goodfellow, W.D., ed., Mineral Deposits of Canada: A Synthesis of Major Deposit-Types, District Metallogeny, the Evolution of Geological Provinces, and Exploration Methods. Geological Association of Canada, Mineral Deposits Division, **Special**: 49–73.

Dubé, B., Williamson, K., Mcnicoll, V., Malo, M., Skulski, T., Twomey, T., and Sanborn-Barrie, M. 2004. Timing of gold mineralization at red lake, northwestern Ontario, Canada: new constraints from U-Pb geochronology at the Goldcorp high- grade zone, red lake mine, and the madsen mine. Economic Geology, **99**: 1611–1641.

Fougerouse, D., Micklethwaite, S., Miller, J., and Mccuaig, T.C. 2013. Multistage mineralization of the giant Obuasi gold deposit , Ghana. *In* MINERAL DEPOSIT RESEARCH FOR A HIGH-TECH WORLD. 12th SGA Biennial Meeting. pp. 1105–1108.

Gourd, B.-B. 1983. La Mine Lamaque et le Village Minier Bourlamaque. Une Histoire de Mine. College de L'Abitibi-Temiscamingue.

Groves, D.I., Goldfarb, R.J., Gebre-Mariam, M., Hagemann, S.G., and Robert, F. 1998. Orogenic gold deposits: a proposed classification in the context of their crustal distribution and relationship to other gold deposit types. Ore Geology Reviews, **13**: 7–27.

Hannington, M.D., Barrie, C.T., and Bleeker, W. 1999. The giant Kidd Creek volcanogenic massive sulfide deposit, western Abitibi Subprovince, Canada, in Hannington, M.D., and Barrie, C.T., eds., The Giant Kidd Creek Volcanogenic Massive Sulfide Deposit, Western Abitibi Subprovince, Canada. Economic Geology Monograph, **10**: 1–30.

Heaman, L.M., and Kjarsgaard, B.A. 2000. Timing of eastern North American kimberlite magmatism; Continental extension of the Great Meteor Hotspot track? Earth and Planetary Science Letters, **178**: 253–268.

Imreh, L. 1984. Sillon de La Motte-Vassan et son avant-pays méridional: Synthèse volcanogénique, lithostratigraphique et gîtologique.

Kerrich, R. 1989. Archean gold: relation to granulite formation or felsic intrusions? Geology, **17**: 1011–1015.

Lafrance, B. 2015. Geology of the orogenic cheminis gold deposit along the larder lake – cadillac deformation zone, Ontario. Canadian Journal of Earth Sciences, **52**: 1093–1108.

Latulippe, M. 1976. Excursion gelologique: La Region de Val-d'Or-Malartic; Mini. : 130.

Lavoie, S. 2003. Géologie de la mine East-Sullivan, Abitibi-Est, Val-d'or, Québec. Université du Québec a Chicoutimi.

Mccuaig, T.C., and Kerrich, R. 1998. P—T—t—deformation—fluid characteristics of lode gold deposits: evidence from alteration systematics. Ore Geology Reviews, **12**: 381–453.

Monecke, T., Mercier-Langevin, P., Dubé, B., and Frieman, B.M. 2018. Geology of the Abitibi Greenstone Belt. In Archean base and precious metal deposits, southern Abitibi greenstone belt, Canada: 7–39.

Morasse, S. 1998. Geology, Structure and Timing of Gold Mineralization at the Keena Deposit, Val d'Or, Quebec. Queens Univeristy.

Mortensen, J.K. 1993. U - Pb geochronology of the eastern Abitibi Subprovince. Part 1: Chibougamau - Matagami - Joutel region. Canadian Journal of Earth Sciences, **30**: 11–28.

Mueller, W.U., Daigneault, R., Mortensen, J.K., and Chown, E.H. 1996. Archean terrane docksin: upper crust collision tectonics, Abitibi greenstone belt, Quebec, Canada. Tectonophysics, **265**: 127–150.

Neumayr, P., and Hagemann, S.G. 2002. Hydrothermal fluid evolution within the Cadillac tectonic zone, Abitibi greenstone belt, Canada: Relationship to auriferous fluids in adjacent

second- and third-order shear zones. Economic Geology, **97**: 1203–1225.

Neumayr, P., Hagemann, S.G., and Couture, J.F. 2000. Structural setting, textures, and timing of hydrothermal vein systems in the Val d'Or camp, Abitibi, Canada: Implications for the evolution of transcrustal, second- and third-order fault zones and gold mineralization. Canadian Journal of Earth Sciences, **37**: 95–114.

Percival, J.A. 2007. Geology and metallogeny of the Superior Province, Canada, in Goodfellow, W.D., ed., Mineral Deposits ofCanada: ASynthesis ofMajor Deposit-Types, District Metallogeny, the Evolution ofGeological Provinces, and Exploration Methods. Geological Association of Canada, Mineral Deposits Division, **Special**: 903–928.

Percival, J.A., Sanborn-Barrie, M., Skulski, T., Stott, G.M., Helmstaedt, H., and White, D.J. 2006. Tectonic evolution of the western Superior Province from NATMAP and Lithoprobe studies. Canadian Journal of Earth Sciences, **43**: 1085–1117.

Percival, J.A., Skulski, T., Sanborn-Barrie, M., Stott, G.M., Leclair, A.D., Corkery, M.T., and Boily, M. 2012. Geology and Tectonic Evolution of the Superior Province, Canada. The Lithoprobe Perspective. Tectonic Styles in Canada: The LITHOPROBE Perspective,: 321–378.

Perrouty, S., Gaillard, N., Piette-Lauzière, N., Mir, R., Bardoux, M., Olivo, G.R., Linnen, R.L., Bérubé, C.L., Lypaczewski, P., Guilmette, C., Feltrin, L., and Morris, W.A. 2017. Structural setting for Canadian Malartic style of gold mineralization in the Pontiac Subprovince, south of the Cadillac Larder Lake Deformation Zone, Québec, Canada. Ore Geology Reviews, **84**: 185–201.

Pilote, P., Daigneault, R., David, J., and Mcnicoll, V. 2015. Architecture of the Malartic, Piché and Cadillac groups and the Cadillac Fault: Geological revisions, new dates and interpretations. Ministère de l'Énergie et des Ressources Naturelles, **DV 2015-04**: 37.

Pilote, P., Machado, N., and Desrochers, J.-P. 1994. Timing of Gold Mineralization in the Val-

d'Or District, Southern Abitibi Belt: Evidence for Two Distinct Mineralizing Event. Economic Geology, **89**: 1542–1551.

Pilote, P., Scott, C.R., Mueller, W.U., Lavoie, S., and Riopel, P. 1999. Géologie des formations de Val-d'Or, Héva et Jacola : nouvelle interprétation du groupe de Malartic. In: Explorer au Québec: le défi de la connaissance. Séminaire d'information sur la recherche géologique, programme et résumés. Minsitère de l'énergie et des Ressources, **DV 99-03**: 52.

Robert, F. 1989. Internal structure of the Cadillac tectonic zone southeast of Val d'Or, Abitibi greenstone belt, Quebec. Canadian Journal of Earth Sciences, **26**: 2661–2675.

Robert, F., Brommecker, R., and Bubar, D.S. 1990. The orenada zone 4 deposit: deformed vein-type gold mineralization within the cadillac tectonic zone, SE of Val d'Or. Institut Canadien des mines et de la métallurgie, Volume spécial,: 255–268.

Robert, F., and Brown, A.C. 1986. Archean gold-bearing quartz veins at the Sigma Mine, Abitibi greenstone belt, Quebec: Part I. Geologic relations and formation of the vein system. Economic Geology, **81**: 578–592.

Robert, F., and Poulsen, K.H. 1997. World-class Archaean gold deposits in Canada: An overview. Australian Journal of Earth Sciences, **44**: 329–351.

Savard, C., Carrier, A., and Durieux, G. (n.d.). NI 43-101 Technical Report and Updated Mineral Resource estimate for the Orenada Zones 2 and 4 Projects, Orenada Group Properties. Prepared by Innov Explo– Conseil for Alexandria Minerals Corporation.

Scott, C.R., Mueller, W.U., and Pilote, P. 2002. Physical volcanology, stratigraphy, and lithogeochemistry of an Archean volcanic arc: Evolution from plume-related volcanism to arc rifting of SE Abitibi Greenstone Belt, Val d'Or, Canada. Precambrian Research, **115**: 223–260.

Siddorn, J.P. 2011. The Giant-Con Gold Deposit: A Once-Linked Archean Lode-Gold System.

University of Toronto.

Simard, M. 2008. Synthese du Nord-Est de la Province du Superieur.

Simard, M. 2011. Multi Événments de Déformation, de Métamorphism d'Hydothermalisme a l'Origine du Gisment du Lapa. Universite du Quebec a Chicoutimi.

Simard, M., Gaboury, D., Daigneault, R., and Mercier-Langevin, P. 2013. Multistage gold mineralization at the Lapa mine, Abitibi Subprovince: Insights into auriferous hydrothermal and metasomatic processes in the Cadillac-Larder Lake Fault Zone. Mineralium Deposita, **48**: 883–905.

Thurston, P.C., Ayer, J.A., Goutier, J., and Hamilton, M.A. 2008. Depositional gaps in abitibi greenstone belt stratigraphy: A key to exploration for syngenetic mineralization. Economic Geology, **103**: 1097–1134.

Trudeau, Y., and Raymond, D. 1992. Geology and structure, Orion mine (No. 8 zone), Val d'Or district, Quebec. Exploration and Mining Geology, **1**: 223–230.

Vaughan, J.P., and Kyin, A. 2004. Refractory gold ores in Archaean greenstones,Western Australia: mineralogy, gold paragenesis, metallurgical characterization and classification. Mineralogical Magazine, **68**: 255–277.

Wong, L., Davis, D.W., Krogh, T.E., and Robert, F. 1991. UPb zircon and rutile chronology of Archean greenstone formation and gold mineralization in the Val d'Or region, Quebec. Earth and Planetary Science Letters, **104**: 325–336.

Zhou, X., and Lafrance, B. 2017. Stratigraphic and structural setting of gold and nickel deposits in the La Motte-Malartic area, southern Abitibi and Ponkiak Subprovinces, Superior Province, Quebec. *In* Projets 2017, Initiative Metal Earth, Ministère de l'Ènerie et Ressources naturelles Québec, MB.

Chapter 2

2 Integrated Paper

2.1 Introduction

Gold production in the Abitibi Subprovince, the southernmost Subprovince of the Superior Province, is widely recognized for gold production where the Subprovince produces 81% of the gold in Canada and has produced more than 4500 tonnes of Au hosted in lode gold, intrusion and Au-rich VMS deposits (Dubé and Gosselin, 2007; Monecke et al., 2018). Most of the gold deposits within the Abitibi are considered lode gold deposits, also termed mesothermal, orogenic or greenstone hosted quartz-carbonate vein deposits (Dubé and Gosselin, 2007). These deposits are structurally controlled, distributed along major, crustal-scale, east-west trending structures, which define the convergent margins between two major lithological boundaries (Dubé and Gosselin, 2007). Because of the distribution about crustal-scale fault zones, many deposits are located proximally to each other and form clusters of gold deposits termed ”gold camps”. The major camps in the Abitibi Subprovince are Kirkland Lake, Timmins gold camp and the Val-d’Or gold camps (Dubé and Gosselin, 2007).

The Val d’Or gold camp is home to numerous historic and current gold mines including Sigma-Lamaque, Canadian Malartic, Kiena and Louvicourt. Gold occurrences in the area are spatially associated with the Cadillac Larder Lake Deformation Zone (CLLDZ) along second and third order structures however, gold within the main first order fault is rare and extremely localized (Kerrich, 1989; Robert et al., 1990; Neumayr et al., 2000). The CLLDZ is considered to be the main conduit for gold-bearing hydrothermal fluids in the Val d’Or camp which, is interpreted by the spatial relationship between the first-second and third-order fault zones, and hydrothermal alteration found within the camp (Robert et al., 1990; Neumayr et al, 2000). The Orenada deposit is located 8 km south-east of Val d’Or within the Val d’Or camp and shows many similarities to other greenstone vein hosted deposits within the Camp including but is situated directly within the first order CLLDZ.

The Orenada deposit is characterized by a number of features that result in it being classified as an orogenic/greenstone hosted vein deposit, similar to the other deposits in the Val d'Or camp. These include, deformed and metamorphosed host rocks, the presence of quartz-carbonate-tourmaline veins and, a spatial association with a transpressional structure (Groves et al., 1998; McCuaig and Kerrich, 1998; Simard et al., 2013). However, the Orenada deposit is unique to many of other deposits in the area because, it is located directly within the first order, crustal scale, CLLDZ, mineralization is hosted within a volcanoclastic horizon within the Cadillac Group sediments (and not the Piché Group) and, mineralization is associated with both auriferous veins and arsenopyrite sulphidation, instead of pyrite, which is the dominant mineral that reflects sulphidation in the region. This style of mineralization is rare in the Val d'Or camp and therefore poorly understood.

Robert et al., (1990) and Neumayr et al. (2002) have previously studied Orenada however, these investigations focused more on the structural characteristics of the deposit instead of the petrographic and chemical constraints of mineralization, especially the relationship of gold to arsenopyrite. Gold mineralization can be associated with arsenopyrite as refractory gold in Archean greenstone terranes however, the association between arsenopyrite and free gold deposition is less common and very limited literature is available on the subject.

This paper presents the results of a study into the Orenada deposit that provides new petrographic, lithogeochemical and mineral chemical observations pertaining to the controls of mineralization. The following questions will be investigated: 1) What is the mineralogical and chemical attributes of the host rock? 2) what are the main alteration styles and are any of them associated with mineralization? 3) what is the timing of gold relative to the veins, host rock and alteration? 4) what is the relationship between mineralization and the quartz-carbonate-tourmaline veins and are there different generations of veins? 5) What is the relationship between arsenopyrite and gold mineralization and how much (if any) of the gold is refractory?

All of these questions will aid in understanding the gold deportment at Orenada however, characterizing the arsenopyrite grains is a key factor to understand the deportment of gold. The chemical and physical controls of arsenopyrite will be studied in relation to mineralization to evaluate if they are associated with gold deposition and what role they play in gold deportment. This study can then be used as a blueprint for similar deposits within the Abitibi and within greenstone terranes with similar mineralization styles.

2.1.1 Regional Geology

The Val d'Or area is made up of several geological groups which include, the Malartic Group, the Louvicourt Group, the Cadillac Group and, the Pontiac Group (Figure 2-1). The Malartic Group (2714–2704 Ma) is composed of komatiitic and basaltic to andesitic flows are interpreted to having been emplaced in a deep ocean-floor volcanic environment (Dimroth et al. 1982; Scott et al. 2002; Bedeaux et al, 2018). It is composed of the following formations, from oldest to youngest, the La Motte–Vassan Formation (2714±2 Ma), Dubuisson Formation (2708±2 Ma), and Jacola Formation (2706±2 Ma). All of the major rock formations can be observed on a geologic map of the Val d'Or area (Figure 2-2).

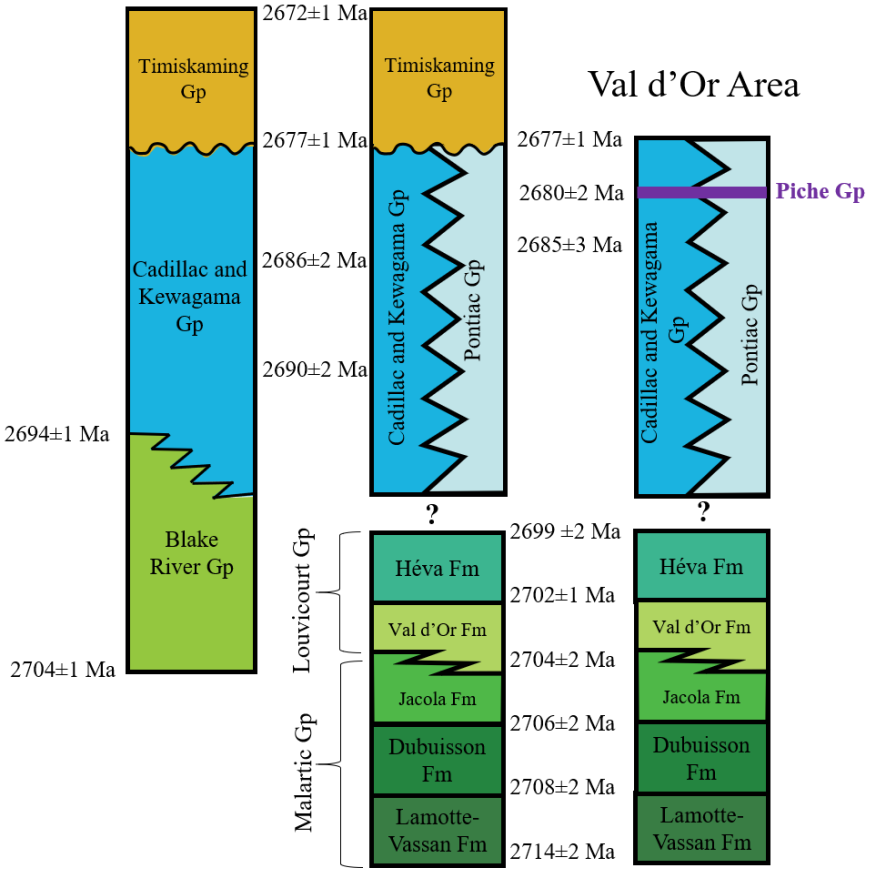

Figure 2-1. Stratigraphic chart of the Rouyn, Malartic and Val d'Or (this study) areas with the relevant isotopic ages. Stratigraphic relationships are based on Dimroth et al., (1982), Mueller et al., (1996), Pilote et al., (1999), Davis, (2002), Scott et al., (2002) and Bedeaux et al., (2018). Sawtooth lines indicate coeval units and wavy lines indicate unconformities.

The Louvicourt Group (2704-2699 Ma) conformably overlies the Malartic Group (Fig. 2-1) and is composed of massive to pillowed mafic flows and felsic volcanoclastic horizons which represent a transition towards a volcanic arc phase (Scott et al,. 2002). The Louvicourt Group is made up of the Val d'Or Formation (2704±2 Ma), which is synchronous with the Jacola formation, and the Héva Formation (2702 ±2 Ma). Both formations are intruded by diorite and gabbro dykes and sills (Pilote et al., 1999; Zhou and LaFrance, 2017).

The Cadillac Group (2686±2 Ma) is comprised of flysh-type sedimentary rocks which overlie the Louvicourt Group (Figure 2-1, Figure 2-2). The sedimentary rocks include turbidites, greywackes, mudstones and minor sequences of conglomerate and banded iron formations (Davis et al 2002; Bedeaux et al, 2018).

The Piché Group, observed south of the Cadillac Group, is a discordant <2 km thick band of strongly strained ultramafic to mafic volcanic rocks located roughly 150 km along the CLLDZ (Figure 2-2). The volcanics of the Piché Group are considered to outline the CLLDZ (Dimroth et al, 1982; Simard et al., 2013; Bedeaux et al., 2018). The group is composed of tholeiitic basalts, komatiites, talc schists, porphyritic andesites and calc-alkaline tuffs. The volcanics are crosscut by felsic to mafic dykes and sills (Dimroth et al., 1982; Imreh, 1984; Simard et al., 2013). In some regions along the CLLDZ, the Piché Group is not visible and instead, the Cadillac Group is in contact with the Pontiac Group sediments**.**

The Pontiac Group (2685.3±3 Ma) is located south of the CLLDZ within the Pontiac Subprovince (Figure 2-2). It consists of greywacke, siltstone, mudstone, rare monomictic conglomerate layers and ultramafic to felsic intrusions (Dimroth et al., 1982; Davis, 2002; Perrouty et al., 2017). The Pontiac and Cadillac sedimentary groups are spatially separated by the CLLDZ and are coeval in age (Davis, 2002).

The rocks in the Val d'Or area are intruded by several late plutons, dykes and sills. Most notably in the area, is the East Sullivan pluton (2684±1 Ma) a felsic alkaline pluton observed in the rocks of the Val d’Or and Héva formation (Lavoie, 2003).

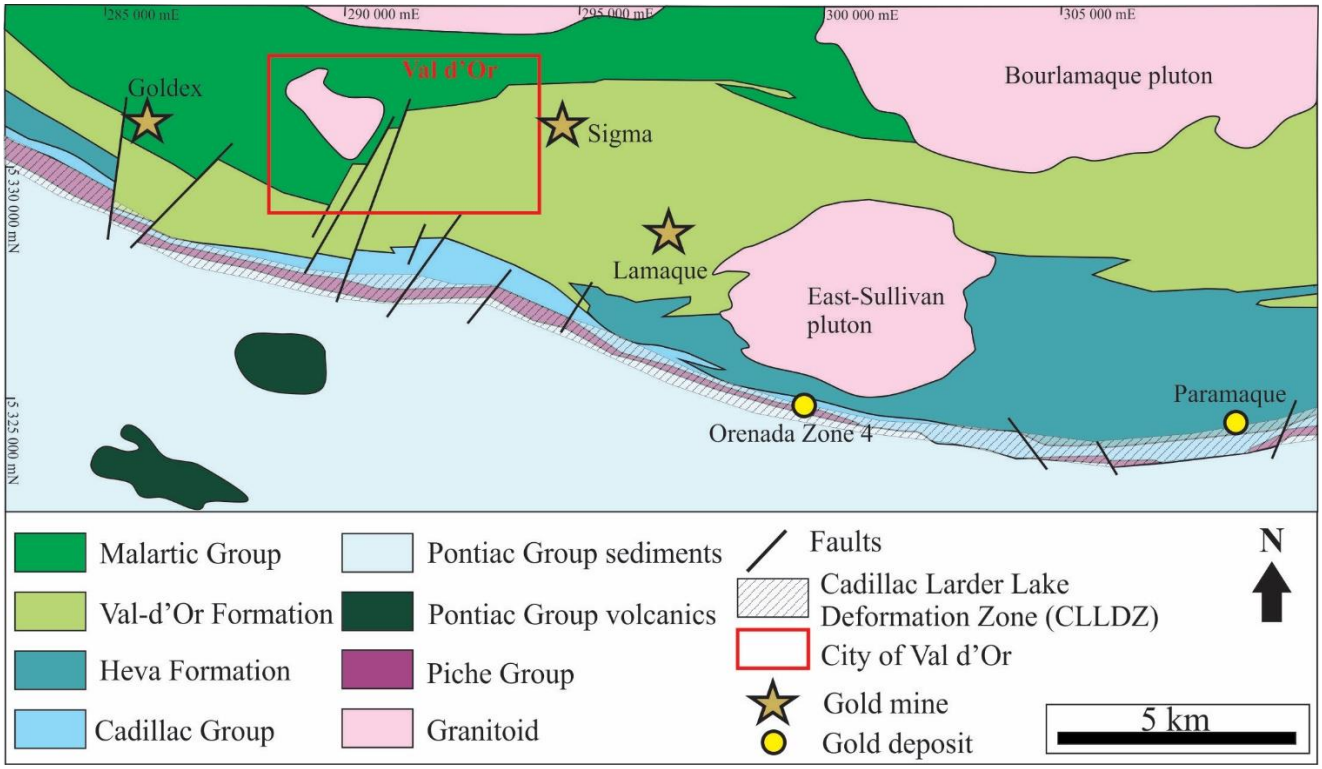

Figure 2-2. Geological map of the southern Abitibi, Val d'Or area with the main lithological units. Adapted from Bedeaux et al., 2017.

2.1.1.1 Deformation

Deformation in the Val d'Or area is characterized by two multiphase, distinct, ductile deformation events. It is important to note that different studies denote the deformation events with different numerical values however, many of them refer to the same events. The following description follows the denotations of Robert, (1989, 1990).

D1 is defined as an early, pre metamorphic, ductile, northerly-directed shortening event that is expressed as an E-trending, subvertical, penetrative schistosity (S_1) with a well-developed subparallel stretching lineation. The north-focused shortening and strong stretching lineations are attributed to locally-derived dip-slip movements that were synchronous with dextral transcurrent shearing (Robert, 1989). The primary lithological contacts were folded by tight isoclinal folds (F1) (Robert, 1989; Bedeaux et al., 2017). This D1 event is responsible for most of the structural

framework of the Abitibi and represents deformation in the area that occurred over a long period of time. The S_1 penetrative schistosity may have overprinted fabrics of former deformational events thus, erasing evidence of past events (Bedeaux et al., 2017).

D2 is defined as a NE-SW shortening event that caused regional, dextral strike-slip faulting along the CLLDZ. D2 is most notably characterized by the development of shallowly plunging, meter-to-kilometer-scale asymmetric Z-shaped F2 folds. F2 folds are spatially associated with several gold deposits along the CLLDZ and is responsible for a NE-SW steeply-dipping foliation S_2, which crenulated S_1 and is best developed in the F2 fold hinges. Structures associated with D2 are locally overprinted by late dextral strike-slip reactivation along the CLLDZ.

2.1.1.2 Metamorphism

Metamorphism within the south-eastern Abitibi (Val d'Or, Cadillac, Malartic, etc.) occurred from 2680 to 2643 Ma and reaches lower-greenschist to sub-greenschist facies metamorphism (Jolly, 1978; Powell et al. 1993, 1995). By contrast, the Pontiac Subprovince has been metamorphosed to amphibolite facies (Daigneault et al., 2002), thus there is a strong contrast in metamorphic grades of the two subprovinces. The juxtaposition of metamorphic grades across the CLLDZ is interpreted to reflect a structural displacement of 5 to 7 km. This displacement is attributed to both extensional and vertical components of movement along the CLLDZ (Daigneault et al., 2002; Neumayr et al., 2002). This displacement is interpreted to have occurred during late D1 to early D2 events, before the regional F2 asymmetric folding (Daigneault et al., 2002; Neumayr et al., 2002).

2.1.2 Deposit Geology

At the start of this study the Orenada property was owned by Alexandria Minerals Corp. but was subsequently acquired by O3 mining. There are 5 zones of mineralization on the property, but the focus of this study is zone 4 and zone 2 (Figure 2-3). Both zones share the same lithological units, vein types, alteration assemblages and style of sulphide mineralization. However, some difference between the zones are noted such as, zone 2 shows a higher degree of deformation

and, zone 4 has higher cut-off grade (inferred resources). Zone 4 also contains an historic open pit mine that opened in 1981 and was shortly closed thereafter in 1982 (Robert et al., 1990).

The Orenada deposit is characterized by a number of features defining it as an orogenic gold deposit similar to the other deposits in the Val d'Or gold camp. These include, deformed and metamorphosed host rocks, the presence of quartz-carbonate-tourmaline veins and, a spatial association with a transpressional structure (Groves et al., 1998; McCuaig and Kerrich, 1998; Simard et al., 2013). That being said, the Orenada deposit is unlike other orogenic deposits in the region because it is located directly within the first order, crustal scale, CLLDZ, mineralization is hosted within a volcanoclastic horizon within the Cadillac Group sediments and, mineralization is linked to arsenopyrite sulphidation. This style of mineralization is rare in the Val d'Or camp and therefore poorly understood.

For the purpose of this study, Drill core was logged, and samples collected in the summer of 2017 at the Alexandria Minerals office in Val d'Or. Fourteen diamond drill holes were re-logged: 9 intersected the Orenada zone 4, 1 intersected the Orenada zone 2 and 4 are of least-altered lithologies outside of the mineralized zones. The sample collection focused on the volcanoclastic horizon of the Cadillac Group and the auriferous quartz-carbonate-tourmaline veins. A total of 101 core samples were collected that consisted of 15 from least-altered core, 60 from the volcanoclastic wall rock proximal to mineralization and, the remainder are of quartz-carbonate-tourmaline±arsenopyrite veins. All samples names, their sampled DDH and the depth they were taken are listed in **Appendix A**. Assays of the sampled intervals were made available by Alexandria Minerals Corp. The lithological units observed at zone 4 and zone 2 are shown in figure 2-3 and Figure 2-4 below, are from north to south: A diorite intrusion of the Héva Formation, the Cadillac Group sediments and volcanoclastic horizon and, the Piché Group metavolcanics.

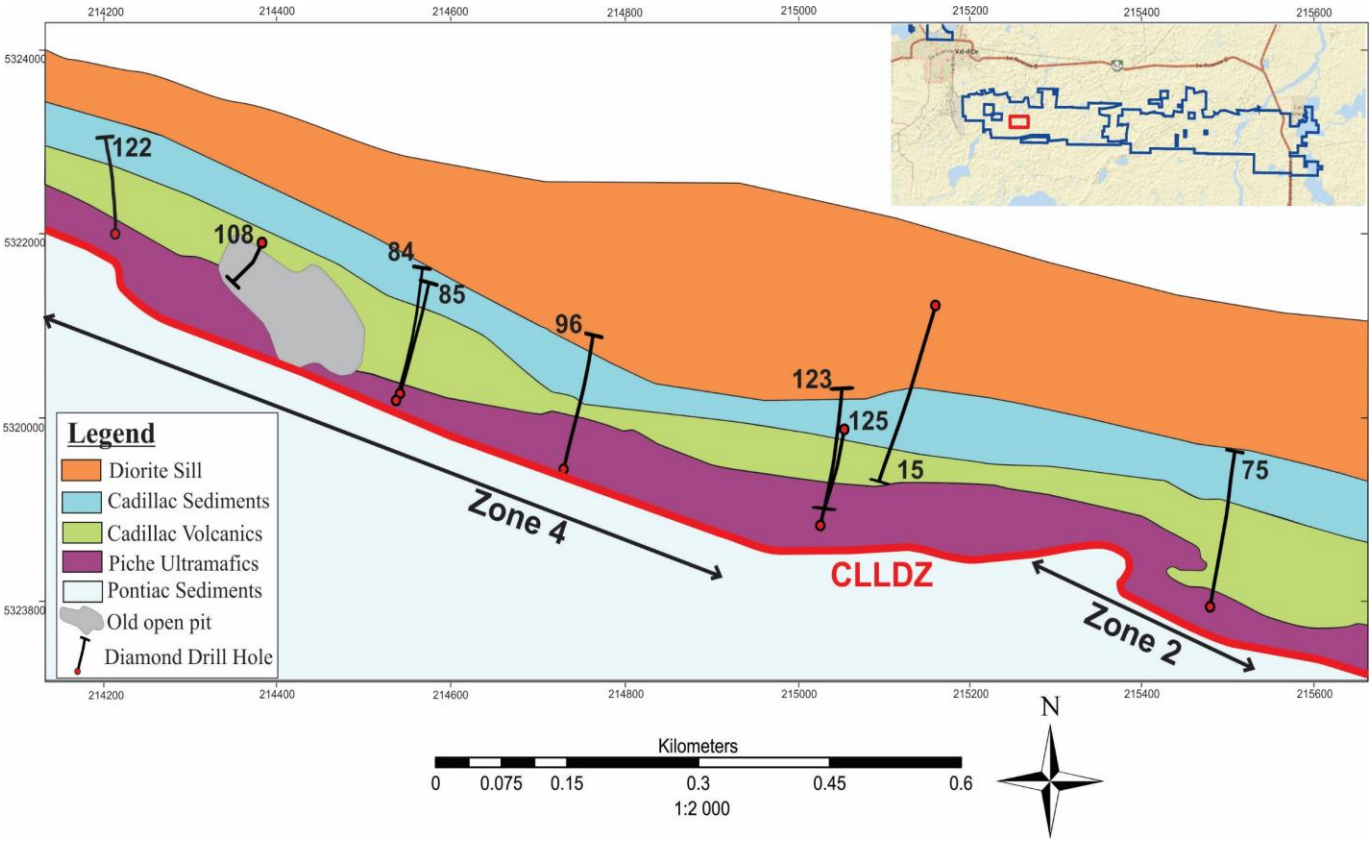

Figure 2-3. Plan view section of the Orenada deposit including the sampled drill holes from this study.

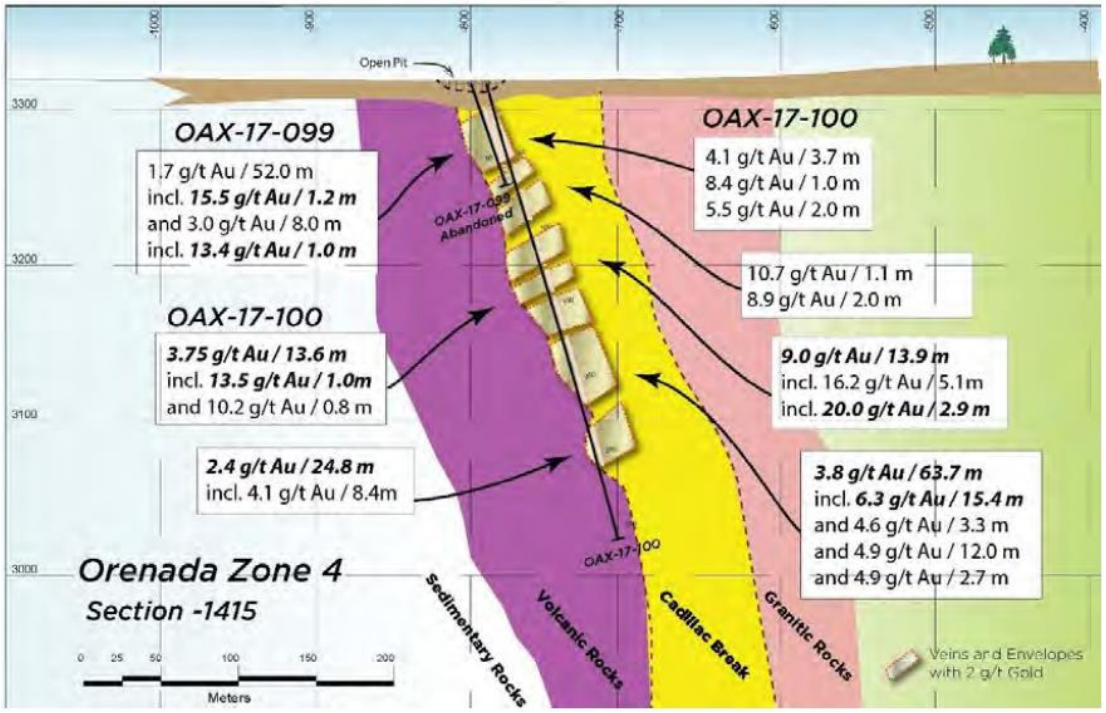

Figure 2-4. Cross section of mineralized zone in Orenada Zone 4 deposit. Image taken from Alexandria Minerals Corp 2018 NI-43-101 Technical report.

The diorite intrusion/sill is observed at the southern edge of the volcanic Héva Formation within the Malartic Group. The diorite is quartz-rich, with local chlorite and biotite alteration. The intensity of foliation in the diorite increases towards the contact to the Cadillac Group sediments (Latulippe, 1976).

The Cadillac Group sediments consist of interlayered fine-grained siltstone and medium-grained greywacke that are foliated and show local chloritization. A fine-grained graphitic argillite horizon is observed towards the lower contact of the sediments. This graphitic horizon is intersected by many drill holes on the property and consists of 5-10% pyrite and pyrrhotite veinlets. A volcanoclastic horizon occurs within the Cadillac Group that is interlayered with the Cadillac sediments. This volcanoclastic horizon is the main host of mineralization and is subdivided in this study into two different porphyritic rock types. The first type is a quartz porphyroclastic quartz-muscovite schist, defined in this study as quartz volcanoclastic rock

(QV). QV is comprised of 2-10% smoky quartz porphyroclast in a quartz-sericite-rich matrix (Figure 2-5A). The second, type is a feldspar porphyroclastic schist, defined in this study as a feldspar volcanoclastic rock (FV). FV is comprised of 20-40% feldspar porphyroclast in a fine-grained sericite-feldspar-quartz-chlorite-carbonate groundmass (Figure 2-5B). Robert et al., (1990), Neumayr et al. (2002) and Bedeaux et al. (2017), report a volcanoclastic horizon as being part of the Piché Group. However, based on core logging observations in this study, the volcanoclastic horizon is located exclusively interlayered with the Cadillac Group sediments. Consequently, the volcanoclastic unit is therefore assigned as part of the Cadillac Group. It is important to note, that both rock types are found in the same drill holes and do not form consistent contacts. However, the volcanoclastic unit as a whole can be mapped, although the QV and FV lithologies do not have a discernable distribution.

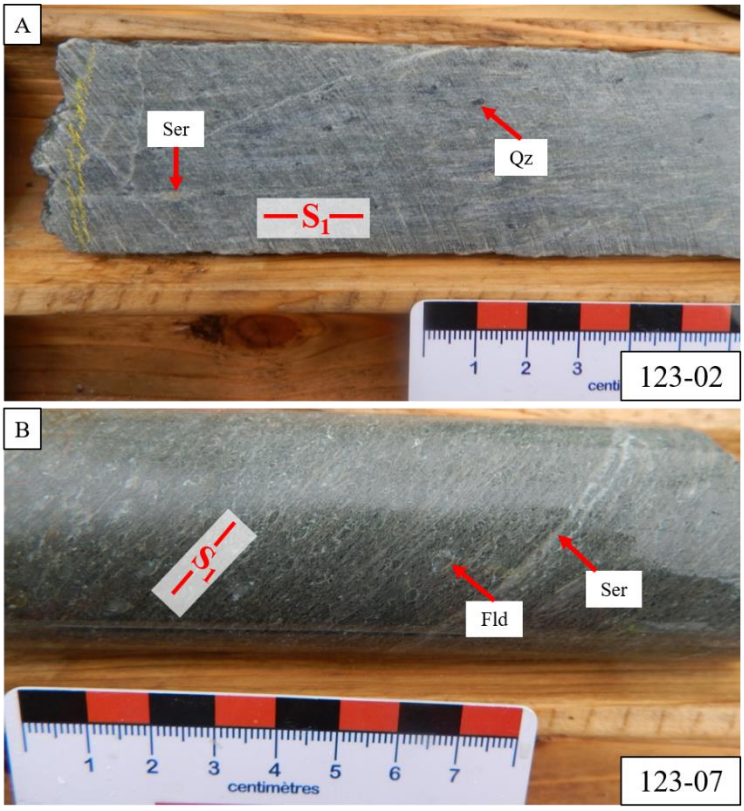

Figure 2-5. Drill core samples of the Cadillac volcanoclastic rocks. A) Quartz porphyritic volcanoclastic rock (QV), which consists of smoky quartz porphyroclasts in a green-grey

chlorite-sericite rich matrix. B) Feldspar porphyritic volcanoclastic rock (FV), which consists of pale feldspar porphyroclasts in a grey-beige albite-sericite-chlorite rich matrix. Sericite bands in both volcanoclastic rocks define the main penetrative S_1 fabric. Sample numbers are displayed in the bottom right corner of each photograph.

The Piché Group metavolcanics at the property consist of a talc-chlorite-sericite-carbonate schist, which is highly foliated and strained. Thin carbonate veinlets are observed subparallel to the main foliation. Closer to the contact to the Cadillac Group rocks, the Piché Group mafic rocks transition to a massive, dark green, chloritized, mafic flow. Moderate deformation is observed by a penetrative chlorite-rich schistosity and thin carbonate veinlets.

Robert et al., (1990) and Neumayr et al., (2002) previously reported that mineralization at the Orenada deposit can be linked to both quartz-carbonate-tourmaline veins primarily in the Cadillac Group rocks and, to euhedral-subhedral arsenopyrite grains observed in the visibly altered wall-rock. Core logging identified four types of veins, each having its own structural and textural characteristics. All vein types belong to overlapping deformation events of varying generations however not all are associated with mineralization. All vein descriptions and their timing related to deformation events are presented in Table 2-1.

Table 2-1. Characteristics and structural timing of quartz veins found at Orenada zone 4 deposit. Quartz (Qz), Carbonate (Cc), Tourmaline (Tm), Gold (Au), Arsenopyrite (Asp)

Vein type	Vein thickness	Structural setting	Vein minerals	Mineralization	Timing				
					D1	D2		D3	
						Early	Late	Early	Late
V1	<5cm	Along S_1, boudinaged	Qz-Cc	-					
V2	1-5cm	Subparallel along S_1, folded	Qz-Cc-Tm-Asp	Au					
V3A	<15cm	Veins crosscut S_1	Qz-Cc-Tm-Asp	Au					
V3B	<2cm	Veins crosscut S_1 along S_2	Qz-Cc	-					

The first vein type, V1 occur as thin (<2cm) barren, quartz-carbonate veins, oriented along the main S_1 foliation and are commonly as boudinaged sections of a continuous vein (Figure 2-6A). These veins are present within most rock types at Orenada including: QV, FV, the Cadillac sediments and the Piché Group metavolcanics. V1 are documented to have formed during D1 steep-reverse shearing (Robert, 1989).

The second type of veins, V2, are thin (1-10cm) auriferous quartz-carbonate veins that are observed parallel (Figure 2-6 B) and folded (Figure 2-6 C) with the main sericite-chlorite S_1 foliation. In core, V2 are characterized by thin (0.5-2cm) tourmaline alteration haloes and, in some samples, euhedral to subhedral arsenopyrite grains are observed within and/or surrounding the veins (Figure 2-6B,C). This study as well as others (Robert, 1989, 1990; Neumayr et al., 2000, 2002) have noted that the V2 are spatially associated with F2 asymmetric Z-shaped folds, are interpreted to have formed during early to mid D2 and are folded along F2 (Robert, 1989, 1990; Neumayr et al., 2002). However, V2 were likely formed prior to the F2 folding due to the

increased abundance of veins in the folds from S_2 parallel shortening (Robert, 1989). Given that these veins are parallel to S_1, have been folded by F2 and are concentrated in the large F2 fold domains, it is likely that V2 formed from the delamination of S_1 along short limbs of F2 folds as these limbs rotated and subsequently shortened (Robert, 1989, 1990).

The third type of veins crosscut S_1 and are oblique to S_2 foliation. V3A are thick (<20cm), auriferous quartz±carbonate veins that contain coarse visible gold and share the same mineralogy to V2 veins. However, these veins are enveloped by massive tourmaline haloes (<5cm) where in all cases, there is a transition from the massive tourmaline to thin tourmaline veinlets which follow S_1 up to 10cm away from the main vein (Figure 2-6D). V3A veins cross-cut V2 veins (Figure 2-6E) and are not folded indicating that they post-date the development of F2 asymmetric folds. For this reason, V3A are interpreted to have formed during late D2 (Robert, 1989).

Both V2 and V3A are predominantly found in QV and FV and display higher vein density concentrated at the contacts between the Piché Group and Cadillac Group sediments.

The last vein type, V3B, are thin (<1cm) barren, quartz-carbonate veins that crosscut S_1 and are parallel to S_2 foliation (Figure 2-6F). V3B veins are the youngest veins observed at Orenada, are not deformed and are assumed to have formed post-D2 deformation (Neumayr et al., 2000).

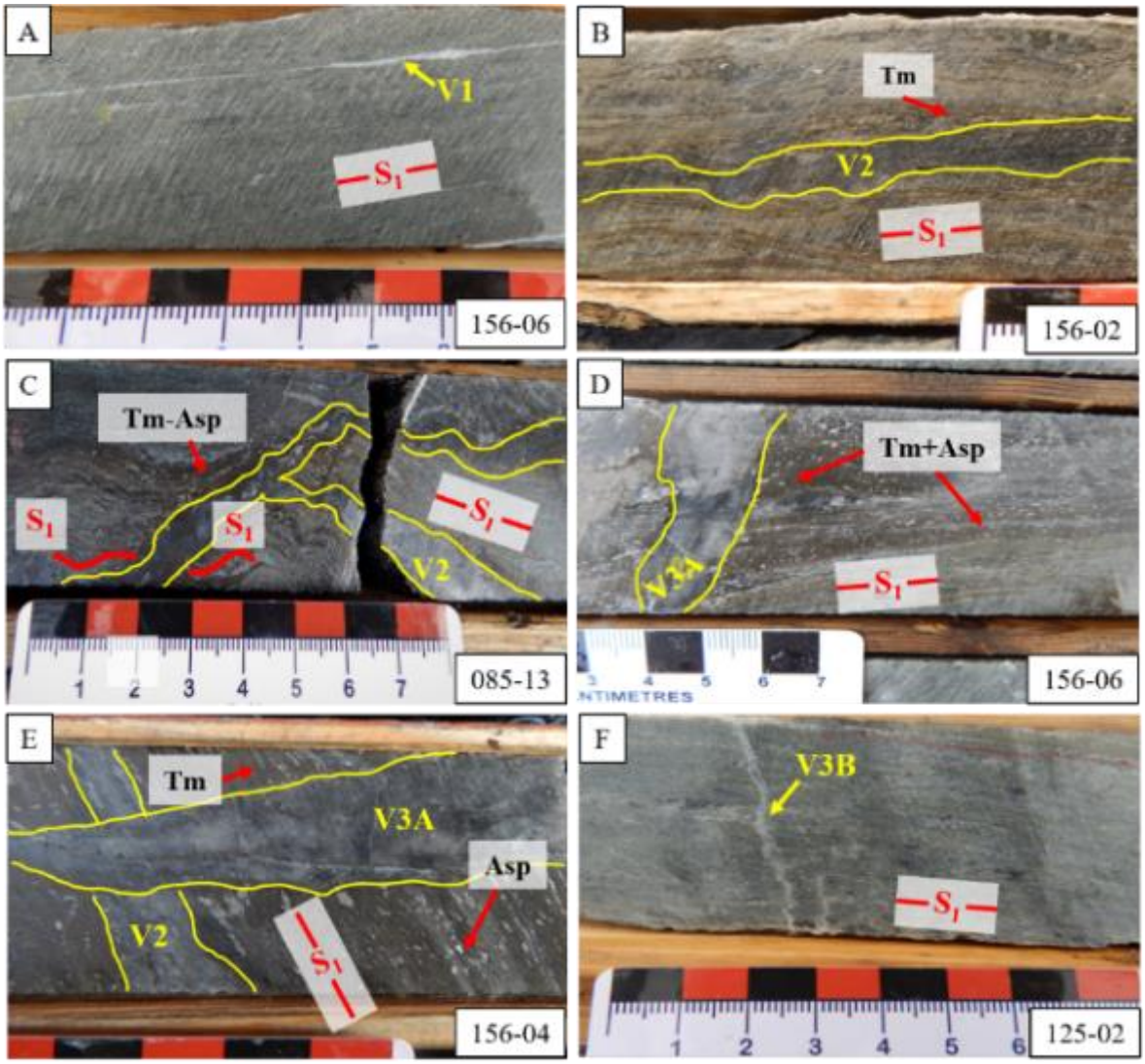

Figure 2-6. Drill core samples of the four different quartz (Qz)-carbonate (Cb) veins observed at the Orenada Zone 4 deposit. A) V1 Qz-Cb barren thin veins which follow the main penetrative foliation (S_1). B) V2 Qz-Cb vein that is parallel to S_1. The vein is surrounded by tourmaline (Tm) alteration. C) A folded V2 vein that follows and crosscuts S_1. The vein is surrounded by Tm alteration that propagates away from the vein. Arsenopyrite (Asp) is associated with the Tm alteration. D) V3A quartz vein that crosscuts S_1 along S_2. The vein is surrounded by Tm alteration. Asp is observed in the Tm halo and aligned along S_1. E) V3A Qz vein crosscuts V2 Qz-Cb vein. F) Barren V3B Qz-Cb vein that

crosscuts S_1 along S_2. Sample numbers are displayed in the bottom right corner of each photomicrograph.

2.2 Analytical Methods

Ninety-eight polished thin sections were prepared by Vancouver Petrographics Ltd. The mineralogy, deformation and alteration were characterized using an Olympus BX51 transmitted and reflected light microscope with 2.5x, 5x, 10x, and 20x magnifications. An Olympus UC30 digital camera with AnalySIS Getit 5.1 software at the Earth and Planetary Material Imaging Facility was used to take images of the thin sections. In some cases, mineral identification was aided using a JEOL JCM-6000 benchtop Scanning Electron Microscope (SEM) equipped with and Energy Dispersive System (EDS).

Sixty-five volcanoclastic samples were selected for whole rock lithogeochemical analysis to characterize compositional changes resulting from mineralization and alteration. Sample preparation was completed by ALS Global labs in Val d'Or, Quebec by a combination of crushing, splitting and pulverizing followed by lithium borate fusion and acid dissolution. Major element concentrations (Al_2O_3, BaO, CaO, Cr_2O_3, Fe_2O_3, K_2O, LOI, MgO, MnO, Na_2O, P_2O_5, SiO_2, SrO and TiO_2) were determined by inductively coupled plasma atomic emission spectroscopy (ICP-AES). Minor and trace element concentrations (Ba, Ce, Cr, Cs, Dy, Er, Eu, Ga, Gd, Hf, Ho, La, Lu, Nb, Nd, Pr, Rb, Sm, Sn, Sr, Ta, Tb, Th, Tm, U, V, W, Y, Yb, Zr) were measured by inductively coupled plasma mass spectrometry (ICP-MS). Major elements (Al, Ca, Fe, K, Mg, Mn, Na, P, S and Ti) and other minor and trace elements (Ag, As, Be Bi, Cd, Co, Cu, Hg, Mo, Ni, Pb, Sb, Sc, Tl and Zn) were measured using aqua regia dissolution of powders with ICP-AES finish. Boron values were measured by NaOH fusion and ICP-AES finish and, gold values were measured by fire assay and ICP-AES. Quality control of samples involved placement of internal standards every 12 samples.

Electron microprobe analysis (EMPA) was completed on a JEOL JXA-8530F field-emission electron microprobe at the Earth and Planetary Materials Analysis Laboratory in the Earth Sciences department at Western University. Electron dispersive spectrometers (EDS),

wavelength dispersive spectrometers (WDS) and back-scatter electron imaging (BSE) maps were obtained at an accelerated voltage of 15kV and a beam current of 100nA. The resolution of the maps of arsenopyrite and gold varied depending on the size of the grains. Pixel size ranged from 0.5µm to 2µm with a dwell of 8-10ms. EDS is used for the detection of major elements at a range of 1000s of ppm and, can simultaneously record data from numerous elements over a wide energy range (Borghi et al. 1998). By contrast, WDS is used for the detection of trace elements at the order of 100s of ppm and, elements are measured one at a time where, the data acquisition time depends on the number and type of spectrometers used (Borghi et al. 1998). Both EDS and WDS maps were used to identify the element compositions of the mineral inclusions in the arsenopyrite grains and to study the element compositions and primary zoning of arsenopyrite grains. Elements measured by EDS include Al, Si, Ca, Na, K, Fe, S, Ti, Ni and Cu whereas, As, Co, Ni, Sb, Au, Ag and Te were measured by WDS. Additionally, WDS point analyses of the arsenopyrite were conducted to evaluate whether refractory gold contents are greater than the detection limit of this technique (105ppm). The elements measured by WDS include, As, S, Sb, Te, Au, Ag, Fe, Co and Ni. Standards include: LIFL (Fe, Ni, Co); PETJ (S, Sb, Te); PETH (Au, Ag); TAP (As). The average detection limit for each sample and element can be observed in Table 2-2.

EMPA Spot Analysis Average Detection Limit (ppm)									
Sample	**As**	**S**	**Sb**	**Te**	**Au**	**Ag**	**Fe**	**Co**	**Ni**
75-06-Asp01	120	57	111	117	105	49	67	59	61
75-10-Asp01	119	57	111	116	104	49	67	59	61
75-10-Asp02	120	57	111	118	104	49	67	59	61
75-13-Asp01	120	57	111	116	105	49	67	59	61
84-9A-Asp01	120	57	112	117	105	50	67	59	61
84-9B-Asp02	120	57	111	117	105	50	67	59	62
84-9B-Asp03	121	57	112	116	105	50	67	59	62
85-13-Asp02	121	57	111	117	105	50	67	59	62
85-13-Asp03	121	57	111	115	105	50	67	59	62
85-2A-Asp01	120	57	111	114	104	50	67	59	61
96-08-Asp01	120	57	111	115	105	49	67	59	61
108-03-Asp01	120	57	115	117	104	50	67	60	63
122-04-Asp01	120	57	111	116	105	50	67	59	61
156-02-Asp02	120	57	111	116	105	50	67	59	62
156-04-Asp01	120	57	111	116	105	50	67	59	62
156-06-Asp01	120	57	111	117	105	50	67	59	61

Table 2-2. The average detection limit for each element (ppm) measured by Electron microprobe analysis (EMPA) Spot analysis in 16 Arsenopyrite grains.

The trace element compositions of arsenopyrite were determined by Laser Ablation Inductively Coupled Plasma Mass Spectrometry (LA-ICP-MS) at the Element and Heavy Isotope Analytical Laboratories (EHIAL) at the University of Windsor. A Photon Machines 193 nm short pulse width Analyte Excite excimer laser ablation system was used coupled with an Agilent 7900 quadrupole mass spectrometer. Forty-two line-traverses on 14 arsenopyrite grains were completed to characterize the distribution of Au and other trace elements within the grains and, to determine the relationship, if any, between trace element contents and the zonation of each grain. The elements and isotopes measured were B11, Al27, Si29, S34, K39, Ca42, Co59, Ni60, Cu63, Zn66, As75, Se78, Ag107, Sb121, Te130, W184, Au197, Hg202, Pb208 and Bi209. The average detection limit for each sample and element are listed in Table 2-3.

Table 2-3. The average detection limit of each isotopic element (ppm) measured by Laser

Samples	LA-ICP-MS Arsenopyrite Traverse Average UQAC standard Detection Limit (ppm)																			
	B11	Al27	Si29	S34	K39	Ca42	Co59	Cu63	Ni60	Zn66	As75	Se78	Ag107	Sb121	Te130	W184	Au197	Hg202	Pb208	Bi209
75-06	0	0.9	755	2771	0	0	0.1	0.4	0.56	1.01	27.0	12.7	0.1	0.3	3.5	0.2	0.1	1.0	0.1	0.1
75-10	0	10.4	5775	20236	0	0	1.8	2.8	4.97	10.64	194.2	111.9	1.1	2.9	29.6	2.3	0.9	24.3	1.0	1.0
96-08	0	0.5	205	835	0	0	0.1	0.3	0.74	0.14	0.2	3.0	0.2	0.1	3.0	0.1	0.2	3.3	0.1	0.1
108-03	0	0.8	702	2749	0	0	0.1	0.4	0.49	0.96	38.8	12.1	0.1	0.3	3.1	0.2	0.1	1.0	0.1	0.1
122-04	0	1.0	581	2455	0	0	0.1	0.3	0.54	0.74	7.2	11.7	0.1	0.3	3.0	0.1	0.1	1.6	0.1	0.1
156-02	0	1.4	562	1946	0	0	0.2	0.4	0.63	0.42	5.1	12.9	0.1	0.2	3.7	0.3	0.1	2.5	0.2	0.1
156-04	0	5.4	3132	8191	0	0	0.8	1.3	2.53	4.83	203.8	102.0	0.4	1.4	13.4	1.4	0.6	22.2	0.5	0.5
156-06	0	2.9	1860	5090	0	0	0.5	0.8	1.31	2.83	123.9	51.6	0.2	0.8	8.2	1.1	0.2	14.0	0.3	0.3
75-13	0	0.6	220	1080	0	0	0.1	0.2	0.39	0.11	0.7	4.5	0.1	0.1	2.2	0.3	0.1	1.2	0.1	0.0
84-9Basp02	0	1.0	454	1420	0	0	0.2	0.4	0.57	0.70	1.8	8.5	0.1	0.3	3.5	0.2	0.2	2.8	0.2	0.1
84-9Basp03	0	1.4	562	1946	0	0	0.2	0.4	0.63	0.42	5.1	12.9	0.1	0.2	3.7	0.3	0.1	2.5	0.2	0.1
85-13asp02	0	4.9	2944	7649	0	0	0.7	1.2	2.24	4.44	187.4	88.3	0.3	1.3	12.7	1.4	0.6	21.7	0.4	0.5
85-13-asp03	0	1.6	734	2194	0	0	0.2	0.5	0.64	1.09	68.3	17.6	0.1	0.4	4.5	0.3	0.2	3.4	0.2	0.2
85-2A	0	0.6	255	1203	0	0	0.2	0.4	11.50	0.31	0.6	4.5	0.2	0.1	3.3	0.5	0.3	2.8	0.1	0.1

NIST 610, UQAC and MASS1 standards were used for the calibration of the analyses. Iron (Fe57) was chosen as the index channel where Fe results were obtained from the EMPA values. The analyses consisted of a 30 second background run and a 60-90 second analysis time. Two to three transects were completed on each grain. The traverse locations were chosen based on the zonation observed from EMPA data. The laser beam power was set to 10Hz with a beam size of 40µm. Iolite software, an add on of Igor Pro by Wavemetrics, was used to interpret the data where each traverse was manually grouped by homogenous and heterogenous cobalt peaks (Paton et al., 2011).

2.3 Results

2.3.1 Petrography

The textural relationships between both volcanoclastic rock types, alteration, deformation, sulphidation and gold mineralization were identified by transmitted and reflected light petrography. The quartz porphyritic volcanoclastic consists of a ground mass with crenulated layers of white mica and fine-grained, granoblastic quartz-sericite-chlorite-carbonate±feldspar

layers. The white mica layers contain grains that define the main penetrative foliation S_1, which are crenulated by S_2 (Figure 2-7 A, B).

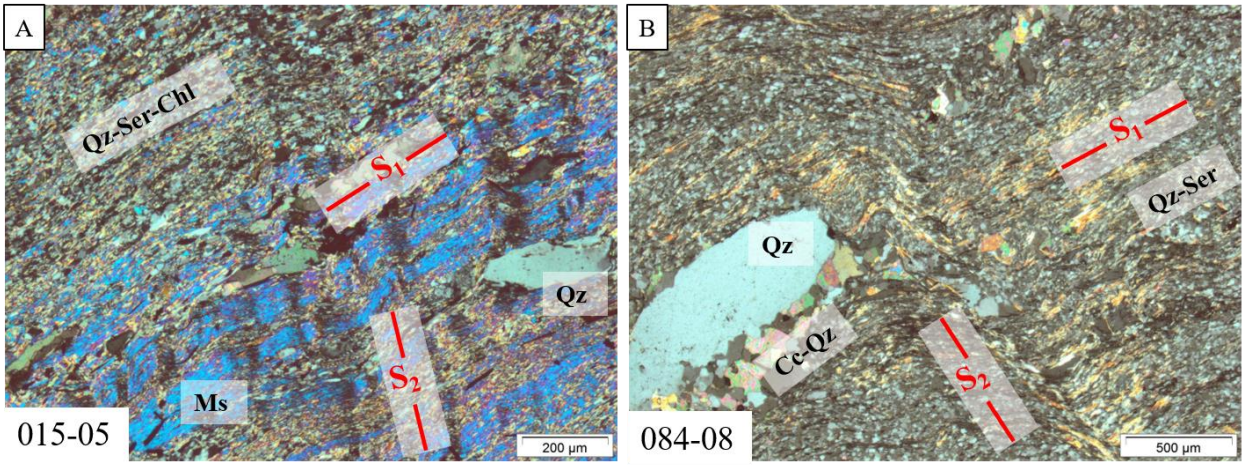

Figure 2-7. Photomicrographs of the QV ground mass with main penetrative foliation S_1 crenulated by S_2 foliation. A) Alternating muscovite and quartz-sericite-chlorite layers crenulated by S_2 foliation. A fine-grained quartz porphyroclast is aligned and elongated along S_1. B) Thin layers of muscovite and quartz are crenulated by S_2 foliation. A coarse-grained quartz porphyroclast is aligned and elongated along S_1 with visible quartz-carbonate pressure shadows. Sample numbers are displayed in the bottom left corner of each photomicrograph.

The quartz-rich granoblastic layers, sutured quartz grain boundaries and heterogeneous grain sizes are all evidence of recrystallization. The quartz porphyroclasts are medium- to coarse-grained, round to sub-rounded, lenticular and are aligned and elongated along the main penetrative foliation S_1, indicating a formation prior S_1. The porphyroclasts also exhibit undulous extinction, pressure shadows, are folded, cracked or broken grains and the foliation that surrounds porphyroclasts is deflected (Figure 2-8A-D). These textural features indicate a pre-kinematic growth. In some samples, quartz carbonate veins (V1) have been boundinaged into lenses of quartz, that are similar in appearance to the quartz porphyroclast but consist of clusters

of varied grain sizes of quartz and carbonate crystals with sutured grain boundaries (Figure 2-8D).

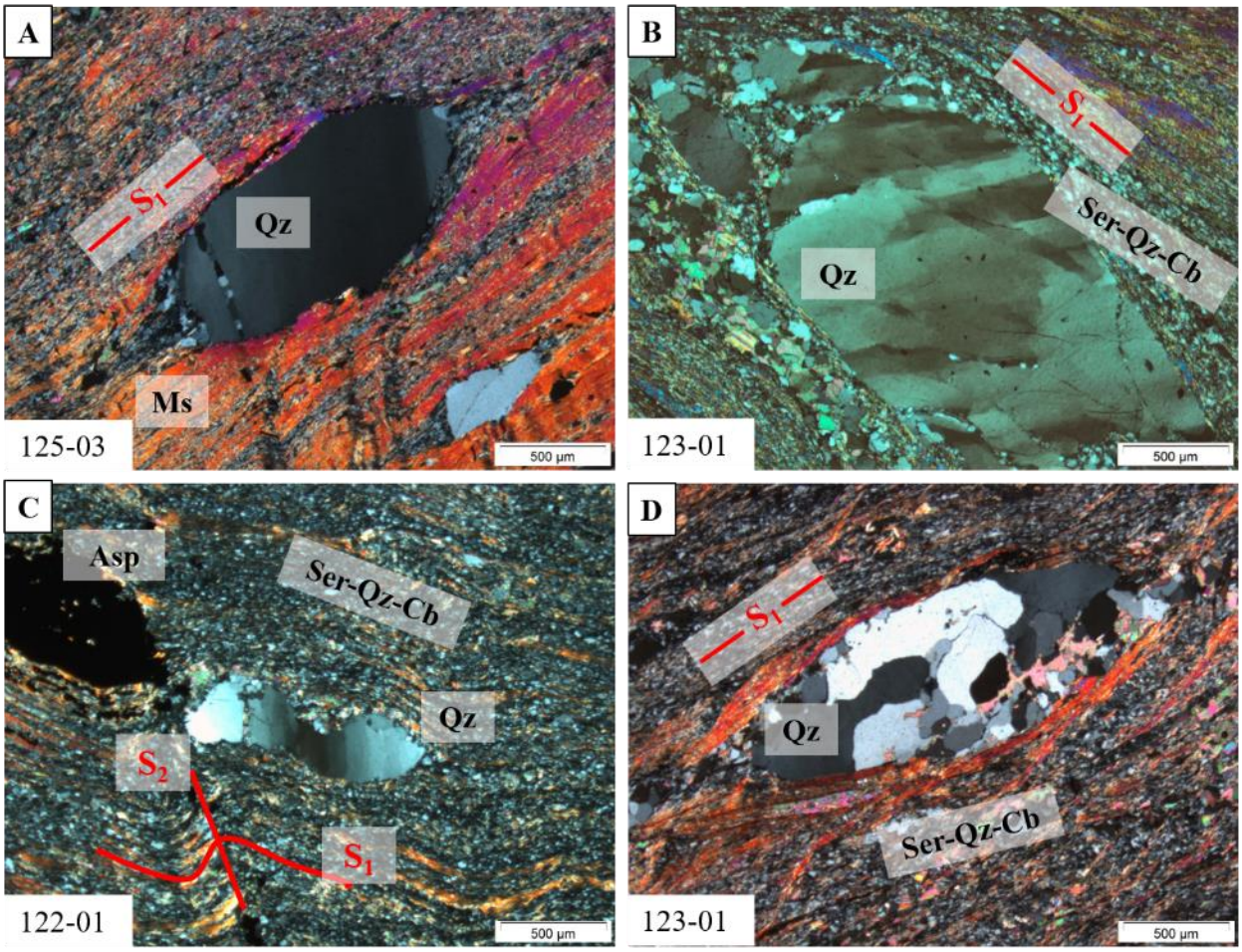

Figure 2-8. Photomicrographs of quartz porphyroclasts with pre-kinematic textures. A) Lenticular quartz porphyroclast with external muscovite foliation around the grain. The quartz porphyroclast is fractured and has fine-grained quartz pressure shadows. B) Coarse-grained quartz porphyroclast with undulous extinction. C) A folded quartz porphyroclast elongated along S1 and folded by S_2. D) V1 quartz-carbonate boudin with sutured grain boundaries surrounded by muscovite foliation and elongated along S1. The boudin appears like a porphyroclast. Sample numbers are displayed in the bottom left corner of each photomicrograph.

The feldspar porphyritic volcanoclastic rock consists of coarse-grained, euhedral to subhedral feldspar porphyroclasts which are aligned parallel to S_1. The porphyroclasts exhibit cracks, pressure shadows and are enveloped by a muscovite-rich foliation (Figure 2-9A-C). These textures indicate a pre-kinematic growth. The main foliation S_1 is defined by thin crenulated streamers of white mica, chlorite and fine-grained albite grains (Figure 2-9A-C). The ground mass is sericitized so S_1 and S_2 are more difficult to identify via optical microscope. In samples with a high volume of porphyroclasts, the feldspar is locally observed as randomly orientated clusters of grains (Figure 2-9D).

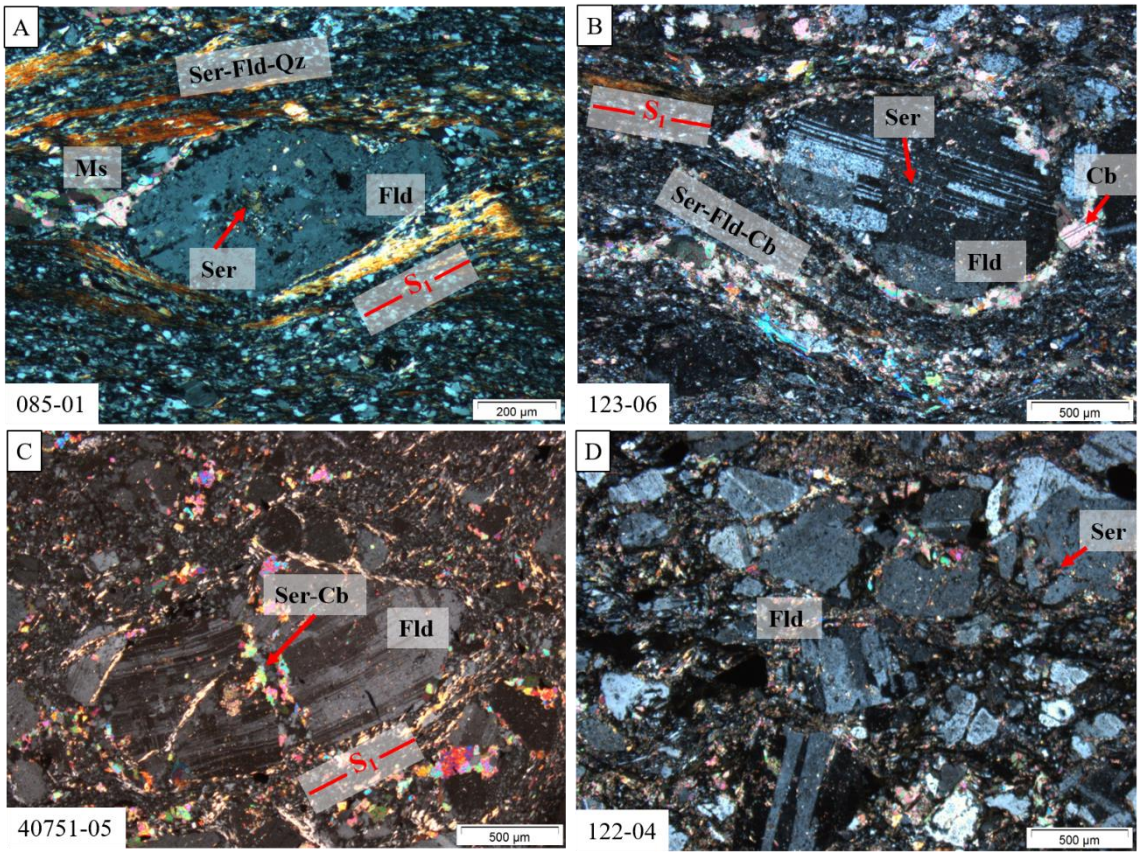

Figure 2-9. Photomicrographs of feldspar porphyroclasts with pre-kinematic textures. A) S_1 foliation wrapped around a feldspar porphyroclast. B) A coarse-grained feldspar porphyroclast surrounded by carbonate pressure shadow. The feldspar is aligned along S_1. C) A fractured feldspar porphyroclast infilled with carbonate and sericite. D) A cluster of

randomly oriented feldspar porphyroclasts. Minor sericite alteration is observed in all feldspar porphyroclasts. Sample numbers are displayed in the bottom left corner of each photomicrograph.

2.3.2 Alteration

Both QV and FV lithologies share the same sericite-chlorite-albite-carbonate alteration mineral assemblage however, different minerals are is more dominate depending on the original composition of the rock before metamorphism. It is important to note, that this alteration assemblage is present in both the altered and least-altered rock samples from both volcanoclastic rock types.

The main alteration assemblage for QV is chlorite-sericite-carbonate where the groundmass consists of interlayered chlorite-sericite-rich and granoblastic quartz and carbonate-rich layers (Figure 2-10).

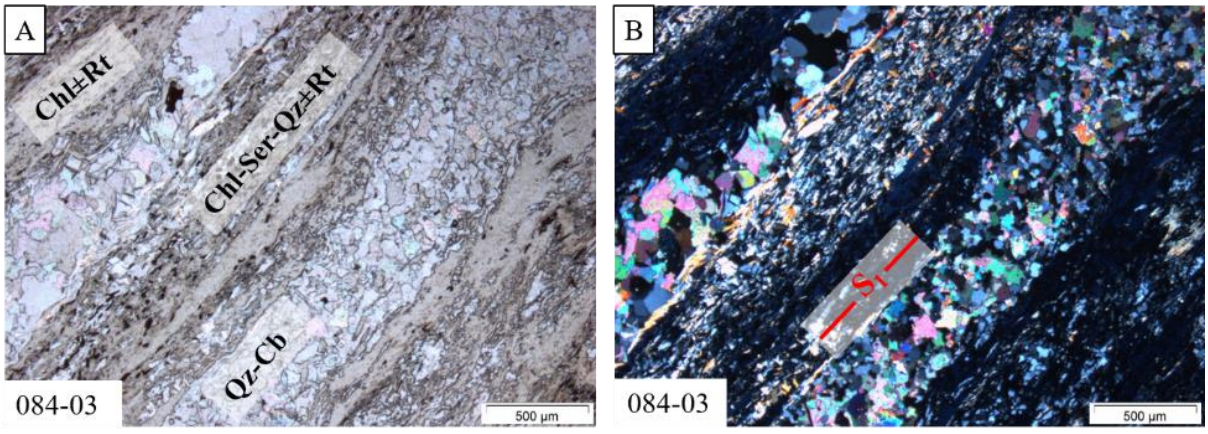

Figure 2-10. Photomicrographs of QV groundmass that displays chlorite-sericite±rutile (Chl-Ser±Rt) rich layers and, quartz (Qz) granoblastic carbonate (Cb) rich layers. Image A) is in plane polarized light and B) is in crossed polarized light. Fine-grained rutile is present in the chloritized layers. Sample numbers are displayed in the bottom left corner of each photomicrograph.

The main alteration assemblage of the FV is sericite-albite-chlorite-carbonate where, all alteration minerals are observed aligned along S_1. The FV groundmass is chlorite and sericite rich, where these schistose minerals define the main foliation. Sericite alteration is also observed locally within the feldspar porphyroclasts (Figure 2-9). Fine-grained albite is observed in the groundmass, where all euhedral grains are aligned along S_1 (Figure 2-11). Carbonate alteration within the groundmass and locally within the feldspar porphyroclasts is rare but visible in some samples.

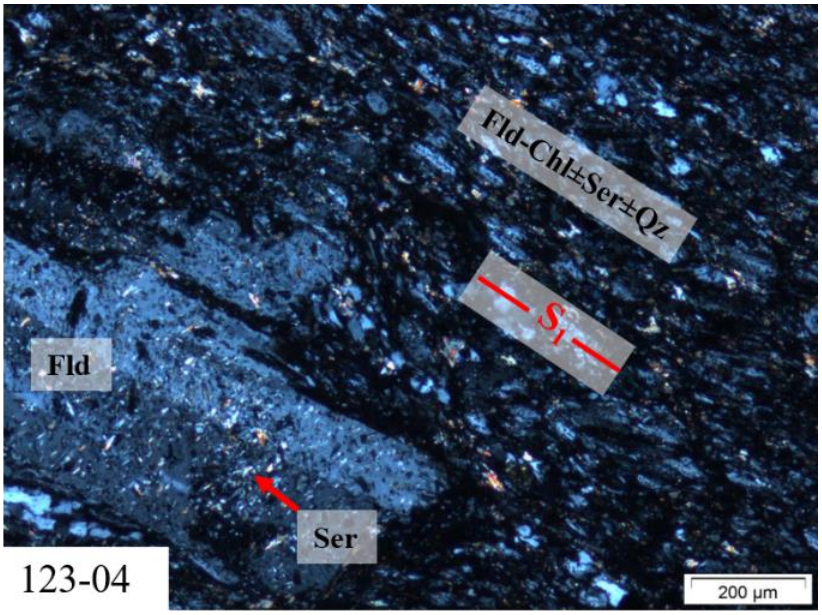

Figure 2-11. Photomicrograph of albitization and chloritization of the FV groundmass. Feldspar crystals in the groundmass are fine grained and aligned along the penetrative foliation S1 which is defined by chlorite and sericite. A coarse grained feldspar porphyroclast is observed with pervasive sericite alteration. Sample numbers are displayed in the bottom left corner of the photomicrograph.

The tourmaline alteration at Orenada overprints the sericite-chlorite-albite-carbonate background alteration. The tourmaline is observed as massive halos surrounding both V2 and V3A auriferous quartz-carbonate veins (Figure 2-12A, B) and, as thin folded veinlets that follow the main penetrative foliation S_1 (Figure 2-12C). With distance from V3A host rock contacts there is a

transition from massive tourmaline to thin stringers that are parallel to the sericite and chlorite fabric (Figure 2-12A). The tourmaline is also observed to have been folded along the S_2 foliation (Figure 2-12D). This indicates that the quartz-carbonate V2 veins were emplaced prior to the S_2 foliation.

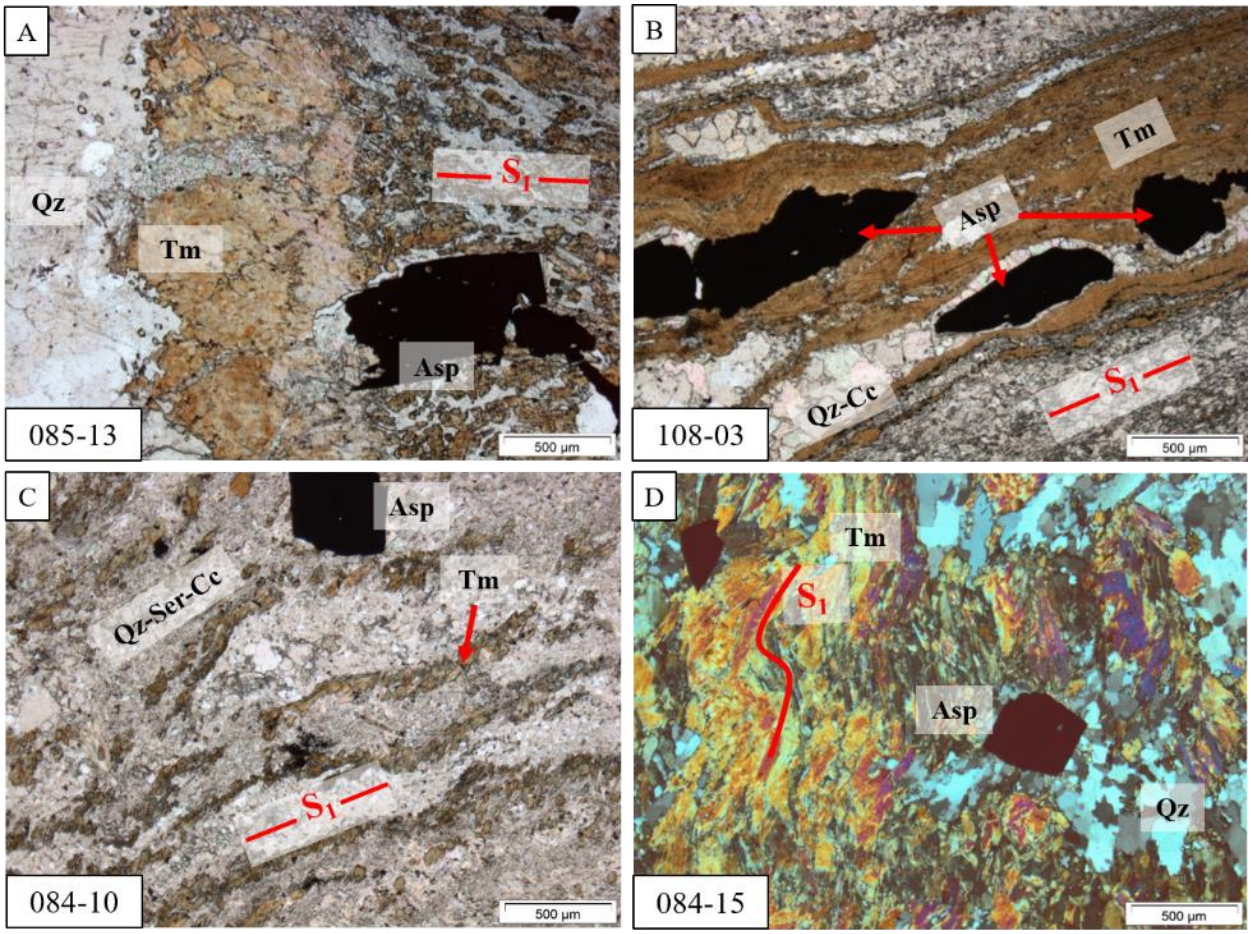

Figure 2-12. Photomicrographs of tourmaline (Tm) alteration. A) V3A quartz (Qz) vein with massive Tm halo which transitions into thin veinlets along S_1. An anhedral arsenopyrite (Asp) grain is observed at the outer boundary of the halo. B) V2 quartz-carbonate (Qz-Cb) vein parallel to S_1 with subhedral Asp grains. C) Thin folded Tm veinlets along S_1. The veinlets propagated from a proximal V3A vein which is not pictured.

D) Cross-polarized photomicrograph of Tm folded along S_2. Sample numbers are displayed in the bottom left corner of each photomicrograph.

2.3.3 Ore Mineralogy

Quartz-carbonate veins and sulphidation is an integral part of the gold mineralization at the Orenada deposit. As previously described, there are four generations of veins present at the deposit (Table 2-1). With the aid of microscopic petrography, the four vein types are further characterized based on microstructural features.

The first type, barren quartz-carbonate veins, V1, are boudinaged and parallel to S_1 (Figure 2-13A). At some locations individual boudins are completely detached, which gives them an appearance similar to the quartz porphyroclasts (Figure 2-8D). The quartz grains in the veins are granoblastic and display sutured grain boundaries (Figure 2-13B). The second type are auriferous quartz-carbonate veins, V2, which are parallel to the main fabric (Figure 2-12B). The V2 veins can also be folded and display deformational textures like sutured grain boundaries and heterogeneous grain sizes. The third type (V3A) are auriferous quartz-carbonate-tourmaline veins that crosscut S_1 along a S_2 foliation (Figure 2-12A). The quartz displays microstructural textures like grain size reduction, undulous extinction and heterogenous grain sizes (Figure 2-13C). These microstructural examples indicate that the grains have undergone deformation and recrystallization (Stipp et al., 2011). In sections where there is an abundance of V3A, the veins occur as closely spaced, subparallel groups where, their individual tourmaline halos coalesce to form a broader alteration envelope. The fourth type of veins, V3B, are thin, barren quartz-carbonate veins, which are equigranular, display polygonal grain boundaries and crosscut S_1 along the late S_2 foliation (Figure 2-13D).

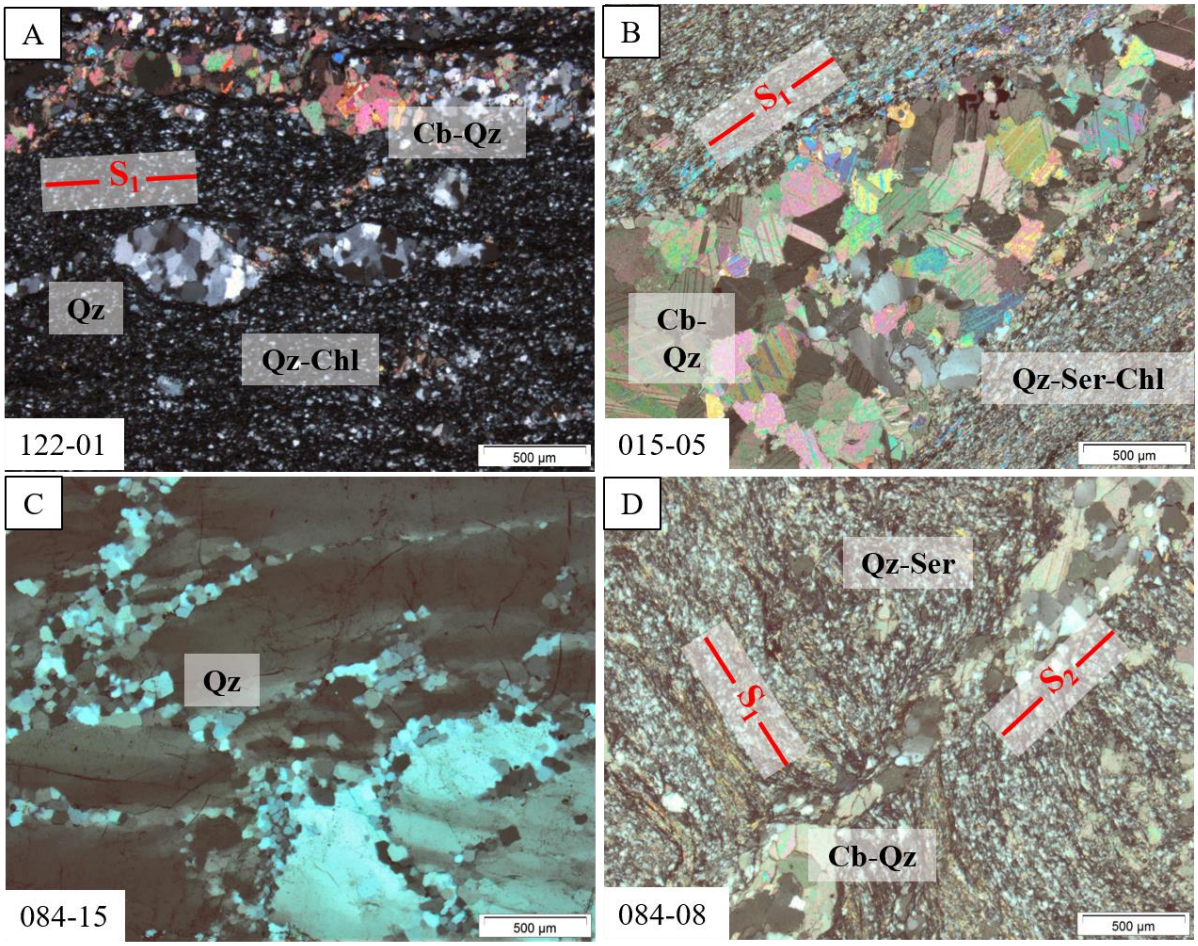

Figure 2-13. Cross polarized photomicrographs of quartz-carbonate veins. A) V1 quartz-carbonate vein boudinaged and aligned along S_1. B) V1 quartz-carbonate vein with sutured grain boundaries and heterogenous grain sizes. C) Quartz of a V3A auriferous vein with sutured grain boundaries, undulous extinction and heterogenous grain sizes. D) Late V3 quartz-carbonate vein aligned along S_2 that crosscut main S_1. Sample numbers are displayed in the bottom left corner of each photomicrograph.

Arsenopyrite is the dominant sulphide mineral at the deposit, where it occurs as two textural types. The first type, are medium-grained euhedral to subhedral grains Figure 2-14A) and the

.

second, are coarse-grained, anhedral, fractured grains (Figure 2-14B). Both textural types are observed adjacent to each other in the tourmaline alteration haloes and along the tourmaline stringers in the altered wall rock (Figure 2-14C). All the arsenopyrites observed distal to the massive tourmaline halos, are aligned along the main penetrative foliation S1 and, decrease in abundance with increasing distance from V2 vein contacts. The anhedral arsenopyrites have undergone higher amounts of strain than the euhedral grains observed by the numerous amounts of pits and fractures within these grains. It is important to note, that the anhedral grains are also present at the quartz-tourmaline V2 inner halo boundary (Figure 2-12A) whereas, euhedral grains are absent at the inner boundaries.

Both textural types of arsenopyrite are aligned along S_1 and show pressure shadows of medium-grained quartz-carbonate grains (Figure 2-14D). In many samples, both textural types of arsenopyrite are poikilitic and contain fine-grained rutile inclusions that define a pre-existing foliation (Figure 2-14E). The rutile inclusions also define S_1 foliation and are observed in the groundmass and within arsenopyrite grains. The inclusions are concentrated at the center of the arsenopyrite grains and are locally accompanied by other coarser-grained muscovite and carbonate inclusions. The above observation indicates that the arsenopyrite grains were rotated during deformation indicating a syn-deformational timing of growth. An excellent example of this is in Figure 2-14F which shows a subhedral arsenopyrite grain rotated along the rutile defined S_1. Rutile inclusions within the arsenopyrite grain define S_1 highlighted by the dashed red lines.

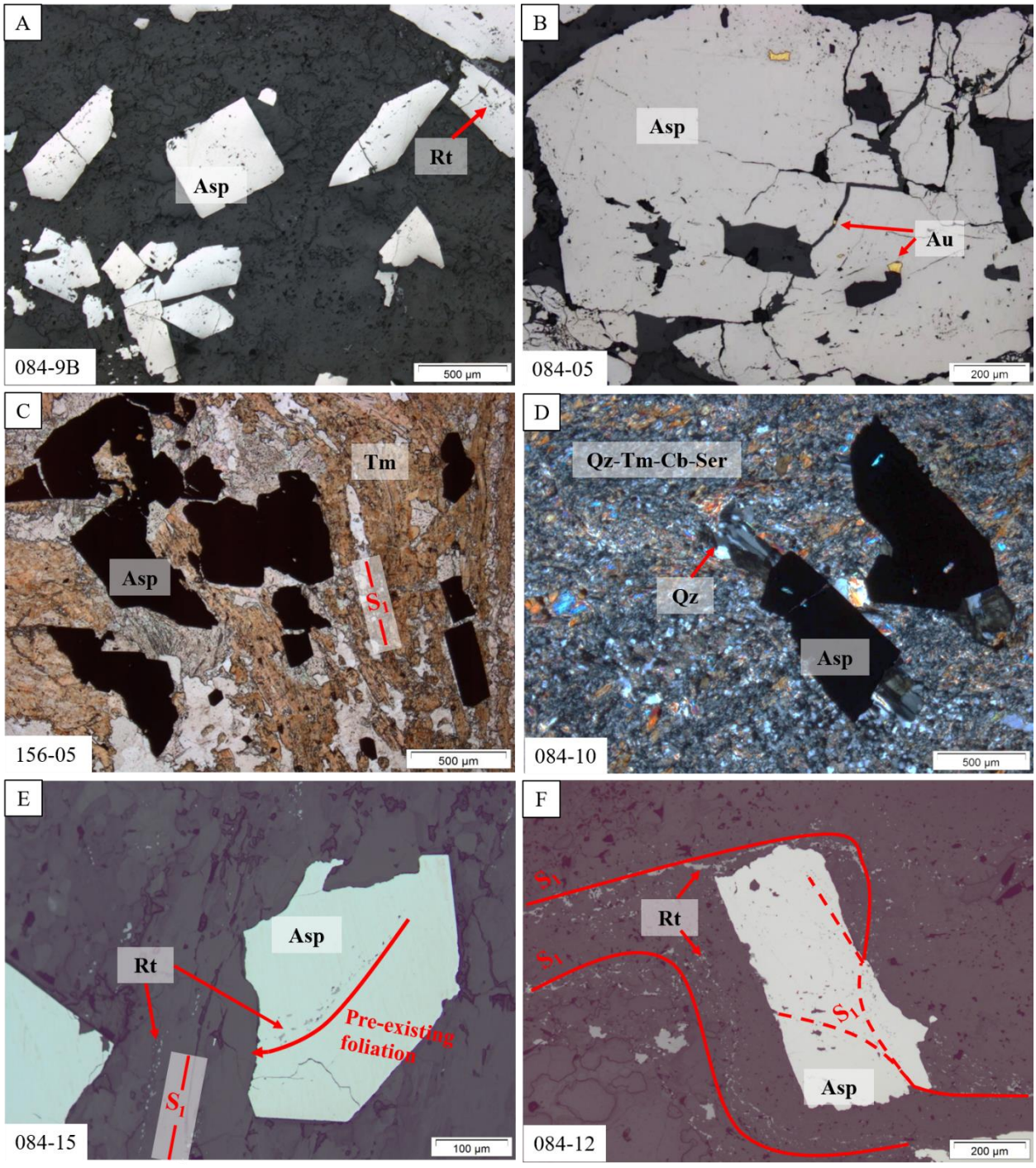

Figure 2-14. Reflected and transmitted light photomicrographs of arsenopyrite (Asp) grains. A) Euhedral Asp grains. B) Corroded Asp grain with visible gold (Au) within pits

and fractures. C) Shows both anhedral and euhedral Asp aligned along S_1 defined by thin tourmaline stringers. D) A subhedral arsenopyrite grain with pre-existing foliation defined by rutile inclusions. S_1 is defined by rutile inclusions adjacent to the arsenopyrite. E) Arsenopyrite grains with quartz pressure shadows. F) A subhedral arsenopyrite grain rotated along S_1 defined by rutile inclusions. The red dashed lines indicate the S_1 inside of the arsenopyrite grain whereas the solid red lines indicate rutile S_1 in the groundmass. Sample numbers are displayed in the bottom left corner of each photomicrograph.

Lesser amounts of pyrite, pyrrhotite, chalcopyrite and rutile are observed in the groundmass of both volcanoclastic rock types and as fine-grained inclusions within arsenopyrite grains. The pyrite grains are always coarse, corroded grains preferentially aligned along the S_1 (Figure 2-15A) Fine-grained pyrrhotite are present in many chlorite rich groundmass samples where grains are aligned along S_1 (Figure 2-15B). Sulphide inclusions within arsenopyrite are rare, and where present, they are adjacent and aligned with the rutile inclusions along S_1 (Figure 2-15C). Based on the fact that all of these secondary sulphide minerals are aligned to S1 and are not observed to be associated with mineralization, they are assumed to have formed during late D1 early D2 deformation events.

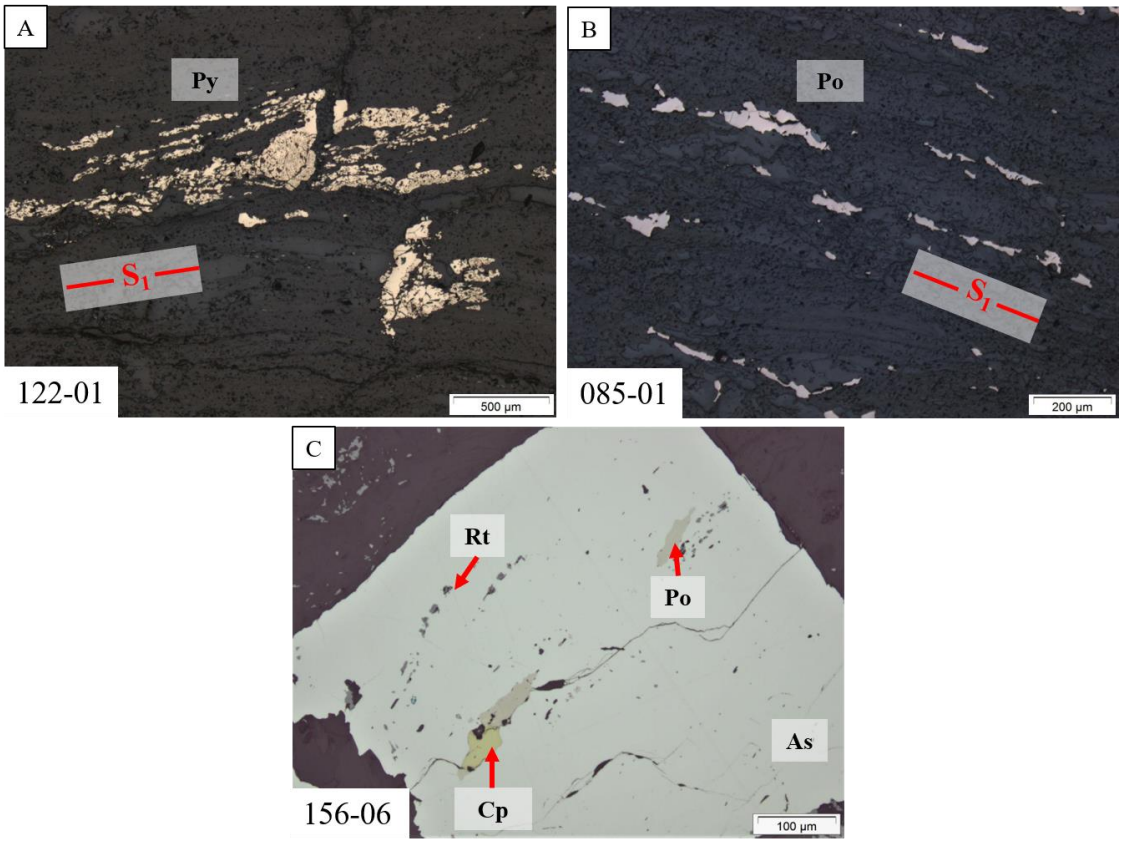

Figure 2-15. Transmitted light photomicrographs of secondary sulphides. A) Coarse-grained anhedral pyrite elongated along S_1. B) Fine-grained pyrrhotite aligned along S_1. C) Fine-grained chalcopyrite, pyrrhotite and rutile inclusions in anhedral arsenopyrite aligned along S_1. Sample numbers are displayed in the bottom left corner of each photomicrograph.

Gold mineralization is closely associated with V2 and V3A veins, fractured anhedral arsenopyrite and tourmaline alteration. Two types of mineralization are observed. The first, is as free gold in the V2 and V3A quartz±carbonate veins, typically observed at the contact between the tourmaline-rich halo, but also within the quartz vein itself (Figure 2-16).

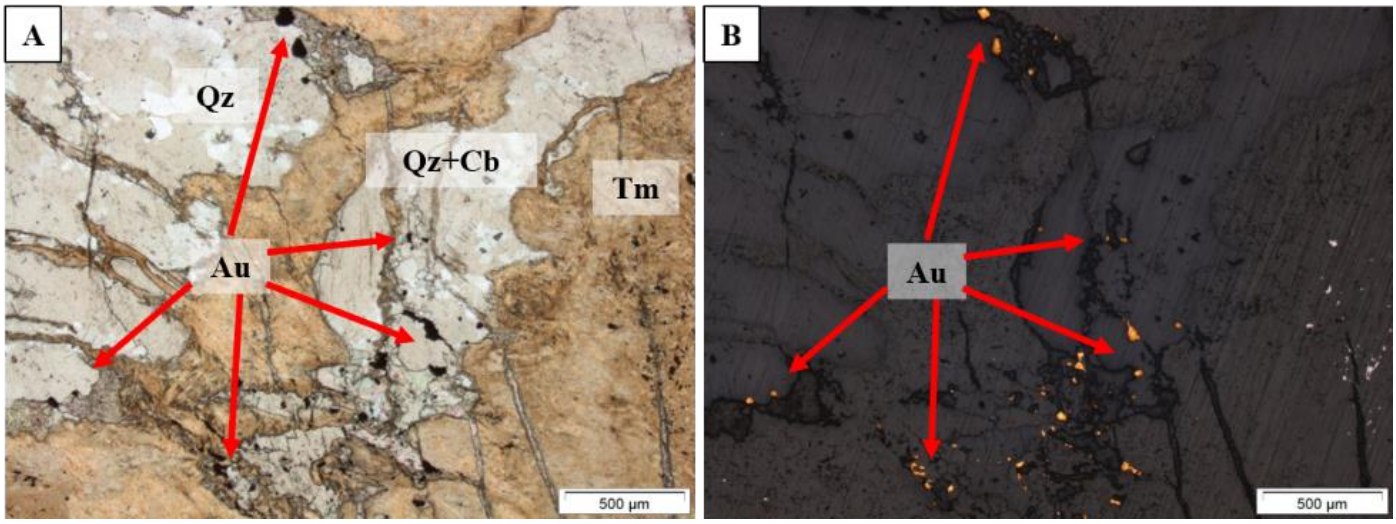

Figure 2-16. Photomicrographs of free gold in V3A quartz±carbonate veins. A) is in plane polarized light and B) is in reflected light. The gold is present in the quartz-carbonate vein. The vein is surrounded by a massive tourmaline alteration halo.

The second type of gold occurs in corroded arsenopyrite grains, most commonly present within quartz-carbonate filled fractures and pits (Figure 2-17). It is important to note that visible gold is only observed within these grains. No gold has been observed gold in the euhedral grains.

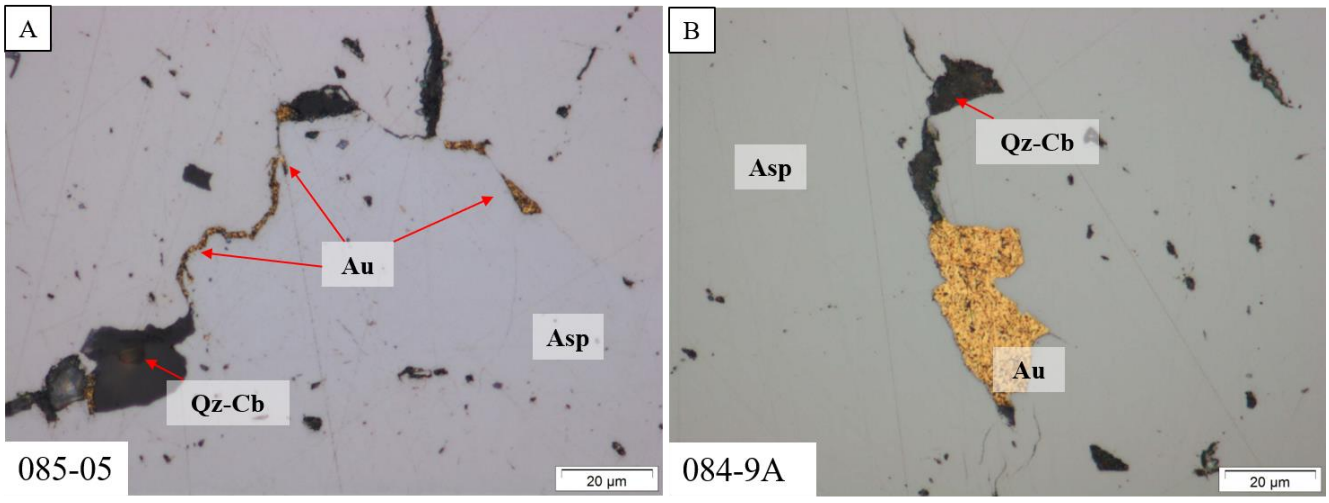

Figure 2-17. Transmitted light photomicrographs of gold filling in fractures and pits of

anhedral arsenopyrite grains. A) shows gold in fractures B) shows gold in a pit. Sample numbers are displayed in the bottom left corner of each photomicrograph.

The above petrographic observations, paragenetic sequences are summarized in Table 2-4 for each volcanoclastic rock type where mineral abundances are categorized by least-altered, altered wall rock and ore mineralogy.

Table 2-4. Paragenetic sequence of QV and FV rock types

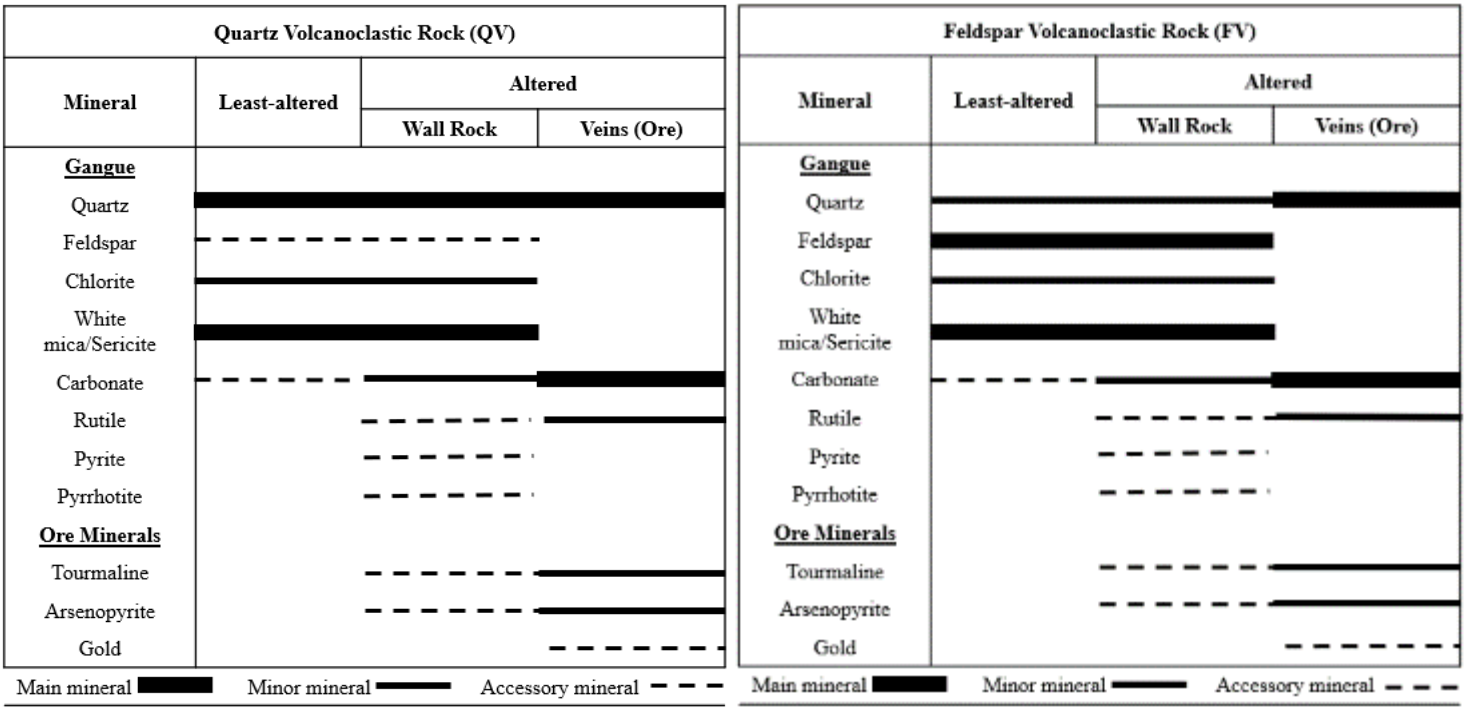

2.3.4 Whole Rock Lithogeochemistry

All of the collected rock samples display distinct trace element signature (Figure 2-18), which is best illustrated by the Cabanis and Lecolle (1989) diagram of tectonic classification of magma igneous rocks. This figure was chosen because the samples in this study are altered and metamorphosed, thus diagrams which use elements mobile during metasomatism and metamorphism cannot be reliably used to identify pre-metamorphic and altered igneous rock

types Both altered and least-altered QV and FV samples are clustered in the arc calc-alkaline field (Figure 2-18). However, two data points cluster within the back arc field (BA: Orange) and two cluster within the late- to post orogenic intra-continental field (OIC: green) (Figure 2-18).

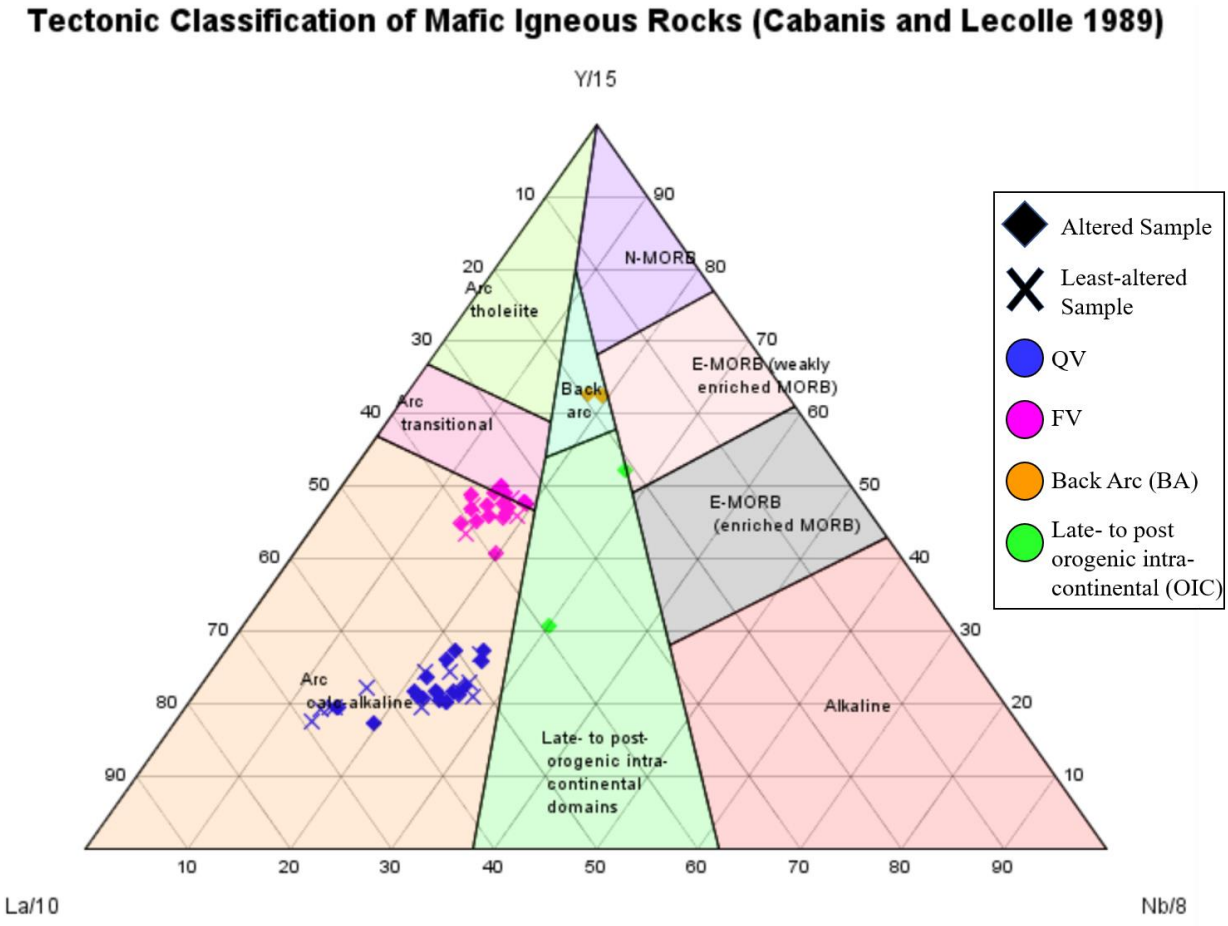

Figure 2-18. Tectonic Classification of Mafic igneous rocks (Cabanis and Lecolle, 1989).

To further distinguish QV and FV and the four outlier data points (BA & OIC), a chondrite normalized REE spider diagram (McDonough and Sun, 1995) was created (Figure 2-19). Both QV and FV display similar elemental trends suggesting they are a part of the same magma series. Differently, both the BA and OIC trends are distinguishably different from the QV and FV (Figure 2-19). The flat BA trends suggests a MORB volcanic affinity for the two samples (Figure 2-19).

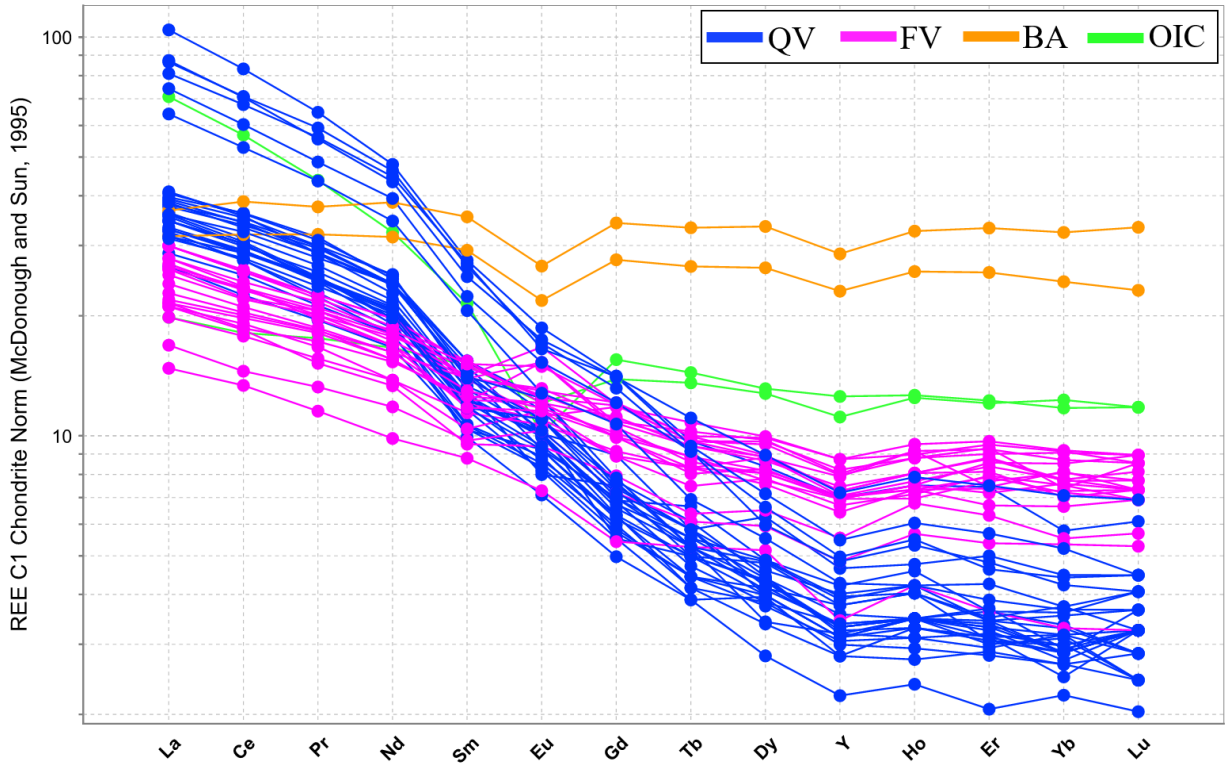

Figure 2-19. REE Spider diagram normalized to chondrite (McDonough and Sun, 1995) illustrating the average values of each volcanoclastic rock type. Four rock types are observed.

Major oxides and, major and trace elements of both rock types are displayed in box and whisker percentile plots (Figure 2-20 & Figure 2-21) where the blue boxes correspond to QV and pink boxes correspond to FV. Plots are compared by the average concentrations displayed by the black X in the center of each plot. The black middle line within the plot defines the median values. The lower bar defines the minimum limit and the upper bar defines the max limit. Outlier data points are observed either above or below the min and mix bars.

In the major oxide elements plots (Figure 2-20), QV is characterized by higher SiO_2 (63.2 wt.%) relative to FV (52.6 wt. %). In addition, the FV has elevated concentrations of Na_2O (5.48 wt. %) and CaO (6.04 wt.%) compared to QV (2.46 wt. % and 4.21 wt.%, respectively). These

variations correspond to the quartz and feldspar porphyroclasts found in the respective rock types. In addition, QV displays elevated amounts of K_2O (2.44 wt. %) relative to FV (0.62 wt. %) which corresponds to the increased amount of white mica in the QV groundmass. In contrast, FV exhibits higher Al_2O_3 (17.60 wt.%), Fe_2O_3 (7.05 wt.%), MgO (2.71 wt.%), TiO_2 (0.75 wt.%) and LOI (6.50 wt.%) relative to QV (15.07 wt.%, 4.31 wt.%, 1.79 wt.%, 0.39 wt.% and 5.64 wt.% respectively). The elevated Fe_2O_3, MgO and TiO_2 in FV likely correspond to a more mafic protolith, consistent with the classification on Figure 2-18.

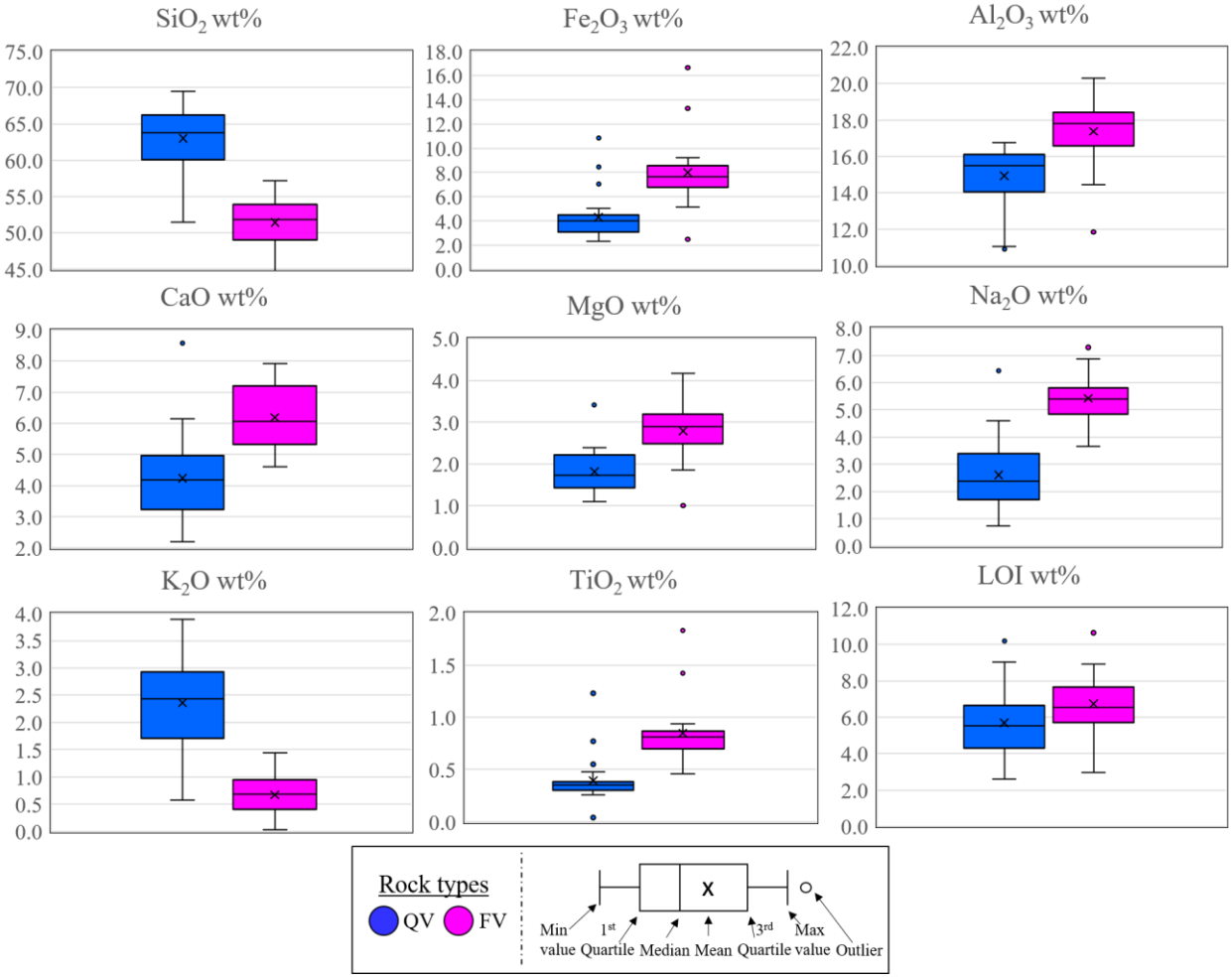

Figure 2-20. Box and whisker diagrams showing primary whole-rock lithogeochemical variations for major oxide group elements. The samples are subdivided into two groups

from the Cadillac Group volcanoclastic rocks, QV (dark blue; n=24) and FV (pink; n=19). All diagrams are displayed in weight percent.

Box and whisker plots of Au, As, S and B are shown in Figure 2-21. These elements are extremely important because gold mineralization is associated with arsenopyrite (As, S) and tourmaline alteration (B). The average As, S and B concentrations are similar in both rock types however, arsenic values for QV display a higher range in values compared to FV values. The average Au concentrations in QV (570 ppb) are slightly higher than in FV (240 ppb). Both QV and FV display outliers, however QV displays more with values as high as 6000 ppb. The similarity in gold values, excluding the outlier points, between the two rock types indicates that gold mineralization is not preferentially hosted by either rock type. This is also true for tourmaline alteration and sulphidation associated with arsenopyrite.

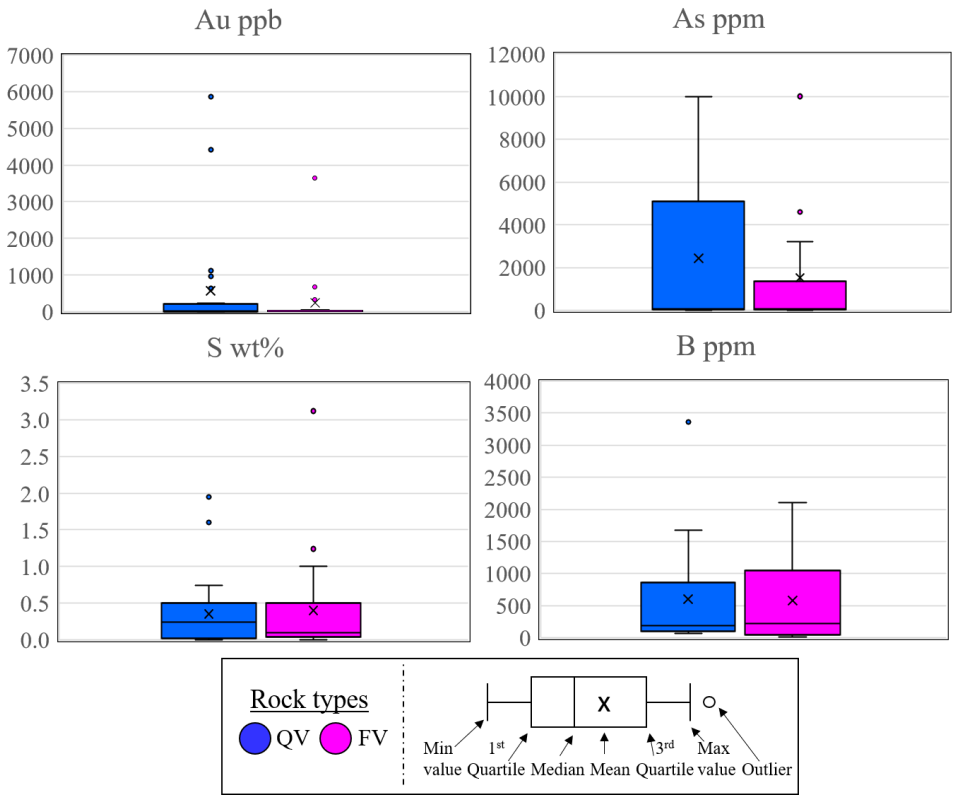

Figure 2-21. Box and whisker diagrams showing primary whole-rock lithogeochemical variations for Au, As, S and B. The samples are subdivided into two groups from the Cadillac Group volcanoclastic rocks, QV (blue; n=25) and FV (pink; n=22).

To further investigate the geochemical relationships between gold mineralization, arsenopyrite sulphidation and tourmaline alteration, As was plotted against S with the shape, size, color of the symbols representing the volcanoclastic rock type, B concentrations and Au concentrations, respectively. Figure 2-22 displays a positive correlation between As, S and Au where the data points with the greatest S (wt.%) and As (ppm) values correspond to the largest Au ppb concentrations (most red). Interestingly, high boron concentrations (largest size) is observed with both high and low gold values. This means tourmaline alteration is not directly associated with high gold grades and tourmaline-rich samples can be either strongly or weakly mineralized. One possible interpretation is that where tourmaline is in veins with sulphides gold contents tend to be high, but where tourmaline is in the wallrock, lacking significant sulphides, the gold contents tend to be low. Figure 2-22 displays three main trends taken from the arsenic and sulphur weight ratios in (ppm). The first, As/S=1 corresponds to high gold grades and varied boron values. The arsenopyrite at Orenada have a As/S weight ratio of approximately 2.04 to 2.45. Thus, the first group corresponds to rocks where most and possibly all of the sulfur is contained within arsenopyrite. The second group have As/S=0.1, which corresponds to the lowest gold grades and have varied boron content. Some of the sulphur in this group is contained within arsenopyrite, but the low As/S ratio implies that most of the sulphur must be in an additional phase such as pyrite. In the third group the As/S=0.001 and corresponds to low-medium gold grades. The very low As/S ratio indicates that arsenopyrite is absent or present in trace amounts and that most if not all of the sulphur is contained in a different phase, likely pyrite.

These geochemical observations agree with the petrography in section 2.3.3. Both QV (squares) and FV (triangles) are scattered along the trend and display data points of varying sizes and colors. This further proves that gold mineralization is not related to the type of volcanoclastic rock.

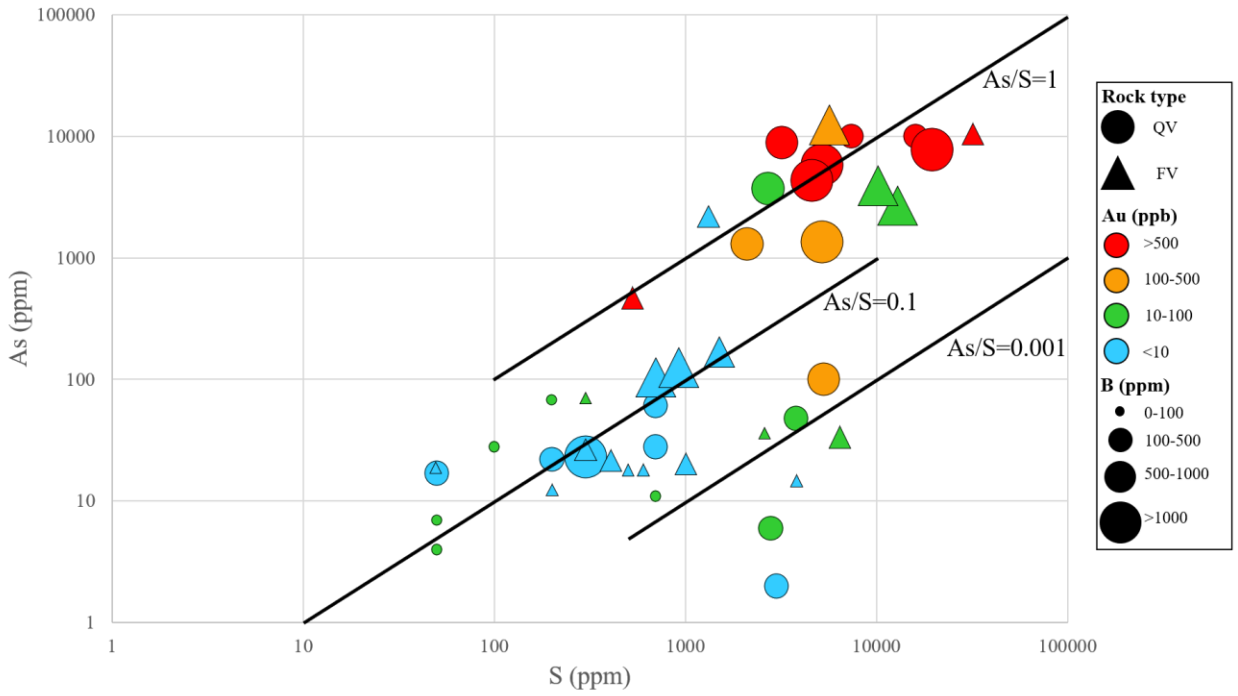

Figure 2-22. As-S-Au-B graph of altered Qv and FV samples. The graph displays a correlation between all four elements. Color represents Au concentrations and size represents B concentrations. Three main trends are observed. The graph is displayed in log scale.

2.3.4.1 Alteration Diagrams

Major and trace element lithogeochemical data was used to interpret the prominent alteration in each rock type by characterizing and comparing the altered and least-altered samples. The main alteration minerals observed are chlorite, sericite, albite, quartz, carbonate and tourmaline. Petrographic observations indicate that the main alteration assemblage is chlorite-sericite-albite, which occurred prior to the formation of V2 and V3A quartz-carbonate-tourmaline veins. A General Element Ratio (GER) diagram was used to interpret the mineral distribution of the alteration within the two volcanoclastic rock types. The data in GER diagrams are presented in terms of molar ratios where the denominator of each axis is not a conserved

element but instead fully contributes in the material transfer (Pearce, 1968; Pearce and Cann, 1973; Stanley, 2020). The chosen denominator element used for this study is Al.

Figure 2-23 is a GER diagram of molar (Na+K)/Al versus Na/Al. This specific GER was chosen because it clearly illustrates all the prominent alteration minerals observed in this study. Each mineral is defined by the red nodes which are based on the amount of Na, K and Al in the chemical formula of each mineral. All the data points fall within the chlorite-albite-muscovite field defined by the red lines connected from each node. This suggests that there is chlorite, albite and sericite alteration within both rock types. As an added variable, gold concentrations are defined by the size of the data points. All data points show variability in sizes scattered along the alteration trend. This suggests that the gold mineralization is not related to sericitization and albitization.

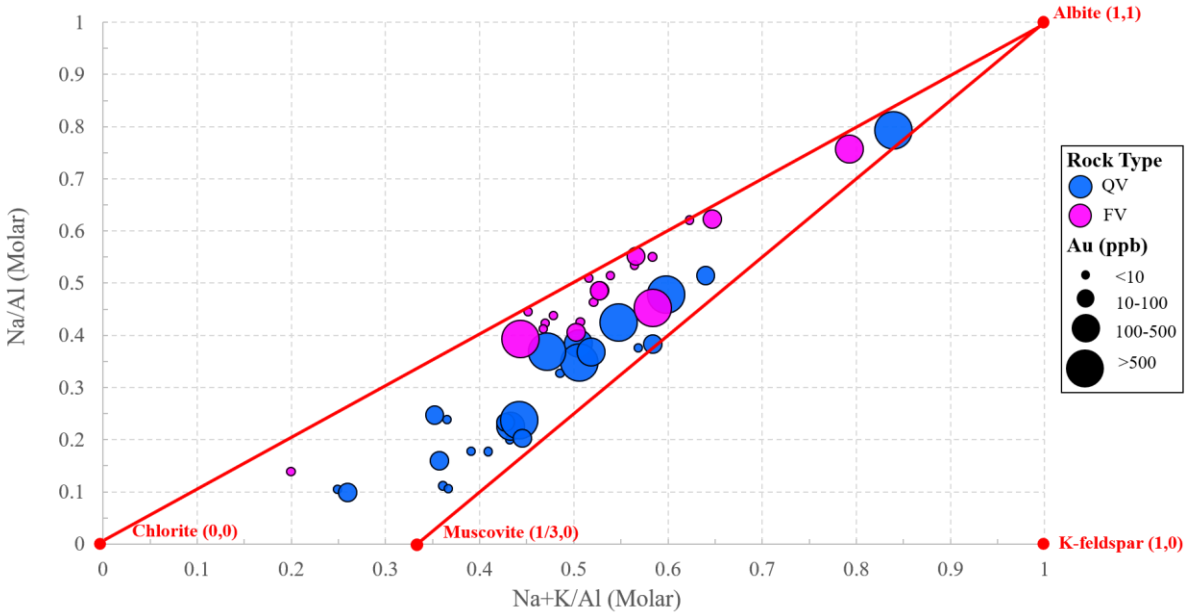

Figure 2-23. General Element Ratio (GER) diagram illustrating an alteration trend of Na and K from whole rock analyses. QV is defined by the blue data points whereas FV is defined by the pink points. All data points of each rock type are observed with the chlorite-

muscovite-albite alteration zone as defined by the red lines connected from each node. Gold concentrations, defined by the size of the data points, are scattered throughout the trend.

Another way to evaluate the effects of hydrothermal alteration, is to calculate the mass changes of the altered rock samples normalized to the least-altered (precursor) samples (MacLean and Kranidiotis, 1987; MacLean and Barrett, 1993; Gaillard et al., 2018). Mass change is an effective tool that can help examine the alteration assemblages to evaluate the effects of metasomatism associated with ore-forming processes (Gaillard et al., 2018). The resulting mass gains or losses can thus lead to potentially identifying pathfinder elements that can be used as vectors towards mineralization. This method, defined by MacLean and Barrett (1993), was adapted form Gresens (1967) method using density and volume values. However, the MacLean and Barrett (1993) method uses immobile element ratios which gives a simplified expression to Gresens (1967) mass change equation.

Mass change calculations are completed with the use of immobile element ratios with elements such as Al, Ti and Zr, which are generally considered to be immobile in hydrothermal systems (MacLean and Barrett, 1993; Gaillard et al., 2018). Using immobile element ratios involves the calculation of the reconstructed composition (RC) which is calculated from the initial chemical analysis (based on 100 mass units) of the precursor rocks using the ratio of the immobile monitor and the weight percent of a component X (1). MacLean and Barrett (1993) mention that for igneous rocks Zr is the most useful element to monitor fractionation because it is immobile and highly incompatible in calc-alkaline rocks. For this reason, Zr was ultimately chosen as the immobile element for this study however, Ti and Al were also tested and produced similar results.

The formulas to calculate the reconstructed composition (RC), the mass change (MC) and the percent change (ΔX) is described below:

$$RC = (Zr_P/Zr_A) \times Cx_A \quad (1)$$

Where:

- RC: The mass of component X after alteration
- (Zr_P/Zr_A): The concentration ratio of immobile element Zr in the precursor (P) to altered (A)
- Cx_A: The concentration of a component X in an altered rock (A)

Mass changes (MC) for each element corresponds to the ratio of RC in equation (1) and component X in the precursor rock.

$$MC= RC-Cx_P \quad (2)$$

Where:

- MC: The mass change of a component X
- Cx_P: The concentration of a component X in a precursor (P)

The results can also be expressed in percent change (ΔX), which corresponds to the absolute value of the MC of component X to the precursor concentration of component X multiplied by 100.

$$\Delta X= |MC/Cx_P| \times 100 \quad (3)$$

Where:

- ΔX: The percent change of component X relative to the precursor composition

The immobile elements for the mass change calculations were determined from bivariate plots constructed where two immobile elements, one compatible and one incompatible, define one or a series of least-altered rock precursors. For igneous hosts, the precursors outline a continuous trend which indicates that the elements remained immobile during alteration (Barrett and

MacLean, 1993). The trend is extremely important because points along this trend are used to calculate the mass balance of altered samples. It is important to note, that both the OIC and BA samples were omitted from the mass balance calculations.

For this study, both immobile element plots Zr vs. TiO_2 and Zr vs. Al_2O_3 show well defined trends however, MacLean and Barrett (1993) recommend that strongly feldspar porphyritic rocks should be excluded from Al plots due to a data bias from the high Al contents. For this reason, Zr vs. TiO_2 was chosen for this study. Immobile element ratios calculated from TiO_2 concentrations were therefore used to evaluate the mass changes associated with alteration. Figure 2-24 displays the Zr vs. TiO_2 plot of this study where two distinct rock types, QV (blue square) and FV (pink circle), are defined with their corresponding precursors (grey). The geochemistry of the precursors corresponds to QV and FV, which were petrographically defined in section 3.3.3. The least-altered samples for FV (grey circles) cluster amid the altered FV data points. The average of all least-altered FV id defined by the black circle on Figure 2-24. For the QV data, both the least-altered and altered data points show the same linear spread where, the least-altered samples for QV (grey squares) produce a linear trendline (Figure 2-24). This linear trend and the similarity in altered to least-altered data is not likely to produce meaningful mass balance results. For this reason, QV will be omitted from the mass balance calculations.

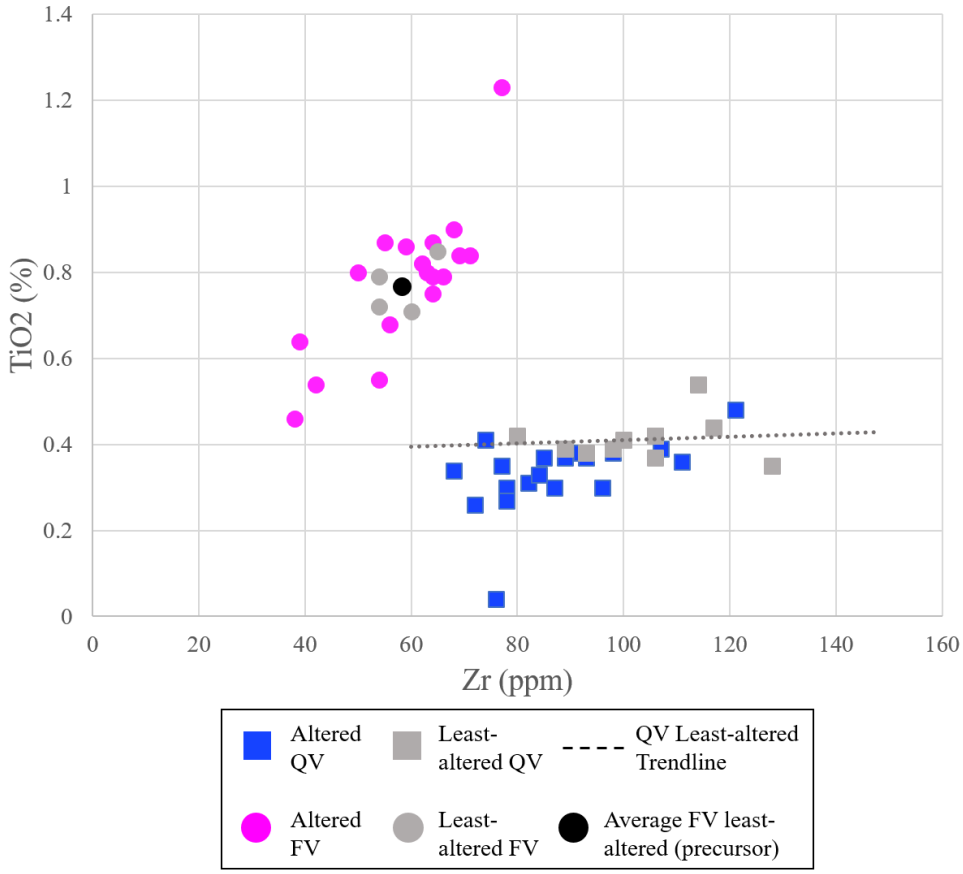

Figure 2-24. Immobile element binary plot of Zr vs. TiO_2 for all samples. Altered samples display two distinct units: QV (blue) & FV (pink). QV least-altered samples (grey square) display a horizontal trend. FV least-altered samples (grey circles) are averaged to estimate the precursor (black circle) in which Mass balance calculations will be based on.

The mass change values are tabulated in the appendix and results are divided into two main sections: 1) Wall rock alteration not associated with Au, 2) alteration associated with Au.

1. Wall rock alteration not associated with mineralization

The wall rock alteration not associated with mineralization can be observed on three binary plots (Figure 2-25) where gains and losses display specific alteration processes. The binary plots include: A) SiO_2 % vs. K_2O %, which monitors sericitization, silicification and chloritization, B)

FeO + MgO % vs. K_2O %, which displays chloritization and sericitization, and C) CaO + Na_2O % vs. FeO + MgO %, which monitors albitization, chloritization and carbonatization.

The FV samples display variable mass gain and loss results. Samples which displayed mass gains in K_2O correlate to mass losses in FeO+MgO and CaO+Na_2O and both gains and losses in SiO_2 (Figure 2-25ABC). This likely corresponds to increased sericitization with variable silicification. Samples which displayed mass loss in K_2O corelate to mass gains in FeO+MgO and losses in SiO_2 and CaO+Na_2O (Figure 2-25ABC). This likely corresponds to chloritization of white micas.

Samples which experienced mass gains in FeO+MgO, K_2O and CaO+Na_2O (B,C) correspond to an increased addition of Fe+Mg during chloritization as the feldspar component of the rock is destroyed (MacLean & Barrett, 1993). The addition of Fe+Mg likely resulted in the SiO_2 loss of the corresponding FV samples (Figure 2-25A) and, caused an increase in chloritization and the addition of Fe+Mg rich carbonatization (Figure 2-25C).

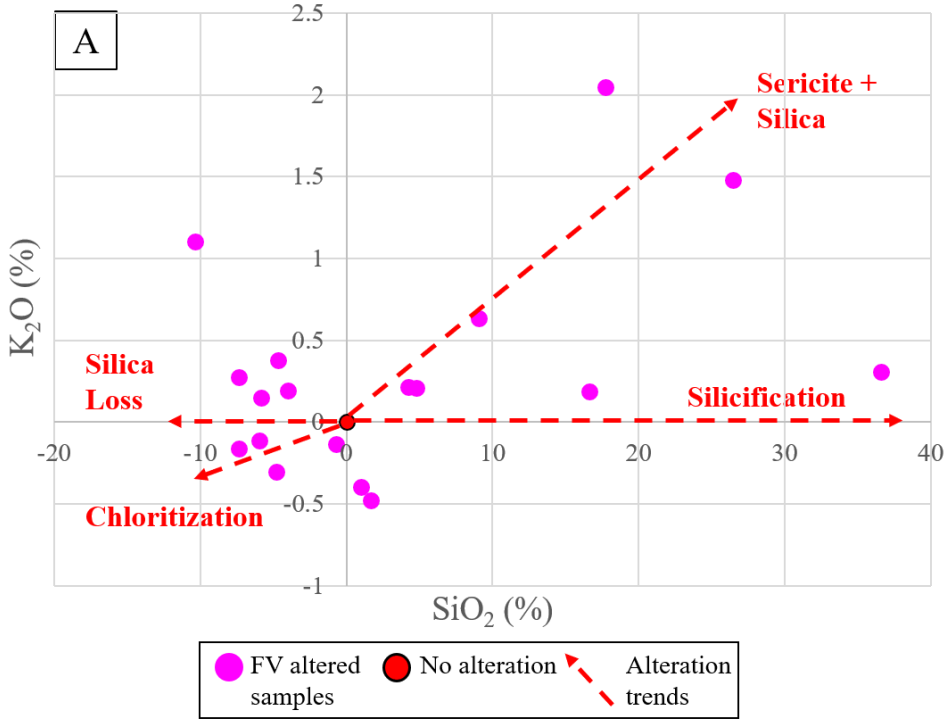

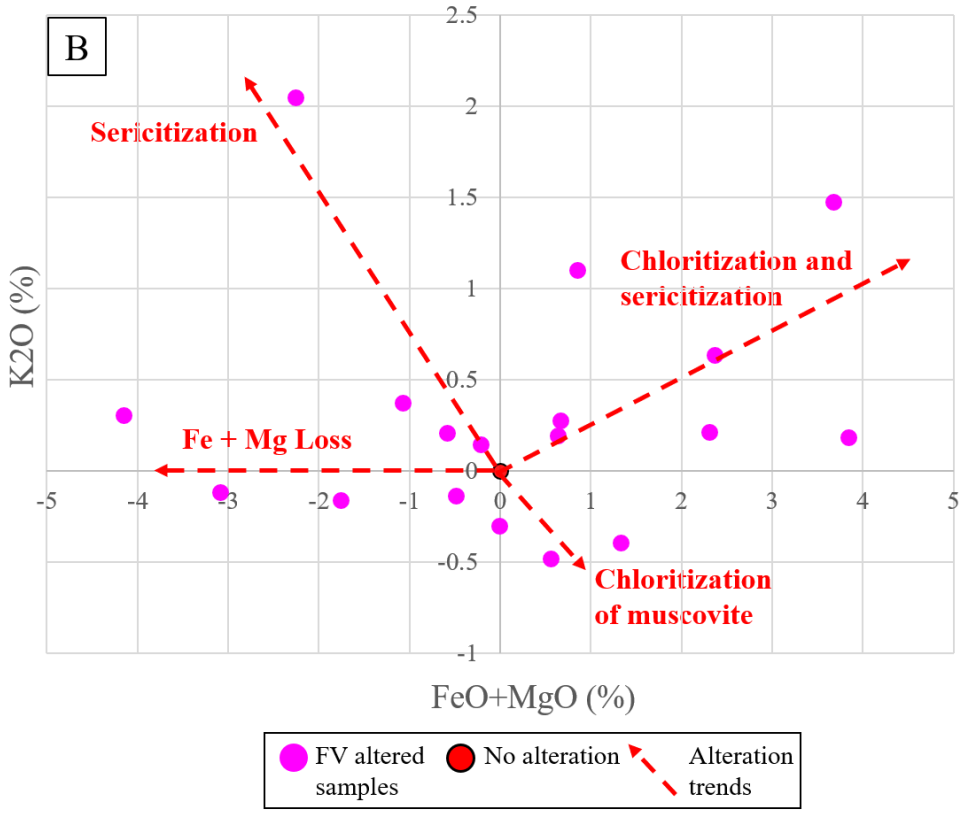
B
Sericitization
Chloritization and sericitization
Fe + Mg Loss
Chloritization of muscovite
K2O (%)
FeO+MgO (%)
FV altered samples
No alteration
Alteration trends

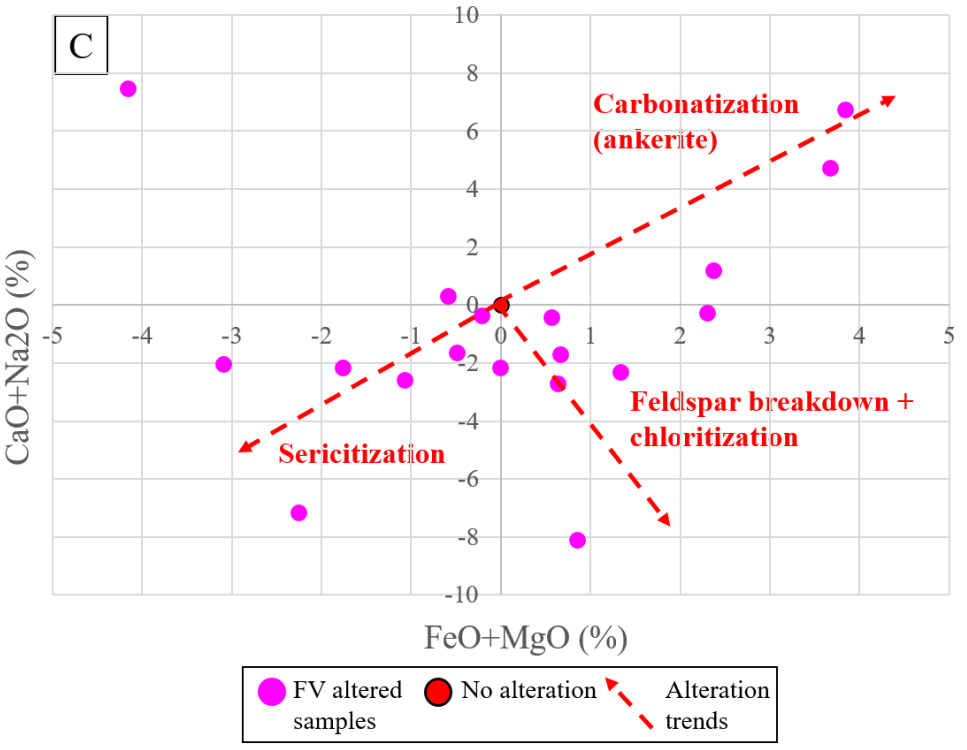
C
Carbonatization (ankerite)
Feldspar breakdown + chloritization
Sericitization
CaO+Na2O (%)
FeO+MgO (%)
FV altered samples
No alteration
Alteration trends

Figure 2-25. Mass change binary plots which display FV (pink) altered samples. Samples display alteration trends (red dashed lines) based on the mass change % of presented elements. Plots are defined as: A) SiO_2 % vs. K_2O %, B) FeO + MgO % vs. K_2O %, and C) CaO + Na_2O % vs. FeO + MgO %. The red circle visible in all graphs, is the precursor and is at the point (0, 0).

2. alteration associated with mineralization

Percent changes of elements associated with tourmaline alteration and arsenopyrite sulphidation are examined by: A) ΔB vs. ΔAu (ppb), which monitors tourmaline alteration related to gold and B) ΔAs/S (ppm) vs ΔAu (ppb) which monitors the relationship between arsenopyrite and gold mineralization. It is important to note, based on petrographic observations (Figure 2-12A,B, Figure 2-14, Figure 2-16) it an be concluded that arsenopyrite and gold entered the system after rock formation. Because of this, the concentration of As, S and Au in the precursor rock (Cx_P in equation 2) were given arbitrary concentrations of 10 ppm, 100 ppm 0.5 ppb, respectively. Boron mass change and Au (ppb) values do not show any observable trend (Figure 2-26A). The three samples with the high Au values corresponds to high B mass gain values of >1500 ppm (Figure 2-26A). However, these three samples could be considered outliers because all other samples have very low gold values (<10ppb) and low B values (<500ppm) (Figure 2-26A). This corresponds to tourmaline alteration not being associated with gold mineralization.

Figure 2-26B illustrates mass change B and Au (ppb), which displays a correlation between high gold grades and an As/S ratio of 1, as was previously observed in Figure 2-22. The highest gold grades are scattered at an As/S ratio of 1 i.e., gold is associated with the highest As/S ratios, which correspond to the highest arsenopyrite contents.

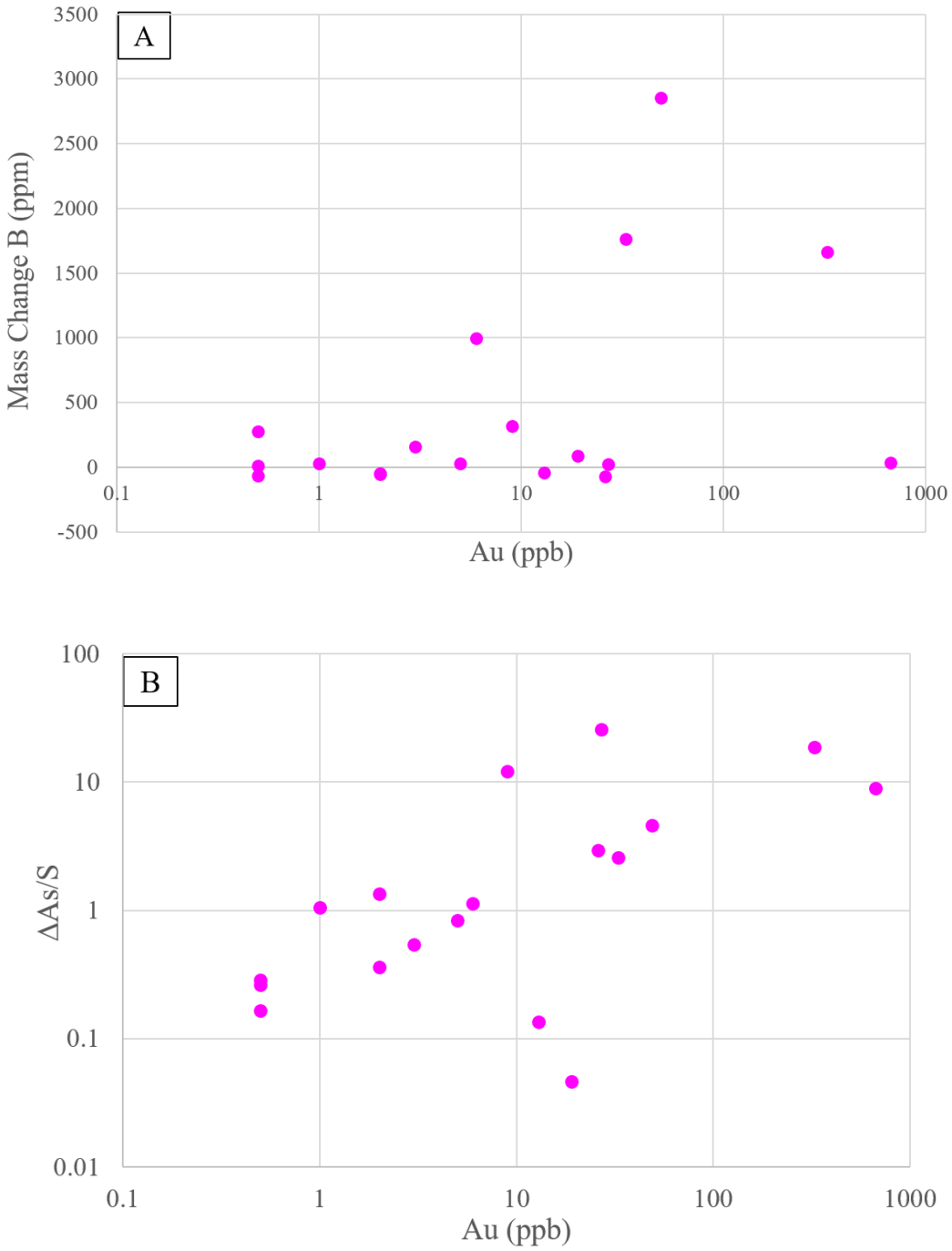

Figure 2-26. Percent change binary plots which display alteration FV (pink) altered samples related to arsenopyrite, tourmaline and gold mineralization. Plots are: A) B vs. Au, B) As/S vs. Au.

The mass change and percent change results for the major element oxides and the major/minor elements are presented in a series of box and whisker plots (Figure 2-27A,B; Figure 2-28A,B). The results are comprised of the altered samples of FV and are based on calculations from equations (1, 2 & 3). All mass change observations will be discussed based on the average values. The mass change results of FV rocks correspond to a large mass gain in SiO_2 relative to all other major oxides (Figure 2-27A). However, smaller gains are also present in FeO, MgO, K_2O and LOI (Figure 2-27A). This could reflect the sericitization and chlorization in the FV groundmass. All of the other major oxides (Al_2O_3, CaO, Na_2O) display small mass losses which likely refects the sericitization and chloritization of the feldspar porphyroclats (Figure 2-27A).

The percent change results of the FV rocks displays an increased percent change in K_2O (Av: 96%) relative to all ther other major oxides (Figure 2-27B). However, CaO, Na_2O and LOI also display slightly elevated percent change (Av: 28%, 26%, 28%) respectively.

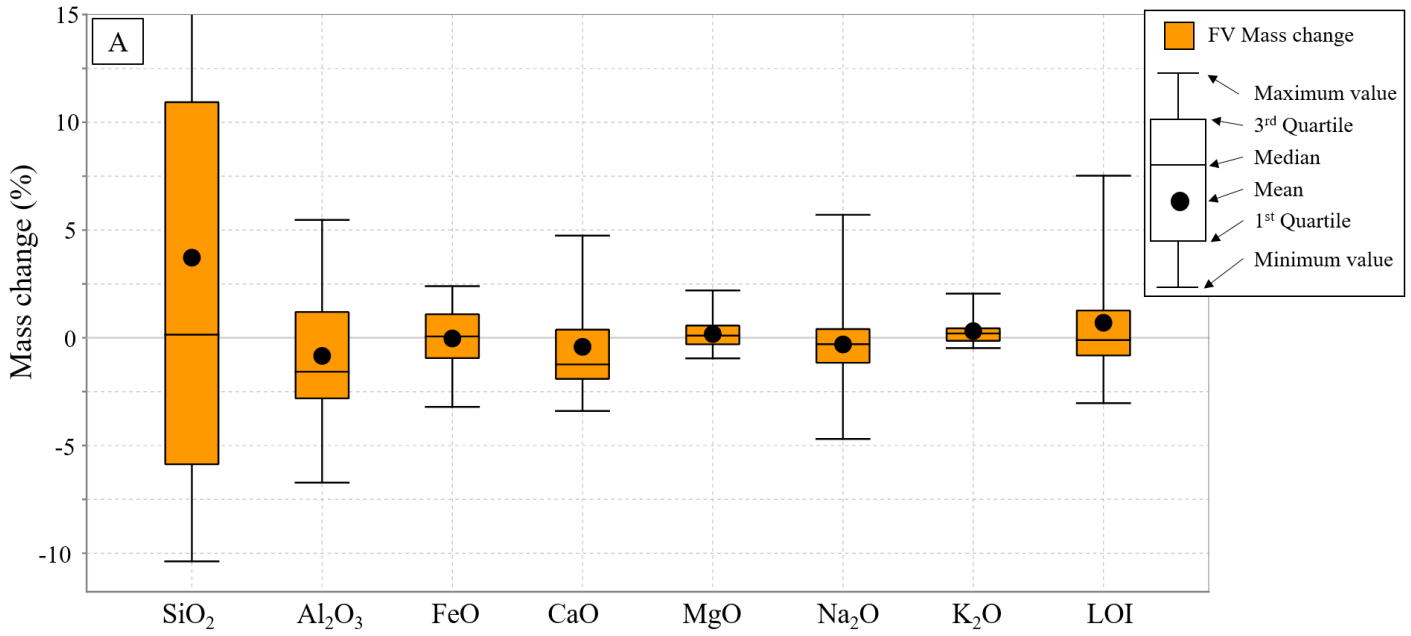

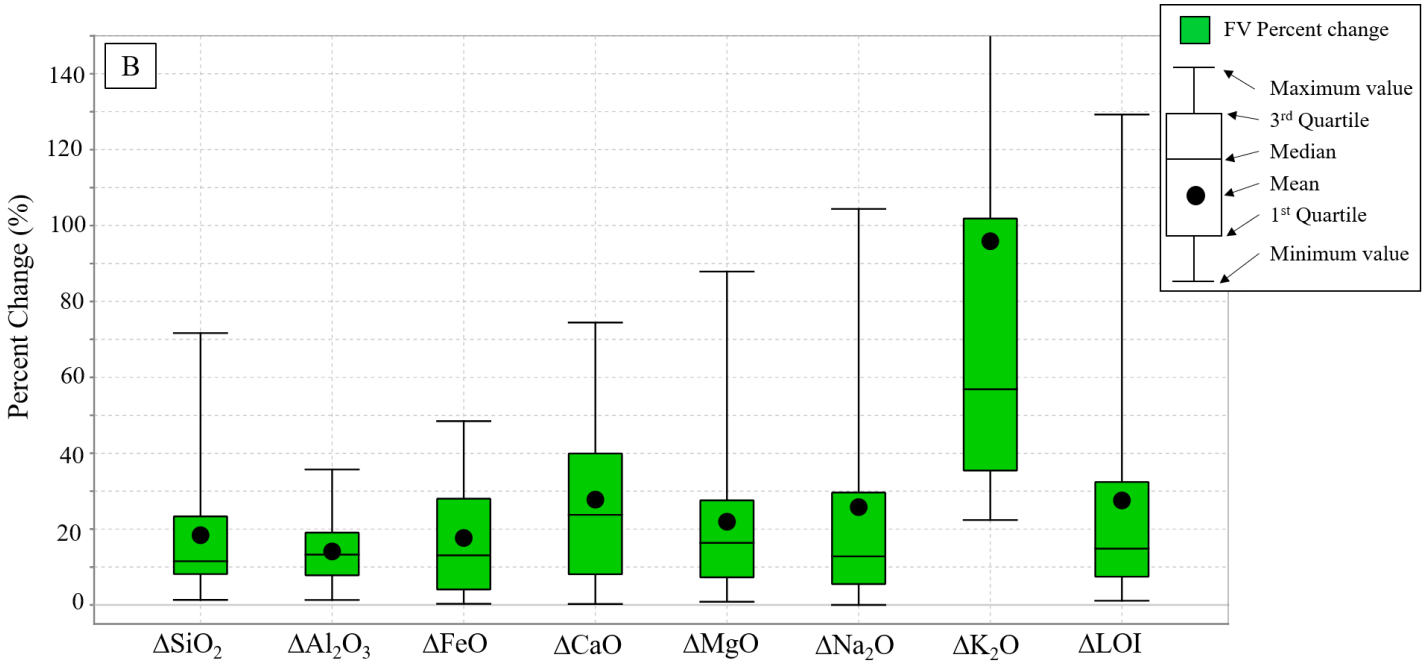

Figure 2-27. Box and whisker plots representing mass change (A) and percent change (B) changes for the major oxide elements of the altered samples of FV rocks.

Figure 2-28A,B illustrates the mass change and percent change of the main elements related to gold minerlaization (Au, As, B & S), presented in box and whisker plots. All four elements displays mass gains however, Au mass gain is low relative to the other three elements (Figure 2-28A). In figure 2-28B, both Au and As display large percent changes (14000 and 16000) respectively. This could correspond to a strong chemical relationship between gold and arsenopyrite which has been previously observed on Figure 2-22.

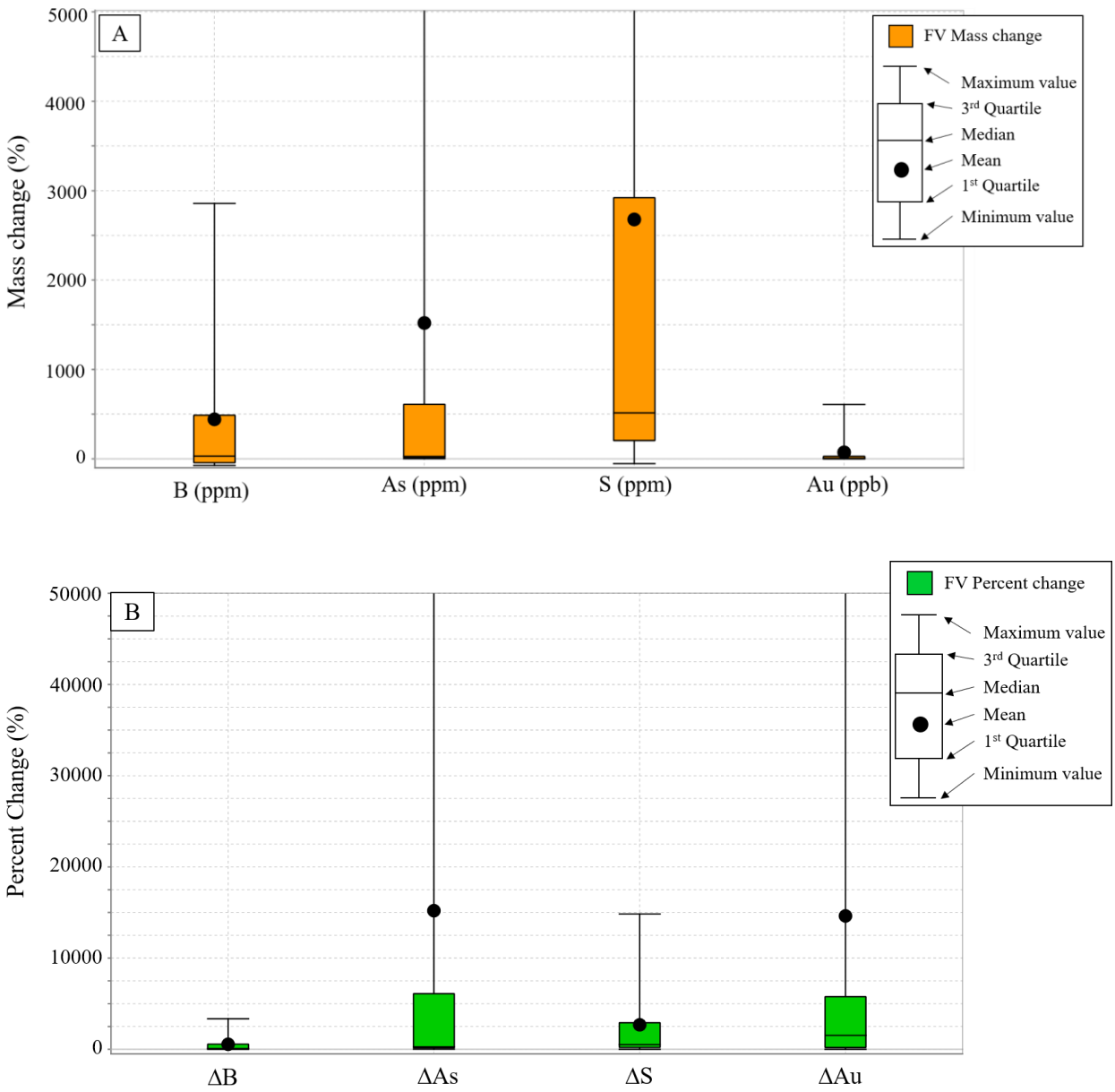

Figure 2-28. Box and whisker plots representing mass change(A) and mass percent (B) for the four main elements associated with gold mineralization (Au, As, B, S). Plots only illustrate the altered samples of FV rocks.

2.3.5 Arsenopyrite chemistry

Arsenopyrite grains were analyzed by EMPA and LA-ICP-MS to better understand the chemical compositions of the two textural types and, to determine if either and/or both types contained refractory gold. The EMPA analyses consisted of analyzing 15 grains and approximately 5-20 points per grain where major, minor and trace elements As, S, Fe, Au, Co, Ni, Te and Sb were examined.

Back scatter electron (BSE) images for each grain show that arsenopyrite is zoned with variable As-S compositions and, that each textural type displays a different type of zonation. The spot locations were selected based on the type of zonation observed in each analyzed grain. For euhedral/subhedral grains the dark cores, the light outer rims and, where applicable, the medium-hued inner rims were analyzed. For the anhedral grains, the light and dark patchy regions were both analyzed. The results of one euhedral and one anhedral grain are displayed in Figure 2-29A & Figure 2-29B where the analyses are expressed in atomic percent.

The euhedral (n=6) and subhedral grains (n=3) are concentrically zoned where the cores are enriched in S relative to the As-rich rims. Figure 2-29A illustrates a euhedral grain where points 3, 4, 8 & 10 are located in the dark core and are elevated in S and depleted in As. Points 1, 6, 7 & 12 are located in the light rim and are elevated in As and depleted in S. Fe is relatively constant throughout the grain when compared to S and As values. However in some regions, elevated Fe values are connected to elevated S values (Figure 2-29).

The anhedral grains (n=5) display patchy zonation of dark and light regions that are irregularly distributed throughout the grain. Figure 2-29B displays an anhedral grain where the points 2, 8 & 12 are located in light patches and correspond to elevated As and depleted in S. By contrast, points 4, 7 & 9 and are located in dark patches and correspond to high S and low As. Fe is constant throughout the grain. Overall, despite the different zonation of each textural type, dark regions are rich in S and light regions are rich in As.

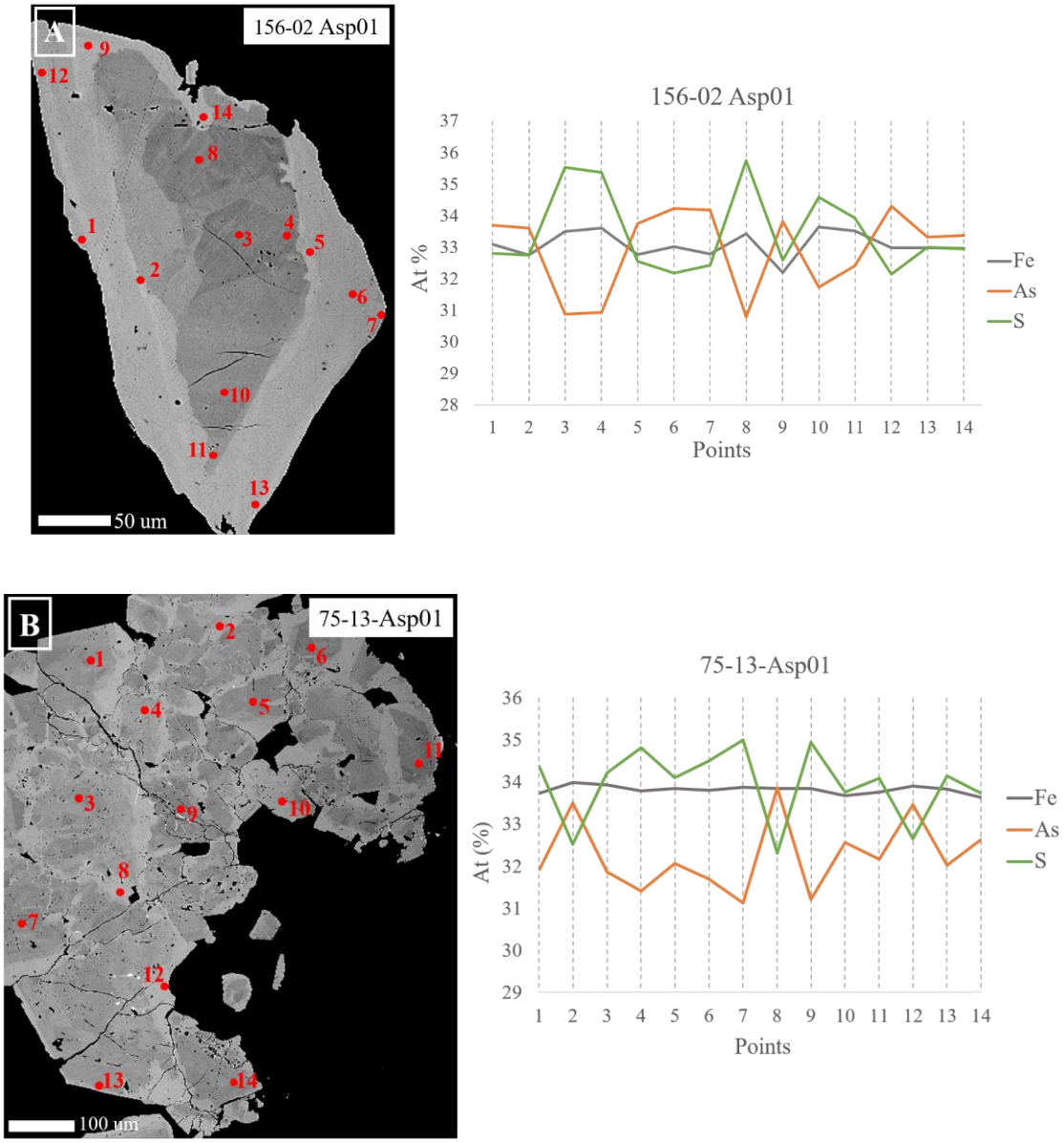

Figure 2-29. EMPA back scatter electron (BSE) images of arsenopyrite grains with spot analysis points (red) adjacent to their corresponding line plots of Fe (grey), As (orange) and S (green). Figure A displays a euhedral grain with concentric zonation. Figure B displays an anhedral grain with patchy zonation. For both A & B, dark regions correspond to high S (at%), and low As (at%) and, light regions correspond to high As (at%), and low S (at%). Sample numbers are displayed in the top right corner of each image.

When all the EMPA data points were plotted on an As-S binary plot (Figure 2-30), a negative 1:1 trend is observed which defines S-As exchange (Lentz, 2002). To examine if the S-As compositions differ based on zonation type, Figure 2-30 divides each data point into one of four groups which define the zonation location of the point analysis. The four groups are: core (grey), inner rim (purple), outer rim (green) and patchy (blue). As an added variable, the shape of the data point defines the shade of the point analysis (dark= square, light= triangle).

The inner and outer rim points (purple n=20, green n=45) generally have lower S and high As atomic %. The core points (grey n=57) plot throughout the trend however a large portion of the data point are concentrated towards the high S and low As region of the trend. The patchy zonation (blue n=52) data points are scattered throughout the trend (Figure 2-30). The dark spots (square) are concentrated towards high S and low As, whereas the light spots (triangle) are concentrated towards high As and low S.

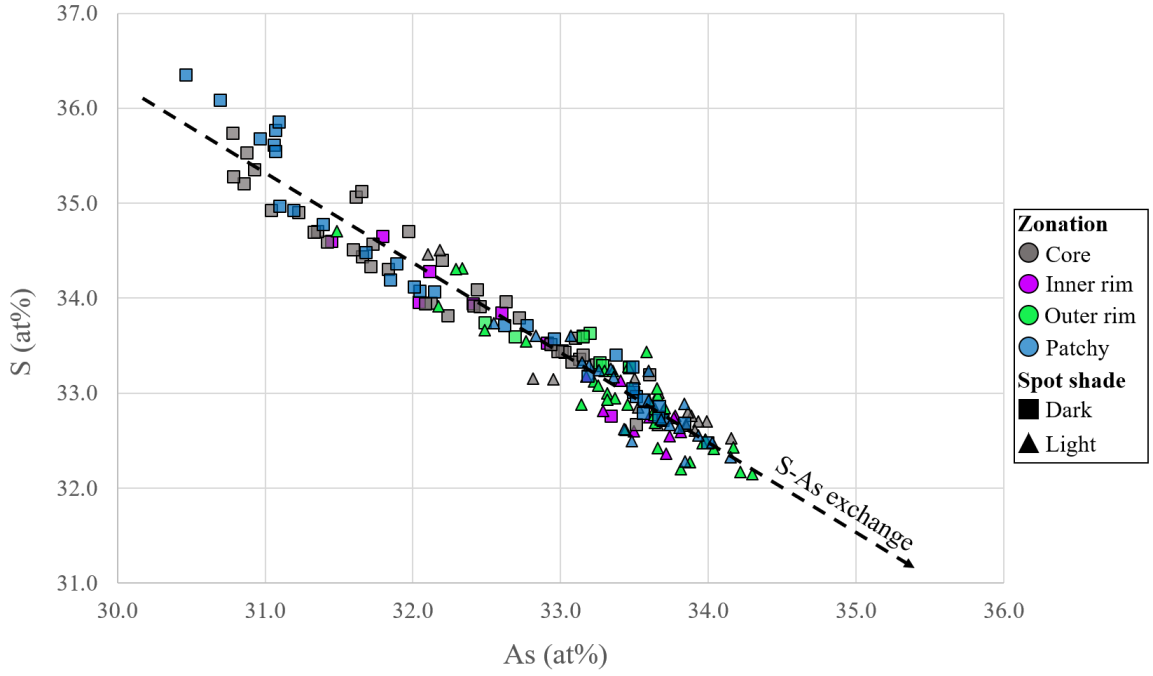

Figure 2-30. Binary As-S graph of all EMPA data points (n=174) from 14 arsenopyrite grains. Data points align a long a negative trend which represents S-As exchange. Color

corresponds to the location of the point analysis: core=grey, inner rim= purple , outer rim=green & patchy=blue. The shape of the points corresponds to the whether the Spot analysis was taken from a dark (square) or light area (triangle).

Wavelength Dispersive Spectrometer (WDS) maps of all 15 arsenopyrite grains were acquired to determine if there is any other elemental zonation within the grain structures and, if the two textures display different elemental abundances. The WDS maps displayed a strong Co zonation for both textural types. Nickel, Sb and Te EDS maps were also acquired however, none of these elements displayed zonation.

In the zoned euhedral/subhedral grains, the Co zonation occurs in the rim (Figure 2-31). The Co zonation is observed in many of the analyzed grains; however, the Co concentrations are variable. The Co zonation is less intense in the anhedral grains but is defined as Co bright patches which correspond to the light As-rich regions (Figure 2-31).

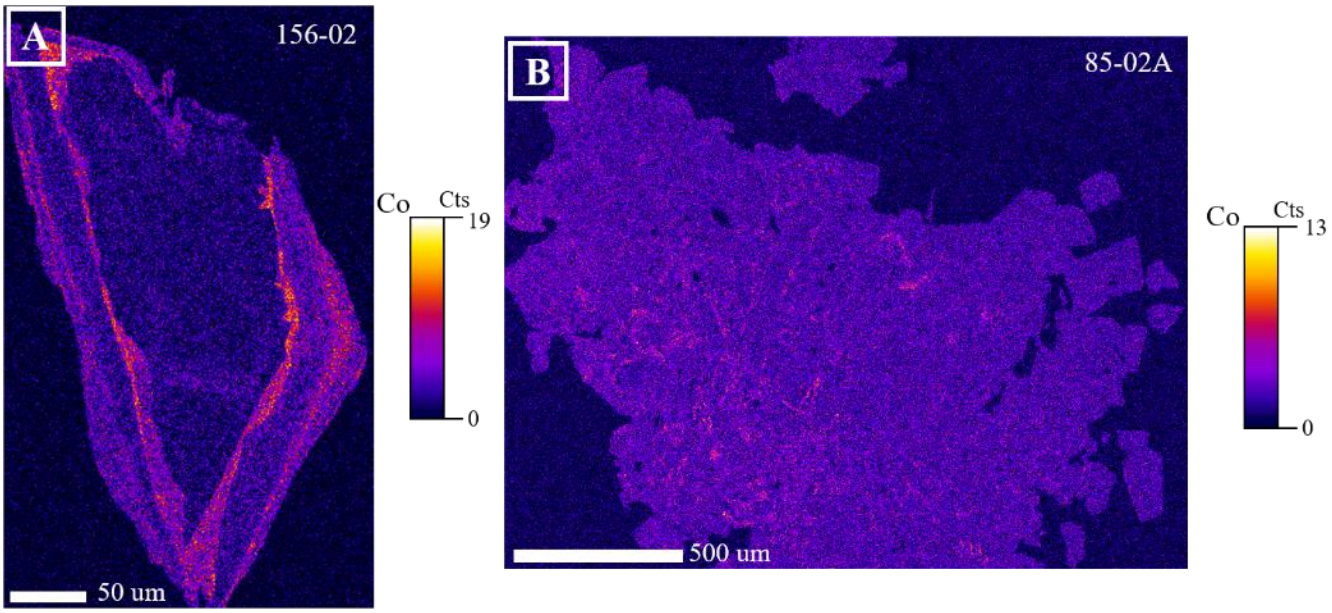

Figure 2-31. WDS images of arsenopyrite grains with cobalt (Co) zonation. A) Euhedral arsenopyrite grain with concentric Co zones in the rims. B) Anhedral arsenopyrite grain

with patchy Co zonation. The brighter colors correspond to increased Co concentrations. Sample numbers are displayed in the top right corner of each image.

Even though the Co zonations are more apparent in the euhedral/subhedral grains, zoning is not present in all samples. However, in rock samples that contains both textural types, if the euhedral grains are zoned then the anhedral grains will also display weak Co rich regions.

The concentration of Au of each point analysis for all 14 grains measured below the detection limit of 200 ppm. Consequently, LA-ICP-MS traverses were completed to determine the amount of refractory gold in the grains.

Fourteen arsenopyrite grains of all three textural types (euhedral n=6; subhedral n=3; anhedral n=5) were analyzed with two to four traverses completed on each sample, depending on the size of the grain. Figure 2-32A, B & C illustrates a euhedral and anhedral grain with their specific traverse path and the signal intensities of As, S, Fe, Co, Ag and Au.

The Co (light blue) signal intensity is heterogenous, which is consistent with the Co zonation represented in Figure 2-31A. There is a positive correlation between Co and Ni (green) with their line scans showing similar patterns (Figure 2-32). The most notable feature is the lack of gold values from the traverse graphs. The gold peaks in Figure 2-32A, B & C are at 1000 counts/second which, is interpreted to be below the detection limit and background values. The narrow spikes of Au in the line scan correspond to gold inclusions within the grain (Figure 2-32C). Only three examples are illustrated however, all 14 grains (40 traverses) display similar results showing no significant gold values. The LA-ICP-MS average detection limits for each analyzed element are given in Table 2-3, and Au specifically ranges from 0.1 to 0.9 ppm.

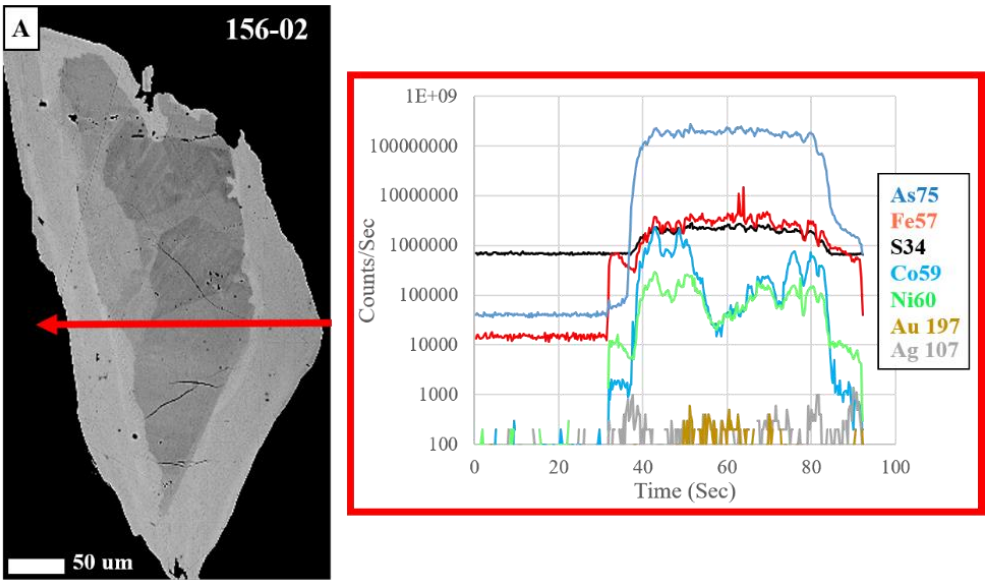
A
156-02
50 um
1E+09
100000000
10000000
1000000
100000
10000
1000
100
Counts/Sec
0
20
40
60
80
100
Time (Sec)
As75
Fe57
S34
Co59
Ni60
Au 197
Ag 107

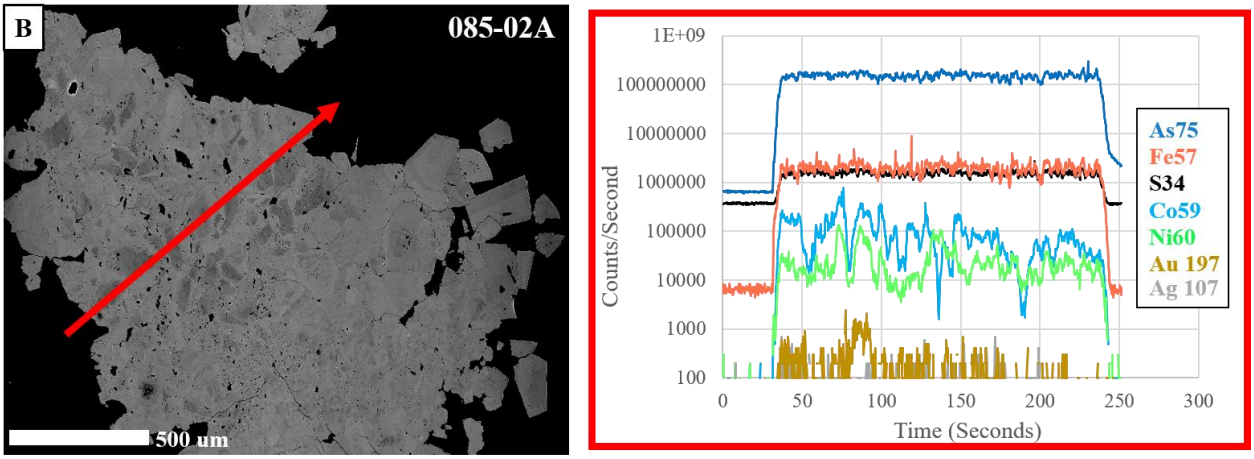
B
085-02A
500 um
1E+09
100000000
10000000
1000000
100000
10000
1000
100
Counts/Second
0
50
100
150
200
250
300
Time (Seconds)
As75
Fe57
S34
Co59
Ni60
Au 197
Ag 107

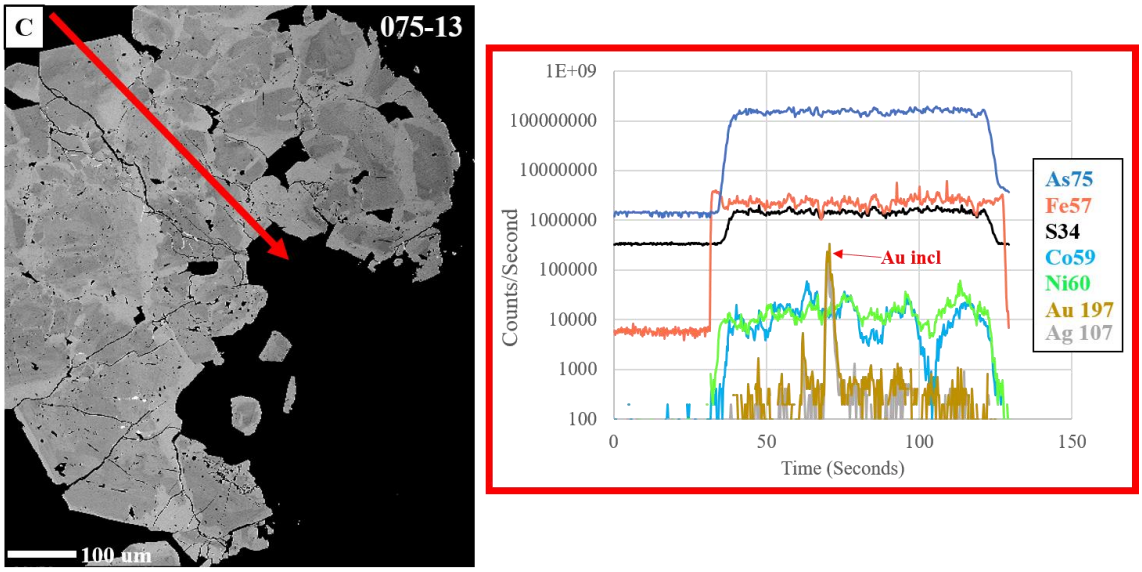

Figure 2-32. BSE images of arsenopyrite with ICP-MS traverses (red line) with accompanying signal intensity displayed in time (sec) by counts/second. A) Euhedral arsenopyrite grain. B) Anhedral arsenopyrite grain. C) anhedral grain with gold inclusions (Au incl). Both traverses display lack no elevated gold values. Sample numbers are displayed in the top right corner of each image.

LA-ICP-MS results were grouped by cobalt peaks to see if there was a correlation between the Co and gold concentrations. The analyzed trace elements are Co, Ni, Cu, Zn, Pb, Sb, Te, Ag and Au. Two or three time intervals were selected for each traverse where the intervals were selected to represent high, medium and low Co concentrations. Time intervals ranged from 5-10 seconds where each interval produced its own trace element abundances**.** The concentration of trace elements in euhedral, subhedral and anhedral arsenopyrites are displayed in box and whisker plots (Figure 2-33). The mean, median, maximum and minimum values of the analyzed elements: Co, Ni, Cu, Zn, Pb, Sb, Te, Ag and Au, are shown in Table 2-5.

Table 2-5. Mean, median, maximum and minimum values of elements for segments of LA-ICP-MS traverses of different arsenopyrite textures

Element (ppm)	Anhedral				Subhedral				Euhedral			
	Minimum	Maximum	Mean	Median	Minimum	Maximum	Mean	Median	Minimum	Maximum	Mean	Median
Co59	14.3	1460	273	162	49.4	42600	5948	420	20.0	4420	861	281
Ni60	27.8	2055	685	548	94.7	1202	338	210	51.0	2530	503	237
Cu63	7.5	430	43.6	20.3	9.9	40.4	24.8	25.9	4.9	1470	80.9	21.0
Zn66	7.0E-03	8.2	9.7E-01	1.5E-01	6.0E-01	211	25.8	3.0	1.1E-01	7800	233	4.4
Ag107	1.0E-02	2.0	4.6E-01	3.1E-01	8.0E-02	2.4	7.4E-01	2.8E-01	3.6E-02	9.8	6.6E-01	2.4E-01
Sb121	5.0	698	110	25.7	70.0	1089	504	444	10.5	5450	820	494
Te130	5.0E-01	1748	219	81.5	1.1	393	112	72.0	3.0E-01	579	113	49.6
Au197	5.1E-02	5.0	6.0E-01	3.4E-01	1.0E-02	6.4E-01	1.4E-01	9.0E-02	5.0E-03	1.5	4.3E-01	2.3E-01
Pb208	1.7	750	53.1	17.4	1.0	64.0	11.6	4.5	5.7E-01	138	24.7	7.2

All three textural types of arsenopyrite are enriched in Co, Ni, Cu, Pb and Te. However, the anhedral grains are depleted in Sb and Zn with the Zn value being below the average detection limit value (dotted black line) represent by the arrow in Figure 2-33. The values for Au and Ag in all three arsenopyrite textures are below the detection limit line (Figure 2-33). For comparison, the arsenopyrite at the Lapa mine have average refractory gold content of 602 ppm and display relatively uniform gold counts during LA-ICP-MS analysis (Simard et al., 2013). These results indicate that there is in no refractory gold within any of the textural types of arsenopyrite at the Orenada deposit.

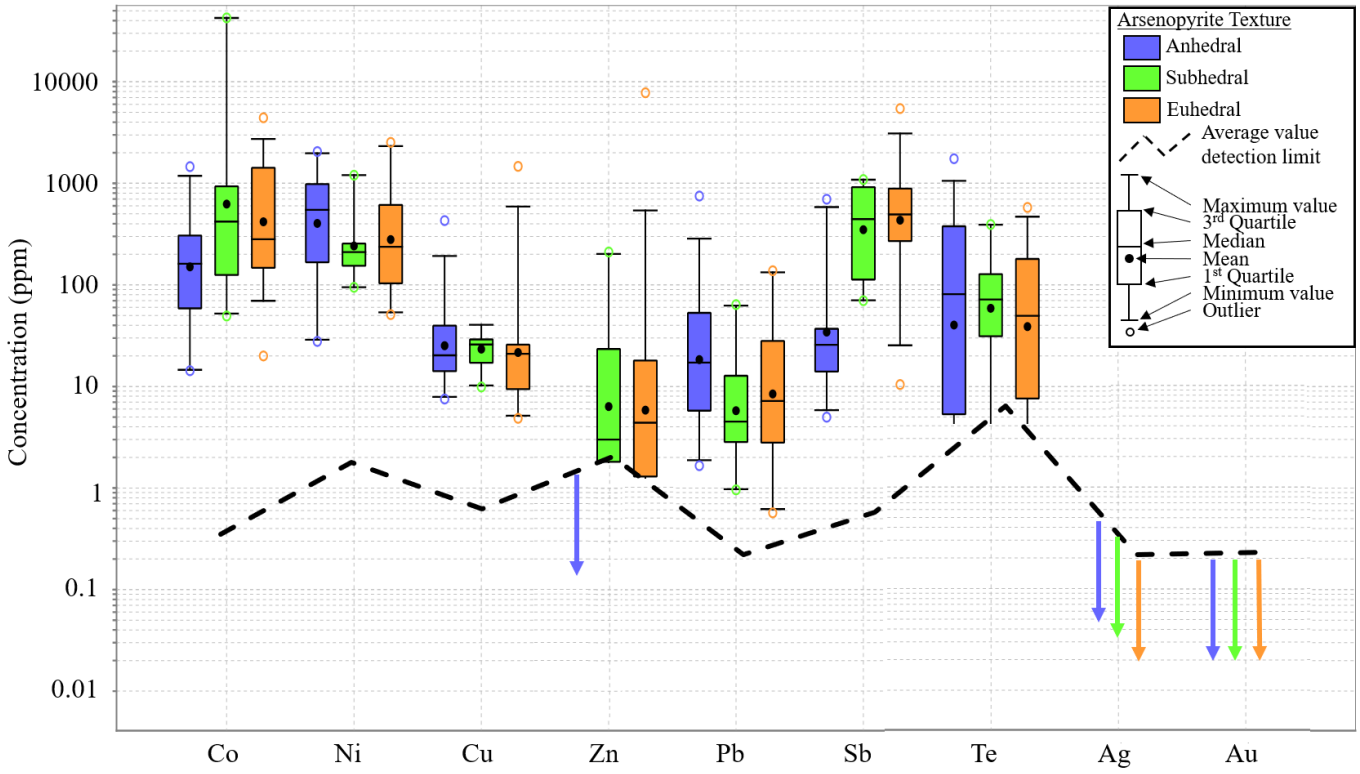

Figure 2-33. Box and whisker plots representing the variation of trace elements measured by LA-ICP-MS for anhedral (violet), subhedral (orange) and euhedral (green) arsenopyrite grains. The black dotted line represents the average detection limit for each element. Large arrows below the line represents values which are below the detection limit. Both gold (Au) and silver (Ag) values in all arsenopyrite textures are below the detection limit.

2.4 Discussion

Petrographic (hand-sample and microscopic), lithogeochemical and mineral chemical studies at the Orenada deposit have helped establish the relationship between mineralization and, rock type, alteration, sulphidation and veining. The following section will discuss all of the lines of evidence to then define key features and theories for the timing and deportment of mineralization.

2.4.1 Timing of mineralization

The paragenetic sequence for the mineralogical features of each volcanoclastic rock type, as well as the alteration, sulphidation, fabrics and veining are summarized in Figure 2-34.

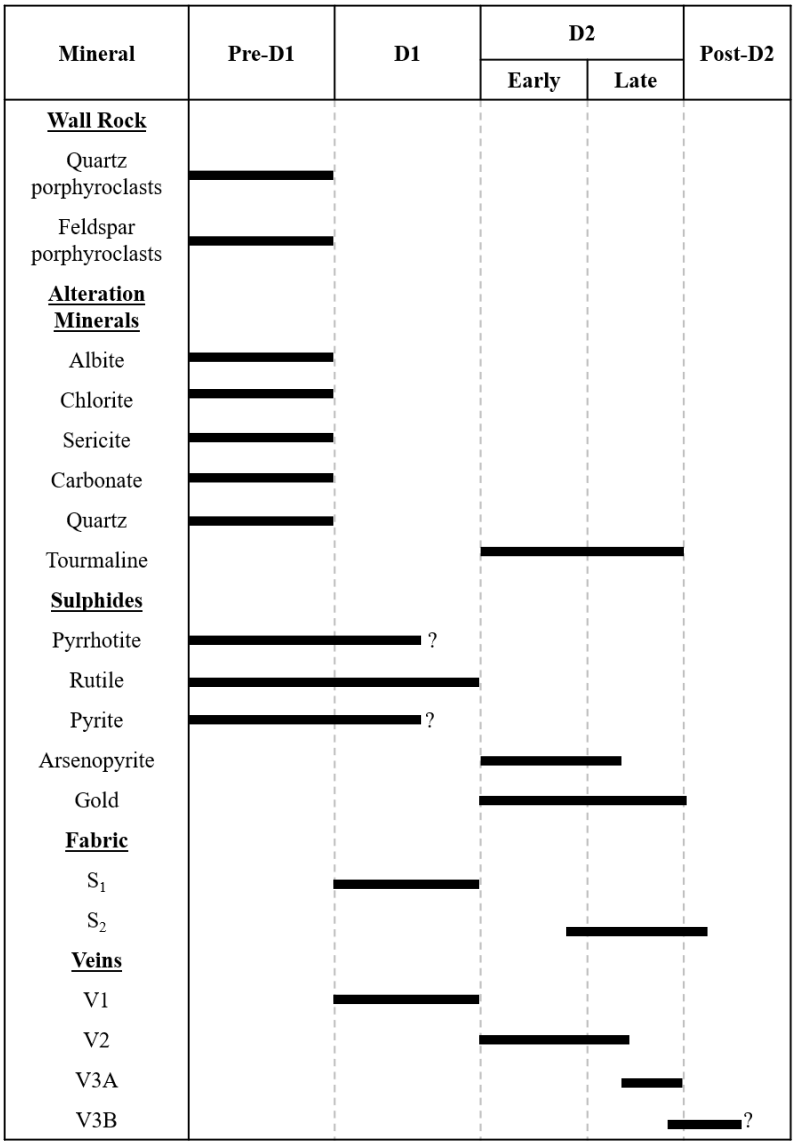

Figure 2-34. Paragenetic sequence for the timing of mineralization related to rock type, alteration, sulphidation, fabric and veins.

As previously mentioned, mineralization is preferentially hosted by the quartz and feldspar volcanoclastic rocks of the Cadillac Group. However, the alignment of porphyroclasts along S_1, pressure shadows, folded porphyroclasts, undulous extinction, pervasive alteration, (Figure 2-7; Figure 2-8; Figure 2-9; Figure 2-10; Figure 2-11; Figure 2-11) indicate a pre-kinematic emplacement for both rock types. The same can be said for the main wall rock alteration assemblage sericite-chlorite-albite where whole rock lithogeochemical results displayed in a GER diagram (Figure 2-23) illustrates that wall rock alteration is not associated with mineralization. It can thus be concluded that both rock types and their pervasive alteration predate the timing of the auriferous fluids. Also, mass change results for both rock types (Figure 2-27; Figure 2-28) displays differing mass gains and losses but none of these changes correspond to mineralization (Figure 2-26). This indicates that, although the volcanoclastic lithology is a preferential host, neither sub-unit is preferential to mineralization.

The spatial association between gold, arsenopyrite and quartz-carbonate-tourmaline veins (Figure 2-12; Figure 2-14B, C; Figure 2-16; Figure 2-17) illustrates that all of these mineralogical features are related to each other. However, tourmaline is always visible enveloping auriferous veins but gold is not directly associated with the tourmaline alteration (Figure 2-16; Figure 2-22). This association can be observed in Figure 2-22 where there is a positive correlation between As, S and Au but B is unrelated to gold grades.

The arsenopyrite grains are aligned along S_1 (Figure 2-14C), and display pressure shadows (Figure 2-14D) and rotations (Figure 2-14E, F). These features indicate that the arsenopyrite are syn-deformational and likely crystallized throughout D2. Other than the structural features, the most prominent feature of the arsenopyrite grains are the different textures, euhedral-subhedral (Figure 2-14A) and corroded-anhedral (Figure 2-14B). There is a correlation between gold and arsenopyrite (Figure 2-22; Figure 2-26B however, the mineralization has only been observed with the anhedral-corroded grains as infilled fractures and pits (Figure 2-17).

The arsenopyrite are also observed within and adjacent to V2 and V3A veins (Figure 2-12A, B) which suggests that the veins were emplaced during D2. However, despite the fact that V2 and

V3A veins share the same mineralogy, they are texturally different. V2 veins are folded and follow the main penetrative foliation S_1 (Figure 2-4B, C). These observations show that V2 were affected by the regional Z-shaped asymmetric folds which corresponds to emplacement during early to mid D2. By contrast, V3A are not folded, are oblique to S_1 and, cross-cut V2 veins (Figure 2-6D, Figure 2-12A, Figure 2-6E). This means that V3A veins are younger than V2 veins which thus corresponds to emplacement after the regional Z-shaped asymmetric folds, likely during late to post D2 deformation. The other two types of veins, V1 and V3B (Figure 2-6A; Figure 2-6F; Figure 2-13A; Figure 2-13B; Figure 2-13D) are both barren, thin quartz-carbonate veins which pre-date (D1) and post-date (post D2) mineralization, respectively.

Tourmaline alteration is exclusively observed surrounding the auriferous V2 and V3A veins as well as thin folded veinlets which propagated from massive (<5cm) tourmaline alteration halos (Figure 2-12C). From these observations, it is assumed that the boron was brought into the system with the fluids that formed the auriferous veins. It is unlikely that the boron was already in the host rock prior to the emplacement of the auriferous veins as the V1 are not associated with tourmaline alteration. For this reason, it is assumed that the auriferous fluids were boron rich. The spatial association of the tourmaline altered auriferous veins with F2 folds is consistent with the observations of Robert and Brown (1986) at the Sigma deposit which is located just 6.8 km SE from Orenada Zone 4.

2.4.2 Arsenopyrite

To fully understand the controls of mineralization at Orenada, the textures and mineral chemistry of the arsenopyrites must be considered. As previously mentioned, (Section 2.3.5), both textures show cobalt zonation where, the euhedral-subhedral grains are concentrically zoned (Figure 2-31A) and the anhedral-corroded grains show patchy irregular zonation (Figure 2-31B). An additional observation is that the core of the euhedral/subhedral grains appears to have the same patchy texture as the anhedral grains. This suggests that core of the euhedral/subhedral grains belong to the same generation of the anhedral/corroded grains and, that the outer zoned region of the euhedral/subhedral grains belong to a new generation of arsenopyrite growth. To test this

interpretation, the spot Co ppm EMPA values (n=165) of each textural type was compared in a series of box-and-whisker plots (Figure 2-35). The core, inner rim and outer rim locations correspond to the euhedral/subhedral grains and, the irregularly zoned dark and light locations correspond to the anhedral/corroded grains. All cobalt values below the detection limit (n=46) of 60ppm were assigned the value of half the detection limit of 30ppm. The Co values in the euhedral/subhedral grains are distinguishably higher than those from the patchy anhedral/corroded grains (Figure 2-35).

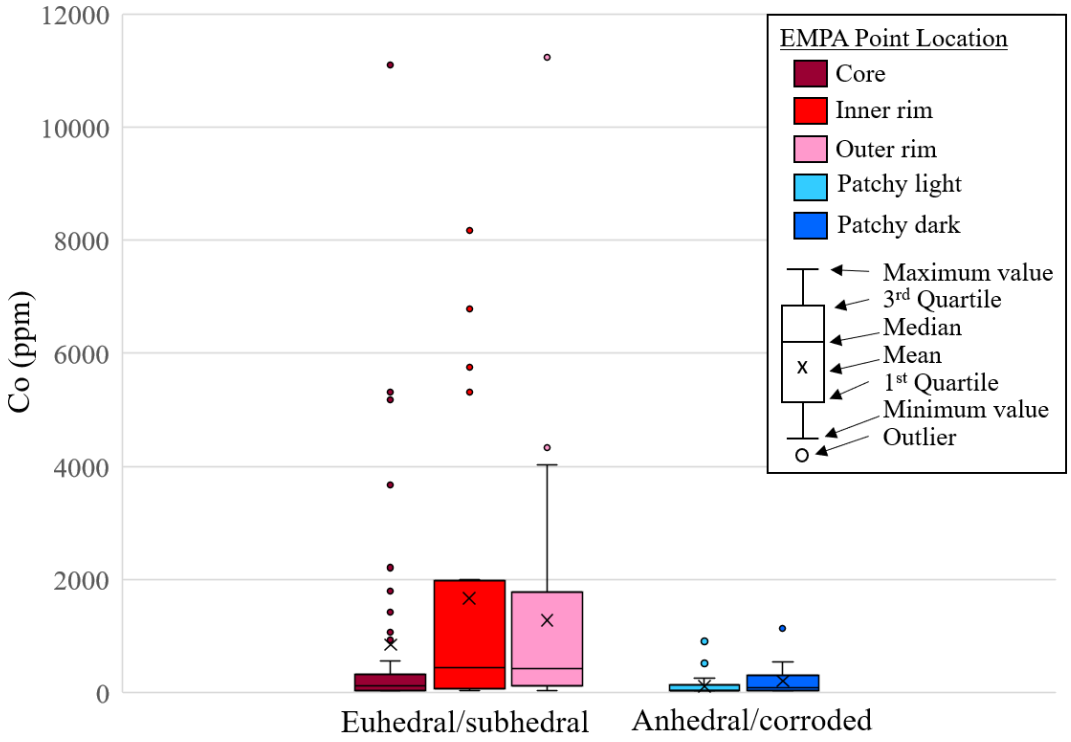

Figure 2-35. Box-and whisker plots of Co (ppm) concentrations in EMPA Spot data (n=165) of euhedral/subhedral (n=8) and anhedral/corroded (n=6) arsenopyrite grains. The plots were divided into spot location where the red-hued plots correspond to the euhedral/subhedral grains and the blue hued plots correspond to the anhedral/corroded plots. Overall the euhedral/subhedral points show higher Co values when compared to the anhedral/corroded points.

Interestingly, the core values of the euhedral/subhedral grains display higher Co values than the anhedral/corroded values where, the average Co (ppm) for the core is 851 ppm whereas, the dark and light patchy regions are 116 ppm and 204 ppm respectively (Table 2-6). This observation suggests that the cores of the euhedral grains are not equivalent to the patchy anhedral grains. This implies that there was likely 2 stages of arsenopyrite deposition.

Table 2-6. Average Co (ppm) values for the different electron microprobe (EMPA) spot analysis for all location of both arsenopyrite textures. The table includes the number (n) of spot analysis per spot location.

Spot location	Average Co value (ppm)	Number of spots (n)
Core	851	51
Inner rim	1672	20
Outer rim	1285	42
Dark patchy	116	32
Light patchy	204	20

From the LA-ICP-MS traverse results, both textural types have elevated Co (ppm) values however, the euhedral/subhedral grains have an average Co of 2484 ppm whereas, the anhedral/corroded grains have an average Co of 264 ppm (Figure 2-35). From both the EMPA and ICP-MS data it is clear that the euhedral/subhedral grains have elevated amounts of Co compared to the anhedral/corroded grains.

The source of the cobalt in the arsenopyrites is unknown. No past studies on cobalt zoned arsenopyrites from the Abitibi were found however the cobalt cation Co^{2+} is a mobile element so it can be easily transported (Migdisov et al., 2011). This could correspond to a Co-rich fluid entering the system where Co^{2+} replaced Fe^{2+} in the crystal lattice of the arsenopyrite grains. This can be observed in a very simplified equation (4).

$$Co^{2+} + FeAsS \rightarrow CoAsS + Fe^{2+} \quad (4)$$

Based on the Figure 2-29A,B, Fe is constant within both textural types of arsenopyrite. However, a substitution could still be valid because the cobalt values in the arsenopyrite are more than two

orders of magnitude lower than the Fe values. Thus, it would not be possible to observe cobalt substitution in arsenopyrite by comparing the stoichiometric amounts of Co and Fe.

Another important feature of the cobalt zonation is that the Co enrichment corresponds to regions of elevated As and depleted S (Figure 2-29; Figure 2-30). A change in the As-S ratio changes the size of the octahedral site, which affects the ability for the crystal structure to accommodate like charged cations. In this case, the coordination octahedral for Fe^{2+} (with a crystal ionic radius of 106 pm) can be substituted by elements of similar crystal ionic radius sizes like Co^{2+} (104 pm) (Shannon, 1976).

A similar relationship was observed at the vein-hosted orogenic Obuasi deposit in Ghana, where As-rich and S-poor regions in euhedral arsenopyrite grains corresponds to concentric nickel zonation (Fougerouse et al., 2016). Fougerouse et al., (2016) further state that the Ni^{3+} replaces Fe^{3+} as a solid solution between FeAsS (arsenopyrite) and NiAsS (gersdorffite) which causes a the arsenopyrites to be depleted in S, based on the chemical formula:

$$Au_x Fe_{1-x} AsS_{high\ S} + yNiCl_{2(aq)} + 2H_2O_{(aq)} + e^- \rightarrow Ni_yFe_{1-x}AsS_{low\ S} + xAu(HS)^-_{2(aq)} + 2yHCl_{(aq)} + O_2$$

Where x and y represent the trace element concentration of Au and Ni, respectively (Fougerouse et al., 2016). Fougerouse et al., (2016) interpret that the loss of S associated with the Ni replacement of Fe is critical for gold deposition because it increases the solubility of gold as $Au(HS)^-_2$ complex (Liu et al., 2014) at the crystal fluid interface. This promotes remobilization where the gold is liberated from the solid phase.

Similar processes could have been possible at Orenada because, orogenic fluids typically include chloride species (3-7% NaCl; Fougerouse et al., 2016), which could transport Ni and Co (Liu et al., 2012; Fougerouse et al., 2016). Also, the proximity to the Piché Group ultramafic rocks is a local source for these metals, as fluids likely interacted with the ultramafic rocks before deposition (Fougerouse et al., 2016). However, at Obuasi overprinting of different arsenopyrite generations is very obvious as well as, the gold is observed in fractures adjacent to the euhedral

arsenopyrite. These key features are not observed at Orenada, but the fluids that transported may also have been cobalt-rich.

Regardless of the cobalt anomaly, the LA-ICP-MS indicate that Au is not related to the Co contents of arsenopyrite (Figure 2-33). It is important to note that out of 101 data points only 27 are above the average detection limit of 0.3 ppm Au (Figure 2-36). Nevertheless, it can be concluded that cobalt enrichment is not associated with mineralization.

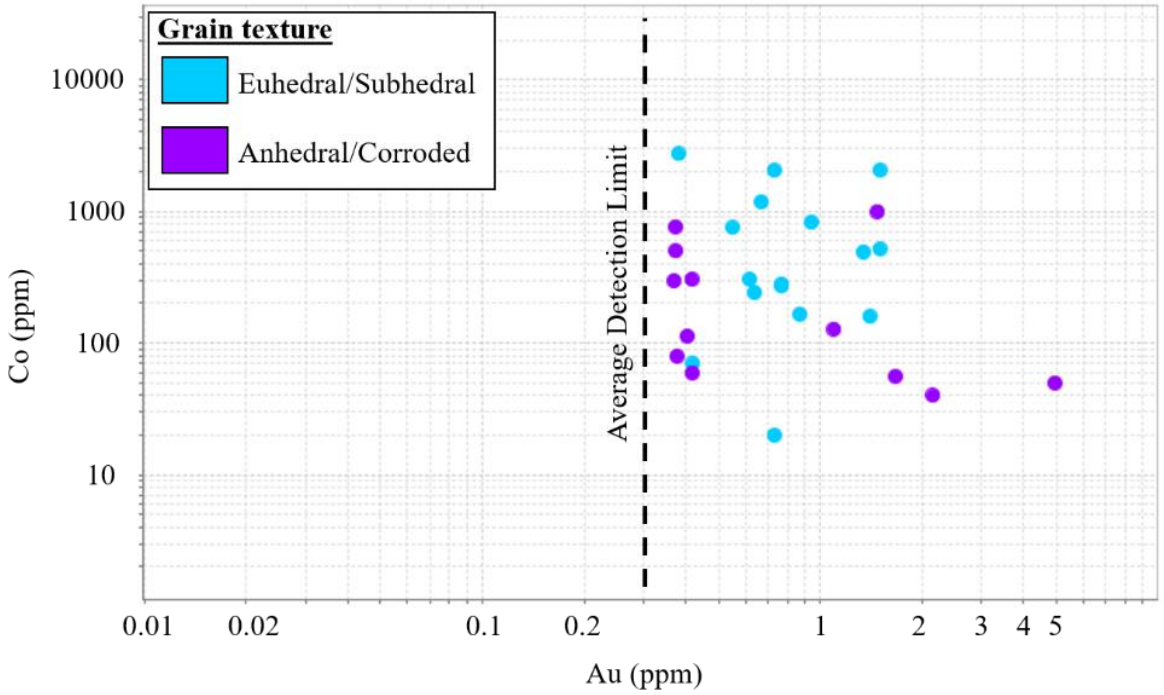

Figure 2-36. Binary Au (ppm) vs. Co (ppm) plot from LA-ICP-MS results of both euhedral/subhedral (blue) and anhedral/corroded (purple) arsenopyrite grains. All data points correspond to cobalt group peaks where on average 2 groups were selected per arsenopyrite traverse. Only data points (n=27) above the average detection limit of 0.3 ppm are displayed.

2.4.3 Gold deportment

Prior to the current study the association between gold and arsenopyrite was recognized but the deportment of gold was unknown. However, two potential theories exist for the occurrence of gold at Orenada. The first, is the gold is refractory in arsenopyrite and, that the free gold observed is from the remobilization of an earlier stage of refractory gold. The second, is that mineralization post-dates sulphidation where gold-rich fluids were related to the event(s) where quartz-carbonate veins were emplaced**.**

1) Refractory gold within arsenopyrite:

To evaluate refractory gold within the arsenopyrite grains, two factors need to be discussed. The first is that gold is refractory within arsenopyrite, i.e., that gold is in solid solution with the arsenopyrite crystals where the Au^{+1} cation is structurally bound to the lattice of the arsenopyrites (Morishita et al., 2019). The second, is that the gold was initially refractory but was then remobilized out of the arsenopyrite crystal lattice. The former theory can be ruled out because the very low Au (ppm) values observed from the LA-ICP-MS results (Figure 2-32; Figure 2-33) indicates that the gold is not trapped within the arsenopyrite grains. The average Au (ppm) values from the LA-ICP-MS is 0.4 ppm for the euhedral/subhedral grains and 0.6 ppm for the anhedral/corroded grains. These values are very low when compared to the refractory gold values observed in the arsenopyrites form the Lapa mine which had an average gold value of 602 ppm and reach as high as 1,825 ppm (Simard et al., 2013). Also, gold is visble in both hand and thin sections samples. So all of the gold at Orenada cannot be refractory.

Considering the remobilization of arsenopyrite, it is possible that Au was initially concentrated in the arsenopyrites and then at some point (likely during deformation) the gold cation was liberated from the arsenopyrite crystal lattice. The most likely process for this to occur in orogenic gold deposits is fluid-assisted recrystallization. This is normally caused from metasomatic/metamorphic fluids entering the system where they interact with the sulphide crystals causing them to recrystallize. The recrystallization causes the expulsion of

the gold cation from the sulphide crystal lattice (Cook et al., 2009; Pokrovski, et al., 2019). The liberated gold would then deposit as blebs or nanoparticles within the cores of arsenopyrites and/or reconcentrated around the margins of the same arsenopyrite grains within fractures (Cook et al., 2013).

This theory, although common in other Archean orogenic gold deposits (Giant mine in Yellowknife, Oberon deposit in Northern Australia, Lapa deposit in the Abitibi; Coleman, 1957, Cook et al., 2013 and Simard et al., 2013 respectively) is not the cause for mineralization at Orenada. The typical model for recrystallization and gold deposition is that gold is remobilized into the cores of euhedral grains (Cook et al., 2009, 2013). However, at Orenada gold in the euhedral arsenopyrite is negligible. Instead the free gold is only observed in fractures within the anhedral grains.

This theory assumes that 100% of the gold came from the arsenopyrite however, the euhedral and subhedral zoned grains are omitted because concentrically zoned sulphides were not recrystallized (Cook et al., 2013). That only leaves the anhedral/corroded arsenopyrite grains which make up about 50% of the total arsenopyrite that has been observed throughout this study. On average a typical high-grade region of core (~1m) has about 6 g/t Au and about 10000 ppm As. However, since half of the arsenopyrite are not considered for the recrystallization, the As value is closer to 5000 ppm. With this hypothetical example, there is not enough arsenopyrite to fully recrystallize to form the 6 g/t Au. All of the above indicates that that the gold has to have been added from later, external fluids.

2) Late-stage of gold associated with quartz carbonate veins:

In this theory, the mineralization at Orenada is exclusively associated with quartz-carbonate veins. This style of mineralization is very common within the southern Abitibi where the majority of greenstone-hosted Au deposits are associated with quartz-carbonate veins (Dubé and Gosselin, 2007). The features at Orenada are consistent with quartz-carbonate vein-hosted deposits. It is structurally controlled by a transpressional crustal-scale fault zone (CLLDZ), which marks a convergent boundary between lithological units (Cadillac Group

and Pontiac Group). It shows evidence for sub-greenschist facies metamorphism and, the timing of mineralization is syn-to late-deformational. Geological features of Orenada, such as, timing of vein emplacement, vein mineralogy, structure, and hydrothermal alteration are similar to the world-class, vein-hosted Sigma deposit, which is located only 6.8 km away. Both deposits show evidence for vein emplacement during mid to late D2 deformation where, U-Pb zircon ages collected from the veins of Sigma display an age of 2682 ± 8 Ma, which is coeval with D2 deformation within the Val d'or area (Claoué-Long et al. 1990, Garofalo, 2000). Barren quartz-carbonate veins are present at both Orenada and Sigma, where they are also observed to crosscut all rock types. However, the main stage of mineralization at both deposits is associated with quartz and tourmaline (with minor carbonate), and show textural equilibrium between vein minerals, i.e., quartz, tourmaline and carbonates. In terms of gold precipitation, both Orenada and Sigma are located adjacent to the CLLDZ, which is considered to be a fluid pathway for Au-bearing fluids to have repeatedly entered the system (Robert and Brown, 1986; Dubé and Gosselin, 2007). The syn-deformational Au-bearing fluid would not have been as a single pulse. Instead, Au-bearing fluids were associated with a system that pulsed numerous times (Sibson et al., 1988). This hypothesis best describes why there are two different generation of auriferous veins at Orenada. Both V2 and V3A have the same vein mineralogy but different structural parameters. This resembles the different vein styles at the Sigma deposit where vein emplacement was a gradual process which occurred both during and shortly after the formation of the ductile shear zone (Robert and Brown, 1986). The strong similarity of both deposits is consistent with what Robert (1994) implied as a quartz-tourmaline 'vein field' within the Val d'Or gold camp, grouped on the basis of their hydrothermal and structural features.

However, unlike the Sigma deposit, the gold at Orenada is observed in quartz-carbonate fractures and pits within the anhedral/corroded arsenopyrite grains (Figure 2-17). Gold precipitation associated with these grains can be described by their structural position adjacent to auriferous veins. It is interpreted that where the mineralized veins were emplaced

into the host rock, the arsenopyrite grains that were proximal to the vein became highly deformed. The fluids must have been periodically undersaturated with arsenopyrite and, as a result, pits and fractures were formed within these grains, that later became the sites of gold deposition from auriferous fluids.

One model that could explain the deposition of gold within these pits and fractures is electrochemical gold deposition (Moller and Kersten, 1994). Depending on the arsenic content of the sulphide, sulphide minerals are either n- or p-type conductors where, n-type (negative) act as electron donors and p-type (positive) act as electron acceptors (cathodes). P-type conductors are preferential to gold mineralization where gold is plated on the surface of the sulphide or at the grain boundary between a p-type and n-type sulphide. The distinction between n and p-type conductors comes down to the As/S ratio of the grains. Arsenic is the most important element in p-type conductivity so, As/S>1.0 are considered p-type conductors where as As/S<1.0 are n-type. Along with p-type conductors, visible gold also accumulates on n-p type junctions. N-p junctions are systems where electrons are transferred from n- to p-type conductors (galvanic cell) which usually occurs in zoned grains of differing As content. A zoned grain only becomes electrochemically active (accessible to fluids) after the crystal is fractured (Moller and Kersten, 1994).

Based on the gold precipitation within fractures and the As-rich and poor zonations it is likely that the anhedral grains at Orenada were a site of n-p junctions. Moller and Kersten (1994) explains that where sulphides that are chemically zoned (As, S, Co, Ni, etc.) are fractured, the grain exposes a great number of n-p junctions to infiltrating fluids. This would explain the deposition of gold within the cracks of these grains. Both arsenopyrite textures display strong As zonations however, only the corroded grains underwent deformation caused from the emplacement of proximal auriferous veins.

From the arsenopyrite grains analyzed in this study, 58 visible gold grains were documented. Of these, 50 (86%) gold grains are located within light colored As rich regions (Figure 2-37),

2 within dark S-rich regions and 6 are undetermined dark or light. The undetermined grains are all very fine grained (≤2 um) and are located at the boarder between light and dark zones where it is difficult to determine their true location.

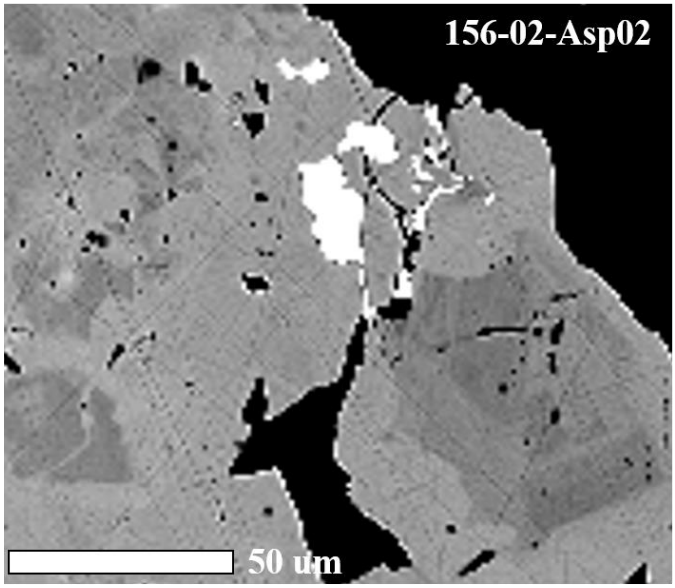

Figure 2-37. Corroded arsenopyrite grain with visible gold within a fracture. Visible gold is observed in light As-rich region of the grain.

The large proportion (86%) of visible gold grains found in the light sections corresponds to preferential mineralization within these As-rich regions. This is consistent with the electrochemical model where n-p junctions are likely controlling the deposition of gold. However, since some gold grains were undetermined or observed in dark As-poor regions, a more in-depth study should be undertaken and the As-S ratio of arsenopyrite adjacent to gold grains should be analyzed.

2.5 Conclusions

The Orenada deposit, situated 8 km south-east of the city of Val d'Or Quebec, displays some unusual characteristics that differentiate it from other orogenic gold deposits in and proximal to

the Val d'Or gold camp. Orenada is different from other deposits in the Val d'Or camp because it is located directly within the first order, crustal scale, Cadillac Larder-Lake deformation zone (CLLDZ) and is mineralized within a volcanoclastic horizon of the Cadillac Group sediments. Mineralization is associated with both quartz-carbonate-tourmaline veins and arsenopyrite sulphidation. However, there is a lack of research done on these arsenopyrite grains where gold deportment and precipitation are poorly understood. This study examined alteration, sulphidation and vein processes to investigate the controls of mineralization and how gold was deported into the rock system.

1. Field, petrography, geochemistry and mass balance calculations indicate that there are two different types of volcanoclastic rocks within the mineralized horizon which are both altered to a pervasive sericite-chlorite-albite assemblage. However, this alteration is not associated with mineralization.
2. Mineralization at the Orenada is the result of hydrothermal auriferous fluids, likely synchronous with mid- to late-D2 deformation. These fluids formed the quartz-carbonate-tourmaline veins, which have been recognized throughout the Val d'Or gold camp as major hosts for mineralization.
3. Sulphidation at Orenada is exclusively related to arsenopyrite grains where two different textures have been identified: Euhedral/subhedral and Anhedral/corroded. Electron Microprobe Analysis (EMPA) results show cobalt zonation for both textures however, this the cobalt is not associated with mineralization.
4. Laser Ablation Induced Coupled Plasma Mass Spectrometry (LA-ICP-MS) results indicate that neither textural type of arsenopyrite contain significant refractory gold values.
5. Gold deportment at Orenada is linked to early-D2 subparallel, folded V2 veins and late-D2, non-deformed V3A veins. Both vein generations share the same quartz-carbonate-tourmaline mineralogy. Corroded arsenopyrite is observed adjacent to the V3A veins where the mid to late deformational timing resulted in these grains to be fractured and deformed.

6. The precipitation of gold within the fractures is likely related to electrochemical gold deposition where As-rich regions act as p-type conductors which attract the gold. From the arsenopyrite of this study, 86% of the visible gold grains are preferentially mineralization within the As-rich regions. However, since the locations of some gold grains were undetermined, further examination is recommended.

2.5.1 Recommendations for future work

To further understand the deportment and timing of gold at Orenada deposit, a more in-depth study should be undertaken in regard to the arsenopyrite chemistry. Electrochemical gold deposition is very likely for the source of gold deposition at Orenada however, a more intensive study should be undertaken where more arsenopyrite grains are examined with specific focus on the compositions of both textural types of arsenopyrite and the gold within and outside of fractures.

The lack of literature on arsenopyrite, especially related to Archean terranes, makes projects like this very important when trying to find commonalities between arsenopyrite rich deposits. However, a more global survey should be conducted comparing the arsenopyrite chemistry of Archean mesothermal gold deposits to define common models for mineralization.

2.6 References

Bedeaux, P., Mathieu, L., Pilote, P., Rafini, S., and Daigneault, R. 2018. Origin of the Piché structural complex and implications for the early evolution of the archean crustal-scale Cadillac – Larder lake fault zone, Canada. Canadian Journal of Earth Sciences, **55**: 905–922.

Bedeaux, P., Pilote, P., Daigneault, R., and Rafini, S. 2017. Synthesis of the structural evolution and associated gold mineralization of the Cadillac Fault, Abitibi, Canada. Ore Geology Reviews, **82**: 49–69.

Borghi, A., Cossio, R., Olmi, F., and Vaggelli, G. 1998. Compositional X-Ray Maps of Metamorphic and Magmatic Minerals. Modern Developments and Applications in Microbeam Analysis, **235**: 227–235.

Cabanis, B and Lecolle, M. 1989. Le diagramme La/10-Y/15-Nb/8: Un outil pour la discrimination des series volcaniques et lamise en evidence des processus demelange et/ou de contamination crustale. Compte Rendus de I'Académie des Sciences Series II, **309**: 2023-2029.

Claoué-Long, J.C., King, R.W., and Kerrich, R. 1990. Archaean hydrothermal zircon in the Abitibi greenstone belt: constraints on the timing of gold mineralisation. Earth and Planetary Science Letters, **98**: 109–128.

Cook, N.., Ciobaniu, C.L., Meria, D., Silcock, D., and Wade, B. 2013. Arsenopyrite-Pyrite Association in an Orogenic Gold Ore : Economic Geology, **108**: 1273–1283.

Cook, N.J., and Chryssoulf, S.L. 1990. CONCENTRATIONS OF "INVISIBLE GOLD" IN THE COMMON SULFIDES. Canadian Mineralogist, **28**: 1–16.

Cook, N.J., Ciobanu, C.L., and Mao, J. 2009. Textural control on gold distribution in As-free pyrite from the Dongping, Huangtuliang and Hougou gold deposits, North China Craton (Hebei Province, China). Chemical Geology, **264**: 101–121.

Daigneault, R., Mueller, W.U., and Chown, E.H. 2002. Oblique Archean subduction: Accretion

and exhumation of an oceanic arc during dextral transpression, Southern Volcanic Zone, Abitibi Subprovince Canada. Precambrian Research, **115**: 261–290.

Davis, D.W. 2002. U-Pb geochronology of Archean metasedimentary rocks in the Pontiac and Abitibi subprovinces, Quebec, constraints on timing, provenance and regional tectonics. Precambrian Research, **115**: 97–117.

Dimroth, E., Imreh, L., Rocheleau, M., and Goulet, N. 1982. Evolution of the south-central part of the Archean Abitibi belt, Quebec. Part I: stratigraphy and paleogeographic model. Canadian Journal of Earth Sciences, **19**: 1729–1758.

Dubé, B., and Gosselin, P. 2007. Greenstone-hosted quartz-carbonate vein deposits, in Goodfellow, W.D., ed., Mineral Deposits of Canada: A Synthesis of Major Deposit-Types, District Metallogeny, the Evolution of Geological Provinces, and Exploration Methods. Geological Association of Canada, Mineral Deposits Division, **Special**: 49–73.

Fougerouse, D., Micklethwaite, S., Tomkins, A.G., Mei, Y., Kilburn, M., Guagliardo, P., Fisher, L.A., Halfpenny, A., Gee, M., Paterson, D., and Howard, D.L. 2016. Gold remobilisation and formation of high grade ore shoots driven by dissolution-reprecipitation replacement and Ni substitution into auriferous arsenopyrite. Geochimica et Cosmochimica Acta, **178**: 143–159.

Gaillard, N., Williams-Jones, A.E., Clark, J.R., Lypaczewski, P., Salvi, S., Perrouty, S., Piette-Lauzière, N., Guilmette, C., and Linnen, R.L. 2018. Mica composition as a vector to gold mineralization: Deciphering hydrothermal and metamorphic effects in the Malartic district, Quebec. Ore Geology Reviews, **95**: 789–820.

Garofalo, P.S. 2000. Gold precipitation and hydrothermal alteration during fluid flow through the vein network of the mesothermal gold deposit of Sigma, (Abitibi belt, Canada). Swiss Federal Institue of Technology Zurich.

Gresens, R.L. 1967. Composition-volume relationships of metasomatism. Chemical Geology, **2**: 47–65.

Groves, D.I., Goldfarb, R.J., Gebre-Mariam, M., Hagemann, S.G., and Robert, F. 1998. Orogenic gold deposits: a proposed classification in the context of their crustal distribution and relationship to other gold deposit types. Ore Geology Reviews, **13**: 7–27.

Imreh, L. 1984. Sillon de La Motte-Vassan et son avant-pays méridional: Synthèse volcanogénique, lithostratigraphique et gîtologique.

Kerrich, R. 1989. Archean gold: relation to granulite formation or felsic intrusions? Geology, **17**: 1011–1015.

Lavoie, S. 2003. Géologie de la mine East-Sullivan, Abitibi-Est, Val-d'or, Québec. Université du Québec a Chicoutimi.

Lentz, D.R. 2002. Sphalerite and arsenopyrite at the Brunswick No. 12 massive-sulfide deposit, Bathurst camp, New Brunswick: Constraints on P-T evolution. Canadian Mineralogist, **40**: 19–31.

Liu, W., Etschmann, B., Testemale, D., Hazemann, J.L., Rempel, K., Müller, H., and Brugger, J. 2014. Gold transport in hydrothermal fluids: Competition among the Cl-, Br-, HS- and NH3(aq) ligands. Chemical Geology, **376**: 11–19.

Liu, W., Migdisov, A., and Williams-Jones, A. 2012. The stability of aqueous nickel(II) chloride complexes in hydrothermal solutions: Results of UV-Visible spectroscopic experiments. Geochimica et Cosmochimica Acta, **94**: 276–290.

MacLean, W.H., and Barrett, T.J. 1993. Lithogeochemical techniques using immobile elements. Journal of Geochemical Exploration, **48**: 109–133.

MacLean, W.H., and Kranidiotis, P. 1987. Alteration: Phelps Dodge Massive Sulfide Deposit, Matagami, Quebec. Economic Geology, **82**: 1898–1911.

Mccuaig, T.C., and Kerrich, R. 1998. P—T—t—deformation—fluid characteristics of lode gold deposits: evidence from alteration systematics. Ore Geology Reviews, **12**: 381–453.

Migdisov, A.A., Zezin, D., and Williams-Jones, A.E. 2011. An experimental study of Cobalt (II)

complexation in Cl- and H2S-bearing hydrothermal solutions. Geochimica et Cosmochimica Acta, **75**: 4065–4079.

Möller, P., and Kersten, G. 1994. Electrochemical accumulation of visible gold on pyrite and arsenopyrite surfaces. Mineralium Deposita, **29**: 404–413.

Monecke, T., Mercier-Langevin, P., Dubé, B., and Frieman, B.M. 2018. Geology of the Abitibi Greenstone Belt. In Archean base and precious metal deposits, southern Abitibi greenstone belt, Canada. : 7–39.

Morishita, Y., Hammond, N.Q., Momii, K., Konagaya, R., Sano, Y., Takahata, N., and Ueno, H. 2019. Invisible gold in pyrite from epithermal, banded-iron-formation-hosted, and sedimentary gold deposits: Evidence of hydrothermal influence. Minerals, **9**: 1–24.

Mueller, W.U., Daigneault, R., Mortensen, J.K., and Chown, E.H. 1996. Archean terrane docksin: upper crust collision tectonics, Abitibi greenstone belt, Quebec, Canada. Tectonophysics, **265**: 127–150.

Neumayr, P., and Hagemann, S.G. 2002. Hydrothermal fluid evolution within the Cadillac tectonic zone, Abitibi greenstone belt, Canada: Relationship to auriferous fluids in adjacent second- and third-order shear zones. Economic Geology, **97**: 1203–1225.

Neumayr, P., Hagemann, S.G., and Couture, J.F. 2000. Structural setting, textures, and timing of hydrothermal vein systems in the Val d'Or camp, Abitibi, Canada: Implications for the evolution of transcrustal, second- and third-order fault zones and gold mineralization. Canadian Journal of Earth Sciences, **37**: 95–114.

Paton, C., Hellstrom, J., Paul, B., Woodhead, J., and Hergt, J. 2011. Iolite: Freeware for the visualisation and processing of mass spectrometric data. Journal of Analytical Atomic Spectrometry, **26**: 2508–2518.

Pearce, J.A., and Cann, J.R. 1973. Tectonic setting of basic volcanic rocks determined using trace element analyses. Earth and Planetary Science Letters, **19**: 290–300.

Pearce, T.H. 1968. A contribution to the theory of variation diagrams. Contributions to Mineralogy and Petrology, **19**: 142–157.

Perrouty, S., Gaillard, N., Piette-Lauzière, N., Mir, R., Bardoux, M., Olivo, G.R., Linnen, R.L., Bérubé, C.L., Lypaczewski, P., Guilmette, C., Feltrin, L., and Morris, W.A. 2017. Structural setting for Canadian Malartic style of gold mineralization in the Pontiac Subprovince, south of the Cadillac Larder Lake Deformation Zone, Québec, Canada. Ore Geology Reviews, **84**: 185–201.

Pilote, P., Scott, C.R., Mueller, W.U., Lavoie, S., and Riopel, P. 1999. Géologie des formations de Val-d'Or, Héva et Jacola : nouvelle interprétation du groupe de Malartic. In: Explorer au Québec: le défi de la connaissance. Séminaire d'information sur la recherche géologique, programme et résumés. Minsitère de l'énergie et des Ressources, **DV 99-03**: 52.

Pokrovski, G.S., Kokh, M.A., Proux, O., Hazemann, J.L., Bazarkina, E.F., Testemale, D., Escoda, C., Boiron, M.C., Blanchard, M., Aigouy, T., Gouy, S., de Parseval, P., and Thibaut, M. 2019. The nature and partitioning of invisible gold in the pyrite-fluid system. Ore Geology Reviews, **109**: 545–563. Elsevier.

Robert, F. 1989. Internal structure of the Cadillac tectonic zone southeast of Val d'Or, Abitibi greenstone belt, Quebec. Canadian Journal of Earth Sciences, **26**: 2661–2675.

Robert, F. 1994. Vein fields in gold districts: the example of Val-d'Or, southeastern Abitibi Subprovince, Québec. In Current Research. Geological Survey of Canada,: 295–302.

Robert, F., Brommecker, R., and Bubar, D.S. 1990. The orenada zone 4 deposit: deformed vein-type gold mineralization within the cadillac tectonic zone, SE of Val d'Or. Institut Canadien des mines et de la métallurgie, Volume spécial,: 255–268.

Robert, F., and Brown, A.C. 1986. Archean gold-bearing quartz veins at the Sigma Mine, Abitibi greenstone belt, Quebec: Part I. Geologic relations and formation of the vein system. Economic Geology, **81**: 578–592.

Savard, C., Carrier, A., and Durieux, G. (2018). NI 43-101 Technical Report and Updated

Mineral Resource estimate for the Orenada Zones 2 and 4 Projects, Orenada Group Properties. Prepared by Innov Explo– Conseil for Alexandria Minerals Corporation.

Scott, C.R., Mueller, W.U., and Pilote, P. 2002. Physical volcanology, stratigraphy, and lithogeochemistry of an Archean volcanic arc: Evolution from plume-related volcanism to arc rifting of SE Abitibi Greenstone Belt, Val d'Or, Canada. Precambrian Research, **115**: 223–260.

Shannon, R.D. 1976. Revised effective ionic radii and systematic studies of interatomic distances in halides and chalcogenides. Acta Crystallographica Section A, **32**: 751–767.

Sibson, R.H., Robert, F., and Poulsen, K.H. 1988. High-angle reverse faults, fluid-pressure cycling, and mesothermal gold-quartz deposits. Geology, **16**: 551–555.

Simard, M., Gaboury, D., Daigneault, R., and Mercier-Langevin, P. 2013. Multistage gold mineralization at the Lapa mine, Abitibi Subprovince: Insights into auriferous hydrothermal and metasomatic processes in the Cadillac-Larder Lake Fault Zone. Mineralium Deposita, **48**: 883–905.

Stanley, C.R. 2020. Molar element ratio analysis of lithogeochemical data: a toolbox for use in mineral exploration and mining. Geochemistry: Exploration, Environment, Analysis, **20**: 233–256.

Stipp, M., Stunitz, H., Heilbronner, R., and Schmid, S.M. 2002. Dynamic recrystaUization of quartz : correlation between natural and experimental conditions. Geological Society, London, Special Publications, **200**: 171–190.

Zhou, X., and Lafrance, B. 2017. Stratigraphic and structural setting of gold and nickel deposits in the La Motte-Malartic area, southern Abitibi and Ponkiak Subprovinces, Superior Province, Quebec. *In* Projets 2017, Initiative Metal Earth, Ministère de l'Ènerie et Ressources naturelles Québec, MB.

Appendix A: Drill hole sample locations

Project	DDH	Azimuth	Dip	Start	End	Length	MTM83-9 - East	MTM83-9 - North	MTM83-9 Elevation	Orenada - East	Orenada - North	Orenada - Elevation	UTM83-18 - East	UTM83-18 - North	UTM83-18 - Elevation
ORENADA	OAX-17-122	16	-82	0	267	267	214064.7	5324250	3317.24	-1842.73	-740.89	3317.24	297515.6	5325508.2	3317.2
ORENADA	OAX-17-108	198	-90	0	183	183	214349.8	5324188	3315.89	-1551.73	-716.45	3315.89	297799.5	5325440.2	3315.9
ORENADA	OAX-17-096	20	-76	0	417	417	214749.2	5323997	3317.04	-1113.64	-780.83	3317.04	298195.1	5325241.7	3317
ORENADA	OAX-17-084	20	-65	0	427	427	214504.9	5324024	316.4	-1357.64	-828.86	3313	297948.5	5325272.6	3313
ORENADA	OAX-17-085	20	-63	0	300	300	214510.8	5324037	3317.23	-1353.52	-812.51	3317.23	297957.5	5325286.8	3317.2
ORENADA	OAX-17-156	15.7	-72	0	312	312	21456.21	5324044	3316.4	-1340.81	-801.28	3316.4	297973.1	5325293.5	3316.4
ORENADA	OAX-16-075	16	-60	0	316.5	316.5	215447	5323820	3316.76	-394.32	-743.87	3316.76	298889.4	5325051.2	3316.8
ORENADA	OAX-17-123	16.7	-50	0	218	218	214995	5323904	3319	-851.1	-797.25	3319	298439.1	5325143.8	3319
ORENADA	OAX-17-125	195.7	-72	0	273	273	215023.6	5324003	3317	-853.26	-693.51	3317	298469.6	5325242.9	3317
ORENADA	OAX-07-15	195	-65	0	423	423	215128.7	5324128	3315.11	-789.74	-542.98	3315.11	298577.1	5325365.9	3315.1
ORENADA	407-40	196	-48.5	0	276.45	276.45	216326.4	5323863	3322.32	433.74	-443.45	3322.32	299769.6	5325076.7	3322.3
ORENADA	407-51	196	-53	0	206.35	206.35	216612	5323755	3319.87	-791.46	-319.06	3319.87	-	-	-
ORENADA	OU-5-24	196.28	10	0	117.35	117.35	214544.8	5324155	3167.79	-1355.81	-689.56	3167.79	297993.9	5325404.2	3167.8
ORENADA	OU-5-26	196.28	-46.5	0	84.12	84.12	214544.8	5324155	3167.18	-1355.81	-689.56	3167.18	297993.9	5325404.2	3167.2
ORENADA	407-57	196	-46.5	0	129.84	129.84	214538.4	5324131	3318.56	-1354.8	-714.55	3318.56	297987	5325380.2	3318.6

Drill hole	Sample number	Altered/ Least altered	Rock/vein type	Zone	Depth (m)
OAX-17-122	cp-122-01	Altered	QV	4	79.5
OAX-17-122	cp-122-02	Altered	FV	4	87.5
OAX-17-122	cp-122-03	Altered	FV	4	92
OAX-17-122	cp-122-04	Altered	FV	4	192
OAX-17-122	cp-122-06	Altered	FV	4	208
OAX-17-108	cp-108-02	Altered	FV	4	71.8
OAX-17-108	cp-108-03	Altered	FV	4	75
OAX-17-108	cp-108-05	Altered	QV	4	97
OAX-17-108	cp-108-06	Altered	QV	4	103
OAX-17-108	cp-108-08	Altered	QV	4	124.4
OAX-17-096	cp-96-01	Altered	QV	4	81.5
OAX-17-096	cp-96-02	Altered	FV	4	97.3
OAX-17-096	cp-96-05	Altered	QV	4	310.2
OAX-17-096	cp-96-06	Altered	QV	4	316.25
OAX-17-096	cp-96-08	Altered	QV	4	326.3
OAX-17-096	cp-96-11	Altered	QV	4	378.1
OAX-17-096	cp-96-12	Altered	QV	4	402.3
OAX-17-084	cp-84-01	Altered	QV	4	66.7
OAX-17-084	cp-84-02	Altered	QV	4	90.9
OAX-17-084	cp-84-03	Altered	QV	4	96.65
OAX-17-084	cp-84-04	Altered	QV	4	110.5
OAX-17-084	cp-84-06	Altered	QV	4	125.25
OAX-17-084	cp-84-07	Altered	QV	4	134.15
OAX-17-084	cp-84-08	Altered	QV	4	138
OAX-17-084	cp-84-09A	Altered	V3A	4	153.3
OAX-17-084	cp-84-09B	Altered	V3A	4	153.5
OAX-17-084	cp-84-10	Altered	QV	4	159.9
OAX-17-084	cp-84-11	Altered	V2	4	278.95
OAX-17-084	cp-84-12	Altered	V2 cut by V3A	4	279.7
OAX-17-084	cp-84-13	Altered	QV	4	301.7
OAX-17-084	cp-84-14	Altered	QV	4	325.6
OAX-17-084	cp-84-15	Altered	V3A	4	353.9
OAX-17-084	cp-84-16	Altered	QV	4	92.55
OAX-17-085	cp-85-01	Altered	QV	4	46.1
OAX-17-085	cp-85-02A	Altered	V3A	4	48
OAX-17-085	cp-85-02B	Altered	V3A	4	48
OAX-17-085	cp-85-03	Altered	FV	4	52.3
OAX-17-085	cp-85-04	Altered	FV	4	53.2
OAX-17-085	cp-85-05	Altered	V3A	4	60.5
OAX-17-085	cp-85-08	Altered	QV	4	146
OAX-17-085	cp-85-09	Altered	QV	4	153.55
OAX-17-085	cp-85-10	Altered	QV	4	155.2
OAX-17-085	cp-85-11	Altered	QV	4	166.25
OAX-17-085	cp-85-12	Altered	QV	4	72.5
OAX-17-085	cp-85-13	Altered	V3A	4	167.25
OAX-17-156	CP-156-01	Altered	QV	4	34.9
OAX-17-156	CP-156-02	Altered	V2	4	35.8
OAX-17-156	CP-156-03	Altered	V2 cut by V3A	4	153
OAX-17-156	CP-156-04	Altered	V2	4	210
OAX-17-156	CP-156-05	Altered	V2	4	232
OAX-17-156	CP-156-06	Altered	V2	4	307.8
OAX-17-156	CP-156-07	Altered	V3A	4	108.5
OAX-16-075	CP-75-01	Altered	FV	2	35.65
OAX-16-075	CP-75-02	Altered	V3A	2	40.15
OAX-16-075	CP-75-03	Altered	FV	2	57
OAX-16-075	CP-75-04	Altered	FV	2	58.4
OAX-16-075	CP-75-05	Altered	FV	2	67.15
OAX-16-075	CP-75-06	Altered	V2	2	76.85
OAX-16-075	CP-75-07A	Altered	V3A	2	81
OAX-16-075	CP-75-07B	Altered	FV	2	81.2
OAX-16-075	CP-75-08	Altered	FV	2	97.3
OAX-16-075	CP-75-09	Altered	V3A	2	115.4
OAX-16-075	CP-75-10	Altered	QV	2	129.6
OAX-16-075	CP-75-11	Altered	FV	2	160.55
OAX-16-075	CP-75-12	Altered	FV	2	171,9
OAX-16-075	CP-75-13	Altered	QV	2	185
OAX-16-075	CP-75-14	Altered	V2	2	269.4

OAX-17-123	cp-123-01LIB	Least-altered	QV	btw 2 and 4	118
OAX-17-123	cp-123-02	Least-altered	QV	btw 2 and 4	118.2
OAX-17-123	cp-123-03	Least-altered	QV	btw 2 and 4	125
OAX-17-123	cp-123-04	Least-altered	FV	btw 2 and 4	129.15
OAX-17-123	cp-123-05LIB	Least-altered	FV	btw 2 and 4	130.07
OAX-17-123	cp-123-06	Least-altered	FV	btw 2 and 4	131.2
OAX-17-123	cp-123-07LIB	Least-altered	FV	btw 2 and 4	131.8
OAX-17-123	cp-123-08	Least-altered	FV	btw 2 and 4	132
OAX-17-125	cp-125-01LIB	Least-altered	QV	btw 2 and 4	59.85
OAX-17-125	cp-125-02	Least-altered	QV	btw 2 and 4	60.6
OAX-17-125	cp-125-03	Least-altered	QV	btw 2 and 4	125.3
OAX-07-015	cp-15-01	Least-altered	FV	btw 2 and 4	383.3
OAX-07-015	cp-15-05	Least-altered	QV	btw 2 and 4	379.3
OAX-07-015	cp-15-06	Least-altered	QV	btw 2 and 4	381.8
OAX-07-015	cp-15-07	Least-altered	QV	btw 2 and 4	382.65
407-51	Cp-40751-01	Least-altered	FV	east of 2	24.68
407-51	Cp-40751-04	Least-altered	FV	east of 3	87.5
407-51	Cp-40751-05	Least-altered	FV	east of 4	97.84
407-51	Cp-40751-06	Least-altered	FV	east of 5	96.9
407-40	Cp-40740-01LIB	Least-altered	FV	east of 6	171.15
407-40	Cp-40740-02	Least-altered	FV	east of 7	171.8

Appendix B: Thin section petrography

Least Altered Thin Sections

Sample	Drill Hole	Rock Type	Key Features	Alteration	Sulphides	Deformation	Modal Abundance
Cp-15-01	OAX-07-015	FV	• Fine to coarse feldspar porphyroclasts, subangular within a very-fine grained Qz-Ser-Fld-Cb matrix. Fine matrix is observed alternating coarse Qz-Cc layers • S1 is in the direction of the layers, defined by ser-chl alteration	• Ser-chl alteration in ground mass and as thin streamers • Ser alteration in Fld porphyroclasts	• Fine rutile aligned in groundmass • <1% disseminated pyrite in groundmass	• Chl-ser S1 crenulated by S2 • Pressure shadows of Cb-ser surrounding porphyroclasts	• 30% fine matrix • 20% feldspar • 20% mica • 15% carbonate • 10% quartz • 5% chlorite • Trace sulphides
Cp-15-05	OAX-07-015	QV	• Fine to medium grained quartz porphyroclasts, rounded, elongated in the direction of S1, within a very-fine grained Qz-Ser matrix. Fine matrix is observed alternating coarse Qz-Cc layers. • Ms packages enveloppe Qz porphyroclast • Thin V1 veins are observed parallel to S1 • S1 defined by Ms layers	• Ser alteration in ground mass	• Fine rutile aligned in groundmass • <1% disseminated pyrite in groundmass	• Mica S1 crenulated by S2	• 35% Quartz • 35% mica • 30% carbonate
Cp-15-07	OAX-07-015	QV	• Fine to medium grained quartz porphyroclasts, rounded, elongated in the direction of S1, within a very-fine grained Qz-Ser matrix. Fine matrix is observed alternating coarse Qz-Cc layers. • Ser-chl enveloppe Qz porphyroclats • medium V1 veins are observed parallel to S1 • S1 defined by ms-chl layers	• Ser-chl alteration in ground mass as thin veinlets	• Fine rutile aligned in groundmass	• Mica S1 crenulated by S2	• 35% Quartz • 30% mica • 25% carbonate • 10% chlorite

Cp-15-07	OAX-07-015	QV	• Fine grained quartz porphyroclasts, rounded, elongated in the direction of S1, within a very-fine grained Qz-Ser-chl matrix. • Ms packages envelope Qz porphyroclats • Thin V1 veins are observed parallel to S1 • S1 defined by Ms layers	• Ser-cb alteration in ground mass • Chloritization of mica packages	• Fine rutile aligned in groundmass • Fine grained anhedral pyrite aligned along S1	• Mica S1 crenulated by S2	• 30% Quartz • 30% carbonate • 28% Chlorite • 15% mica • 2% sulphide
Cp-123-01LIB	OAX-17-123	QV	• Medium grained quartz porphyroclasts, rounded, elongated in the direction of S1, within a very-fine grained Qz-Ser matrix. • Groundmass is made up of alternating layers of ms rich and qz-cc-ser rich layers • Qz-cb pressure shadows at the edges of porphyroclast. • Ms packages envelope Qz porphyroclats • S1 defined by Ms layers	• Ser alteration in ground mass		• Ser S1 crenulated by S2	• 40% Quartz • 35% mica • 25% carbonate
Cp-123-02	OAX-17-123	QV	• Medium to coarse grained quartz porphyroclasts, rounded, elongated in the direction of S1, within a very-fine grained Qz-Ser matrix. • Groundmass is made up of alternating layers of ms rich and qz-cc-ser rich layers • Qz-cb pressure shadows at the edges of porphyroclast. • Ms packages envelope Qz porphyroclats • S1 defined by Ms layers	• Ser alteration in ground mass		• Ser S1 crenulated by S2	• 40% Quartz • 35% mica • 25% carbonate
Cp-123-03	OAX-17-123	QV	• Fine to medium grained quartz porphyroclasts, rounded, elongated in the direction of S1, within a very-fine grained Qz-Ser matrix.	• Ser alteration in ground mass		• Ser S1 crenulated by S2	• 40% Quartz • 35% mica • 25% carbonate

			• Groundmass is made up of alternating layers of ms rich and qz-cb-ser rich layers • Qz-cb pressure shadows at the edges of porphyroclast. • Thin V1 qz-cb veins observed parallel to S1 • Ms packages envelope Qz porphyroclats • S1 defined by Ms layers				
Cp-123-04	OAX-17-123	FV	• Fine to coarse feldspar porphyroclasts, subangular within a very-fine grained Qz-Ser-Fld-Cb matrix. • S1 is in the direction of the layers, defined by ser-chl alteration • Porphyroclast are clustered and appear to be rotated • Pressure shadows of Cb-ser surrounding porphyroclasts	• Groundmass is very albitized • Ser alteration in Fld porphyroclasts		• Chl-ser S1 crenulated by S2	• 50% Feldspar • 20% mica • 20% carbonate • 5% quartz • 5% chlorite
Cp-123-05LIB	OAX-17-123	FV	• Fine to coarse feldspar porphyroclasts, subangular within a very-fine grained Fld-Qz-cb-ser matrix. Fine matrix is observed alternating coarse Qz-Cc layers • S1 is in the direction of the layers, defined by ser-chl alteration. • Porphyroclast are aligned along S1 • Some Porphyroclast appear to be rotated	• Groundmass is very albitized • Ser alteration in Fld porphyroclasts		• Chl-ser S1 crenulated by S2	• 50% Feldspar • 20% mica • 20% carbonate • 5% quartz • 5% chlorite
Cp-123-06	OAX-17-123	FV	• coarse feldspar porphyroclasts, subangular within a very-fine grained Fld-Qz-cb-ser matrix. • Porphyroclast are aligned along S1 defined by ms/ser rich streamers • Some Porphyroclast appear to be rotated and have qz-cb pressure shadows	• Groundmass is albitized and chloritized • Ser alteration in Fld porphyroclasts		• Chl-ser S1 crenulated by S2	• 40% Feldspar • 25% mica • 15% carbonate • 10% quartz • 10% chlorite

Cp-123-07LIB	OAX-17-123	FV	• coarse feldspar porphyroclasts, subangular within a very-fine grained Fld-Qz-cb-ser matrix. • Porphyroclast are aligned along S1 defined by ms/ser rich streamers • Some Porphyroclast appear to be rotated and have qz-cb pressure shadows	• Groundmass is albitized and chloritized • Ser alteration in Fld porphyroclasts		• Chl-ser S1 crenulated by S2	• 40% Feldspar • 25% mica • 15% carbonate • 10% quartz • 10% chlorite
Cp-123-08	OAX-17-123	FV	• Fine to coarse feldspar porphyroclasts, subangular within a very-fine grained Qz-Ser-Fld-Cb matrix. • S1 is in the direction of the layers, defined by ser-chl alteration • Porphyroclast are aligned along S1 • Pressure shadows of Cb-ser surrounding porphyroclasts	• Groundmass is very albitized • Ser alteration in Fld porphyroclasts		• Chl-ser S1 crenulated by S2	• 50% Feldspar • 20% mica • 20% carbonate • 5% quartz • 5% chlorite
Cp-125-01LIB	OAX-17-125	QV	• Fine to medium grained quartz porphyroclasts, rounded, elongated in the direction of S1, within a very-fine grained Qz-Ser matrix. • Groundmass is made up of alternating layers of ms rich and qz-cb-ser rich layers • Qz-cb pressure shadows at the edges of porphyroclast. • Thin V1 qz-cb veins observed parallel to S1. V1 is boudinaged • Ms packages envelope Qz porphyroclats • S1 defined by Ms layers	• Ser-cb alteration in ground mass		• Ser S1 crenulated by S2	• 40% Quartz • 35% mica • 25% carbonate
Cp-125-02	OAX-17-125	QV	• Fine to medium grained quartz porphyroclasts, rounded, elongated in the direction of S1, within a very-fine grained Qz-Ser matrix.	• Ser-cb alteration in ground mass		• Ser S1 crenulated by S2	• 40% Quartz • 35% mica • 25% carbonate

			• Groundmass is made up of alternating layers of ms rich and qz-cb-ser rich layers • Qz-cb pressure shadows at the edges of porphyroclast. • Thin V1 qz-cb veins observed parallel to S1. V1 is boudinaged • Ms packages envelope Qz porphyroclats • S1 defined by Ms layers				
Cp-125-03	OAX-17-125	QV	• Fine to medium grained quartz porphyroclasts, rounded, elongated in the direction of S1, within a very-fine grained Qz-Ser matrix. • Groundmass is made up of alternating layers of ms rich and qz-cb-ser rich layers • Qz-cb pressure shadows at the edges of porphyroclast. • Thin V1 qz-cb veins observed parallel to S1. V1 is boudinaged • Ms packages envelope Qz porphyroclats S1 defined by Ms layers	• Ser-cb alteration in ground mass		• Ser S1 crenulated by S2	• 40% Quartz • 35% mica • 25% carbonate
Cp-40751-01	407-51	QV	• Fine grained quartz porphyroclasts, rounded, elongated in the direction of S1, within a very-fine grained Qz-Ser-fld-chl matrix. • Groundmass is made up of alternating layers of ms rich and qz-cb-ser rich layers • Thin V1 qz-cb veins observed parallel to S1. V1 is boudinaged • S1 defined by Ms-chl streamers	• Ser-fld-chl alteration in ground mass	• Fine grained clusters of pyrite observed In chl rich region	• Ser S1 crenulated by S2	• 30% Quartz • 20% mica • 20% feldspar • 15% carbonate • 15% chlorite
Cp-40751-04	407-51	FV	• Fine to medium feldspar porphyroclasts, subangular within a very-fine grained Qz-Ser-Fld-Cb matrix.	• Fld-ser-cb alteration in groundmass		• Chl-ser S1 crenulated by S2	• 40% Feldspar • 20% mica • 20% carbonate

			• Porphyroclasts are aligned along S1 and are clustered. • Some porphyroclasts are rotated and are broken or cracked • Pressure shadows of Cb-ser surrounding porphyroclasts	• Ser alteration in Fld porphyroclasts			• 10% quartz • 10% chlorite
Cp-40751-05	407-51	FV	• Fine to medium feldspar porphyroclasts, subangular within a very-fine grained Qz-Ser-Fld-Cb matrix. • Porphyroclasts are aligned along S1 and are clustered • Some porphyroclasts are rotated and are broken or cracked • Pressure shadows of Cb-ser surrounding porphyroclasts	• Fld-ser-cb alteration in groundmass • Ser alteration in Fld porphyroclasts	• Disseminated pyrite in groundmass	• Chl-ser S1 crenulated by S2	• 40% Feldspar • 20% mica • 20% carbonate • 10% quartz • 10% chlorite • Trace sulphide
Cp-40751-06	407-51	FV	• Fine grained feldspar porphyroclasts, subangular within a very-fine grained Qz-Ser-Fld-Cb matrix. • Porphyroclasts are aligned along S1 • S1 is defined by ms crenulated ribbons • Pressure shadows of Cb-ser surrounding porphyroclasts	• Fld-qz-ser-cb alteration in groundmass • Ser alteration in Fld porphyroclasts		• ser S1 crenulated by S2	• 40% Feldspar • 30% mica • 20% quartz • 10% carbonate
Cp-40740-01LIB	407-40	FV	• Fine grained feldspar porphyroclasts, subangular within a very-fine grained Qz-Ser-Fld-Cb matrix. • Porphyroclasts are aligned along S1 • S1 is defined by ms crenulated ribbons • Alternating layers of fine ground mass and ms rich layers	• Ser-chl-fld alteration in the groundmass	• Disseminated pyrite and pyrrhotite	• Ms rich layers are very crenulated S1 by S2.	• 35% Feldspar • 32% mica • 20% quartz • 5% carbonate • 5% chlorite • 3% sulphide
Cp-40740-02	407-40	FV	• Fine grained feldspar porphyroclasts, subangular within a very-fine grained Qz-Ser-Fld-Cb matrix.	• Ser-chl-fld alteration in	• Disseminated pyrite and pyrrhotite	• Ms rich layers are very	• 35% Feldspar • 32% mica • 20% quartz

			• Porphyroclasts are aligned along S1 • S1 is defined by ms crenulated ribbons • Alternating layers of fine ground mass and ms rich layers	the groundmass		crenulated S1 by S2.	• 5% carbonate • 5% chlorite • 3% sulphide

Altered Thin Sections

Sample	Drill Hole	Rock/ vein Type	Key Features	Alteration	Sulphides	Deformation	Modal Abundance
Cp-122-01	OAX-17-122	QV	• Medium to coarse quartz porphyroclast, rounded, elongated along S1 fabric. • Fine grained ser-qz-cb-fld rich matrix alternating layers with Ms rich layer. • Porphyroclasts are enveloped by Ms packages and cracked and folded grains are observed. • Fine grained tourmaline stringers are observed parallel to S1 • V1 qz-cb veins are observed parallel to S1	• Cb-ser-fld alteration in the groundmass • Fine grained tourmaline in the mica rich regions	• Disseminated pyrrhotite in groundmass • Coarse corroded, poikilitic pyrite elongated with S1 • Fine grained subhedral arsenopyrite aligned along S1	• Ms, including tm, rich layers are very crenulated S1 by S2.	• 40% quartz • 30% mica • 15% carbonate • 5% feldspar • 5% chlorite • 3% sulphide • 2% tourmaline
Cp-122-02	OAX-17-122	FV	• Section abundant with very coarse-grained feldspar porphyroclasts, rounded, with cb pressure shadows • Very fine grained fld-ser-qz-chl matrix • Porphyroclast are aligned with S1	• Highly sericitized section. Ser in ground mass and within porphyroclast • Chl-cb-qz alteration in groundmass	• Fine rutile aligned in groundmass • disseminated pyrite and pyrrhotite in groundmass	• S1 crenulated by S2	• 50% feldspar • 20% mica • 15% carbonate • 5% quartz • 5% chlorite • 5% sulphide

Cp-122-03	OAX-17-122	FV	• Section abundant with very coarse-grained feldspar porphyroclasts, rounded, with cb pressure shadows • Very fine grained fld-ser-qz-chl matrix • Porphyroclast are aligned with S1	• Highly sericitized section. Ser in ground mass and within porphyroclast • Chl-cb-qz alteration in groundmass	• Fine rutile aligned in groundmass • Disseminated pyrite and pyrrhotite in groundmass	• S1 crenulated by S2	• 40% feldspar • 25% mica • 15% carbonate • 8% quartz • 7% sulphide • 5% chlorite
Cp-122-04	OAX-17-122	FV	• Fine to medium grained feldspar porphyroclasts aligned along S1. Grains are sub-angular. • Porphyroclasts are within a tourmaline rich (ser-qz-cb) matrix and is beside a V2 quartz-carbonate-tourmaline.	• Major tourmaline alteration as you move towards the v2 veins. • Ser-cb-qz alteration in groundmass • Ser alteration in the fld grains.	• Medium Asp observed concentrated in tm rich regions • Both euhedral and corroded asp grains	• S1 crenulated by S2	• 30% feldspar • 25% tourmaline • 15 % carbonate • 10% mica • 10% quartz • 10% arsenopyrite
Cp-122-06	OAX-17-122	FV	• Fine grained feldspar porphyroclasts, subangular within a very-fine grained Qz-Ser-Fld-Cb matrix. • Porphyroclasts are aligned along S1 • S1 is defined by ms crenulated ribbons • Cb veinlets are parallel to S1 • Cb pressure shadows at the edges of porphyroclasts	• Ser-cb-fld alteration in the groundmass	• Disseminated pyrite and pyrrhotite	• Ms rich layers are very crenulated S1 by S2.	• 40% Feldspar • 30% mica • 20% carbonate • 7% quartz • 3% sulphide
Cp-108-02	OAX-17-108	FV	• Fine to medium feldspar porphyroclasts, subangular within a very-fine grained Qz-Ser-Fld-Cb matrix.	• Fld-ser-cb alteration in groundmass	• Fine rutile aligned in groundmass	• ser S1 crenulated by S2	• 40% Feldspar • 30% Matrix • 15% mica

			• Porphyroclasts are aligned along S1 and are clustered. • Some porphyroclasts are rotated and are broken or cracked • Pressure shadows of Cb-ser surrounding porphyroclasts	• Ser alteration in Fld porphyroclasts	• Disseminated arsenopyrite		• 13% carbonate • 2% sulphide
Cp-108-03	OAX-17-108	FV	• Fine to medium feldspar porphyroclasts, subangular within a very-fine grained Qz-Ser-Fld-Cb matrix. • Thin tourmaline stringers in the groundmass enveloping feldspar porphyroclast • Porphyroclasts are aligned along S1 and are clustered. • Some porphyroclasts are rotated and are broken or cracked • Pressure shadows of Cb-ser surrounding porphyroclasts	• Tm alteration stringers along S1 • Ser alteration in groundmass and in Fld porphyroclasts • Cb-fld alteration in ground mass	• Fine to medium grained eu-sub asp visible in the tm alteration • Disseminated pyrite • Fine rutile aligned along s1 in the groundmass	• ser S1 crenulated by S2 • tm stringers crenulated	• 35% mica • 20% feldspar • 25% carbonate • 10% quartz • 8% tourmaline • 2% sulphide
Cp-108-05	OAX-17-108	QV	• Medium grained quartz porphyroclasts, rounded, elongated and aligned along S1 • Qz-cb-ser rich fine matrix • Thin tourmaline stringers in the groundmass along S1 • V1 thin qz-cb viens .	• Tm alteration stringers along S1 • Ser-cb alteration in groundmass	• Fine to medium subhedral arsenopyrite observed exclusively in mica rich regions • Disseminated pyrite throughout section • Fine rutile aligned along s1 in the groundmass	• Ser-tm S1 crenulated by S2	• 40% Quartz • 30% Mica • 15% carbonate • 10% tourmaline • 5% sulphide

Cp-108-06	OAX-17-108	QV	• Medium grained quartz porphyroclasts (sparse), rounded, elongated and aligned along S1 • Ser-qz-cb rich fine matrix interlayered with Ms rich layers • Two thick layers of coarse Cc interlayered with ms rich regions • Thin tourmaline stringers in the groundmass along S1	• Tm alteration stringers along S1 • Ser-cb alteration in groundmass •	• Disseminated pyrite throughout section • Fine rutile aligned along s1 in the groundmass	• Ser-tm S1 crenulated by S2	• 35% Quartz • 28% Mica • 20% carbonate • 15% tourmaline • 2% sulphide
Cp-108-08	OAX-17-108	QV	• Layered sample of really thin undulating layers of ser-chl interlayered with fine grained quartz rich layers. There is also fine Tm in the ser rich layers. • There are also a few thicker bands of med grained cb-qz running parallel to the ser-chl thin layers • There is a few very fine to fine larger quartz grains that are the porphyroclasts, but they are very small. They only observed in the micaceous layers	• Tm alteration stringers along S1 • Chl altered ms rich layers	• <1% Disseminated pyrite throughout section	• Ser-tm S1 crenulated by S2 • Mica fish observed	• 35% Quartz • 30% Mica • 25% chlorite • 7% carbonate • 3% tourmaline
Cp-96-01	OAX-17-096	QV	• fin-medium grained quartz porphyroclasts, lenticular, elongated along S1 • fine grained qz-ser-cb rich matrix that's interlayered with thin stringers of fine grained ms • Thin V1 qz-cc veins observed along S1	• Ser-cb in the matrix	• <1% disseminated pyrrhotite	• Ms S1 crenulated by S2	• 60% quartz • 25% mica • 15% carbonate
Cp-96-02	OAX-17-096	FV	• Fine to medium feldspar porphyroclasts, subangular within a very-fine grained Qz-Ser-Fld-Cb matrix.	• Abundant in ser alteration within fld porphyroclast	• Medium grained corroded pyrite aligned along S1	• Ms S1 crenulated by S2	• 30% quartz • 25% feldspar • 20% mica

			• Thin tourmaline stringers in the groundmass enveloping feldspar porphyroclasts • Porphyroclasts are aligned along S1 and are clustered. • Some porphyroclasts are rotated and are broken or cracked • Pressure shadows of Cb-ser surrounding porphyroclasts • Late qz-cc thin V3 veinlets cutting S1	• Ser-fld-cb highly altered in the matrix	• Disseminated pyrrhotite in the ground mass		• 15% carbonate • 8% tourmaline • 2% pyrite
Cp-96-05	OAX-17-096	QV	• fine-medium grained quartz porphyroclasts, lenticular, elongated along S1 • fine grained qz-ser-cb rich matrix that's interlayered with thin stringers of fine grained ms-chl • Thin V1 qz-cc veins observed along S1 • Thin veinlets of tm, euhedral grains • there is the fine quartz surrounding the sulphides as pressure shadows	• chl-ser alteration of ms rich regions • tm stringers in ms rich regions	• eu-sub medium grained asp with noticeable rutile inclusions defining a fabric	• Ms S1 crenulated by S2	• 40% quartz • 20% chlorite • 15% mica • 10% tourmaline • 10% carbonate • 5% arsenopyrite
Cp-96-06	OAX-17-096	QV	• fine-medium grained quartz porphyroclasts, lenticular, elongated along S1 • section has a fine-grained qz-cb-ser matrix • the matrix is interlayered with thin stringers of fine grained ms-chl rich regions • Ms observed enveloping porphyroclasts • V1 veins observed in the section	• Ser-cb-chl alteration in the groundmass	• <1% disseminated pyrite and rutile in groundmass	• Ms S1 crenulated by S2	• 55% quartz • 30% mica • 10% carbonate • 5% chlorite

Cp-96-08	OAX-17-096	QV	• Quartz rich sample but instead of large Qz porphyroclasts it appears V1 boudinaged veins sections appear to be Porphyroclast. Quartz within these bundles are fine-grained and have sutured grain boundaries • Interlayered regions of fine qz-cb-ser groundmass and ms-chl rich micaceous regions. All layers follow S1. • Fine stringers of tm, undulated along ms rich regions	• Ser-chl-cb in groundmass • Chl-tm in ms rich regions	• Coarse-grained corroded asp aligned along S1 • Disseminated pyrite • Visible gold in asp	• Ms S1 crenulated by S2	• 42% quartz • 25% mica • 15% carbonate • 10% chlorite • 5% tourmaline • 3% arsenopyrite
Cp-96-11	OAX-17-096	QV	• fine-medium grained quartz porphyroclasts, lenticular, elongated along S1. • V1 boudinaged vein boudins look like quartz porphyroclasts. Quartz within these bundles are fine-grained and have sutured grain boundaries • fine-grained qz-cb-ser matrix • the matrix is interlayered with thin stringers of fine grained ms-chl rich regions • Ms observed enveloping porphyroclasts • V3 late veins cut S1	• Ser-cb-chl alteration in the groundmass	• Fine grained corroded pyrite along S1 • Also, diss pyrite • A few medium grained asp, subhedral found in ser rich regions	• Ms S1 crenulated by S2	• 45% quartz • 20% mica • 10% carbonate • 10% tourmaline • 10% chlorite • 5% sulphide
Cp-96-12	OAX-17-096	QV	• fine-medium grained quartz porphyroclasts, lenticular, elongated along S1. • fine-grained qz-cb-ser-chl matrix • the matrix is interlayered with thin stringers of fine grained ms-chl rich regions	• Ser-cb-chl alteration in the groundmass	• <1% disseminated pyrite	• Ms S1 crenulated by S2	• 45% quartz • 35% mica • 15% chlorite • 5% carbonate

			• Ms observed enveloping porphyroclasts				
Cp-84-01	OAX-084-17	QV	• fine-medium grained quartz porphyroclasts, lenticular, elongated along S1. • fine-grained qz-cb-ser-chl matrix • the matrix is interlayered with thin stringers of fine grained ms-chl rich regions • Ms observed enveloping porphyroclasts	• Ser-cb alteration in groundmass		• Ms S1 crenulated by S2	• 55% quartz • 35% mica • 10% carbonate
Cp-84-02	OAX-084-17	QV	• fine-medium grained quartz porphyroclasts, lenticular, elongated along S1. • fine-grained qz-cb-ser-chl matrix • the matrix is interlayered with thin stringers of fine grained ms-chl rich regions • thin undulating tm streamers aligned S1 • Ms observed enveloping porphyroclasts	• Ser-cb alteration in groundmass • Silicification in groundmass • Tourmaline alteration in ms regions	• Disseminated pyrite • Few large medium grained anhedral asp observed in ms regions	• Ms S1 crenulated by S2	• 45% quartz • 27% mica • 20% carbonate • 5% sulphides • 3% tourmaline
Cp-84-03	OAX-084-17	QV	• fine-medium grained quartz porphyroclasts, lenticular, elongated along S1. • V1 boudinaged vein boudins look like quartz porphyroclasts. Quartz within these bundles are fine-grained and have sutured grain boundaries • fine-grained qz-cb-ser matrix • fine grained quartz rich matrix with fine grained veinlets of chlorite	• chl alteration in ms rich regions	• Disseminated pyrrhotite in the groundmass aligned to S1	• Ms S1 crenulated by S2	• 45% quartz • 30% mica • 12% carbonate • 10% chlorite • 5% sulphides

			• there are alternating layers of the qz-chl matrix and a thicker fine-grained layers of muscovite				
Cp-84-04	OAX-084-17	QV	• very fine grained qz-cb-ser matrix • Lenticular quartz porphyroclasts, elongated and aligned along S1 • the matrix is interlayered with thin stringers of fine grained ms-chl rich regions • thin undulating tm streamers aligned S1 • Ms observed enveloping porphyroclasts • thicker med-coarse grained undulating qz-cc bands running through the whole section	• ser-cb alteration in groundmass	• Disseminated arsenopyrite, pyrite and pyrrhotite in the groundmass aligned to S1	• Ms S1 crenulated by S2	• 47% fine grained matrix • 35% mica • 10% quartz • 5% carbonate • 3% sulphide
Cp-84-06	OAX-084-17	QV	• very fine grained qz-cb-ser matrix • Lenticular quartz porphyroclasts, elongated and aligned along S1 • the matrix is interlayered with thin stringers of fine grained ms-chl rich regions • thin V1 qz-cb veins along S1 • minor feldspar observed in groundmass • thin undulating tm streamers aligned S1 • Ms observed enveloping porphyroclasts • thicker med-coarse grained undulating qz-cc bands running through the whole section	• cb-ser alteration in ground mass • minor fld alteration in groundmass	• <1% disseminated pyrite	• Ms S1 crenulated by S2	• 40% fine grained matrix • 25% mica • 20% carbonate • 15% quartz

Cp-84-07	OAX-084-17	QV	• Medium-coarse quartz porphyroclasts aligned along S1. Some grains are rounded but many are broken and cracked. Grains are proximal to a V2 mineralized vein • Groundmass is ser-chl--qz-cb rich • Thin ms stringers are seen in groundmass, surrounding quartz porphyroclasts, undulated, defining S1 • V2 is haloed by massive tourmaline alteration chl rich •	• Ser-chl-cb alteration in groundmass	• Many eu-sub arsenopyrite in the chl region • Corroded asp near tm bordering V2 vein • All asp aligned along S1	• V2 vein cuts S1 • Ms S1 crenulated by S2	• 30% quartz • 25% mica • 15% arsenopyrite • 10% chlorite • 15% tourmaline • 5% carbonate
Cp-84-08	OAX-084-17	QV	• fine-medium grained quartz porphyroclasts, lenticular, elongated along S1. • fine-grained qz-cb-ser matrix	• Ser alteration in groundmass		• Ms S1 crenulated by S2	• 55% quartz • 35% mica • 10% carbonate
Cp-84-09A	OAX-084-17	V3A	• Adjacent to a V3A qz-cb-tm vein with massive corroded asp grains. Most of the section is a large chunk of asp. • The tm is massive • Qz-cc are heterogeneous in size and show sutured grain boundaries. • The sample is hard to distinguish the 2 main fabrics, but some tm propagates as thin streamers along S1 • Alexandria assay of 42.5 g/t Au	• Massive tm alteration	• Corroded coarse grained asp everywhere • Visible gold seen in asp in fractures	• V3A along S2	• 40% Arsenopyrite • 30% Quartz • 20% tourmaline • 10% Carbonate
Cp-84-09B	OAX-084-17	V3A	• Same sample as 9A but this sample is of the V3A vein. Most of the section is the crosscutting V3A. the quartz is heterogenous in size and has sutured	• Ser-cb alt in matrix	• Corroded coarse grained asp at vein boundary	• Ms-tm S1 crenulated by S2	• 55% quartz • 15% arsenopyrite • 15% tourmaline • 10% Carbonate

			grain boundaries. Some tm needles are observed within the vein • Massive Tm halos either side of the vein (1cm). after the halo the tm propagates into thin stringers along S1, undulated. • Coarse grained corroded Asp at the halo boarders. As you move away from the vein the asp becomes more eu-sub, less crack and follows S1 • Matrix is qz-ser-cb-chl rich • Alexandria assay of 42.5 g/t Au	• Tm alteration at vein and as thin stringers	• Visible gold seen in asp in fractures of corroded asp • Eu-sub asp away from vein	• V3A along S2	• 5% chlorite
Cp-84-10	OAX-084-17	QV	• Sample is the wall rock away from 9A and B samples. Very chl-ser rich with eu-sub asp aligned along S1 • visible tm stringers in ms rich regions • Matrix is ser-chl-qz-cb rich • Sparse quartz porphyroclasts but they are lenticular, elongated along S1, many are cracked and have cb-qz pressure shadows	• Ser-chl in matrix • Tm stringers	• Eu-sub asp aligned along S1	• Ms-tm S1 crenulated by S2 • Tm stringers undulating	• 35% quartz • 20% mica • 15% carbonate • 15% chlorite • 13% tourmaline • 7% arsenopyrite
Cp-84-11	OAX-084-17	V2	• V2 qz-cb vein haloed with tm. Tm undulating stringers parallel to S1 are observed in the ground mass • Matrix Is ser-qz-cb-chl • Both textures of asp visible. Eu-sub in more ser-chl region and corroded in tm rich region • Quartz in vein show sutured grain boundaries • Tm is observed as massive haloes and as thin stringers	• Chl-ser in wall rock • Tm alteration at vein	• Both eu-sub and corroded asp grains.	• Ms -chl-tm S1 crenulated by S2	• 35% quartz • 20% tourmaline • 15% carbonate • 15% mica • 10% chlorite • 5% arsenopyrite

Cp-84-12	OAX-084-17	V2 cut by V3A	• This sample is of both V2 and V3A. shows a V2 vein being cut by the later V3A. Both veins show massive tm alteration at the vein boundaries and tm is visible within the V3A vein. V3A is qz dominated no cb. V2 is qz-cb • Asp is corroded only visible along tm halo of V2. No asp in V3A. • Quartz grains in V2 are heterogenous in size and show sutured grain boundaries	• Massive tm everywhere	• Medium grained corroded asp • Also see fine grained anhedral disseminated asp at the edge of the section away from vein crosscut	• V2 along S1 cut by V3A at S2 • Tm crenulated	• 35% quartz • 30% tourmaline • 10% carbonate • 15% mica • 10% arsenopyrite
Cp-84-13	OAX-084-17	QV	• fine-medium grained quartz porphyroclasts, lenticular, elongated along S1. • fine-grained qz-chl-cb-ser matrix	• Ser-chl alteration in groundmass	• <1% disseminated pyrite	• Ms -chl S1 crenulated by S2	• 50% quartz • 25% mica • 20% chlorite • 5% carbonate
Cp-84-14	OAX-084-17	QV	• fine-medium grained quartz porphyroclasts, lenticular, elongated along S1. • fine-grained qz-cb-ser matrix	• Ser alteration in groundmass		• Ms S1 crenulated by S2	• 55% quartz • 35% mica • 10% carbonate
Cp-84-15	OAX-084-17	V3A	• This section is of a large V3A vein with the massive tm halo and the tm stringers propagated away along S1 • Most of the section is Tm • There is corroded asp in the Tm at the region where the massive tm turns to stringers • Some of the tm away from the actual vein is observed crenulated • Where groundmass is visible it is qz-ser-tm-cb rich and very fine grained	• Tm alteration everywhere • Ser alteration in groundmass when visible	• Corroded asp in Tm. Some subhedral grain at the bottom of section away from the vein but most of the asp is corroded with major cracks	• Tm S1 crenulated by S2	• 50% tourmaline • 20% quartz • 15% arsenopyrite • 10% carbonate • 5% mica

Cp-84-16	OAX-084-17	QV	• Wall rock sample proximal to a V3A vein. • Medium-grained quartz porphyroclasts which are lenticular, aligned and elongated along S1 • Matrix is ser-chl-qz-cb rich very fine grained • Some tm stringers but only a couple visible	• Chl-ser in ground mass • Some tm as stringers	• Fine grained eu-sub asp along S1	• Ms-chl-tm S1 crenulated by S2	• 35% quartz • 30% mica • 15% carbonate • 15% chlorite • 3% tourmaline • 2% arsenopyrite
Cp-85-01	OAX-085-17	QV	• fine-medium grained quartz porphyroclasts, lenticular, elongated along S1. • fine-grained qz-cb-ser-chl matrix • the matrix is interlayered with thin stringers of fine grained ms-chl rich regions • Ms observed enveloping porphyroclasts	• Ser-cb alteration in groundmass		• Ms S1 crenulated by S2	• 55% quartz • 35% mica • 10% carbonate •
Cp-85-02A	OAX-085-17	V3A	• Adjacent to a V3A qz-cb-tm vein with massive corroded asp grains. • Quartz and cb in the section surrounded by massive tm. Qz-cb grains are all sizes and show sutured grain boundaries • The sample is hard to distinguish the 2 main fabrics because its directly in a vein. • The tm is patchy but massive • Alexandria assay of 3.65 g/t Au	• Tm alteration	• Corroded asp with fractures. • One VG in a fracture		• 45% quartz • 35% tourmaline • 10% Carbonate • 10% arsenopyrite
Cp-85-02B	OAX-085-17	V3A	• Same sample as 2A but this sample is of the V3A vein. the quartz is heterogenous in size and has sutured	• Tm alteration at vein and as thin stringers	• Corroded coarse grained asp at vein boundary	• Ms-tm S1 crenulated by S2	• 60% tourmaline • 20% quartz • 10% arsenopyrite

			grain boundaries. Some tm needles are observed within the vein • Massive Tm halos either side of the vein. Tm is most of the section. After the halo the tm propagates into thin stringers along S1, undulated. • Coarse grained corroded Asp at the halo boarders. As you move away from the vein the asp becomes more eu-sub, less crack and follows S1 • Matrix is qz-ser-cb-chl rich		• Visible gold seen in asp in fractures of corroded asp • Eu-sub asp away from vein	• V3A along S2	• 10% Carbonate
Cp-85-03	OAX-085-17	FV	• Fine grained feldspar porphyroclasts, subangular within a very-fine grained Qz-Ser-chl-Fld-Cb matrix. • Porphyroclasts are aligned along S1 • S1 is defined by ms crenulated ribbons • Cb veinlets are parallel to S1 • Cb pressure shadows at the edges of porphyroclasts	• Ser-chl-cb-fld alteration in the groundmass	• Disseminated pyrite and arsenopyrite	• Ms rich layers are very crenulated S1 by S2.	• 40% Feldspar • 30% mica • 15% carbonate • 10% chlorite • 4% quartz • 1% sulphide
Cp-85-04	OAX-085-17	FV	• Fine-medium grained feldspar porphyroclasts, subangular within a very-fine grained Qz-Ser-Fld-Cb matrix. • Porphyroclasts are aligned along S1 • Thin tm stringers observed along S1 • Cb veinlets are parallel to S1 • Cb pressure shadows at the edges of porphyroclasts • Eu-sub asp observed along tm-ser rich regions along S1	• Ser-cb-fld alteration in the groundmass • Tm stringers	• Fine eu-sub asp	• Ms-tm rich layers are very crenulated S1 by S2.	• 40% Feldspar • 25% mica • 15% carbonate • 10% tourmaline • 10% quartz • 5% arsenopyrite

Cp-85-05	OAX-085-17	V3A	• Proximal to V3A vein. Lots of tm alteration haloes and both corroded, and eu-sub asp all aligned to S1 • Tm stingers along S1 • When groundmass visible ser-qz-cb-rich	• Tm at vein • Ser in groundmass	• Both eu-sub and corroded asp	• Ms-tm rich layers are very crenulated S1 by S2	• 35% quartz • 20% arsenopyrite • 15% tourmaline • 15% Carbonate • 5% mica
Cp-85-08	OAX-085-17	QV	• Sample is the wall rock proximal to vein. Very chl-ser rich with eu-sub asp aligned along S1 • visible tm stringers in ms rich regions • Matrix is ser-chl-qz-cb rich • quartz porphyroclasts are lenticular, elongated along S1, many are cracked and have cb-qz pressure shadows	• Ser-chl in matrix • Tm stringers	• Eu-sub asp aligned along S1 • Disseminated pyrite	• Ms-tm S1 crenulated by S2 • Tm stringers undulating	• 35% quartz • 20% mica • 15% carbonate • 15% chlorite • 13% tourmaline • 7% arsenopyrite
Cp-85-09	OAX-085-17	QV	• Right beside a V3A vein. This section is the tm halo and the propagated tm veinlets which are undulated • Asp is both corroded and eu-sub all of which are aligned along S1 • Groundmass is very ser rich and very fine grained ser-qz-cb-chl • There are no visible quartz or feldspar porphyroclasts just asp-tm with deformed groundmass	• Ser in ground mass • Tm stringers	• Both eu-sub and corroded asp. Corroded are coarse grained. Eu-sub are fine grained.	• Ms-tm S1 crenulated by S2	• 35% quartz • 20% mica • 20% tourmaline • 15% arsenopyrite • 5% carbonate • 5% chlorite
Cp-85-10	OAX-085-17	QV	• fine-medium grained quartz porphyroclasts, lenticular, elongated along S1. • fine-grained qz-cb-chl-ser-chl matrix • the matrix is interlayered with thin stringers of fine grained ms-chl rich regions	• Ser-chl-cb alteration in groundmass	• <1% disseminated pyrite along S1	• Ms-chl S1 crenulated by S2	• 50% quartz • 35% mica • 10% carbonate • 5% chlorite

			• Ms observed enveloping porphyroclasts				
Cp-85-11	OAX-085-17	QV	• Sample is the wall rock proximal to vein. ser rich with eu-sub asp aligned along S1 • There are some visible tm stringers in ms rich regions • Matrix is ser-chl-qz-cb rich • quartz porphyroclasts are lenticular, elongated along S1, many are cracked and have cb-qz pressure shadows	• Ser in matrix • Tm stringers	• Eu-sub asp aligned along S1 • Disseminated pyrite	• Ms-tm S1 crenulated by S2 • Tm stringers undulating	• 45% quartz • 30% mica • 15% carbonate • 5% chlorite • 2% tourmaline • 3% arsenopyrite
Cp-85-12	OAX-085-17	QV	• fine-medium grained quartz porphyroclasts, lenticular, elongated along S1. • fine-grained qz-cb-chl-ser-chl matrix • the matrix is interlayered with thin stringers of fine grained ms-chl rich regions • Ms observed enveloping porphyroclasts	• Ser-chl-cb alteration in groundmass	• <1% disseminated pyrite along S1	• Ms-chl S1 crenulated by S2	• 45% quartz • 30% mica • 15% carbonate • 10% chlorite
Cp-85-13	OAX-085-17	V3A	• this sample is of the V3A vein. Most of the section is the crosscutting V3A. the quartz is heterogenous in size and has sutured grain boundaries. Some tm needles are observed within the vein • Massive Tm halos either side of the vein (1cm). after the halo the tm propagates into thin stringers along S1, undulated. • Coarse grained corroded Asp at the halo boarders. As you move away	• Ser-cb alt in matrix • Tm alteration at vein and as thin stringers	• Corroded coarse grained asp at vein boundary • Visible gold seen in asp in fractures of corroded asp • Eu-sub asp away from vein	• Ms-tm S1 crenulated by S2 • V3A along S2	• 45% quartz • 25% tourmaline • 15% arsenopyrite • 10% mica • 5% Carbonate • trace chlorite

			from the vein the asp becomes more eu-sub, less crack and follows S1 • Matrix is qz-ser-cb-chl rich				
Cp-156-01	OAX-17-156	QV	• proximal to V3A vein. • Some tm stringers and eu-sub asp all aligned to S1 • Chl-ser-qz-cb rich matrix • Sparse quartz porphyroclasts, lenticular, elongated along S1	• Ser-chl alteration in matrix • Tm stringers in ms rich regions	• Eu-sub asp	• Ms-tm S1 crenulated by S2	• 45% quartz • 20% mica • 15% chlorite • 10% carbonate • 5% tourmaline • 5% arsenopyrite
Cp-156-02	OAX-17-156	V2	• Multiple V2 veins all haloed by massive tm. Between the V2 are tm stingers in ser rich regions. • Matrix is ser-qz-chl rich • Fine grained asp sprinkled along V2 vein and in the tm rich halos. Some asp in the ser-chl groundmass. All asp aligned along S1. • Mica deformed, crenulated	• Ser-chl alteration in matrix • Tm halo V2 veins • Tm stringers in ms rich regions	• Eu-sub asp aligned along S1 in V2 vein, tm halos and in chl-ser groundmass	• Ms-chl-tm S1 crenulated by S2 •	• 40% quartz • 20% tourmaline • 15% arsenopyrite • 10% carbonate • 10% mica • 5% chlorite
Cp-156-03	OAX-17-156	V2 cut by V3A	• This sample is of both V2 and V3A. shows a V2 vein being cut by the later V3A. Both veins show massive tm alteration at the vein boundaries and acicular tm is visible within the V3A vein. V3A is qz dominated no cb. V2 is qz-cb • Coarse Asp is corroded visible along tm halo of V2 along S1. • Some asp is visible at the V3A tm halo boundary, corroded	• Massive tm everywhere • Ser alteration in groundmass	• Medium grained corroded asp • Also see fine grained anhedral disseminated asp at the edge of the section away from vein crosscut	• V2 along S1 cut by V3A at S2 • Tm crenulated	• 40% quartz • 30% tourmaline • 10% carbonate • 15% mica • 5% arsenopyrite

			• Quartz grains in both V2 and V3A are heterogenous in size and show sutured grain boundaries • When groundmass is observed it is very fine, deformed ser-qz rich				
Cp-156-04	OAX-17-156	V2	• V2 haloed by massive tm. Above and below V2 massive tm as stringers and halo. Corroded and eu-sub asp visible in V2 and in tm halo. • The rest of section is ser-chl-qz-cb rich matrix, very deformed very fine grained. • Ms-chl-tm deformed, crenulated	• Ser-chl alteration in matrix • Tm halo V2 veins • Tm stringers in ms rich regions	• Corroded and Eu-sub asp aligned along S1 in V2 vein, tm halos and in chl-ser groundmass	• Ms-chl-tm S1 crenulated by S2	• 40% quartz • 20% mica • 15% tourmaline • 10% carbonate • 10% chlorite • 5% arsenopyrite
Cp-156-05	OAX-17-156	V2	• Thick qz-cb subparallel V2 haloed with massive Tm • Lots of corroded and eu-sub asp at the halo and away from v2 in tm stingers • Tm stringers in groundmass take up most of the space • Groundmass tm-ser-qz-cb rich fine grained	• Tm halo and stringers • Ser-cb in groundmass	• Medium-coarse grained corroded and eu-sub grains	• Ms-tm S1 crenulated by S2	• 60% tourmaline • 20% quartz • 10% arsenopyrite • 5% carbonate • 5% mica
Cp-156-06	OAX-17-156	V2	• In very chl rich sample, I think its Piche mafic volcanics not Cadillac volcaniclastics • V2 veins with some tm alteration but mostly in chl rich • Vein in folded and has abundant asp around it with some corroded pyrite • Matrix and V2 and asp follow S1 but S1 folded about S2 • Euhedral asp in chl rich groundmass away from vein	• Chl- ser alteration • Tm halo at V2	• Medium subhedral and corroded asp in v2 • Euhedral asp in chl rich groundmass • Corroded py	• V2 folded at S2	• 45% Chlorite • 10% Tourmaline • 15% Arsenopyrite • 15% Carbonate • 10% Quartz • 5% mica

			• Thin cb stringers in chl rich regions • Micaceous groundmass but all ser, deformed				
Cp-156-07	OAX-17-156	V3A	• Edge of V3A vein with a bit of massive Tm alteration • Asp mostly within the ser rich wall rock • Tm stringers in groundmass along S1 • Asp aligned along S1 • Qz-cc v1 deformed aligned along S1 • Micaceous sample	• Ser-tm alteration	• Corroded asp closer to tm halo • Most of the asp is eu-sub in the ser rich wall rock	• Ms S1 crenulated by S2 •	• 40% quartz • 25% mica • 10% tourmaline • 15% carbonate • 5% chlorite • 5% arsenopyrite

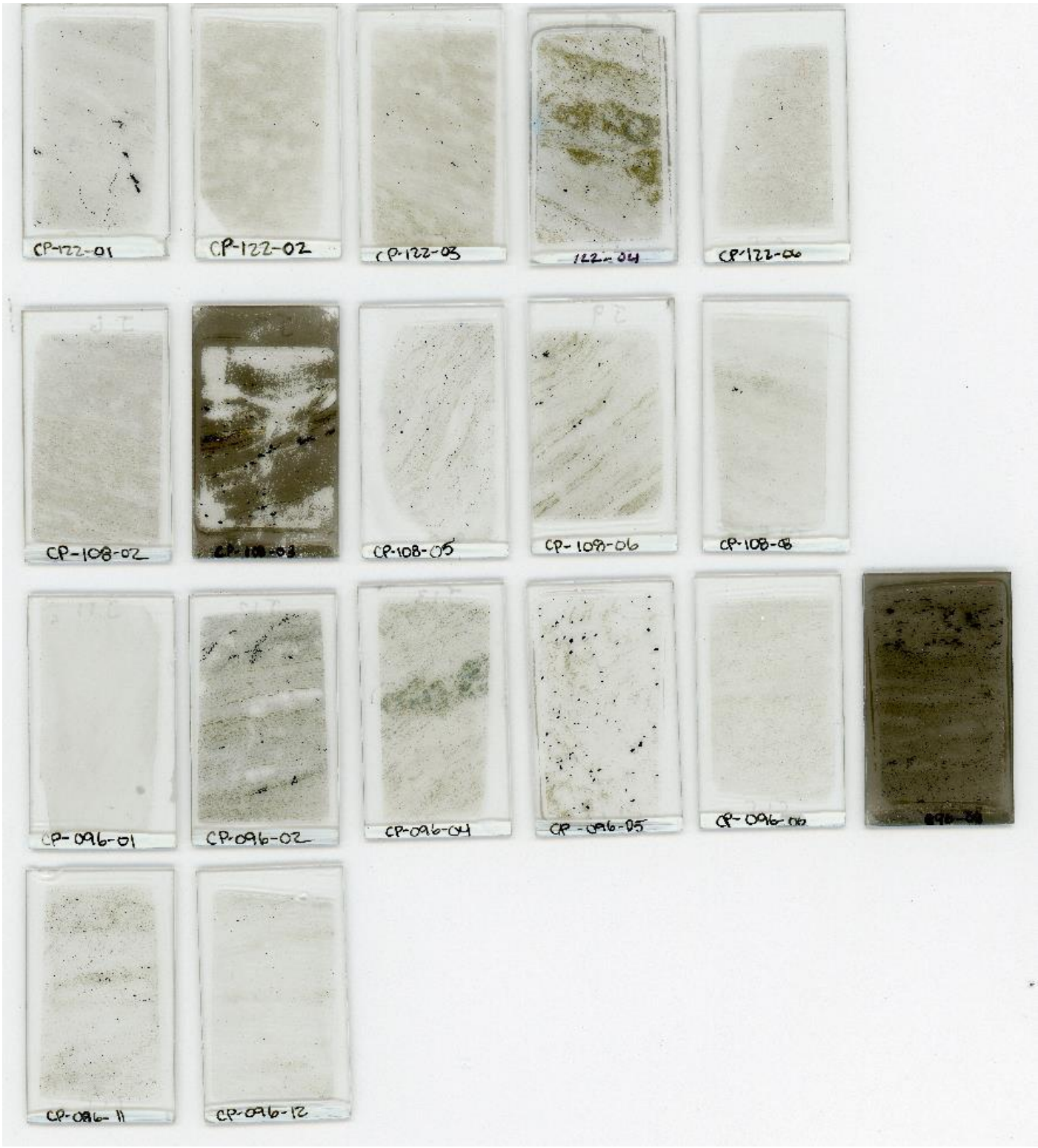
CP-122-01
CP-122-02
CP-122-03
122-04
CP-122-06
CP-108-02
CP-108-05
CP-108-06
CP-108-08
CP-096-01
CP-096-02
CP-096-04
CP-096-05
CP-096-11
CP-096-12

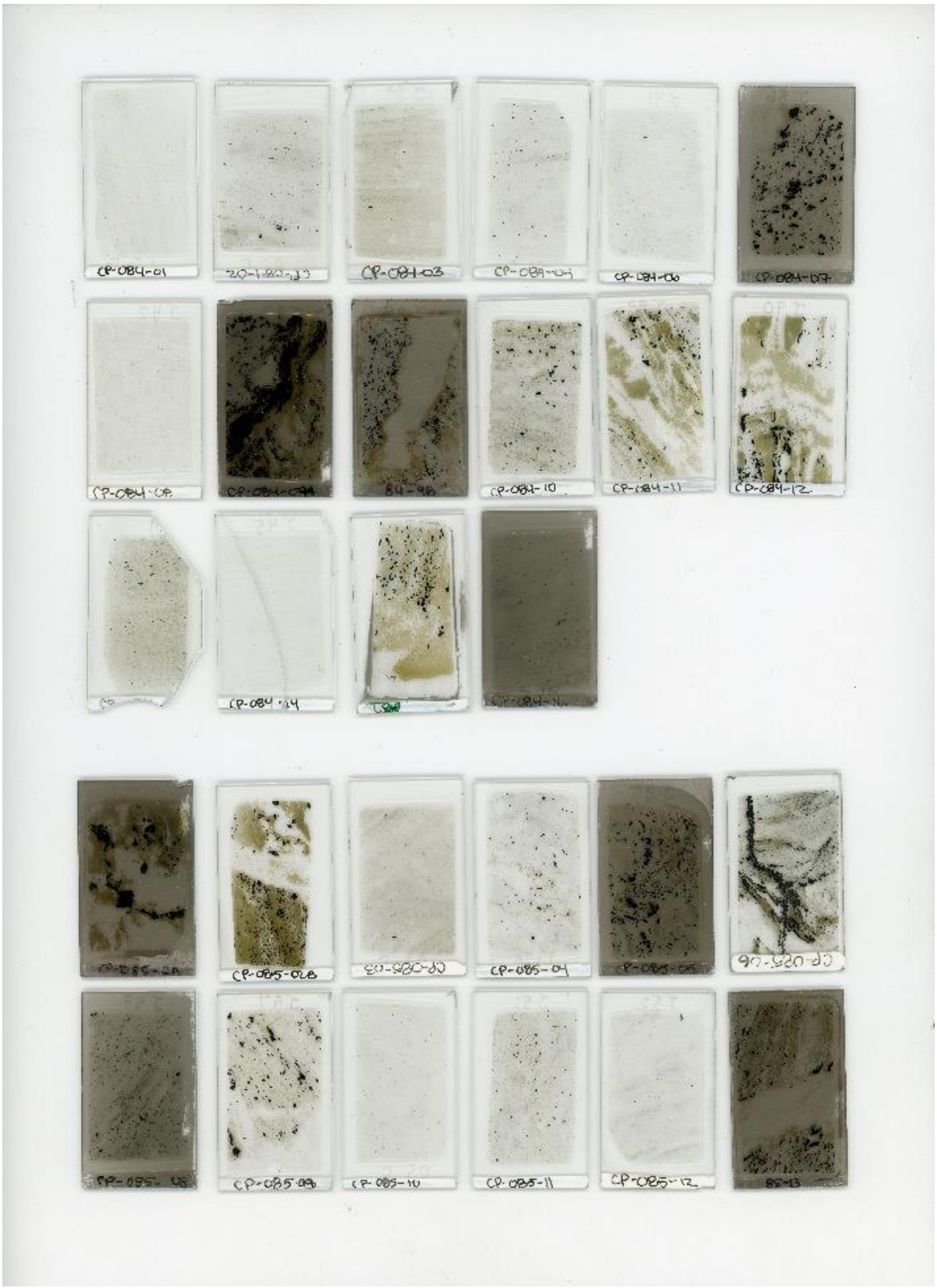
CP-084-01
CP-084-03
CP-084-06
CP-084-07
CP-084-10
CP-084-11
CP-084-12
CP-084-14
CP-085-02
CP-085-04
CP-085-10
CP-085-11
CP-085-12

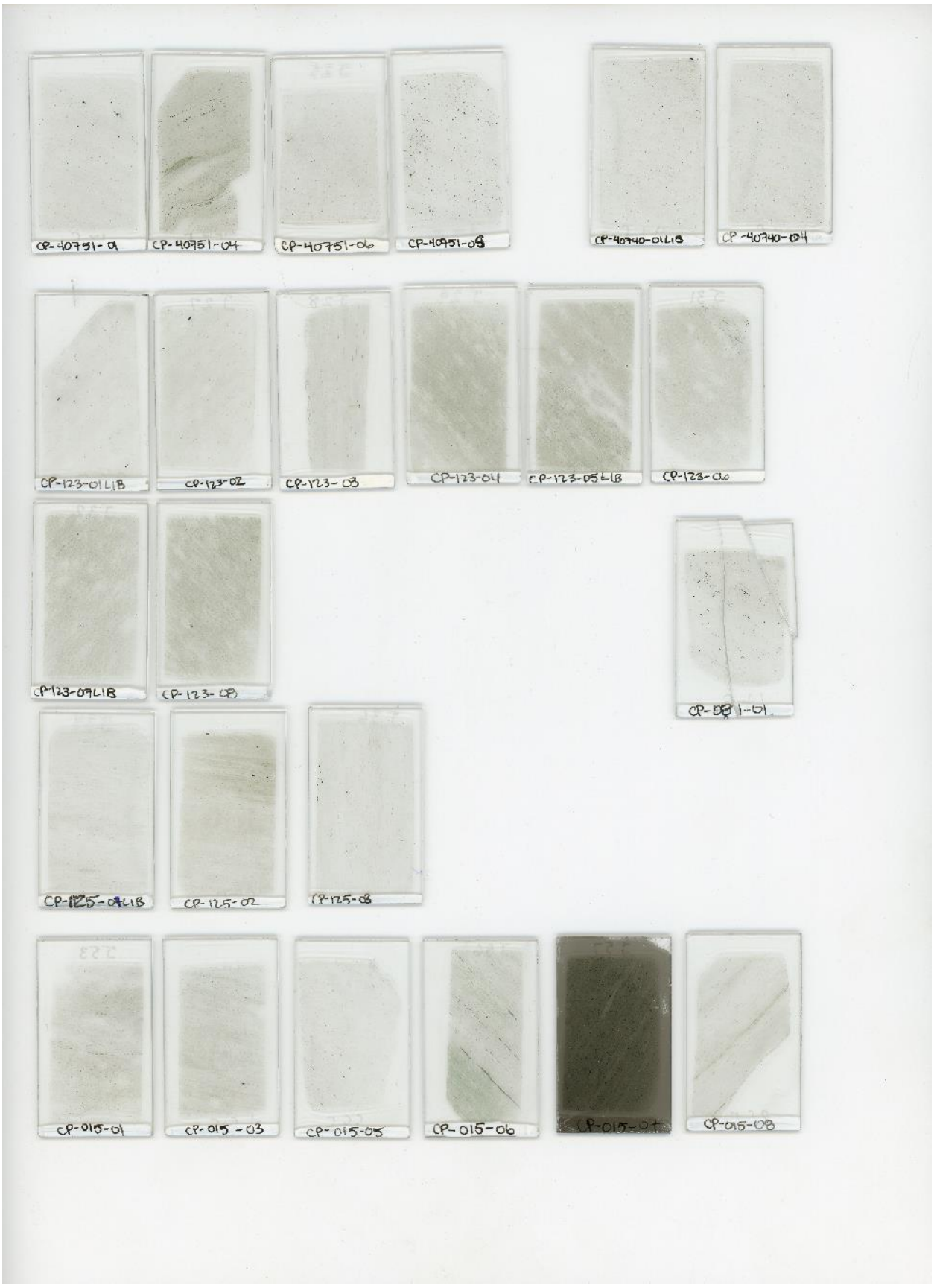
CP-40751-01
CP-40751-04
CP-40751-06
CP-40751-08
CP-40740-01LIB
CP-40740-04
CP-123-01LIB
CP-123-02
CP-123-03
CP-123-04
CP-123-05LIB
CP-123-06
CP-123-07LIB
CP-123-08
CP-125-01LIB
CP-125-02
CP-125-08
CP-015-01
CP-015-03
CP-015-05
CP-015-06
CP-015-07
CP-015-08

CP-156-01
156-02
CP-156-03
CP-156-04
CP-156-05
CP-156-06
CP-156-07
CP-5-24-01
CP-5-24-02
CP-5-26-02
CP-5-26-02
CP-40757-01
CP-40757-02
CP-075-01
CP-075-02
CP-075-03
CP-075-04
CP-075-05
CP-075-07A
CP-075-07B
CP-075-08
CP-075-09
CP-075-10
CP-075-11
CP-075-12
075-13
CP-075-14

Appendix C: Lithogeochemistry

Sample Number	DDH	Tag	Rock type	Altered/ Least Altered	Zone	Au ppb	Ag ppm	S wt.%	B ppm	As ppm	Al wt.%	Be ppm	Bi ppm	C wt.%	Ca wt.%	Cd ppm	Co ppm	Cr ppm	Cu ppm	Fe wt.%	Hg ppm	K ppm
cp-17-122-01	OAX-17-122	82981	QV	Altered	Z4	223.00	0.10	0.21	811	1295	1.24	0.25	1.00	0.80	2.45	0.25	9.00	4.00	47.00	2.33	0.50	0.12
cp-17-122-02	OAX-17-122	82982	FV	Altered	Z4	26.00	0.10	0.03	11	70	2.55	0.25	1.00	1.26	3.99	0.25	26.00	14.00	57.00	4.86	0.50	0.04
cp-17-122-03	OAX-17-122	82983	FV	Altered	Z4	670.00	0.10	0.05	132	359	3.40	0.25	1.00	1.26	4.06	0.25	29.00	14.00	75.00	6.45	1.00	0.05
cp-17-122-04	OAX-17-122	82784	FV	Altered	Z4	33.00	0.10	1.24	2030	3200	2.03	0.25	1.00	1.55	4.52	0.25	23.00	18.00	90.00	4.41	0.50	0.04
cp-17-122-06	OAX-17-122	82785	FV	Altered	Z4	13.00	0.10	0.26	49	45	2.88	0.25	1.00	1.04	3.10	0.25	27.00	40.00	92.00	5.35	1.00	0.02
cp-17-108-02	OAX-17-108	82774	FV	Altered	Z4	0.50	0.10	0.05	23	22	2.85	0.25	1.00	1.15	3.59	0.25	22.00	17.00	83.00	5.18	0.50	0.02
cp-17-108-03	OAX-17-108	82775	FV	Altered	Z4	9.00	0.10	0.15	459	1700	2.76	0.25	2.00	1.04	3.34	0.25	27.00	17.00	66.00	4.93	0.50	0.04
cp-17-108-06	OAX-17-108	82778	QV	Altered	Z4	966.00	0.10	0.46	1350	4340	0.66	0.25	1.00	1.35	2.70	0.25	11.00	5.00	34.00	2.55	0.50	0.11
cp-17-108-05	OAX-17-108	82777	QV	Altered	Z4	192.00	0.10	0.52	3360	1355	0.47	0.25	1.00	1.58	2.55	0.25	8.00	2.00	53.00	1.93	0.50	0.13
cp-17-108-08	OAX-17-108	82780	QV	Altered	Z4	27.00	0.10	0.01	100	28	2.06	0.25	1.00	0.77	2.30	0.25	14.00	22.00	61.00	2.91	0.50	0.09
cp-17-096-01	OAX-17-096	82989	QV	Altered	Z4	0.50	0.10	0.07	89	11	0.99	0.25	1.00	0.84	1.91	0.25	8.00	4.00	16.00	1.93	0.50	0.15
cp-17-096-02	OAX-17-096	82990	FV	Altered	Z4	49.00	0.10	1.00	1970	4590	1.11	0.25	1.00	2.25	5.04	0.25	20.00	6.00	83.00	4.09	0.50	0.08
cp-17-096-04	OAX-17-096	82993	FV	Altered	Z4	1.00	0.10	0.07	2100	108	2.94	0.25	1.00	1.49	4.51	0.25	35.00	140.00	74.00	4.82	1.00	0.01
cp-17-096-05	OAX-17-096	82790	QV	Altered	Z4	18.00	0.10	0.27	803	3730	0.55	0.25	1.00	0.72	1.46	0.25	10.00	2.00	22.00	1.55	0.50	0.16
cp-17-096-06	OAX-17-096	82997	QV	Altered	Z4	1.00	0.10	0.03	1340	23	0.39	0.25	1.00	0.93	1.94	0.25	3.00	3.00	2.00	1.01	0.50	0.16
cp-17-096-08	OAX-17-096	82791	FV	Altered	Z4	3640	0.30	3.12	291	10000	0.78	0.25	2.00	2.77	4.74	0.70	38.00	11.00	37.00	7.93	0.50	0.08
cp-17-096-11	OAX-17-096	82794	QV	Altered	Z4	549.00	0.10	0.52	1680	5830	0.84	0.25	1.00	0.77	2.53	0.25	6.00	3.00	24.00	2.19	0.50	0.09
cp-17-096-12	OAX-17-096	82796	QV	Altered	Z4	13.00	0.10	0.08	192	71	1.43	0.25	1.00	0.39	1.32	0.25	6.00	3.00	7.00	2.60	0.50	0.08
cp-17-084-01	OAX-17-084	82922	QV	Altered	Z4	0.50	0.10	0.01	158	17	1.18	0.25	1.00	0.79	2.58	0.25	7.00	2.00	11.00	1.56	0.50	0.14
cp-17-084-02	OAX-17-084	82921	QV	Altered	Z4	129.00	0.10	0.53	661	101	1.01	0.25	1.00	1.41	3.69	0.25	7.00	2.00	35.00	3.32	1.00	0.19
cp-17-084-03	OAX-17-084	82923	QV	Altered	Z4	5.00	0.20	0.07	149	61	3.70	0.25	1.00	1.03	2.67	0.25	59.00	227.00	172.00	7.36	1.00	0.09
cp-17-084-04	OAX-17-084	82924	QV	Altered	Z4	8.00	0.10	0.30	172	2	0.51	0.25	1.00	2.31	4.32	0.25	6.00	2.00	9.00	2.84	1.00	0.13
cp-17-084-06	OAX-17-084	82926	QV	Altered	Z4	0.50	0.10	0.02	195	22	0.31	0.25	1.00	1.65	2.91	0.70	6.00	2.00	3.00	1.81	0.50	0.13
cp-17-084-08	OAX-17-084	82928	QV	Altered	Z4	0.50	0.10	0.01	94	4	1.59	0.25	1.00	0.67	2.26	0.25	5.00	5.00	3.00	2.64	1.00	0.09
cp-17-084-10	OAX-17-084	82930	QV	Altered	Z4	27.00	0.10	0.53	94	6950	0.75	0.25	1.00	0.67	2.14	0.25	5.00	2.00	52.00	1.84	0.50	0.15
cp-17-084-14	OAX-17-084	82935	QV	Altered	Z4	1.00	0.10	0.01	67	7	0.47	0.25	1.00	1.98	3.39	0.25	1.00	1.00	1.00	2.04	0.50	0.12
cp-17-084-13	OAX-17-084	82934	FV	Altered	Z4	2.00	0.10	0.40	10	13	5.03	0.25	1.00	1.38	3.84	0.25	54.00	37.00	117.00	11.15	1.00	0.04
cp-17-084-16	OAX-17-084	82938	QV	Altered	Z4	13.00	0.10	0.38	180	48	1.27	0.25	1.00	1.33	3.20	0.25	8.00	2.00	7.00	3.30	0.50	0.12
cp-17-085-01	OAX-17-085	82940	QV	Altered	Z4	12.00	0.10	0.28	106	6	0.98	0.25	1.00	1.08	1.77	0.25	8.00	3.00	14.00	2.81	0.50	0.12

cp-17-085-01	OAX-17-085	82940	QV	Altered	Z4	12.00	0.10	0.28	106	6	0.98	0.25	1.00	1.08	1.77	0.25	8.00	3.00	14.00	2.81	0.50	0.12
cp-17-085-03	OAX-17-085	82942	FV	Altered	Z4	6.00	0.10	0.15	780	168	1.95	0.25	1.00	1.91	3.83	0.25	30.00	118.00	90.00	3.47	0.50	0.05
cp-17-085-04	OAX-17-085	82943	FV	Altered	Z4	326.00	0.10	0.54	1140	10000	0.19	0.25	1.00	1.49	3.77	0.25	25.00	14.00	36.00	1.55	0.50	0.06
cp-17-085-08	OAX-17-085	82948	QV	Altered	Z4	644.00	0.10	1.95	1670	7760	0.44	0.25	1.00	2.79	5.84	1.50	14.00	3.00	164.00	5.48	0.50	0.09
cp-17-085-10	OAX-17-085	82950	QV	Altered	Z4	22.00	0.10	0.02	99	68	0.27	0.25	1.00	2.30	4.11	0.25	9.00	2.00	2.00	2.00	0.50	0.16
cp-17-085-11	OAX-17-085	82758	QV	Altered	Z4	1120	0.10	0.32	912	8870	0.54	0.25	1.00	1.48	2.49	0.25	5.00	4.00	12.00	2.00	0.50	0.25
cp-17-085-12	OAX-17-085	82759	QV	Altered	Z4	0.50	0.10	0.07	155	28	0.99	0.25	1.00	0.51	1.57	0.25	12.00	4.00	13.00	1.47	0.50	0.12
cp-17-075-01	OAX-16-075	83776	FV	Altered	Z2	1.00	0.10	0.09	1530	126	1.98	0.25	1.00	1.86	5.19	0.25	33.00	121.00	82.00	3.22	0.50	0.06
cp-17-075-03	OAX-16-075	83778	FV	Altered	Z2	0.50	0.10	0.06	81	22	2.99	0.25	1.00	1.29	4.00	0.25	28.00	32.00	89.00	5.46	0.50	0.05
cp-17-075-04	OAX-16-075	83779	FV	Altered	Z2	0.50	0.10	0.10	369	25	2.82	0.25	1.00	1.02	3.09	0.25	27.00	32.00	93.00	5.10	0.50	0.01
cp-17-075-05	OAX-16-075	83780	FV	Altered	Z2	3.00	0.10	0.04	229	26	3.19	0.25	1.00	1.18	3.64	0.25	27.00	31.00	90.00	5.68	0.50	0.03
cp-17-075-07	OAX-16-075	83782	FV	Altered	Z2	1.00	0.10	0.03	120	31	3.16	0.25	1.00	0.17	0.84	0.25	28.00	25.00	152.00	5.29	0.50	0.01
cp-17-075-08	OAX-16-075	83783	FV	Altered	Z2	2.00	0.10	0.01	36	19	3.32	0.25	1.00	1.07	3.34	0.25	28.00	26.00	70.00	5.68	0.50	0.04
cp-17-075-10	OAX-16-075	83785	QV	Altered	Z4	4420	0.50	1.60	189	10000	0.93	0.25	1.00	1.60	3.46	0.25	24.00	7.00	37.00	4.71	0.50	0.10
cp-17-075-11	OAX-16-075	83786	FV	Altered	Z2	19.00	0.10	0.64	205	41	2.10	0.25	1.00	1.33	3.12	0.25	29.00	15.00	76.00	4.79	0.50	0.03
cp-17-075-12	OAX-16-075	83787	FV	Altered	Z2	2.00	0.10	0.02	49	15	2.29	0.25	1.00	1.35	4.17	0.25	21.00	15.00	93.00	3.81	0.50	0.03
cp-17-075-13	OAX-16-075	83788	QV	Altered	Z4	5860	0.60	0.74	459	10000	0.14	0.25	1.00	2.11	3.27	0.25	19.00	8.00	27.00	2.73	0.50	0.04
cp-17-015-01	OAX-07-015	82958	FV	Least altered	btw Z2-4	8.00	0.10	0.07	50	52	2.15	0.25	1.00	1.91	4.28	0.25	28.00	27.00	96.00	5.32	1.00	0.06
cp-17-015-05	OAX-07-015	82963	QV	Least altered	btw Z2-4	4.00	0.20	0.29	43	9	2.50	0.25	1.00	1.33	4.03	0.25	32.00	102.00	76.00	4.27	0.50	0.03
cp-17-015-06	OAX-07-015	82965	QV	Least altered	btw Z2-4	1.00	0.20	0.01	68	2	1.92	0.25	1.00	1.64	4.76	0.25	6.00	6.00	4.00	2.79	0.50	0.08
cp-17-015-08	OAX-07-015	82968	QV	Least altered	btw Z2-4	0.50	0.20	0.47	81	7	2.02	0.25	1.00	0.50	1.72	0.25	20.00	5.00	30.00	3.20	0.50	0.05
cp-17-123-02	OAX-17-123	82798	QV	Least altered	btw Z2-4	0.50	0.10	0.02	56	1	1.38	0.25	1.00	0.87	2.59	0.25	7.00	4.00	5.00	1.90	0.50	0.08
cp-17-123-04	OAX-17-123	83762	FV	Least altered	btw Z2-4	4.00	0.10	0.05	44	11	2.79	0.25	1.00	0.87	2.95	0.25	28.00	28.00	94.00	4.76	0.50	0.02
cp-17-123-06	OAX-17-123	83764	FV	Least altered	btw Z2-4	2.00	0.10	0.02	55	3	2.61	0.25	1.00	0.95	3.08	0.25	23.00	24.00	73.00	4.60	0.50	0.04
cp-17-123-08	OAX-17-123	83765	FV	Least altered	btw Z2-4	1.00	0.10	0.01	23	8	2.76	0.25	3.00	0.69	2.45	0.25	25.00	23.00	78.00	4.63	0.50	0.02
cp-17-125-01	OAX-17-125	83766	QV	Least altered	btw Z2-4	10.00	0.10	0.01	46	2	1.44	0.25	1.00	0.78	2.63	0.25	7.00	3.00	43.00	2.01	0.50	0.08
cp-17-125-02	OAX-17-125	83767	QV	Least altered	btw Z2-4	1.00	0.10	0.01	48	1	1.92	0.25	1.00	1.06	3.27	0.25	12.00	43.00	29.00	2.56	0.50	0.08
cp-17-125-03	OAX-17-125	83768	QV	Least altered	btw Z2-4	0.50	0.10	0.13	49	1	1.45	0.25	1.00	1.04	3.20	0.25	7.00	3.00	0.50	2.09	0.50	0.08

Mg wt. %	Mn ppm	Mo ppm	Na wt. %	Ni ppm	P ppm	Pb ppm	Sb ppm	Sc ppm	Ti wt. %	Tl ppm	Zn ppm	Ba ppm	Ce ppm	Cs ppm	Dy ppm	Er ppm	Eu ppm	Ga ppm	Gd ppm	Hf ppm	Ho ppm	La ppm	Lu ppm	Nb ppm	Nd ppm
0.71	416	1.00	0.03	17	360	2.00	1.00	1.00	0.01	5.00	31	347	16.90	1.50	0.83	0.50	0.48	17.30	1.19	2.00	0.18	7.70	0.08	2.30	8.20
1.06	1065	0.50	0.05	32	340	1.00	1.00	11.00	0.03	5.00	70	106	11.70	0.71	1.90	1.23	0.65	15.80	1.98	1.60	0.38	5.00	0.19	2.30	6.30
1.42	1440	0.50	0.04	32	350	1.00	1.00	11.00	0.04	5.00	83	111.5	14.30	1.50	2.40	1.48	0.71	18.90	2.16	1.90	0.50	6.20	0.21	2.40	8.10
1.29	830	0.50	0.04	29	360	1.00	2.00	7.00	0.01	5.00	44	184.5	15.80	0.61	2.38	1.49	0.84	21.60	2.38	1.80	0.48	7.10	0.21	2.10	9.00
1.67	765	0.50	0.04	37	470	1.00	1.00	16.00	0.01	5.00	64	86.4	12.90	0.44	2.17	1.34	0.62	19.30	1.77	1.80	0.42	5.70	0.20	2.30	7.40
1.43	770	0.50	0.05	23	430	1.00	1.00	12.00	0.01	5.00	72	180	15.80	0.37	2.13	1.41	0.68	17.90	2.22	1.70	0.44	7.10	0.18	2.00	8.60
1.40	783	0.50	0.05	30	380	1.00	1.00	8.00	0.01	5.00	68	235	12.50	0.76	2.03	1.37	0.68	19.40	1.98	1.80	0.41	5.40	0.22	2.20	7.10
0.83	679	1.00	0.03	24	400	4.00	2.00	1.00	0.01	5.00	30	297	17.60	1.81	1.18	0.55	0.49	18.00	1.26	2.00	0.22	7.80	0.07	2.70	9.40
0.60	669	0.50	0.04	13	340	1.00	1.00	1.00	0.01	5.00	34	256	19.20	1.21	1.08	0.53	0.57	17.70	1.34	2.10	0.19	8.60	0.08	2.70	10.00
1.27	441	0.50	0.03	26	410	1.00	1.00	3.00	0.01	5.00	69	170.5	13.80	1.89	0.98	0.52	0.47	16.40	1.14	1.50	0.19	6.30	0.08	1.30	7.60
0.81	375	1.00	0.02	13	350	1.00	1.00	0.50	0.01	5.00	47	284	21.80	2.70	1.13	0.55	0.45	19.70	1.49	2.40	0.23	9.70	0.09	3.90	10.40
1.20	1085	0.50	0.03	24	320	2.00	1.00	4.00	0.01	5.00	35	257	8.90	0.82	1.46	0.86	0.58	16.00	1.43	1.10	0.31	4.00	0.13	1.60	5.40
2.13	1025	1.00	0.03	82	930	1.00	2.00	17.00	0.01	5.00	74	38.8	20.10	0.24	2.45	1.46	0.81	17.90	2.52	2.30	0.52	8.30	0.23	6.00	11.30
0.55	423	1.00	0.02	14	470	2.00	1.00	0.50	0.01	5.00	18	518	20.70	2.33	1.54	0.80	0.57	20.60	1.78	2.70	0.26	8.90	0.11	3.20	11.00
0.50	417	0.50	0.02	3	440	1.00	1.00	0.50	0.01	5.00	11	324	17.90	1.98	0.73	0.37	0.49	19.70	1.09	2.40	0.13	7.80	0.06	3.00	9.20
1.69	1375	0.50	0.02	30	450	3.00	56.00	7.00	0.01	5.00	32	309	19.60	0.92	6.49	4.11	1.23	14.80	5.50	3.00	1.41	7.50	0.57	5.50	14.40
0.40	503	0.50	0.04	7	480	2.00	1.00	0.50	0.01	5.00	41	350	22.20	0.92	1.03	0.58	0.70	19.90	1.47	3.00	0.19	9.40	0.07	3.00	11.30
0.59	459	0.50	0.04	7	460	1.00	1.00	1.00	0.01	5.00	53	318	21.10	0.83	1.09	0.48	0.65	19.70	1.53	2.70	0.19	9.00	0.06	2.80	11.00
0.70	391	0.50	0.03	8	480	2.00	1.00	0.50	0.01	5.00	41	427	21.00	1.03	1.06	0.49	0.52	22.00	1.23	3.10	0.18	9.20	0.08	3.40	10.90
1.04	1175	0.50	0.04	27	310	3.00	1.00	1.00	0.01	5.00	76	399	18.50	1.79	0.94	0.45	0.56	18.30	1.26	2.60	0.16	8.40	0.07	3.10	9.60
1.92	1080	0.50	0.02	160	300	3.00	1.00	11.00	0.01	5.00	119	530	11.10	1.23	3.14	1.93	0.68	20.80	2.76	2.30	0.68	4.70	0.29	4.80	7.60
1.23	1515	0.50	0.02	16	330	2.00	1.00	1.00	0.01	5.00	36	383	16.90	2.41	0.97	0.46	0.46	17.00	1.10	2.20	0.15	7.50	0.06	2.60	8.50
0.93	641	1.00	0.03	11	390	1.00	2.00	1.00	0.01	5.00	153	296	18.30	1.59	1.20	0.58	0.56	17.80	1.37	2.50	0.25	8.20	0.10	3.50	9.70
0.63	337	0.50	0.04	7	430	2.00	1.00	1.00	0.01	5.00	37	369	21.60	1.05	1.07	0.53	0.62	22.80	1.46	2.50	0.19	9.30	0.08	3.30	11.60
0.36	395	0.50	0.02	6	420	1.00	1.00	0.50	0.01	5.00	17	331	20.20	1.06	0.81	0.38	0.53	20.70	1.24	2.70	0.16	8.90	0.05	3.00	10.60
1.25	799	1.00	0.02	6	90	2.00	1.00	1.00	0.01	5.00	29	245	34.80	3.09	3.23	1.96	0.57	16.50	3.09	3.00	0.69	16.80	0.29	10.30	14.80
1.96	1315	1.00	0.01	56	660	2.00	1.00	26.00	0.01	5.00	155	88.5	23.70	1.12	8.24	5.31	1.50	22.70	6.80	4.00	1.78	8.70	0.82	7.40	17.60
0.91	907	0.50	0.02	33	400	2.00	1.00	1.00	0.01	5.00	81	338	17.90	1.67	0.92	0.47	0.50	18.00	1.16	2.30	0.17	7.90	0.07	3.10	8.70

1.12	748	0.50	0.04	13	320	2.00	1.00	1.00	0.01	5.00	66	412	18.60	1.68	0.98	0.55	0.58	17.40	1.10	2.20	0.19	8.20	0.09	2.80	9.50
1.65	689	0.50	0.06	93	260	1.00	1.00	9.00	0.01	5.00	70	94.7	11.30	0.30	1.60	1.01	0.53	16.30	1.58	1.20	0.37	5.00	0.14	1.60	6.10
0.47	551	0.50	0.08	142	240	3.00	4.00	3.00	0.01	5.00	76	105.5	8.20	0.48	1.27	0.58	0.41	10.00	1.08	1.10	0.23	3.50	0.08	1.40	4.50
1.22	2450	1.00	0.03	52	310	4.00	3.00	2.00	0.01	5.00	313	373	16.10	0.80	1.49	0.89	0.57	14.50	1.61	2.10	0.34	7.20	0.12	2.20	8.20
1.38	809	0.50	0.03	14	400	2.00	1.00	1.00	0.01	5.00	26	290	15.50	1.49	1.02	0.49	0.52	17.40	1.25	2.30	0.22	6.80	0.08	2.90	8.20
0.67	741	0.50	0.04	7	390	3.00	2.00	1.00	0.01	5.00	21	504	18.60	1.81	0.84	0.51	0.57	17.70	1.31	2.40	0.17	8.20	0.06	3.10	9.30
0.51	320	0.50	0.05	21	300	3.00	1.00	0.50	0.01	5.00	67	332	18.80	2.23	0.69	0.33	0.40	20.10	0.99	2.20	0.13	8.50	0.05	2.10	8.90
1.51	803	0.50	0.04	125	200	2.00	3.00	6.00	0.01	5.00	47	150.5	12.40	0.43	1.20	0.73	0.50	13.50	1.27	0.80	0.27	5.20	0.10	4.30	6.30
1.58	770	0.50	0.04	34	370	1.00	2.00	10.00	0.01	5.00	76	191.5	10.90	0.98	1.86	1.07	0.60	18.40	1.82	1.40	0.40	4.70	0.17	1.80	6.30
1.68	734	0.50	0.04	27	400	1.00	2.00	22.00	0.03	5.00	69	16.7	12.10	0.06	1.98	1.26	0.86	18.20	2.09	1.60	0.40	5.10	0.17	2.40	7.10
1.69	860	0.50	0.04	34	380	1.00	1.00	13.00	0.01	5.00	85	228	12.30	0.68	2.18	1.30	0.86	19.60	2.14	1.50	0.44	5.20	0.18	1.90	7.40
1.84	730	0.50	0.04	36	330	1.00	1.00	6.00	0.17	5.00	86	129	14.20	0.47	2.17	1.19	0.74	19.40	2.18	1.80	0.50	6.40	0.18	1.80	7.90
1.85	778	0.50	0.04	39	460	1.00	1.00	12.00	0.01	5.00	84	254	13.60	0.81	2.20	1.40	0.94	17.50	2.39	1.80	0.44	6.20	0.19	2.20	8.20
0.91	980	0.50	0.04	46	540	4.00	23.00	4.00	0.01	5.00	36	287	21.10	1.31	3.31	2.13	0.85	17.60	2.92	2.90	0.70	9.30	0.26	3.70	11.60
1.48	650	1.00	0.06	33	450	4.00	2.00	11.00	0.01	5.00	46	156	14.90	1.30	2.43	1.52	0.73	17.40	2.41	1.90	0.49	6.60	0.21	2.30	8.30
1.27	705	0.50	0.06	28	510	1.00	3.00	10.00	0.01	5.00	68	105	16.00	1.92	2.45	1.55	0.63	18.10	2.35	1.90	0.52	7.10	0.22	2.40	9.00
1.32	670	1.00	0.05	72	200	4.00	15.00	4.00	0.01	5.00	12	193.5	51.00	0.94	2.06	1.19	1.05	10.50	2.81	3.20	0.41	24.70	0.15	4.50	21.90
1.60	961	0.50	0.05	37	420	1.00	3.00	10.00	0.01	5.00	76	225	11.40	2.52	1.98	1.15	0.68	18.80	1.97	1.40	0.41	5.10	0.18	2.10	7.00
0.03	836	0.50	0.06	67	310	1.00	1.00	15.00	0.01	5.00	80	163	14.00	1.91	1.95	1.19	0.55	17.50	1.95	1.70	0.41	6.20	0.19	2.30	7.40
0.08	916	0.50	0.05	10	370	1.00	1.00	3.00	0.01	5.00	46	254	17.10	3.64	1.20	0.56	0.62	18.80	1.39	3.40	0.22	7.40	0.10	3.10	9.20
0.05	469	0.50	0.04	12	480	2.00	1.00	1.00	0.01	5.00	87	170.5	19.90	4.82	1.06	0.50	0.62	21.40	1.52	2.70	0.19	8.50	0.08	3.60	11.00
0.86	319	0.50	0.06	15	460	2.00	1.00	1.00	0.01	5.00	46	278	18.10	3.52	1.00	0.51	0.53	21.40	1.28	3.00	0.18	7.80	0.07	3.70	9.70
1.52	755	0.50	0.05	39	400	1.00	2.00	8.00	0.14	5.00	76	132.5	14.40	0.85	2.34	1.44	0.70	18.20	2.37	1.70	0.48	6.30	0.22	2.80	8.40
1.32	731	0.50	0.05	30	330	1.00	2.00	8.00	0.09	5.00	79	279	14.50	2.80	1.92	1.27	0.65	20.00	1.77	1.60	0.39	6.60	0.17	2.00	7.70
1.43	653	0.50	0.05	28	350	1.00	1.00	5.00	0.14	5.00	75	81.8	13.50	1.06	2.01	1.18	0.66	19.60	2.02	1.50	0.40	6.00	0.18	1.80	7.70
0.91	373	0.50	0.03	13	440	1.00	1.00	1.00	0.01	5.00	43	422	22.10	2.96	0.98	0.50	0.58	20.60	1.43	2.80	0.18	9.60	0.06	3.10	11.50
1.25	456	0.50	0.04	27	420	1.00	1.00	3.00	0.01	5.00	51	345	20.40	2.50	1.19	0.68	0.70	19.60	1.56	2.10	0.23	9.10	0.08	2.80	11.00
0.92	353	0.50	0.05	6	460	1.00	1.00	1.00	0.01	5.00	54	293	17.60	3.26	1.01	0.54	0.52	18.90	1.39	2.90	0.19	7.50	0.08	2.70	9.00

Pr ppm	Rb ppm	Sm ppm	Sn ppm	Sr ppm	Ta ppm	Tb ppm	Th ppm	Tm ppm	U ppm	V ppm	W ppm	Y ppm	Yb ppm	Zr ppm
2.07	43.70	1.57	0.50	117.5	0.20	0.15	0.82	0.07	0.36	48	5.00	4.40	0.46	68
1.55	20.30	1.54	1.00	227	0.10	0.32	0.91	0.18	0.24	183	1.00	10.90	1.30	56
1.86	23.70	2.20	1.00	248	0.20	0.37	0.75	0.22	0.26	189	6.00	12.60	1.40	64
2.09	20.40	2.24	1.00	225	0.20	0.35	0.92	0.21	0.26	214	10.00	12.90	1.19	64
1.73	8.30	1.78	0.50	211	0.20	0.30	1.07	0.21	0.32	208	3.00	11.10	1.25	68
2.05	10.40	2.28	1.00	261	0.20	0.34	1.10	0.18	0.30	181	1.00	11.70	1.25	63
1.71	21.40	1.82	1.00	262	0.20	0.29	0.97	0.18	0.30	201	3.00	10.90	1.37	66
2.29	49.20	1.76	1.00	148.5	0.20	0.18	0.96	0.08	0.39	70	4.00	5.90	0.53	74
2.48	34.80	1.94	1.00	197	0.20	0.20	0.98	0.08	0.43	47	9.00	5.60	0.51	77
1.81	40.60	1.54	0.50	95.8	0.20	0.16	0.73	0.06	0.35	99	2.00	4.90	0.44	54
2.66	59.70	1.94	1.00	133.5	0.40	0.21	1.36	0.08	0.59	44	2.00	6.30	0.57	85
1.23	28.50	1.44	1.00	238	0.10	0.22	0.40	0.13	0.14	152	9.00	7.60	0.86	39
2.73	2.30	2.62	1.00	410	0.30	0.39	0.55	0.23	0.17	179	2.00	13.70	1.47	99
2.74	75.70	2.21	1.00	143	0.30	0.21	1.13	0.11	0.50	49	5.00	7.30	0.72	98
2.27	71.60	1.69	0.50	115	0.20	0.12	0.89	0.05	0.37	32	10.00	3.50	0.34	89
2.97	30.10	4.32	1.00	148	0.40	0.96	0.87	0.62	0.25	333	20.00	36.20	3.92	109
2.92	28.90	2.28	1.00	288	0.30	0.21	1.15	0.07	0.39	51	7.00	5.20	0.54	107
2.77	34.20	2.28	1.00	258	0.20	0.22	1.07	0.06	0.34	41	1.00	5.00	0.50	93
2.66	52.50	2.11	1.00	129	0.20	0.18	1.11	0.07	0.51	44	1.00	5.10	0.48	111
2.30	54.50	1.84	1.00	127.5	0.20	0.15	1.00	0.07	0.41	34	2.00	4.70	0.43	96
1.63	50.10	2.22	1.00	137.5	0.30	0.49	0.55	0.29	0.21	359	4.00	17.50	1.98	77
2.12	59.20	1.72	1.00	127.5	0.20	0.14	0.91	0.07	0.38	29	1.00	4.40	0.43	78
2.39	47.40	1.87	0.50	119	0.20	0.24	1.01	0.10	0.40	42	1.00	6.60	0.58	92
2.78	39.10	1.97	1.00	280	0.20	0.18	1.07	0.07	0.56	47	1.00	5.20	0.46	89
2.60	54.10	2.04	1.00	136	0.20	0.15	1.02	0.06	0.83	44	6.00	4.10	0.36	95
4.06	48.80	3.18	2.00	114	1.20	0.52	4.72	0.30	2.03	8	1.00	19.70	1.89	76
3.48	15.60	5.24	1.00	96.2	0.50	1.20	1.05	0.81	0.32	486	1.00	44.90	5.21	139
2.26	50.80	1.58	1.00	115	0.20	0.16	0.96	0.07	0.43	32	1.00	4.80	0.51	87

2.27	39.00	1.82	0.50	136.5	0.20	0.18	1.00	0.07	0.39	34	2.00	4.90	0.46	78
1.41	10.90	1.41	1.00	194.5	0.10	0.23	1.02	0.15	0.26	152	5.00	8.70	0.89	42
1.07	11.10	1.30	1.00	204	0.10	0.19	0.75	0.09	0.37	80	11.00	5.40	0.53	38
2.07	27.10	1.77	1.00	156	0.20	0.25	0.81	0.14	0.56	61	6.00	8.90	0.80	73
1.97	45.80	1.53	1.00	135.5	0.20	0.16	0.80	0.09	0.36	46	10.00	5.90	0.46	82
2.27	48.90	1.82	1.00	139.5	0.20	0.19	1.10	0.07	0.40	39	3.00	5.00	0.48	84
2.32	55.70	1.47	1.00	186.5	0.20	0.14	1.16	0.04	0.57	39	2.00	3.50	0.36	72
1.59	28.70	1.37	0.50	224	0.10	0.19	0.76	0.09	0.15	171	2.00	6.20	0.63	26
1.45	29.80	1.69	1.00	205	0.20	0.30	0.64	0.15	0.19	193	5.00	10.10	1.07	50
1.68	0.70	1.80	1.00	267	0.20	0.31	0.90	0.17	0.52	218	1.00	11.00	1.16	59
1.70	22.40	2.06	0.50	282	0.20	0.34	0.71	0.23	0.18	224	1.00	11.40	1.13	55
1.91	4.00	2.06	0.50	293	0.20	0.35	1.15	0.20	0.36	198	1.00	12.40	1.31	62
1.91	22.90	2.09	1.00	198.5	0.20	0.36	1.05	0.19	0.33	188	1.00	11.40	1.24	64
2.80	41.50	2.66	1.00	218	0.30	0.49	1.20	0.29	0.41	157	14.00	19.30	1.95	103
2.01	14.10	2.07	1.00	164	0.20	0.36	1.01	0.19	0.30	195	3.00	13.70	1.47	69
2.09	17.00	2.05	1.00	235	0.20	0.39	1.19	0.20	0.32	186	3.00	13.70	1.48	71
6.01	15.70	4.08	0.50	386	0.40	0.35	5.44	0.17	1.61	70	12.00	11.00	0.93	121
1.60	31.30	1.86	2.00	311	0.10	0.30	0.69	0.18	0.23	202	7.00	10.90	1.22	54
1.83	13.40	2.00	1.00	231	0.10	0.32	0.98	0.19	0.32	119	1.00	10.80	1.12	62
2.20	18.80	1.74	1.00	229	0.20	0.20	0.90	0.09	0.42	54	2.00	6.20	0.60	128
2.59	25.00	2.06	1.00	152.5	0.30	0.19	1.05	0.07	0.38	44	2.00	5.20	0.40	89
2.36	36.60	1.92	1.00	239	0.20	0.16	1.19	0.08	0.47	43	1.00	5.00	0.47	110
1.94	8.50	2.24	0.50	321	0.20	0.35	0.94	0.21	0.29	209	1.00	12.50	1.46	65
1.82	28.00	1.74	1.00	375	0.20	0.27	1.17	0.19	0.37	188	2.00	10.50	1.21	60
1.86	7.50	1.92	1.00	363	0.20	0.32	0.94	0.18	0.29	189	1.00	11.10	1.17	54
2.87	45.40	2.12	1.00	191	0.30	0.21	1.15	0.07	0.57	41	1.00	4.90	0.51	98
2.67	36.40	2.08	1.00	184.5	0.30	0.19	1.00	0.09	0.51	67	1.00	6.10	0.60	80
2.33	39.00	1.74	0.50	185.5	0.30	0.19	1.02	0.07	0.45	43	0.50	5.30	0.46	106

SiO_2 wt. %	Al_2O_3 wt. %	Fe_2O_3 wt. %	CaO wt. %	MgO wt. %	Na_2O wt. %	K_2O wt. %	Cr_2O_3 wt. %	TiO_2 wt. %	MnO wt. %	P_2O_5 wt. %	SrO wt. %	BaO wt. %	LOI wt. %
64.60	15.45	3.71	3.58	1.50	3.46	2.14	0.01	0.34	0.05	0.08	0.01	0.04	4.28
53.70	17.85	7.04	6.42	1.86	5.27	0.69	0.01	0.68	0.14	0.10	0.03	0.01	6.25
48.00	18.45	9.20	6.72	2.46	4.41	0.86	0.01	0.75	0.19	0.09	0.02	0.01	6.88
49.70	18.65	7.65	7.11	2.89	5.50	0.72	0.01	0.79	0.12	0.08	0.02	0.02	7.36
54.00	18.10	8.40	5.25	3.07	6.07	0.24	0.01	0.90	0.11	0.11	0.03	0.01	5.52
54.50	17.50	7.60	5.57	2.49	5.47	0.40	0.01	0.80	0.11	0.09	0.03	0.02	6.03
52.60	19.60	7.31	5.57	2.53	4.91	1.00	0.01	0.79	0.11	0.07	0.03	0.03	5.67
62.90	15.50	4.45	4.18	1.85	3.28	2.26	0.01	0.41	0.09	0.09	0.02	0.03	5.63
59.90	15.40	4.07	5.02	1.92	3.60	1.71	0.01	0.35	0.11	0.08	0.02	0.03	6.38
63.80	15.95	4.51	3.37	2.30	0.96	2.37	0.01	0.55	0.06	0.08	0.01	0.02	5.26
65.10	16.15	3.08	2.79	1.58	1.74	3.46	0.01	0.37	0.05	0.08	0.01	0.03	4.81
51.90	14.85	6.70	7.44	2.53	3.66	1.33	0.01	0.64	0.14	0.07	0.03	0.03	8.93
48.30	17.25	7.78	7.25	4.16	5.34	0.11	0.03	0.94	0.14	0.24	0.04	0.01	7.48
66.50	16.70	2.97	2.21	1.46	2.06	3.74	0.01	0.38	0.06	0.10	0.01	0.06	3.90
67.20	16.15	2.34	2.88	1.43	1.04	3.89	0.01	0.35	0.06	0.10	0.01	0.04	5.03
42.90	11.85	13.30	7.75	3.18	3.26	1.44	0.01	1.42	0.20	0.10	0.01	0.04	10.65
64.70	16.65	3.90	4.35	1.20	3.73	1.59	0.01	0.39	0.07	0.10	0.03	0.04	3.59
67.60	16.45	4.01	4.02	1.10	2.47	1.60	0.01	0.37	0.06	0.11	0.03	0.04	2.59
66.00	15.80	2.46	3.63	1.42	1.71	3.11	0.01	0.36	0.05	0.10	0.02	0.05	4.63
62.30	14.30	4.50	4.34	1.76	1.96	2.74	0.01	0.30	0.13	0.09	0.02	0.05	5.75
53.80	16.00	10.85	3.93	3.41	1.02	2.13	0.07	1.23	0.15	0.07	0.02	0.06	6.45
59.40	14.05	4.51	6.16	2.15	1.71	3.01	0.01	0.27	0.19	0.07	0.01	0.04	8.72
63.60	13.75	2.95	4.06	1.73	3.14	2.45	0.01	0.38	0.08	0.09	0.01	0.03	6.69
65.70	16.45	3.98	4.35	1.19	2.39	1.92	0.01	0.37	0.04	0.10	0.03	0.04	4.31
66.40	15.85	3.69	3.11	1.43	1.54	2.89	0.01	0.35	0.05	0.09	0.01	0.04	4.03
68.50	10.90	3.21	4.95	2.27	0.74	2.51	0.01	0.04	0.11	0.03	0.01	0.03	8.13
45.70	14.45	16.65	6.11	3.45	1.22	0.81	0.01	1.83	0.19	0.15	0.01	0.01	7.73
63.10	14.10	5.02	4.59	1.72	2.00	2.53	0.01	0.30	0.12	0.10	0.01	0.04	5.53

64.70	14.70	4.42	3.98	2.63	2.11	4.60	1.70	0.01	0.30	0.10	0.08	0.02	0.05	4.40
48.80	16.35	6.61	5.95	7.92	3.39	5.47	0.50	0.03	0.54	0.10	0.05	0.02	0.01	8.70
57.20	15.85	2.47	2.22	5.31	1.01	7.29	0.53	0.03	0.46	0.07	0.05	0.02	0.01	4.99
51.50	11.05	8.46	7.61	8.58	2.37	2.85	1.26	0.01	0.28	0.32	0.07	0.01	0.04	10.20
60.20	13.10	3.06	2.75	5.80	2.38	3.05	2.43	0.01	0.31	0.10	0.08	0.01	0.03	9.05
63.60	15.70	3.82	3.44	5.00	1.87	2.27	2.96	0.01	0.33	0.11	0.07	0.01	0.06	6.12
69.50	16.75	2.47	2.22	2.54	1.11	3.33	2.45	0.01	0.26	0.04	0.06	0.01	0.03	3.37
50.20	17.80	5.14	4.63	7.62	2.89	4.61	1.33	0.03	0.54	0.11	0.05	0.02	0.02	8.35
51.60	18.55	7.95	7.15	5.97	2.70	5.23	0.98	0.01	0.80	0.10	0.08	0.02	0.02	6.75
53.40	17.75	7.61	6.85	4.87	2.95	6.70	0.03	0.01	0.86	0.10	0.08	0.03	0.01	5.33
52.20	18.40	8.60	7.74	6.03	3.04	4.90	0.68	0.01	0.87	0.12	0.08	0.03	0.02	6.51
55.40	20.30	8.75	7.87	4.64	3.24	5.49	0.12	0.01	0.82	0.11	0.07	0.03	0.01	2.96
51.70	18.10	8.34	7.50	5.39	3.20	4.66	0.77	0.01	0.87	0.11	0.09	0.02	0.03	6.32
55.70	14.90	7.06	6.35	5.02	1.67	4.33	1.65	0.01	0.77	0.13	0.10	0.02	0.03	6.62
51.80	18.15	6.91	6.22	4.61	2.49	6.87	0.41	0.01	0.84	0.08	0.09	0.02	0.02	5.89
55.00	17.60	5.69	5.12	6.24	2.22	5.72	0.48	0.01	0.84	0.09	0.11	0.02	0.01	6.60
58.60	13.35	4.18	3.76	4.80	2.39	6.43	0.58	0.02	0.48	0.09	0.05	0.04	0.02	6.97
49.70	16.55	7.47	6.72	6.58	2.63	5.24	0.84	0.01	0.79	0.12	0.09	0.03	0.02	8.19
52.30	17.85	6.02	5.42	6.80	2.91	5.88	0.38	0.02	0.47	0.11	0.07	0.02	0.02	6.27
59.60	14.75	4.44	4.00	7.81	2.77	3.20	0.98	0.01	0.35	0.12	0.08	0.03	0.03	7.73
64.50	16.15	4.71	4.24	3.51	2.08	2.15	1.26	0.01	0.39	0.06	0.10	0.01	0.02	3.94
65.60	16.10	3.02	2.72	3.88	1.60	2.06	1.77	0.01	0.40	0.04	0.11	0.03	0.03	5.40
50.80	18.90	7.52	6.77	6.52	2.63	5.35	0.29	0.01	0.85	0.11	0.10	0.03	0.02	5.26
51.90	20.10	7.00	6.30	5.85	2.33	5.74	0.71	0.01	0.71	0.10	0.07	0.04	0.03	5.40
51.90	19.75	7.39	6.65	6.53	2.42	5.54	0.19	0.01	0.72	0.10	0.08	0.04	0.01	4.42
67.00	16.35	2.98	2.68	3.65	1.57	2.20	2.32	0.01	0.39	0.05	0.10	0.02	0.05	4.76
62.10	15.85	4.12	3.71	4.89	2.31	2.09	1.95	0.01	0.42	0.06	0.11	0.02	0.04	6.21
65.10	15.35	3.37	3.03	4.61	1.71	1.73	1.91	0.01	0.37	0.05	0.10	0.02	0.03	5.78

GER diagram

Sample number	Rock type	Au ppb	Na mol	K mol	Al mol	(Na+K)/ Al molar	Na/Al molar
cp-17-122-01	QV	223.0	0.112	0.045	0.303	0.518	0.368
cp-17-122-02	FV	26.0	0.170	0.015	0.350	0.528	0.486
cp-17-122-03	FV	670.0	0.142	0.018	0.362	0.444	0.393
cp-17-122-04	FV	33.0	0.177	0.015	0.366	0.527	0.485
cp-17-122-06	FV	13.0	0.196	0.005	0.355	0.566	0.552
cp-17-108-02	FV	0.5	0.177	0.008	0.343	0.539	0.514
cp-17-108-03	FV	9.0	0.158	0.021	0.384	0.467	0.412
cp-17-108-05	QV	192.0	0.116	0.036	0.302	0.505	0.385
cp-17-108-06	QV	966.0	0.106	0.048	0.304	0.506	0.348
cp-17-108-08	QV	27.0	0.031	0.050	0.313	0.260	0.099
cp-17-096-01	QV	0.5	0.056	0.073	0.317	0.409	0.177
cp-17-096-02	FV	49.0	0.118	0.028	0.291	0.502	0.405
cp-17-096-04	FV	1.0	0.172	0.002	0.338	0.516	0.509
cp-17-096-05	QV	18.0	0.066	0.079	0.328	0.445	0.203
cp-17-096-06	QV	1.0	0.034	0.083	0.317	0.367	0.106
cp-17-096-08	FV	3640.0	0.105	0.031	0.232	0.584	0.453
cp-17-096-11	QV	549.0	0.120	0.034	0.327	0.472	0.369
cp-17-096-12	QV	13.0	0.080	0.034	0.323	0.352	0.247
cp-17-084-01	QV	0.5	0.055	0.066	0.310	0.391	0.178
cp-17-084-02	QV	129.0	0.063	0.058	0.281	0.433	0.225
cp-17-084-03	QV	5.0	0.033	0.045	0.314	0.249	0.105
cp-17-084-04	QV	8.0	0.055	0.064	0.276	0.432	0.200
cp-17-084-06	QV	0.5	0.101	0.052	0.270	0.569	0.376
cp-17-084-08	QV	0.5	0.077	0.041	0.323	0.365	0.239
cp-17-084-10	QV	27.0	0.050	0.061	0.311	0.357	0.160
cp-17-084-13	QV	2.0	0.039	0.017	0.283	0.200	0.139
cp-17-084-14	FV	1.0	0.024	0.053	0.214	0.361	0.112
cp-17-084-16	QV	13.0	0.065	0.054	0.277	0.428	0.233

cp-17-085-01	QV	12.0	0.148	0.036	0.288	0.640	0.515
cp-17-085-03	FV	6.0	0.177	0.011	0.321	0.583	0.550
cp-17-085-04	FV	326.0	0.235	0.011	0.311	0.793	0.757
cp-17-085-08	QV	644.0	0.092	0.027	0.217	0.548	0.424
cp-17-085-10	QV	22.0	0.098	0.052	0.257	0.584	0.383
cp-17-085-11	QV	1120.0	0.073	0.063	0.308	0.442	0.238
cp-17-085-12	QV	0.5	0.107	0.052	0.329	0.485	0.327
cp-17-075-01	FV	1.0	0.149	0.028	0.349	0.507	0.426
cp-17-075-03	FV	0.5	0.169	0.021	0.364	0.521	0.464
cp-17-075-04	FV	0.5	0.216	0.001	0.348	0.623	0.621
cp-17-075-05	FV	3.0	0.158	0.014	0.361	0.478	0.438
cp-17-075-07	FV	1.0	0.177	0.003	0.398	0.451	0.445
cp-17-075-08	FV	2.0	0.150	0.016	0.355	0.470	0.424
cp-17-075-10	QV	4420.0	0.140	0.035	0.292	0.598	0.478
cp-17-075-11	FV	19.0	0.222	0.009	0.356	0.647	0.623
cp-17-075-12	FV	2.0	0.185	0.010	0.345	0.564	0.535
cp-17-075-13	QV	5860.0	0.207	0.012	0.262	0.839	0.792
cp-17-015-01	FV	8.0	0.169	0.018	0.325	0.576	0.521
cp-17-015-05	QV	4.0	0.190	0.008	0.350	0.565	0.542
cp-17-015-06	QV	1.0	0.103	0.021	0.289	0.429	0.357
cp-17-015-08	QV	0.5	0.069	0.027	0.317	0.303	0.219
cp-17-123-02	QV	0.5	0.066	0.038	0.316	0.329	0.210
cp-17-123-04	FV	4.0	0.173	0.006	0.371	0.482	0.466
cp-17-123-06	FV	2.0	0.185	0.015	0.394	0.508	0.470
cp-17-123-08	FV	1.0	0.179	0.004	0.387	0.472	0.461
cp-17-125-01	QV	10.0	0.071	0.049	0.321	0.375	0.221
cp-17-125-02	QV	1.0	0.067	0.041	0.311	0.350	0.217
cp-17-125-03	QV	0.5	0.056	0.041	0.301	0.320	0.185

Appendix D: Mass Balance

FV Least-Altered Samples, Precursor for Mass Balance Calculations															
Sample	Rock Type	Zr ppm	Al_2O_3 wt. %	Na_2O wt. %	K_2O wt. %	SiO_2 wt. %	CaO wt. %	MgO wt. %	FeO wt. %	TiO_2 wt. %	LOI wt. %	B ppm	Au ppb	As ppm	S ppm
cp-17-015-01	FV	54.00	16.55	5.24	0.84	49.70	6.58	2.63	6.72	0.79	8.19	105.00	0.50	10.00	100.00
cp-17-123-04	FV	65.00	18.90	5.35	0.29	50.80	6.52	2.63	6.77	0.85	5.26	44.00	0.50	10.00	100.00
cp-17-123-06	FV	60.00	20.10	5.74	0.71	51.90	5.85	2.33	6.30	0.71	5.40	170.00	0.50	10.00	100.00
cp-17-123-08	FV	54.00	19.75	5.54	0.19	51.90	6.53	2.42	6.65	0.72	4.42	23.00	0.50	10.00	100.00
Average: Precursor		58.25	18.83	7.35	0.51	51.08	6.37	2.50	6.61	0.77	5.82	85.50	0.50	10.00	100.00

Sample	Tag number	Na_2O (%)			K_2O (%)			SiO_2 (%)			CaO (%)			MgO (%)			FeO (%)		
		RC	MC	Δ	RC	MC	Δ	RC	MC	Δ	RC	MC	Δ	RC	MC	Δ	RC	MC	Δ
cp-17-075-03	83778	6.09	0.63	11.44	1.14	0.63	124.97	60.11	9.04	17.70	6.96	0.59	9.18	3.15	0.64	25.69	8.33	1.72	26.10
cp-17-075-04	83779	6.61	1.15	20.98	0.03	-0.48	94.16	52.72	1.65	3.22	4.81	-1.56	24.52	2.91	0.41	16.38	6.76	0.15	2.29
cp-17-075-05	83780	5.19	-0.28	5.08	0.72	0.21	41.91	55.28	4.21	8.24	6.39	0.02	0.26	3.22	0.72	28.66	8.20	1.59	24.01
cp-17-075-07B	83782	5.16	-0.31	5.66	0.11	-0.39	77.78	52.05	0.97	1.91	4.36	-2.01	31.56	3.04	0.54	21.64	7.40	0.79	11.92
cp-17-075-08	83783	4.24	-1.23	22.43	0.70	0.19	38.09	47.06	-4.02	7.87	4.91	-1.46	22.99	2.91	0.41	16.38	6.83	0.22	3.35
cp-17-075-11	83786	5.80	0.33	6.08	0.35	-0.16	31.80	43.73	-7.35	14.38	3.89	-2.48	38.90	2.10	-0.40	16.00	5.25	-1.36	20.58
cp-17-075-12	83787	4.69	-0.77	14.17	0.39	-0.11	22.40	45.12	-5.95	11.65	5.12	-1.25	19.63	1.82	-0.68	27.22	4.20	-2.41	36.44
cp-17-084-03	82923	0.77	-4.70	85.89	1.61	1.10	217.50	40.70	-10.38	20.31	2.97	-3.40	53.33	2.58	0.08	3.08	7.39	0.78	11.75
cp-17-085-03	82942	7.59	2.12	38.75	0.69	0.19	36.64	67.68	16.61	32.51	10.98	4.61	72.44	4.70	2.20	87.88	8.25	1.64	24.81
cp-17-085-04	82943	11.17	5.71	104.39	0.81	0.30	60.09	87.68	36.61	71.67	8.14	1.77	27.78	1.55	-0.95	38.13	3.41	-3.20	48.45
cp-17-096-02	82990	5.47	0.00	0.02	1.99	1.48	291.42	77.52	26.44	51.77	11.11	4.74	74.45	3.78	1.28	51.00	9.00	2.40	36.24
cp-17-108-02	82774	5.06	-0.41	7.50	0.37	-0.14	27.12	50.39	-0.68	1.34	5.15	-1.22	19.15	2.30	-0.20	8.00	6.32	-0.29	4.33
cp-17-108-03	82775	4.33	-1.13	20.74	0.88	0.38	73.91	46.42	-4.65	9.11	4.92	-1.45	22.83	2.23	-0.27	10.77	5.81	-0.80	12.16
cp-17-108-08	82780	1.04	-4.43	81.06	2.56	2.05	403.75	68.82	17.75	34.75	3.64	-2.73	42.93	2.48	-0.02	0.86	4.38	-2.23	33.77
cp-17-122-02	82982	5.48	0.01	0.26	0.72	0.21	41.42	55.86	4.78	9.36	6.68	0.31	4.83	1.93	-0.57	22.69	6.59	-0.02	0.30
cp-17-122-03	82983	4.01	-1.45	26.59	0.78	0.28	54.23	43.69	-7.39	14.46	6.12	-0.25	3.98	2.24	-0.26	10.53	7.53	0.93	14.00
cp-17-122-04	82784	5.01	-0.46	8.44	0.66	0.15	29.13	45.23	-5.84	11.43	6.47	0.10	1.59	2.63	0.13	5.11	6.27	-0.34	5.20
cp-17-122-06	82785	5.20	-0.27	4.90	0.21	-0.30	59.49	46.26	-4.82	9.43	4.50	-1.87	29.40	2.63	0.13	5.09	6.47	-0.13	2.03

Al_2O_3 (%)			LOI (%)			Au (ppb)			As (ppm)			S ppm)			B (%)		
RC	MC	Δ	RC	MC	Δ	RC	MC	Δ	RC	MC	Δ	RC	MC	Δ	RC	MC	Δ
21.61	2.79	14.80	7.86	2.05	35.17	0.58	0.08	16.50	25.63	15.63	156.30	699	599	599	94.37	8.87	10.37
17.52	-1.30	6.91	5.26	-0.56	9.54	0.49	-0.01	1.27	24.68	14.68	146.82	987	887	887	364	279	326
19.49	0.66	3.52	6.89	1.08	18.52	3.18	2.68	535	27.54	17.54	175.36	424	324	324	243	157	184
19.07	0.25	1.31	2.78	-3.04	52.20	0.94	0.44	87.90	29.13	19.13	191.25	282	182	182	113	27.24	31.86
16.47	-2.35	12.49	5.75	-0.07	1.12	1.82	1.32	264	17.29	7.29	72.93	45.51	-54.49	54.49	32.77	-52.73	61.68
15.32	-3.50	18.61	4.97	-0.85	14.53	16.04	15.54	3108	34.61	24.61	246.12	5403	5303	5303	173	87.56	102.41
14.44	-4.39	23.30	5.41	-0.40	6.92	1.64	1.14	228	12.31	2.31	23.06	164.08	64.08	64.08	40.20	-45.30	52.98
12.10	-6.72	35.70	4.88	-0.94	16.13	3.78	3.28	656	46.15	36.15	361.46	529.55	429.55	429.55	112.72	27.22	31.83
22.68	3.85	20.46	12.07	6.25	107.41	8.32	7.82	1564	233	223	2230	2080	1980	1980	1082	996	1165
24.30	5.47	29.06	7.65	1.83	31.49	499.72	499	99845	15329	15319	153189	8278	8178	8178	1748	1662	1944
22.18	3.35	17.82	13.34	7.52	129.27	73.19	72.69	14537	6856	6846	68456	14936	14836	14836	2942	2857	3341
16.18	-2.64	14.05	5.58	-0.24	4.16	0.46	-0.04	7.54	20.34	10.34	103.41	462.30	362.30	362.30	21.27	-64.23	75.13
17.30	-1.53	8.11	5.00	-0.81	13.98	7.94	7.44	1489	1500	1490	14904	1324	1224	1224	405	320	374
17.21	-1.62	8.60	5.67	-0.14	2.47	29.13	28.63	5725	30.20	20.20	202.04	107.87	7.87	7.87	108	22.37	26.16
18.57	-0.26	1.37	6.50	0.68	11.75	27.04	26.54	5309	72.81	62.81	628.13	312.05	212.05	212.05	11.44	-74.06	86.62
16.79	-2.03	10.80	6.26	0.44	7.64	610	609	121861	327	317	3167	455	355	355	120	34.64	40.52
16.97	-1.85	9.83	6.70	0.88	15.15	30.04	29.54	5907	2913	2903	29025	11286	11186	11186	1848	1762	2061
15.50	-3.32	17.64	4.73	-1.09	18.72	11.14	10.64	2127	38.55	28.55	285.48	2227	2127	2127	41.97	-43.53	50.91

APPENDIX E: EMPA

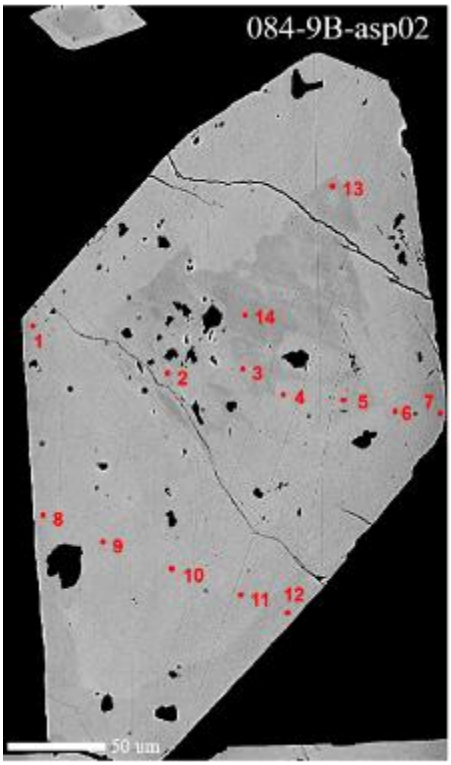

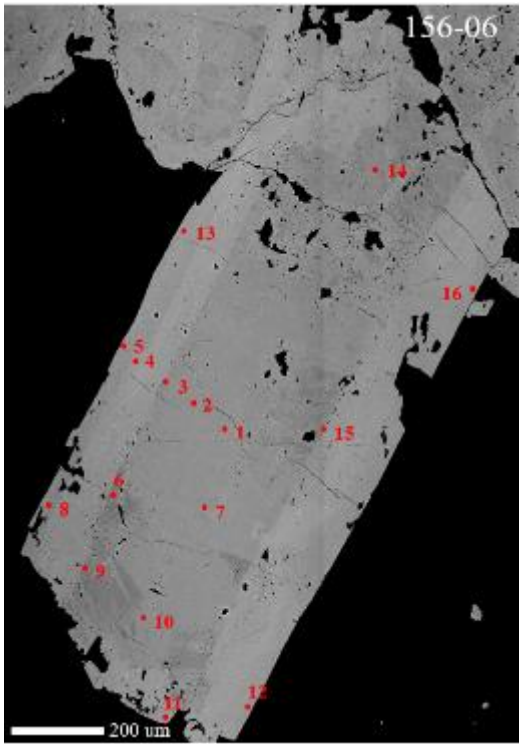

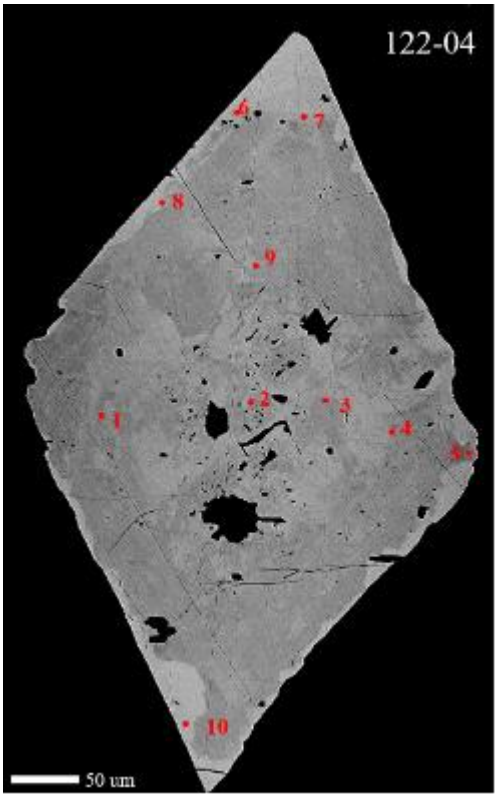

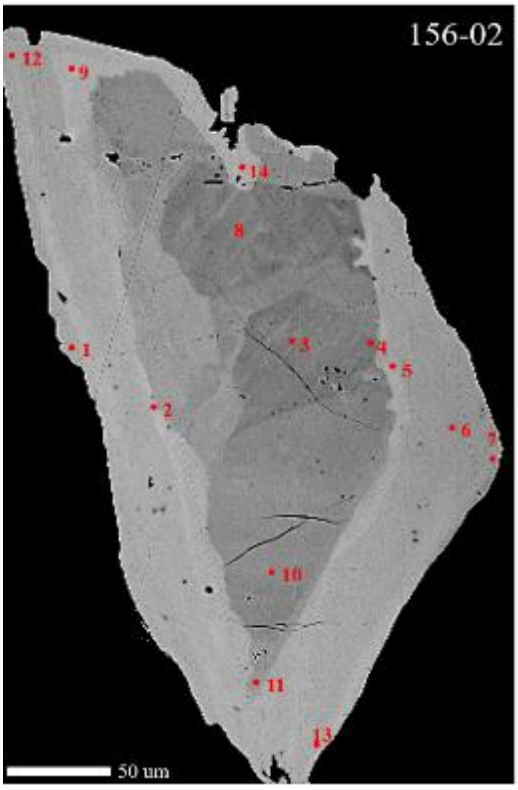

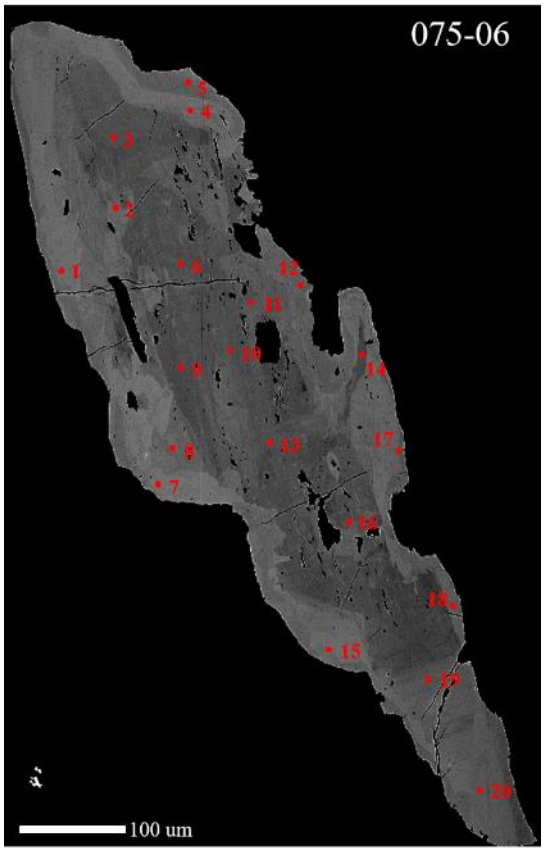
075-06
100 um

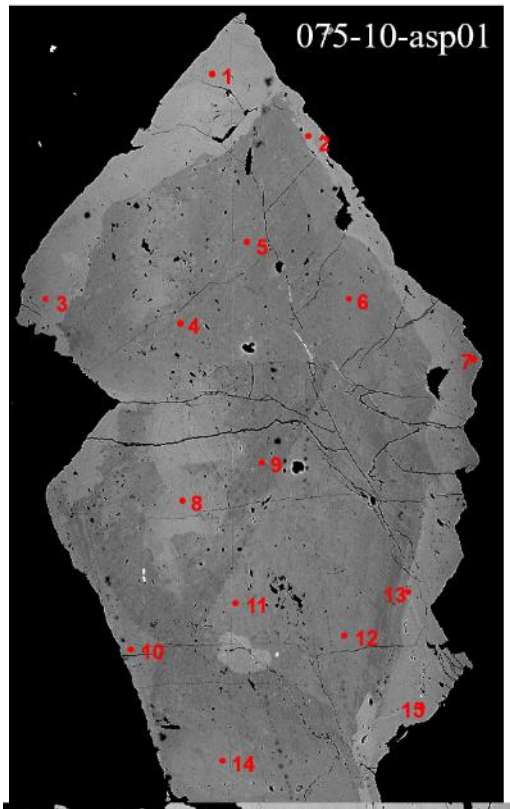
075-10-asp01

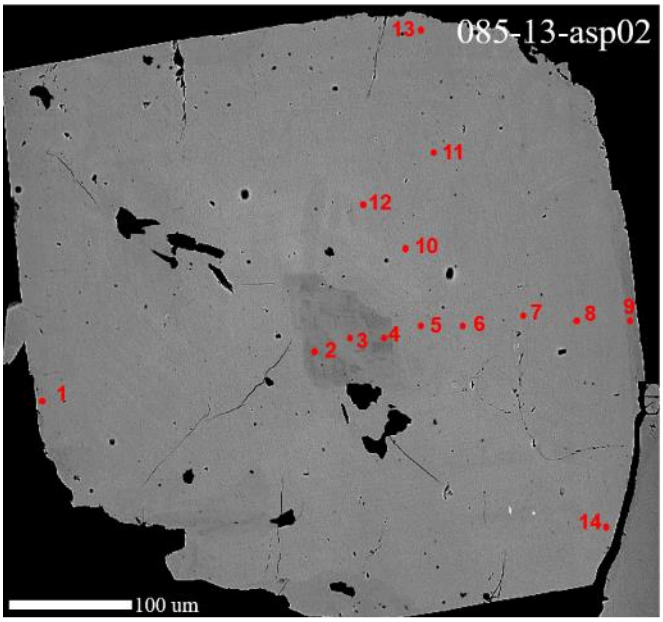
085-13-asp02
100 um

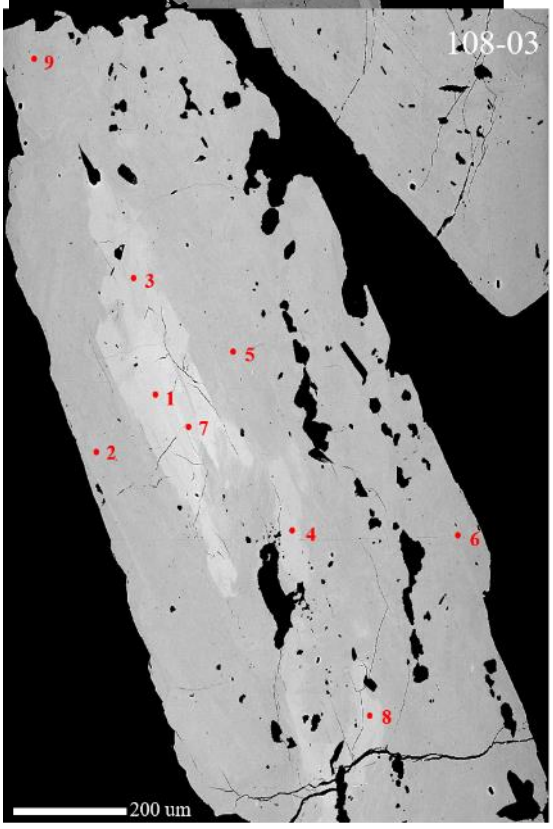
108-03
200 um

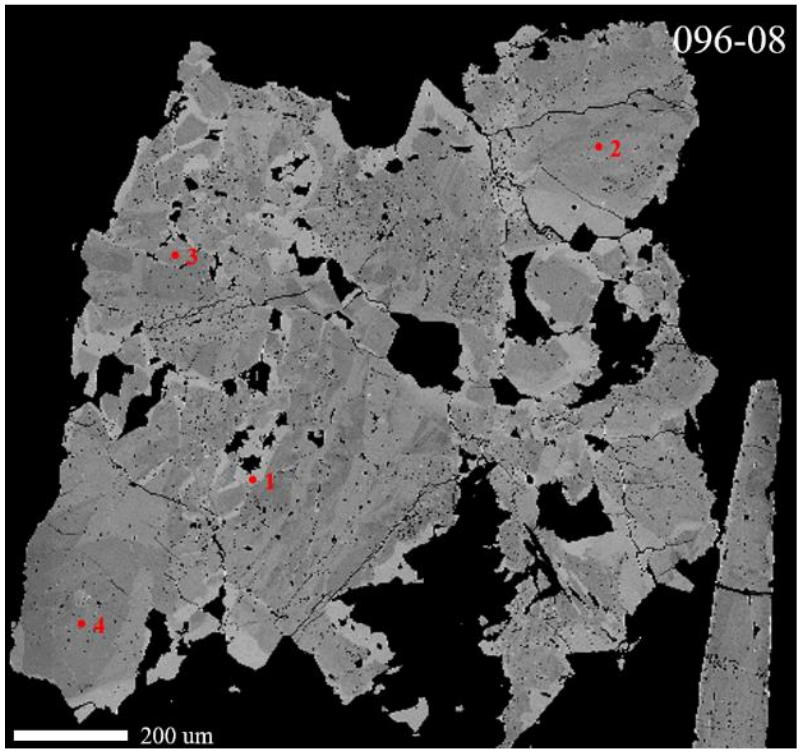
096-08
1
2
3
4
200 um

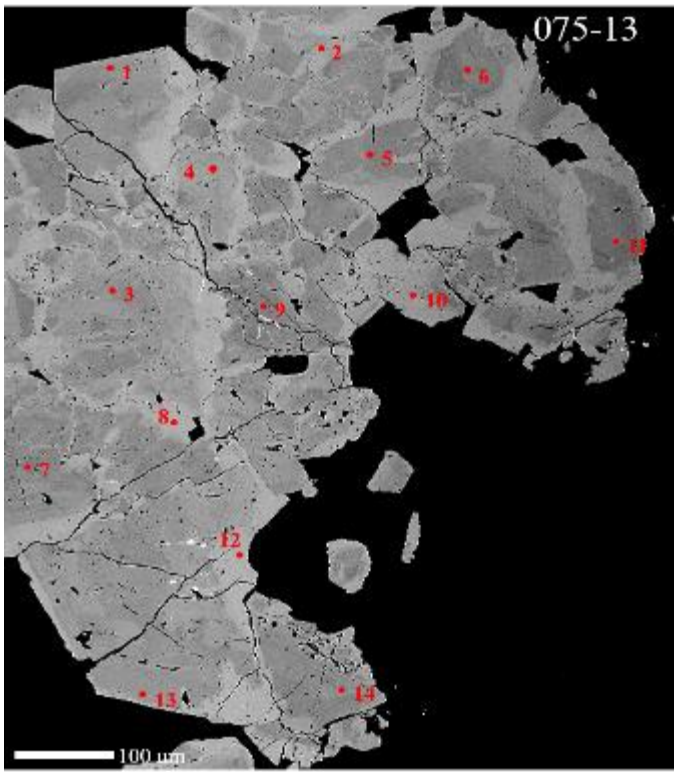
075-13
1
2
3
4
5
6
7
8
9
10
11
12
13
14
100 um

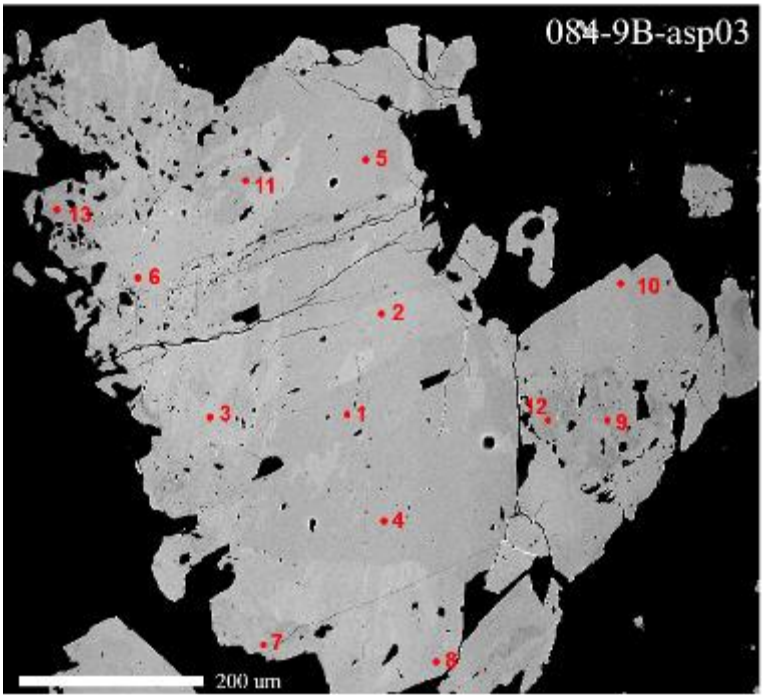
084-9B-asp03
1
2
3
4
5
6
7
8
9
10
11
12
13
200 um

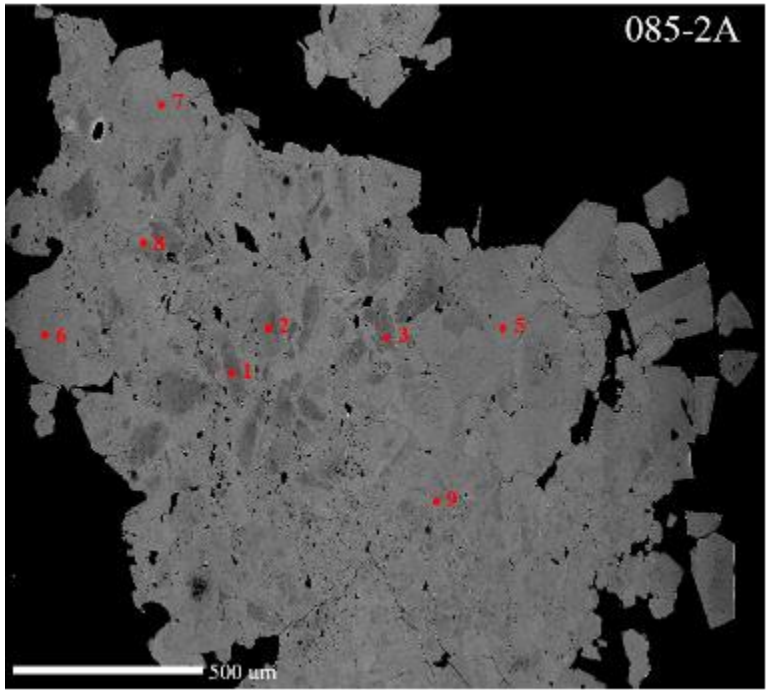
085-2A
1
2
3
4
5
6
7
8
9
500 um

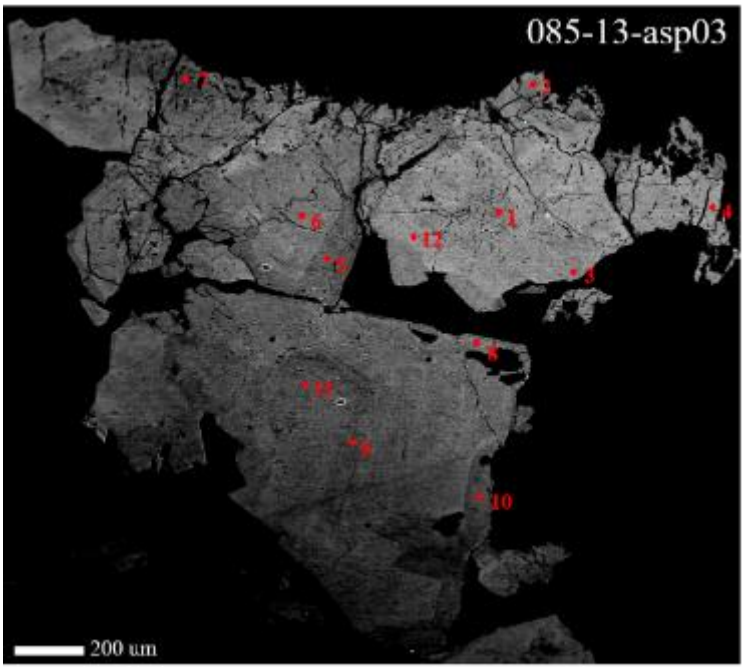
085-13-asp03
200 um

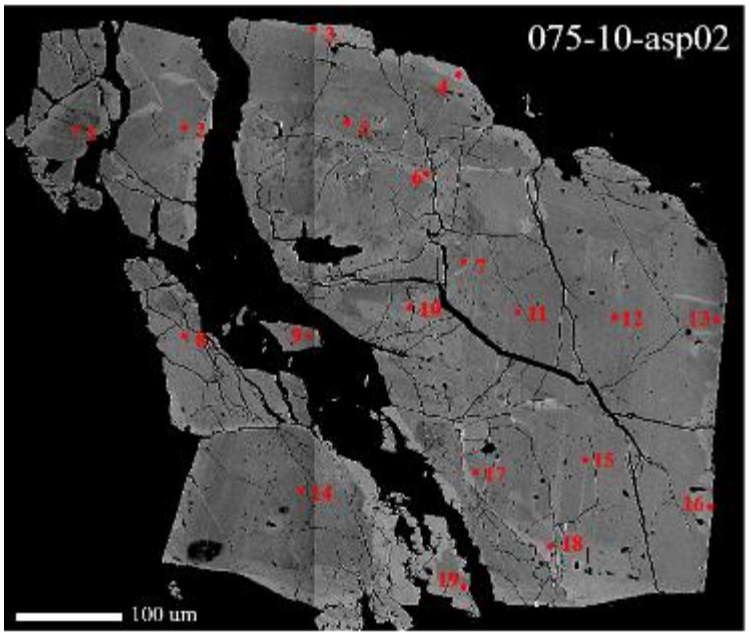
075-10-asp02
100 um

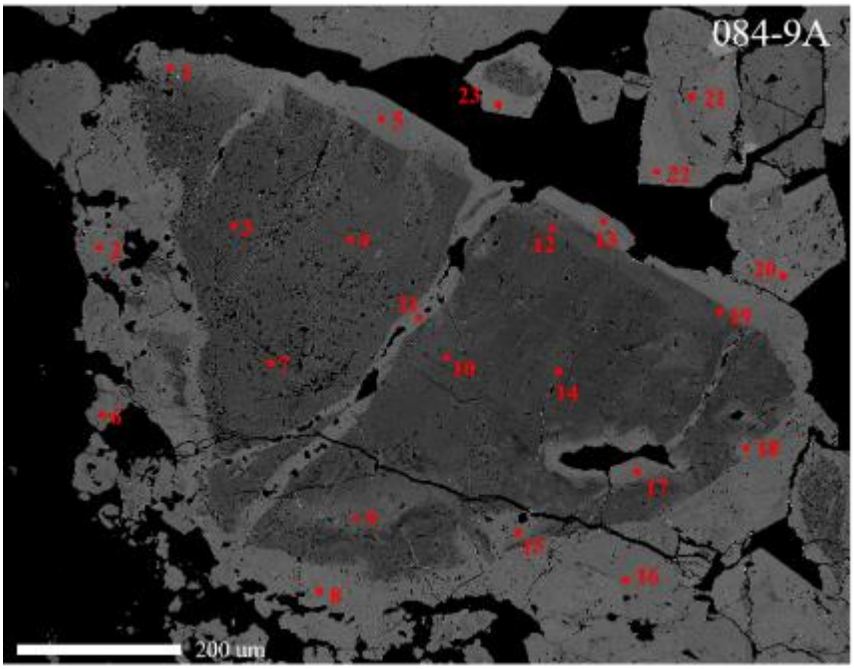
084-9A
200 um

Sample	Point	Texture	Location	Mass Percent (%)									
				As	S	Sb	Te	Au	Ag	Fe	Co	Ni	Total
108-03-Asp01	1	subhedral	core	46.16	19.01	nd	nd	0.01	nd	27.27	6.60	0.19	99.23
108-03-Asp01	2	subhedral	outer rim	45.41	19.69	nd	0.02	0.01	nd	33.73	0.07	0.01	98.93
108-03-Asp01	3	subhedral	core	45.76	19.20	nd	nd	0.00	nd	30.35	3.52	0.09	98.92
108-03-Asp01	4	subhedral	core	45.99	18.97	nd	nd	0.02	nd	28.96	4.86	0.14	98.94
108-03-Asp01	5	subhedral	core	45.83	19.38	0.01	0.01	0.02	nd	33.66	0.06	0.03	98.99
108-03-Asp01	6	subhedral	outer rim	45.61	19.42	0.01	0.02	0.03	nd	33.76	0.00	0.02	98.86
108-03-Asp01	7	subhedral	core	46.33	18.89	nd	nd	0.00	nd	28.95	4.87	0.12	99.17
108-03-Asp01	8	subhedral	core	45.93	19.00	nd	nd	0.01	nd	28.63	5.16	0.18	98.92
108-03-Asp01	9	subhedral	outer rim	45.61	19.41	0.01	0.00	0.02	nd	33.62	0.16	0.02	98.86
122-04-Asp01	1	euhedral	core	43.57	20.69	nd	nd	0.02	nd	33.52	0.53	0.20	98.54
122-04-Asp01	2	euhedral	core	44.00	20.44	0.06	0.00	0.01	nd	34.12	0.02	0.03	98.67
122-04-Asp01	3	euhedral	core	43.74	20.78	0.01	nd	0.01	nd	34.19	0.01	0.01	98.75
122-04-Asp01	4	euhedral	core	44.04	20.23	0.04	nd	0.01	nd	34.12	0.03	0.02	98.50
122-04-Asp01	5	euhedral	outer rim	45.19	19.38	0.00	nd	0.00	nd	33.43	0.38	0.05	98.42
122-04-Asp01	6	euhedral	outer rim	44.11	20.03	0.02	nd	0.01	nd	33.45	0.43	0.03	98.09
122-04-Asp01	7	euhedral	outer rim	44.19	20.10	0.04	0.00	0.01	nd	33.82	0.19	0.05	98.41
122-04-Asp01	8	euhedral	outer rim	45.40	19.33	0.01	nd	0.01	nd	33.45	0.18	0.02	98.40
122-04-Asp01	9	euhedral	core	44.19	20.28	0.06	nd	0.02	nd	34.04	0.02	0.01	98.62
122-04-Asp01	10	euhedral	outer rim	45.12	19.57	0.00	nd	0.02	nd	33.49	0.14	0.12	98.47
156-02-Asp02	1	euhedral	outer rim	45.03	18.77	0.00	nd	0.00	nd	32.97	0.24	0.20	97.20
156-02-Asp02	2	euhedral	inner rim	45.10	18.81	0.02	nd	0.02	nd	32.76	0.58	0.36	97.63
156-02-Asp02	3	euhedral	core	42.29	20.83	0.02	0.00	0.02	nd	34.20	0.02	0.08	97.45
156-02-Asp02	4	euhedral	core	42.24	20.67	0.01	0.01	0.01	nd	34.22	0.03	0.08	97.26
156-02-Asp02	5	euhedral	inner rim	45.17	18.65	0.01	nd	0.02	nd	32.70	0.68	0.31	97.53
156-02-Asp02	6	euhedral	outer rim	45.68	18.38	nd	nd	0.01	nd	32.85	0.40	0.22	97.54

156-02-Asp02	7	euhedral	outer rim	45.44	18.46	0.00	nd	0.01	nd	32.50	0.26	0.37	97.04
156-02-Asp02	8	euhedral	core	42.32	21.03	0.03	0.01	0.01	nd	34.25	0.01	0.05	97.69
156-02-Asp02	9	euhedral	inner rim	45.21	18.65	0.01	nd	0.01	nd	32.08	0.53	0.93	97.43
156-02-Asp02	10	euhedral	core	43.14	20.12	0.02	0.00	0.02	nd	34.09	0.01	0.05	97.46
156-02-Asp02	11	euhedral	core	43.86	19.65	0.07	0.01	0.01	nd	33.81	0.02	0.10	97.53
156-02-Asp02	12	euhedral	outer rim	45.45	18.23	0.00	nd	0.01	nd	32.58	0.18	0.41	96.87
156-02-Asp02	13	euhedral	outer rim	43.94	18.63	nd	nd	0.01	nd	32.42	0.39	0.33	95.72
156-02-Asp02	14	euhedral	inner rim	44.69	18.88	0.00	0.01	0.01	nd	32.91	0.28	0.47	97.25
156-04-Asp01	1	subhedral	core	44.02	19.69	0.02	0.00	0.02	nd	33.98	nd	0.02	97.75
156-04-Asp01	2	subhedral	core	44.64	19.37	nd	0.00	0.00	nd	33.80	0.01	0.02	97.83
156-04-Asp01	3	subhedral	core	45.28	18.81	0.00	0.01	0.01	nd	33.76	0.01	0.00	97.87
156-04-Asp01	4	subhedral	core	43.92	19.69	0.01	0.00	0.01	nd	33.96	0.01	0.01	97.61
156-04-Asp01	5	subhedral	outer rim	44.96	18.70	nd	nd	0.00	nd	33.35	0.13	0.08	97.22
156-04-Asp01	6	subhedral	outer rim	45.16	18.83	0.01	0.00	0.00	nd	33.47	0.06	0.11	97.63
156-04-Asp01	7	subhedral	inner rim	45.27	18.83	0.01	0.01	0.03	nd	33.67	0.00	0.02	97.84
156-04-Asp01	8	subhedral	outer rim	45.69	18.62	nd	nd	0.01	nd	33.45	0.02	0.09	97.88
156-04-Asp01	9	subhedral	outer rim	44.93	18.90	0.00	nd	0.01	0.00	33.51	0.04	0.16	97.54
156-04-Asp01	10	subhedral	core	45.13	18.93	0.01	nd	0.01	nd	33.70	0.00	0.03	97.80
156-06-Asp01	1	euhedral	core	44.51	19.28	0.02	0.01	0.00	0.00	33.67	0.02	0.00	97.51
156-06-Asp01	2	euhedral	core	44.45	19.29	0.02	0.01	0.01	nd	33.70	0.01	0.01	97.49
156-06-Asp01	3	euhedral	inner rim	44.27	19.31	0.01	0.02	0.00	nd	33.60	0.04	0.01	97.25
156-06-Asp01	4	euhedral	outer rim	45.52	18.64	0.01	0.00	0.01	nd	33.43	0.01	0.03	97.63
156-06-Asp01	5	euhedral	outer rim	44.64	19.05	nd	nd	0.02	nd	33.65	0.01	0.04	97.40
156-06-Asp01	6	euhedral	inner rim	43.28	20.19	nd	nd	0.02	nd	33.97	0.05	0.01	97.53
156-06-Asp01	7	euhedral	core	44.59	19.22	0.03	nd	0.01	nd	33.56	0.02	0.04	97.45
156-06-Asp01	8	euhedral	outer rim	44.84	19.16	nd	nd	0.01	nd	33.55	0.01	0.03	97.60
156-06-Asp01	9	euhedral	inner rim	44.08	19.59	0.00	nd	0.00	nd	33.81	0.00	0.01	97.50
156-06-Asp01	10	euhedral	core	44.43	19.35	0.02	nd	0.01	nd	33.69	0.03	0.01	97.54

156-06-Asp01	11	euhedral	outer rim	45.10	18.81	0.00	nd	0.01	nd	33.34	0.01	0.01	97.29
156-06-Asp01	12	euhedral	outer rim	45.23	18.96	nd	nd	0.01	nd	33.41	0.00	0.01	97.62
156-06-Asp01	13	euhedral	outer rim	45.11	18.85	nd	nd	0.01	nd	33.47	0.01	0.02	97.47
156-06-Asp01	14	euhedral	core	44.55	19.22	0.01	0.02	0.01	0.00	33.70	0.01	0.01	97.53
156-06-Asp01	15	euhedral	inner rim	43.59	19.92	0.01	nd	0.01	nd	33.98	0.01	0.01	97.52
156-06-Asp01	16	euhedral	outer rim	44.85	18.96	0.00	nd	0.01	nd	33.35	0.02	0.04	97.24
75-06-Asp01	1	subhedral	outer rim	45.07	18.51	nd	nd	0.00	nd	33.71	0.08	0.02	97.39
75-06-Asp01	2	subhedral	core	44.29	19.16	0.02	nd	0.01	nd	34.16	0.05	0.02	97.71
75-06-Asp01	3	subhedral	core	42.86	20.20	0.02	nd	0.01	nd	34.33	0.18	0.04	97.65
75-06-Asp01	4	subhedral	inner rim	44.90	18.94	0.02	0.00	0.02	nd	33.86	0.19	0.03	97.96
75-06-Asp01	5	subhedral	outer rim	43.93	19.53	0.01	nd	0.01	nd	33.96	0.05	0.03	97.52
75-06-Asp01	6	subhedral	core	43.20	20.11	0.01	0.00	0.02	nd	34.42	0.06	0.00	97.82
75-06-Asp01	7	subhedral	outer rim	45.49	18.55	nd	nd	0.00	nd	33.80	0.07	0.01	97.91
75-06-Asp01	8	subhedral	inner rim	43.51	19.74	0.10	0.01	0.01	nd	34.09	0.20	0.09	97.75
75-06-Asp01	9	subhedral	core	42.79	20.27	0.05	0.01	0.01	nd	34.28	0.22	0.01	97.64
75-06-Asp01	10	subhedral	core	43.10	20.15	0.02	nd	0.01	nd	34.42	0.03	0.00	97.73
75-06-Asp01	11	subhedral	core	43.71	19.63	0.01	nd	0.01	nd	33.08	1.11	0.18	97.73
75-06-Asp01	12	subhedral	outer rim	43.87	19.46	0.00	nd	0.01	nd	34.02	0.04	0.03	97.41
75-06-Asp01	13	subhedral	core	42.34	20.68	0.01	0.00	0.01	nd	34.60	0.09	0.01	97.76
75-06-Asp01	14	subhedral	core	42.83	20.17	0.04	nd	0.01	nd	34.39	0.05	0.01	97.50
75-06-Asp01	15	subhedral	outer rim	45.17	18.62	0.01	0.01	0.01	nd	33.81	0.12	0.01	97.76
75-06-Asp01	16	subhedral	core	43.61	19.73	0.06	0.00	0.00	nd	34.29	0.01	0.01	97.72
75-06-Asp01	17	subhedral	outer rim	44.21	19.37	0.00	nd	0.01	0.00	33.70	0.14	0.04	97.47
75-06-Asp01	18	subhedral	outer rim	43.09	20.33	0.02	nd	0.01	nd	34.45	0.01	0.03	97.93
75-06-Asp01	19	subhedral	inner rim	44.88	18.73	0.01	nd	0.02	nd	33.74	0.01	0.01	97.38
75-06-Asp01	20	subhedral	outer rim	45.01	18.75	nd	0.00	0.00	nd	33.94	0.01	0.01	97.72
75-10-Asp01	1	subhedral	outer rim	44.42	18.86	0.00	nd	0.01	nd	32.72	1.12	0.17	97.30
75-10-Asp01	2	subhedral	outer rim	45.18	18.41	0.01	nd	0.00	nd	33.67	0.13	0.05	97.45

75-10-Asp01	3	subhedral	outer rim	44.78	18.69	0.02	nd	0.00	nd	33.77	0.03	0.09	97.39
75-10-Asp01	4	subhedral	core	42.44	20.12	0.01	nd	0.02	nd	34.27	0.01	0.02	96.88
75-10-Asp01	5	subhedral	core	42.58	20.37	0.00	0.02	0.01	nd	34.41	0.00	0.00	97.40
75-10-Asp01	6	subhedral	core	42.20	20.32	0.09	nd	0.02	nd	34.42	0.00	0.02	97.08
75-10-Asp01	7	subhedral	outer rim	44.74	18.93	0.01	nd	0.01	nd	33.60	0.09	0.11	97.49
75-10-Asp01	8	subhedral	core	44.28	19.07	0.03	0.00	0.02	nd	33.92	0.01	0.01	97.33
75-10-Asp01	9	subhedral	core	41.96	20.58	0.05	0.01	0.01	0.00	34.43	0.00	0.02	97.07
75-10-Asp01	10	subhedral	outer rim	43.42	19.59	0.10	nd	0.01	nd	34.05	0.01	0.02	97.20
75-10-Asp01	11	subhedral	core	43.24	19.95	0.09	nd	0.01	nd	34.18	0.00	0.07	97.54
75-10-Asp01	12	subhedral	core	42.98	19.92	0.08	0.01	0.01	0.00	34.23	0.01	0.03	97.26
75-10-Asp01	13	subhedral	outer rim	44.69	18.79	nd	nd	0.00	0.00	32.99	0.82	0.11	97.40
75-10-Asp01	14	subhedral	core	43.28	19.60	0.00	0.00	0.01	nd	34.14	0.01	0.01	97.04
75-10-Asp01	15	subhedral	outer rim	44.92	19.12	nd	nd	0.02	nd	33.73	0.08	0.08	97.95
75-10-Asp02	1	anhedral	patchy	42.36	20.38	0.03	nd	0.01	nd	34.10	0.06	0.11	97.04
75-10-Asp02	2	anhedral	patchy	42.53	20.51	0.05	0.01	0.02	0.00	34.31	0.02	0.07	97.51
75-10-Asp02	3	anhedral	patchy	44.58	18.70	0.00	nd	0.01	nd	33.06	0.35	0.11	96.81
75-10-Asp02	4	anhedral	patchy	44.74	18.53	nd	nd	0.01	nd	32.31	0.91	0.15	96.66
75-10-Asp02	5	anhedral	patchy	42.51	20.49	0.04	0.02	0.01	nd	34.24	0.01	0.05	97.37
75-10-Asp02	6	anhedral	patchy	43.22	19.82	0.11	0.00	0.01	nd	32.98	0.16	1.15	97.45
75-10-Asp02	7	anhedral	patchy	42.18	20.40	0.04	nd	0.01	nd	33.76	0.43	0.22	97.03
75-10-Asp02	8	anhedral	patchy	43.18	19.74	0.05	nd	0.01	0.00	34.00	0.03	0.08	97.09
75-10-Asp02	9	anhedral	patchy	42.98	20.31	0.09	nd	0.01	nd	33.91	0.07	0.12	97.49
75-10-Asp02	10	anhedral	patchy	42.51	20.30	0.03	nd	0.02	nd	34.13	0.07	0.09	97.16
75-10-Asp02	11	anhedral	patchy	42.86	20.18	0.01	nd	0.01	nd	33.85	0.17	0.28	97.35
75-10-Asp02	12	anhedral	patchy	42.90	20.24	0.01	0.00	0.02	nd	34.24	0.00	0.02	97.44
75-10-Asp02	13	anhedral	patchy	44.12	18.92	0.01	nd	0.01	0.00	33.31	0.06	0.18	96.60
75-10-Asp02	14	anhedral	patchy	42.20	20.64	0.04	0.01	0.01	nd	34.37	0.01	0.03	97.31
75-10-Asp02	15	anhedral	patchy	42.77	20.37	0.04	0.01	0.02	nd	34.06	0.07	0.20	97.53
75-10-Asp02	16	anhedral	patchy	45.28	18.51	0.02	nd	0.01	0.00	33.33	0.09	0.13	97.35

75-10-Asp02	17	anhedral	patchy	44.72	18.99	0.02	0.01	0.01	nd	33.62	0.07	0.12	97.55
75-10-Asp02	18	anhedral	patchy	44.89	18.89	0.02	0.00	0.01	nd	33.49	0.15	0.16	97.61
75-10-Asp02	19	anhedral	patchy	44.06	19.34	0.00	nd	0.01	nd	33.23	0.19	0.29	97.13
75-13-Asp01	1	anhedral	patchy	43.49	20.06	0.02	nd	0.01	nd	34.28	0.00	0.01	97.88
75-13-Asp01	2	anhedral	patchy	44.76	18.59	0.03	0.00	0.01	nd	33.85	0.02	0.03	97.28
75-13-Asp01	3	anhedral	patchy	43.38	19.94	0.02	nd	0.00	nd	34.45	0.01	0.02	97.81
75-13-Asp01	4	anhedral	patchy	42.89	20.34	0.06	0.02	0.02	nd	34.39	0.01	0.02	97.75
75-13-Asp01	5	anhedral	patchy	43.42	19.76	0.05	nd	0.02	nd	34.17	0.00	0.01	97.44
75-13-Asp01	6	anhedral	patchy	43.12	20.09	0.05	nd	0.01	nd	34.29	0.00	0.02	97.58
75-13-Asp01	7	anhedral	patchy	42.48	20.44	0.08	0.07	0.02	nd	34.46	0.00	0.02	97.57
75-13-Asp01	8	anhedral	patchy	45.19	18.45	0.03	0.00	0.01	nd	33.67	0.01	0.03	97.40
75-13-Asp01	9	anhedral	patchy	42.59	20.41	0.06	0.02	0.01	nd	34.43	nd	0.02	97.54
75-13-Asp01	10	anhedral	patchy	44.01	19.53	0.06	nd	0.01	nd	33.93	0.01	0.03	97.57
75-13-Asp01	11	anhedral	patchy	43.66	19.80	0.03	nd	0.01	nd	34.16	0.01	0.02	97.69
75-13-Asp01	12	anhedral	patchy	44.65	18.65	0.05	nd	0.00	0.00	33.72	0.01	0.05	97.13
75-13-Asp01	13	anhedral	patchy	43.35	19.78	0.04	0.01	0.01	0.00	34.14	0.00	0.02	97.35
75-13-Asp01	14	anhedral	patchy	44.38	19.63	0.06	nd	0.01	nd	34.09	0.00	0.01	98.20
84-9A-Asp01	1	anhedral	outer rim	45.01	18.62	0.02	nd	0.01	nd	33.21	0.54	0.02	97.43
84-9A-Asp01	2	anhedral	outer rim	45.26	18.48	0.02	0.01	0.01	nd	33.60	0.05	0.03	97.45
84-9A-Asp01	3	anhedral	core	43.12	20.08	0.06	nd	0.01	nd	34.17	0.00	0.00	97.44
84-9A-Asp01	4	anhedral	core	43.63	19.63	0.05	nd	0.01	nd	34.03	0.00	0.01	97.36
84-9A-Asp01	5	anhedral	outer rim	45.27	18.55	0.02	0.01	0.01	nd	33.71	0.00	0.01	97.58
84-9A-Asp01	6	anhedral	outer rim	45.08	18.61	0.01	0.01	0.01	nd	33.83	0.00	0.03	97.58
84-9A-Asp01	7	anhedral	core	42.93	20.14	0.05	0.01	0.02	nd	34.13	0.00	0.01	97.28
84-9A-Asp01	8	anhedral	outer rim	45.26	18.55	0.01	0.02	0.01	nd	33.65	nd	0.10	97.59
84-9A-Asp01	9	anhedral	core	44.49	19.16	0.04	0.02	0.03	0.00	33.85	0.05	0.01	97.63
84-9A-Asp01	10	anhedral	core	43.20	20.05	0.05	0.00	0.02	nd	34.21	0.01	0.01	97.54
84-9A-Asp01	11	anhedral	core	45.45	18.41	0.01	0.01	0.02	nd	33.63	0.01	0.03	97.57

84-9A-Asp01	12	anhedral	inner rim	43.81	19.50	0.08	0.00	0.01	nd	33.98	0.03	0.05	97.46
84-9A-Asp01	13	anhedral	outer rim	45.32	18.43	0.00	0.01	0.01	nd	33.60	0.03	0.04	97.44
84-9A-Asp01	14	anhedral	core	42.92	20.30	0.04	0.01	0.01	nd	34.33	0.01	0.00	97.63
84-9A-Asp01	15	anhedral	inner rim	44.77	18.83	0.04	nd	0.01	nd	32.85	1.01	0.03	97.53
84-9A-Asp01	16	anhedral	outer rim	45.20	18.59	0.01	0.01	0.01	nd	33.70	0.00	0.03	97.54
84-9A-Asp01	17	anhedral	core	45.22	18.66	0.01	nd	0.00	nd	33.58	0.07	0.01	97.55
84-9A-Asp01	18	anhedral	inner rim	44.84	18.64	0.04	nd	0.02	nd	32.83	0.96	0.03	97.34
84-9A-Asp01	19	anhedral	inner rim	43.47	19.83	0.03	0.00	0.01	nd	34.17	0.00	0.00	97.52
84-9A-Asp01	20	anhedral	outer rim	45.30	18.48	0.01	nd	0.00	nd	33.64	0.02	0.01	97.46
84-9A-Asp01	21	anhedral	outer rim	44.35	19.09	0.00	0.00	0.01	0.00	33.85	0.01	0.07	97.38
84-9A-Asp01	22	anhedral	outer rim	45.71	18.25	0.02	0.00	0.01	nd	33.60	0.04	0.07	97.68
84-9A-Asp01	23	anhedral	outer rim	44.97	18.45	0.01	0.02	0.01	nd	33.63	0.00	0.02	97.11
84-9B-Asp02	1	euhedral	outer rim	45.04	18.73	0.01	nd	0.01	nd	33.47	0.01	0.02	97.28
84-9B-Asp02	2	euhedral	core	45.09	19.57	0.01	nd	0.01	nd	33.56	0.02	0.12	98.38
84-9B-Asp02	3	euhedral	core	44.69	19.76	0.00	nd	0.01	nd	34.08	0.00	0.00	98.54
84-9B-Asp02	4	euhedral	core	45.50	19.27	0.01	nd	0.01	nd	33.74	0.00	0.01	98.54
84-9B-Asp02	5	euhedral	core	45.19	19.63	nd	nd	0.02	nd	33.89	0.00	0.01	98.73
84-9B-Asp02	6	euhedral	inner rim	45.48	19.35	nd	nd	0.01	nd	33.65	0.01	0.02	98.52
84-9B-Asp02	7	euhedral	outer rim	45.43	19.36	0.02	nd	0.01	nd	33.21	0.02	0.02	98.07
84-9B-Asp02	8	euhedral	outer rim	45.42	19.09	0.00	0.00	0.00	nd	33.47	0.01	0.02	98.01
84-9B-Asp02	9	euhedral	inner rim	45.30	19.23	nd	0.00	0.02	nd	33.79	0.01	0.01	98.36
84-9B-Asp02	10	euhedral	inner rim	45.67	18.93	nd	0.00	0.01	nd	33.48	0.01	0.02	98.13
84-9B-Asp02	11	euhedral	inner rim	44.76	19.16	nd	0.00	0.02	nd	33.81	0.02	0.02	97.77
84-9B-Asp02	12	euhedral	outer rim	44.10	19.40	nd	0.01	0.02	nd	33.86	0.01	0.01	97.41

84-9B-Asp03	1	anhedral	patchy	45.16	19.01	nd	0.01	0.01	nd	33.64	0.01	0.01	97.85
84-9B-Asp03	2	anhedral	patchy	45.39	18.96	nd	0.02	0.01	nd	33.60	0.01	0.02	98.01
84-9B-Asp03	3	anhedral	patchy	45.10	19.25	0.02	0.01	nd	nd	33.66	0.00	0.01	98.06
84-9B-Asp03	4	anhedral	patchy	45.00	18.90	0.00	0.01	0.00	nd	33.46	0.02	0.01	97.40
84-9B-Asp03	5	anhedral	patchy	45.16	19.08	nd	0.02	0.00	nd	33.62	0.01	0.01	97.89
84-9B-Asp03	6	anhedral	patchy	44.77	19.15	0.02	0.03	0.01	nd	33.59	0.00	0.01	97.58
84-9B-Asp03	7	anhedral	patchy	44.43	19.46	0.00	0.01	0.01	nd	33.84	0.01	0.00	97.78
84-9B-Asp03	8	anhedral	patchy	44.64	19.46	0.01	0.02	0.01	nd	33.75	0.01	0.02	97.92
84-9B-Asp03	9	anhedral	patchy	44.72	19.16	0.01	0.01	0.01	0.00	33.09	0.02	0.07	97.08
84-9B-Asp03	10	anhedral	patchy	45.34	18.79	0.00	0.01	0.02	nd	33.63	0.01	0.01	97.81
84-9B-Asp03	11	anhedral	patchy	45.07	18.85	nd	nd	0.01	nd	33.66	0.01	0.01	97.60
84-9B-Asp03	12	anhedral	patchy	44.11	19.42	0.01	0.00	0.01	0.00	33.60	0.02	0.01	97.17
84-9B-Asp03	13	anhedral	patchy	44.70	19.01	0.01	0.01	0.01	nd	33.02	0.01	0.02	96.80
85-13-Asp02	1	euhedral	rim	44.96	19.17	0.01	nd	0.02	nd	33.51	0.02	0.04	97.71
85-13-Asp02	2	euhedral	core	44.12	19.85	0.00	nd	0.01	nd	33.91	0.01	0.02	97.93
85-13-Asp02	3	euhedral	core	44.81	19.22	nd	0.01	0.01	nd	33.52	0.03	0.08	97.67
85-13-Asp02	4	euhedral	core	44.87	19.35	nd	0.01	0.01	nd	33.71	0.00	0.03	97.97
85-13-Asp02	5	euhedral	inner rim	45.55	18.81	nd	0.01	0.01	nd	32.79	0.52	0.33	98.02
85-13-Asp02	6	euhedral	inner rim	45.56	18.81	0.00	nd	0.01	nd	33.20	0.11	0.31	97.99
85-13-Asp02	7	euhedral	inner rim	45.46	18.87	0.01	0.00	nd	nd	33.50	0.05	0.02	97.91
85-13-Asp02	8	euhedral	outer rim	45.43	18.85	0.00	0.00	0.01	0.00	33.56	0.00	0.02	97.87
85-13-Asp02	9	euhedral	outer rim	44.86	19.21	0.00	nd	0.00	nd	33.54	0.01	0.03	97.66
85-13-Asp02	10	euhedral	inner rim	45.65	18.70	0.00	nd	0.01	nd	32.58	0.53	0.51	97.97
85-13-Asp02	11	euhedral	inner rim	45.55	18.75	0.01	0.00	0.01	nd	33.36	0.14	0.03	97.84
85-13-Asp02	12	euhedral	inner rim	45.63	18.62	0.01	0.01	0.02	nd	32.80	0.37	0.32	97.79
85-13-Asp02	13	euhedral	outer rim	45.05	18.88	0.00	nd	0.01	nd	33.45	0.01	0.01	97.41
85-13-Asp02	14	euhedral	outer rim	45.61	18.66	nd	0.00	0.01	nd	33.54	0.03	0.04	97.89

85-13-Asp03	1	anhedral	patchy	45.09	19.02	0.01	nd	0.02	nd	33.59	nd	0.01	97.73
85-13-Asp03	2	anhedral	patchy	44.58	19.14	0.01	0.00	0.01	nd	33.35	0.11	0.09	97.29
85-13-Asp03	3	anhedral	patchy	45.02	18.72	0.01	0.00	0.01	nd	33.45	0.00	0.01	97.23
85-13-Asp03	4	anhedral	patchy	45.23	18.69	nd	0.00	0.01	nd	33.45	nd	0.01	97.40
85-13-Asp03	5	anhedral	patchy	45.32	18.74	0.01	0.00	0.01	nd	33.40	0.01	0.01	97.49
85-13-Asp03	6	anhedral	patchy	45.44	18.56	0.01	nd	0.02	nd	33.31	0.01	0.02	97.36
85-13-Asp03	7	anhedral	patchy	44.67	19.12	0.01	0.01	0.01	nd	33.73	0.01	0.01	97.55
85-13-Asp03	8	anhedral	patchy	45.51	18.69	0.00	nd	0.01	nd	33.48	0.00	0.01	97.71
85-13-Asp03	9	anhedral	patchy	45.05	18.72	0.00	0.01	0.01	nd	33.47	0.00	0.01	97.27
85-13-Asp03	10	anhedral	patchy	45.15	18.80	0.00	nd	0.01	nd	33.56	0.00	0.01	97.54
85-13-Asp03	11	anhedral	patchy	45.44	18.58	nd	nd	0.01	nd	33.39	nd	0.01	97.43
85-13-Asp03	12	anhedral	patchy	45.60	18.47	0.00	nd	0.01	nd	33.34	0.01	0.02	97.45
85-2A-Asp01	1	anhedral	patchy	42.96	21.19	0.06	0.01	0.01	nd	34.44	0.00	0.02	98.69
85-2A-Asp01	2	anhedral	patchy	42.43	21.67	0.01	0.01	0.01	nd	34.41	0.00	0.04	98.58
85-2A-Asp01	3	anhedral	patchy	45.24	19.25	0.01	0.01	0.01	nd	33.76	0.05	0.03	98.37
85-2A-Asp01	4	anhedral	patchy	43.05	21.12	0.04	0.00	0.01	nd	34.36	0.03	0.03	98.63
85-2A-Asp01	5	anhedral	patchy	44.99	19.56	0.02	0.01	0.01	nd	33.72	0.03	0.03	98.37
85-2A-Asp01	6	anhedral	patchy	45.43	19.06	nd	0.01	0.02	nd	33.65	0.05	0.05	98.26
85-2A-Asp01	7	anhedral	patchy	45.85	19.07	0.01	0.01	0.00	nd	33.47	0.04	0.11	98.55
85-2A-Asp01	8	anhedral	patchy	42.90	21.01	0.03	0.01	0.01	nd	34.17	0.09	0.10	98.32
85-2A-Asp01	9	anhedral	patchy	45.02	19.37	0.01	nd	0.01	nd	33.86	0.03	0.05	98.34
96-08-Asp01	1	anhedral	patchy	45.74	19.36	0.01	0.01	0.02	0.00	33.64	0.01	0.01	98.78
96-08-Asp01	2	anhedral	patchy	43.21	21.29	0.05	0.01	0.01	nd	34.30	0.05	0.00	98.93
96-08-Asp01	3	anhedral	patchy	43.34	21.39	0.02	0.01	0.01	nd	34.32	0.00	0.01	99.10
96-08-Asp01	4	anhedral	patchy	42.75	21.51	0.05	nd	0.00	0.00	34.46	0.01	0.00	98.78

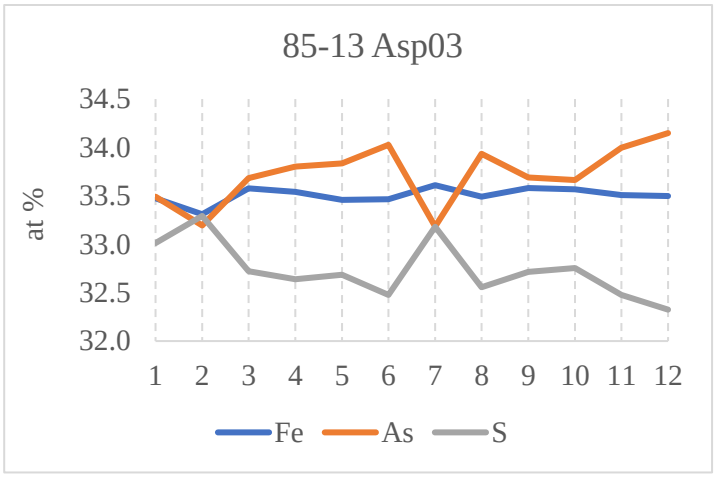
85-13 Asp03
at %
34.5
34.0
33.5
33.0
32.5
32.0
1 2 3 4 5 6 7 8 9 10 11 12
Fe
As
S

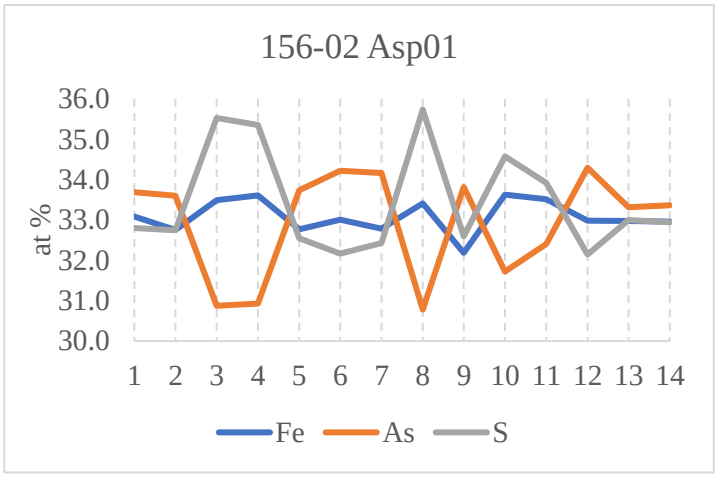
156-02 Asp01
at %
36.0
35.0
34.0
33.0
32.0
31.0
30.0
1 2 3 4 5 6 7 8 9 10 11 12 13 14
Fe
As
S

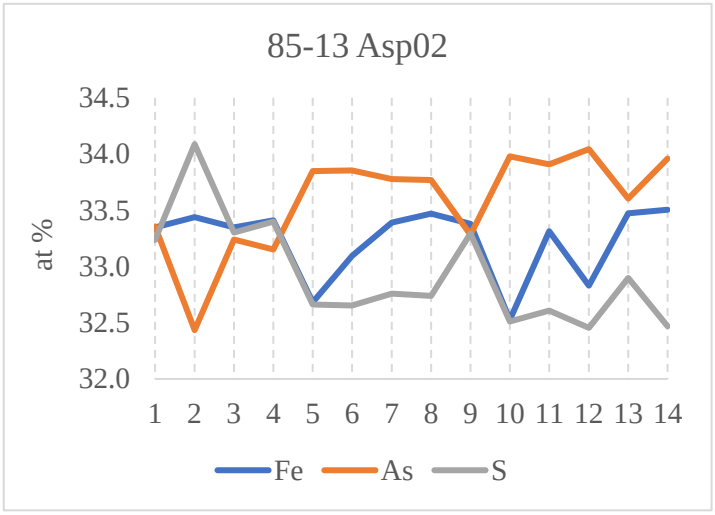
85-13 Asp02
at %
34.5
34.0
33.5
33.0
32.5
32.0
1 2 3 4 5 6 7 8 9 10 11 12 13 14
Fe
As
S

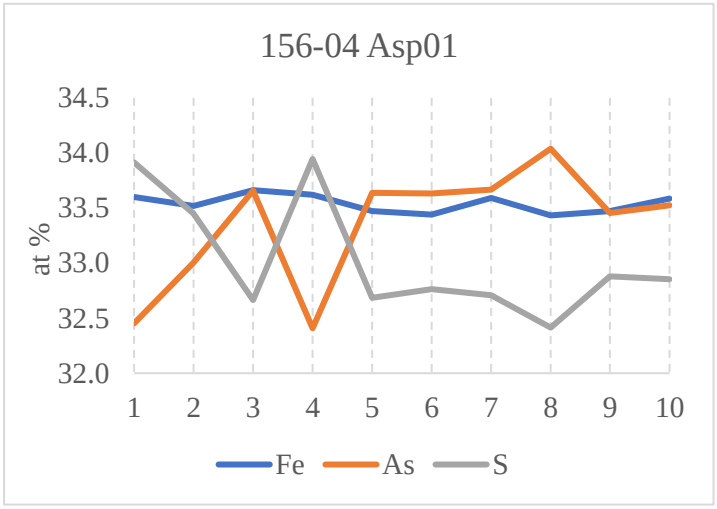
156-04 Asp01
at %
34.5
34.0
33.5
33.0
32.5
32.0
1 2 3 4 5 6 7 8 9 10
Fe
As
S

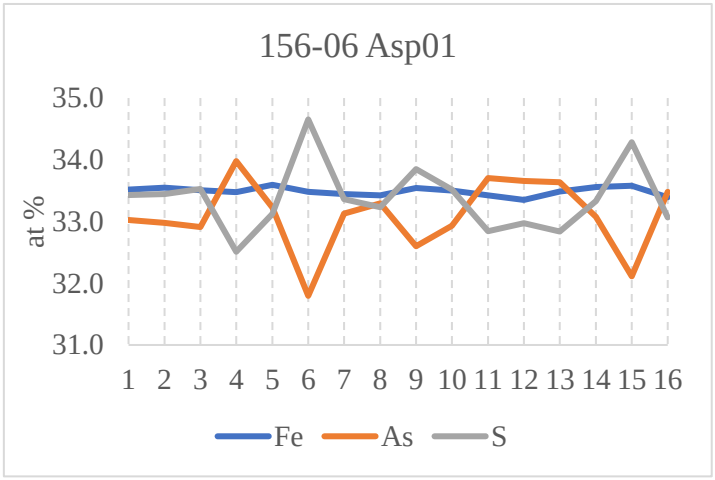
156-06 Asp01
at %
35.0
34.0
33.0
32.0
31.0
1 2 3 4 5 6 7 8 9 10 11 12 13 14 15 16
Fe
As
S

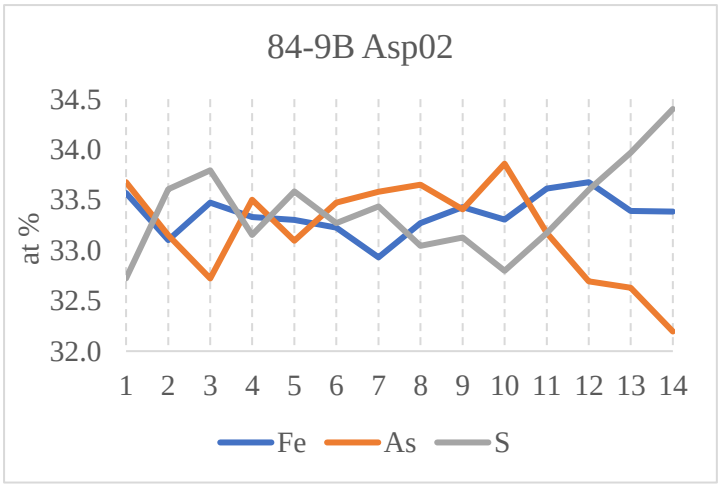
84-9B Asp02
at %
34.5
34.0
33.5
33.0
32.5
32.0
1 2 3 4 5 6 7 8 9 10 11 12 13 14
Fe
As
S

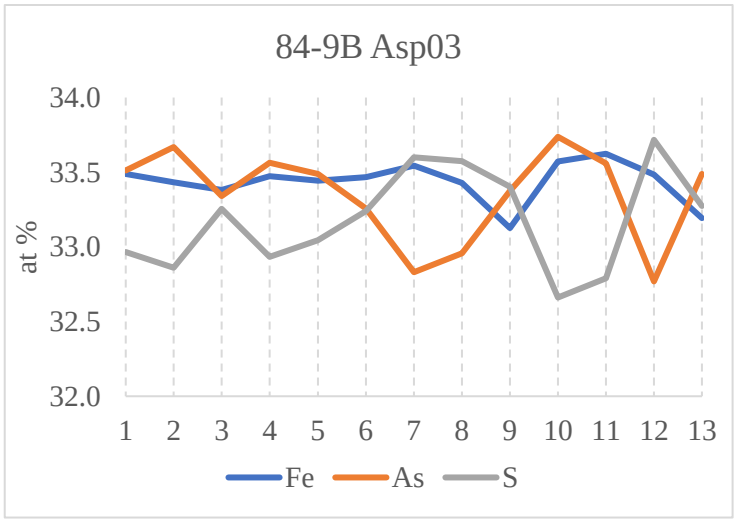
84-9B Asp03
34.0
33.5
33.0
32.5
32.0
at %
1 2 3 4 5 6 7 8 9 10 11 12 13
Fe
As
S

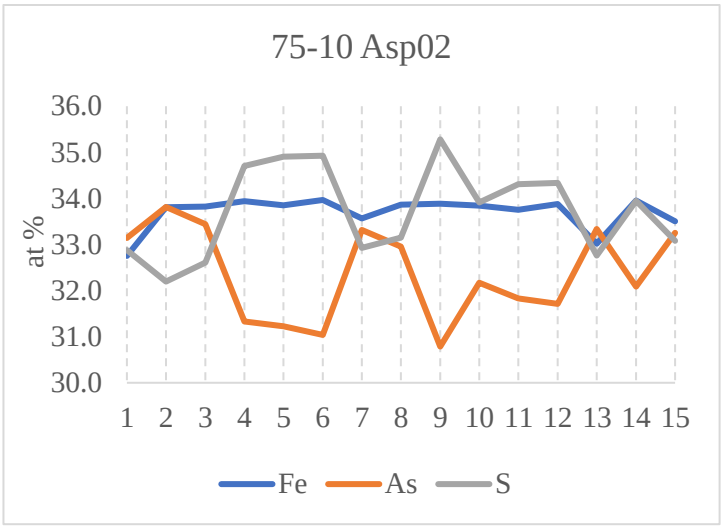
75-10 Asp02
36.0
35.0
34.0
33.0
32.0
31.0
30.0
at %
1 2 3 4 5 6 7 8 9 10 11 12 13 14 15
Fe
As
S

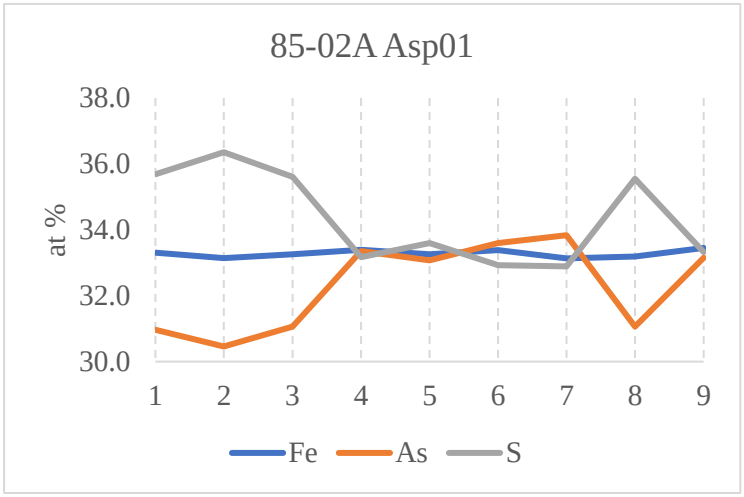
85-02A Asp01
38.0
36.0
34.0
32.0
30.0
at %
1 2 3 4 5 6 7 8 9
Fe
As
S

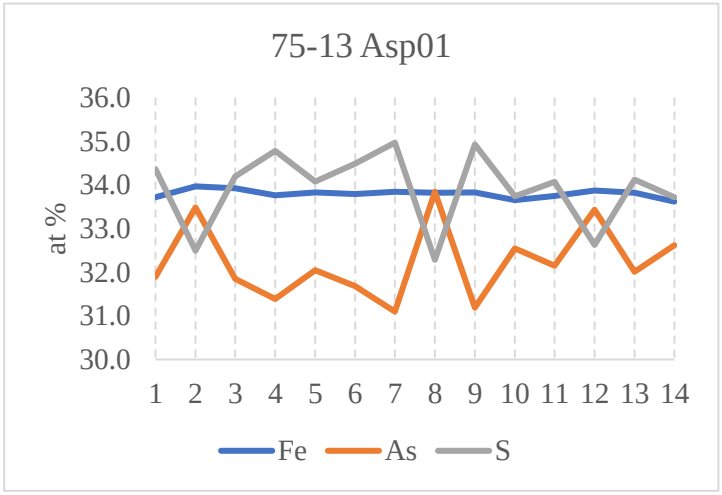
75-13 Asp01
36.0
35.0
34.0
33.0
32.0
31.0
30.0
at %
1 2 3 4 5 6 7 8 9 10 11 12 13 14
Fe
As
S

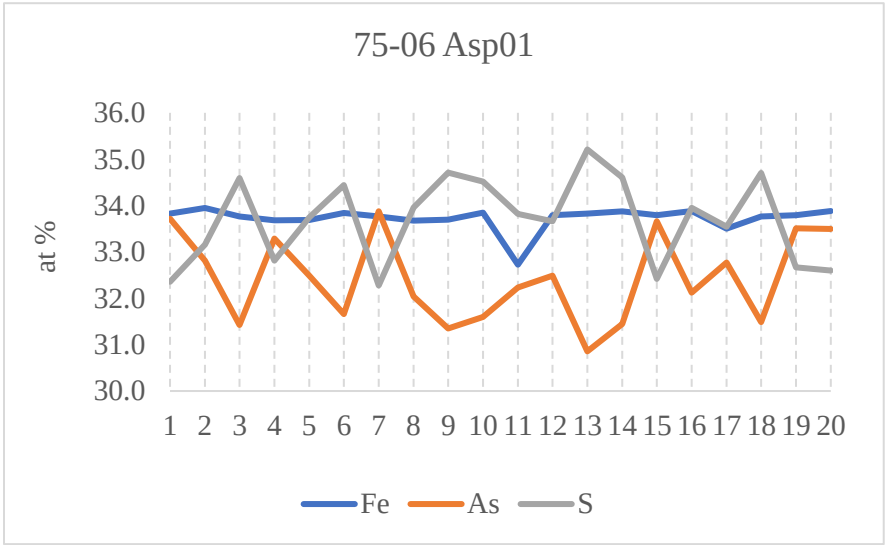
75-06 Asp01
36.0
35.0
34.0
33.0
32.0
31.0
30.0
at %
1 2 3 4 5 6 7 8 9 10 11 12 13 14 15 16 17 18 19 20
Fe
As
S

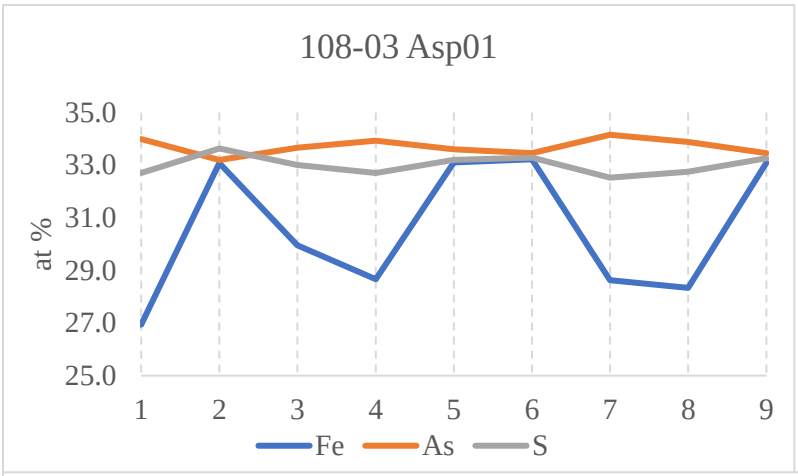
108-03 Asp01
35.0
33.0
31.0
29.0
27.0
25.0
at %
1
2
3
4
5
6
7
8
9
Fe
As
S

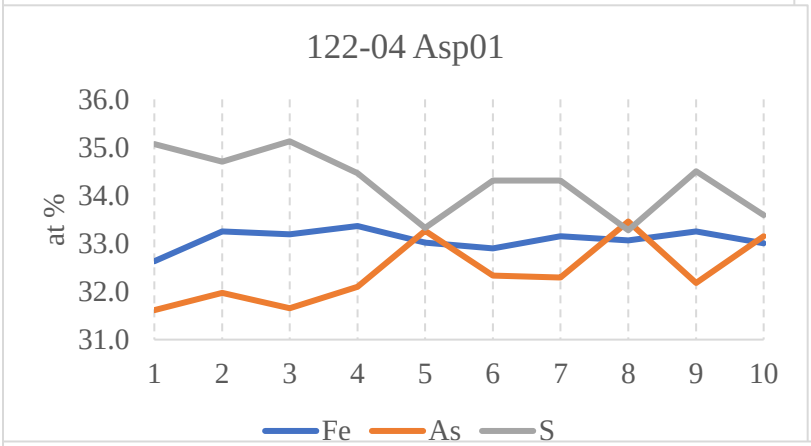
122-04 Asp01
36.0
35.0
34.0
33.0
32.0
31.0
at %
1
2
3
4
5
6
7
8
9
10
Fe
As
S

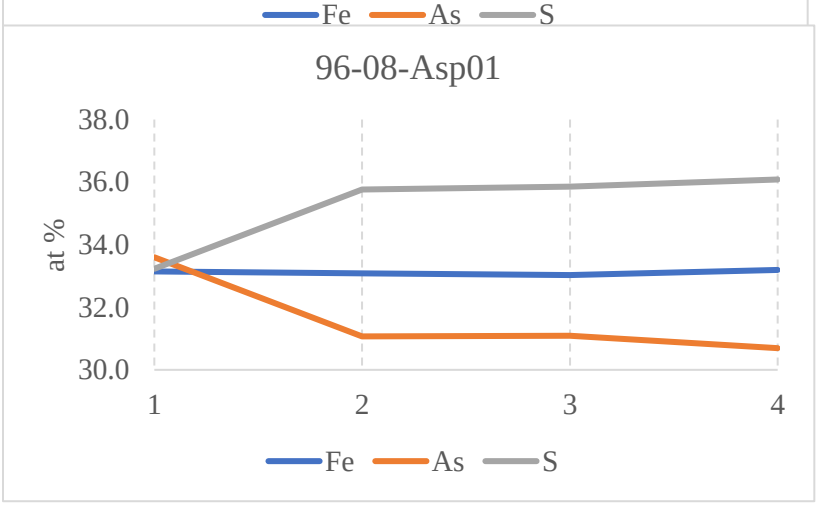
96-08-Asp01
38.0
36.0
34.0
32.0
30.0
at %
1
2
3
4
Fe
As
S

075-10 Asp01

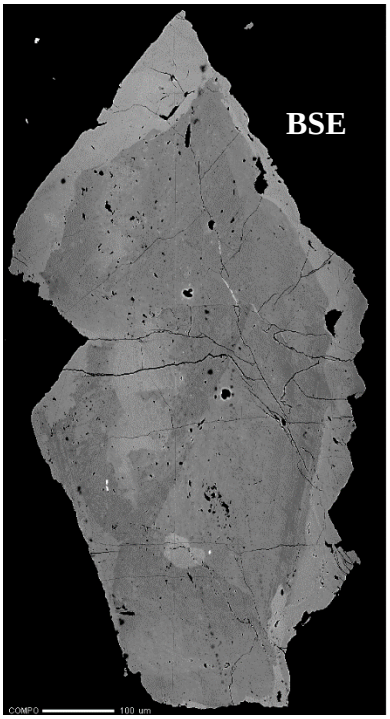
BSE
COMPO
Cts
4,095
0
Project: December_11_2018
Comment: CP-075-10_Asp1_1um
Date: 2018/12/13
Accel Voltage: 20.0 kV
Beam Current: 9.960e-008 A
Dwell Time: 10.0
Image Size: 554 x 1030
COMPO
100 um

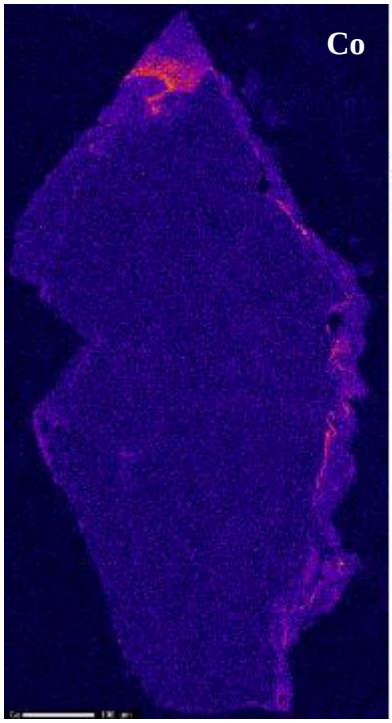
Co

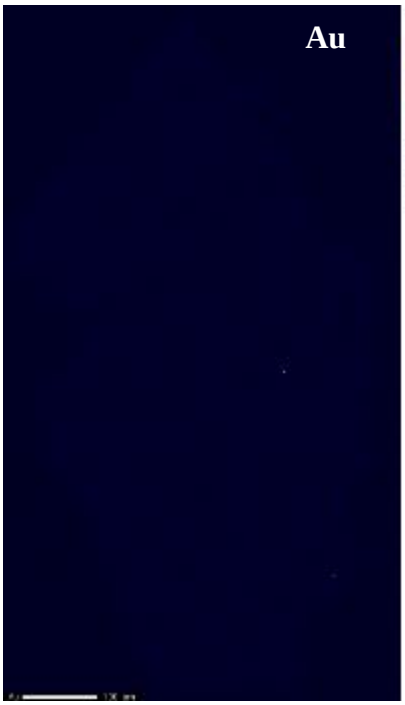
Au

075-14 Asp02

COMPO
Cts
4,095
0
Project: December_11_2018
Comment: CP-075-14_Asp2_0.6um
Date: 2018/12/13
Accel Voltage: 20.0 kV
Beam Current: 1.001e-007 A
Dwell Time: 10.0
Image Size: 274 x 592

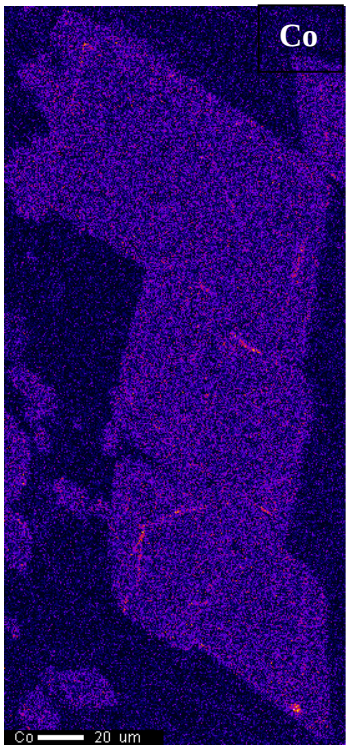

Co
Cts
14
0
Project: December_11_2018
Comment: CP-075-14_Asp2_0.6um
Date: 2018/12/13
Accel Voltage: 20.0 kV
Beam Current: 1.001e-007 A
Dwell Time: 10.0
Image Size: 274 x 592

Au
Cts
284
0
Project: December_11_2018
Comment: CP-075-14_Asp2_0.6um
Date: 2018/12/13
Accel Voltage: 20.0 kV
Beam Current: 1.001e-007 A
Dwell Time: 10.0
Image Size: 274 x 592

075-06 Asp01

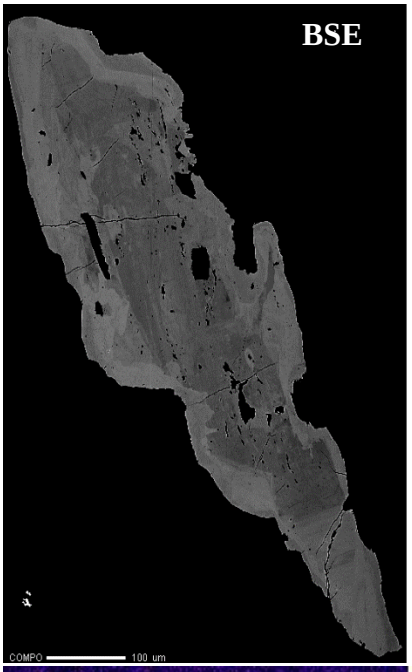
BSE
COMPO
Cts
4,095
0
Project: December_11_2018
Comment: CP-075-06_Asp1_1um
Date: 2018/12/12
Accel Voltage: 20.0 kV
Beam Current: 9.849e-008 A
Dwell Time: 10.0
Image Size: 530 x 777
COMPO
100 um

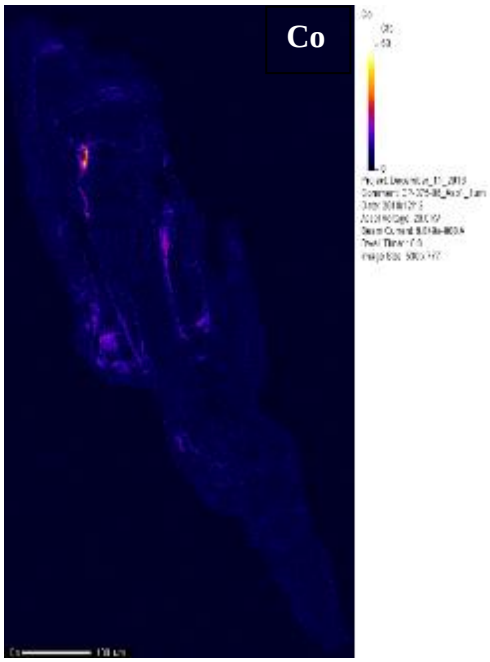
Co

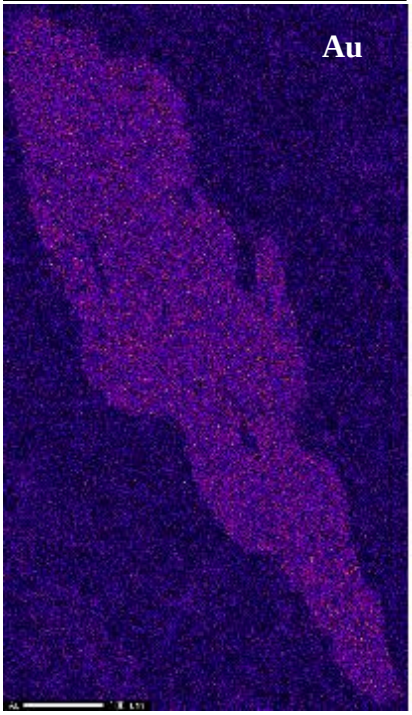
Au

084-09B Asp02

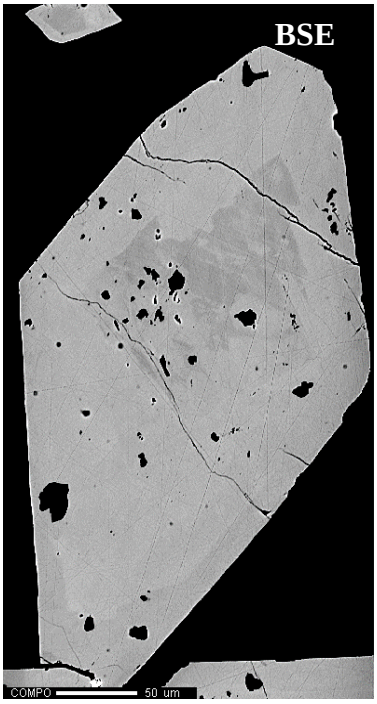

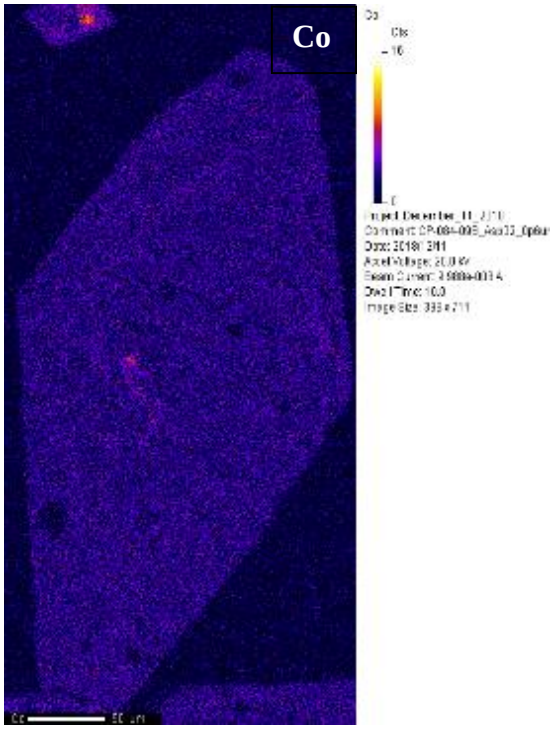

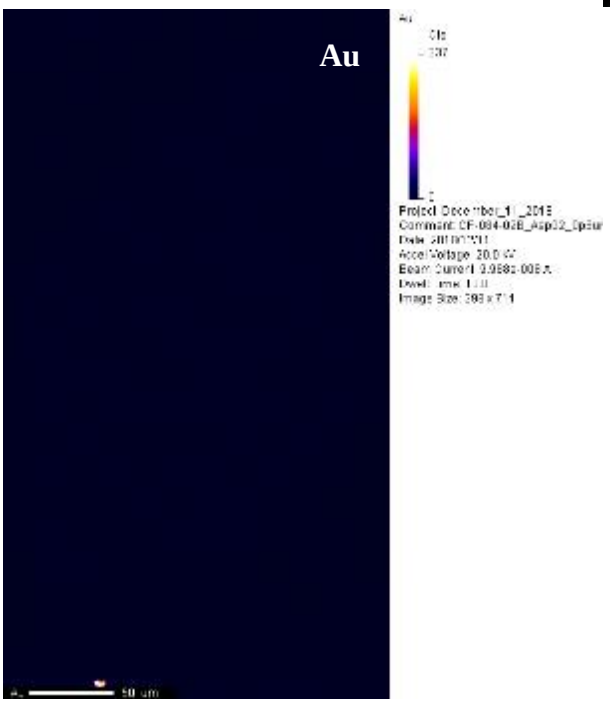

084-09A Asp01

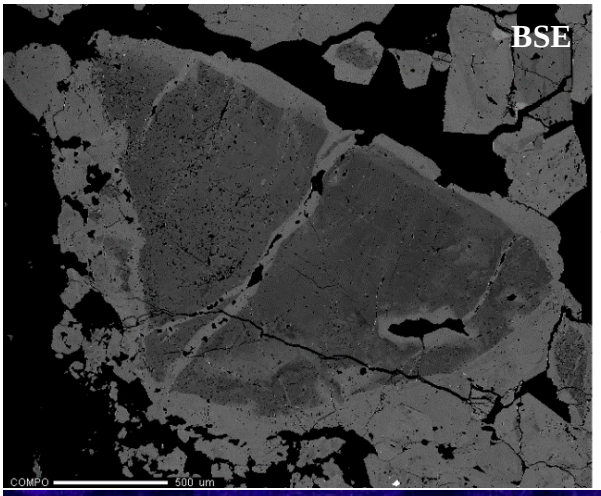

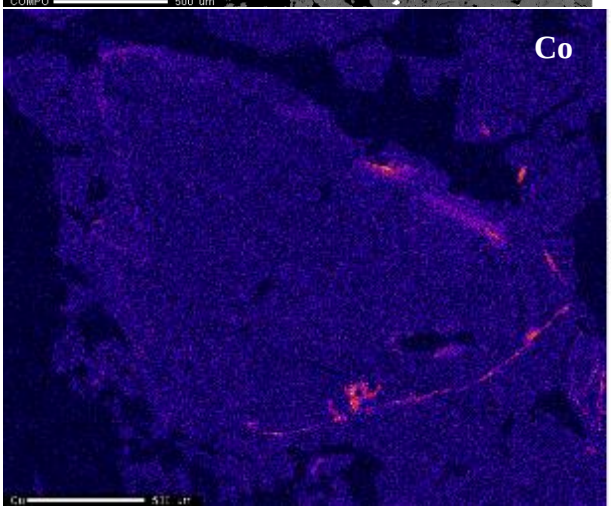

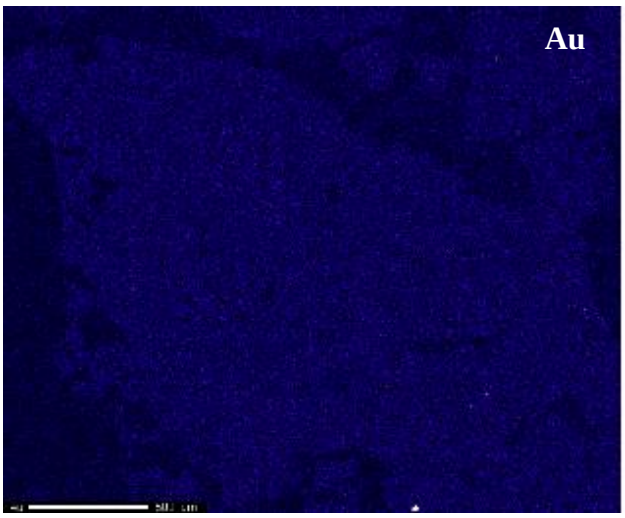

075-13 Asp01

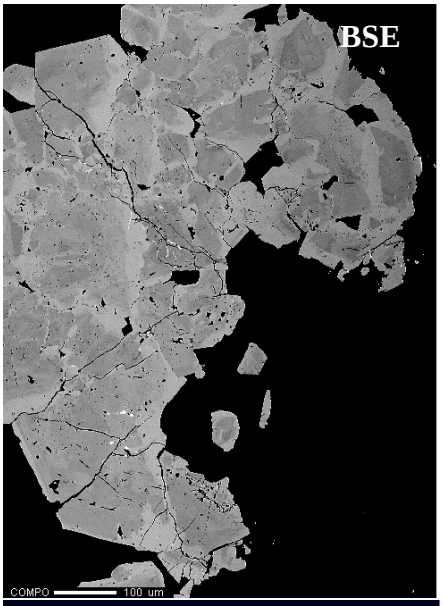
BSE
COMPO
Cts
4,095
0
Project: December_11_2018
Comment: CP-075-13_Asp1_1p5um
Date: 2018/12/12
Accel Voltage: 20.0 kV
Beam Current: 1.003e-007 A
Dwell Time: 10.0
Image Size: 485 x 665
COMPO 100 um

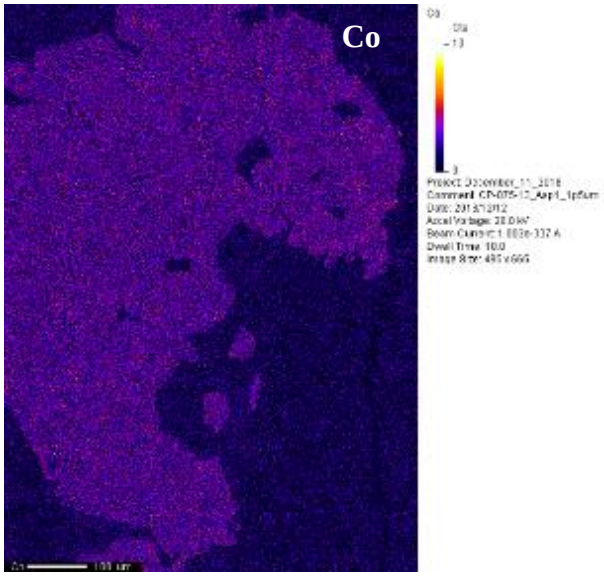
Co
Cts
13
0
Project: December_11_2018
Comment: CP-075-13_Asp1_1p5um
Date: 2018/12/12
Accel Voltage: 20.0 kV
Beam Current: 1.003e-007 A
Dwell Time: 10.0
Image Size: 485 x 665

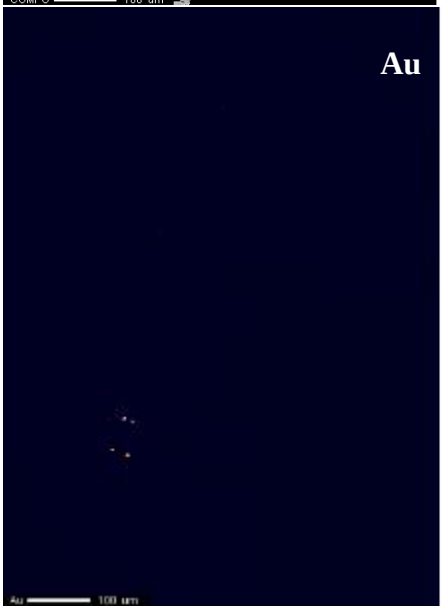
Au
Cts
356
0
Project: December_11_2018
Comment: CP-075-13_Asp1_1p5um
Date: 2018/12/12
Accel Voltage: 20.0 kV
Beam Current: 1.003e-007 A
Dwell Time: 10.0
Image Size: 485 x 665
Au 100 um

084-07 Asp01

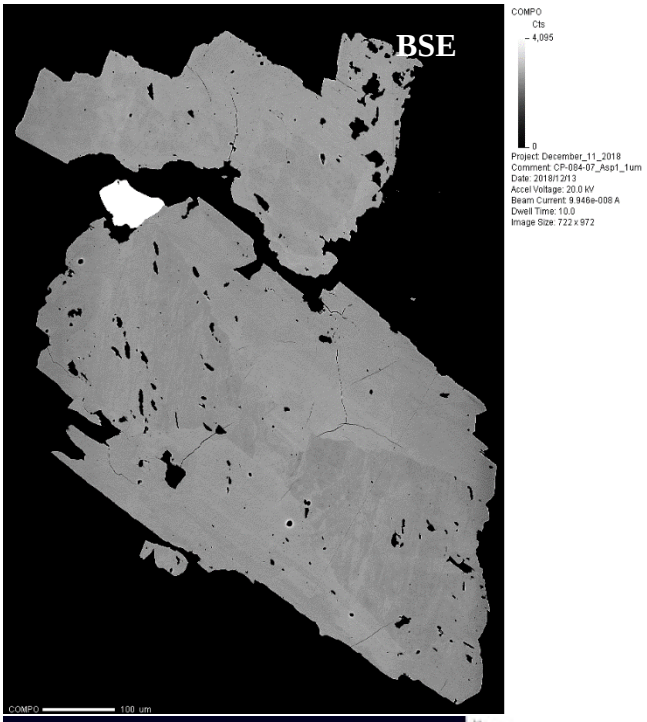
BSE
COMPO
Cts
4,095
0
Project: December_11_2018
Comment: CP-084-07_Asp1_1um
Date: 2018/12/13
Accel Voltage: 20.0 kV
Beam Current: 9.946e-008 A
Dwell Time: 10.0
Image Size: 722 x 972
COMPO
100 um

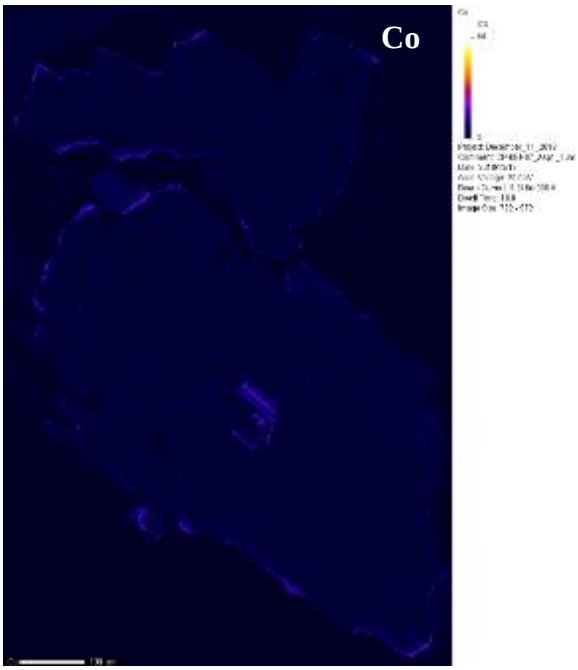
Co

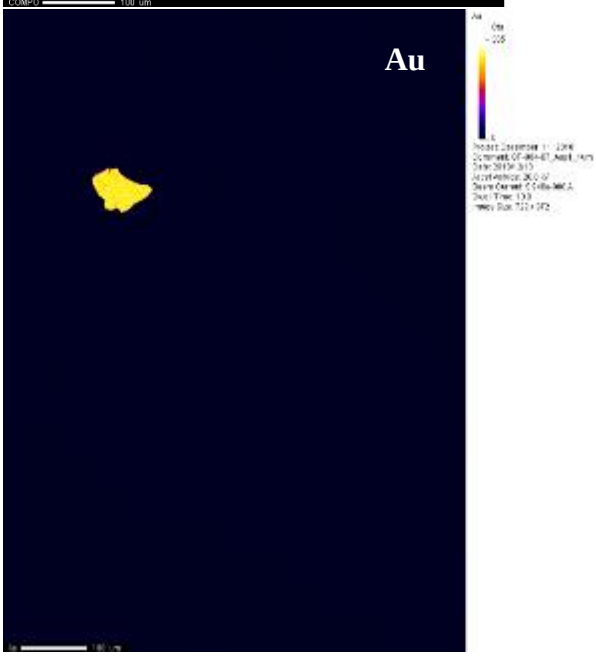
Au

075-10 Asp02

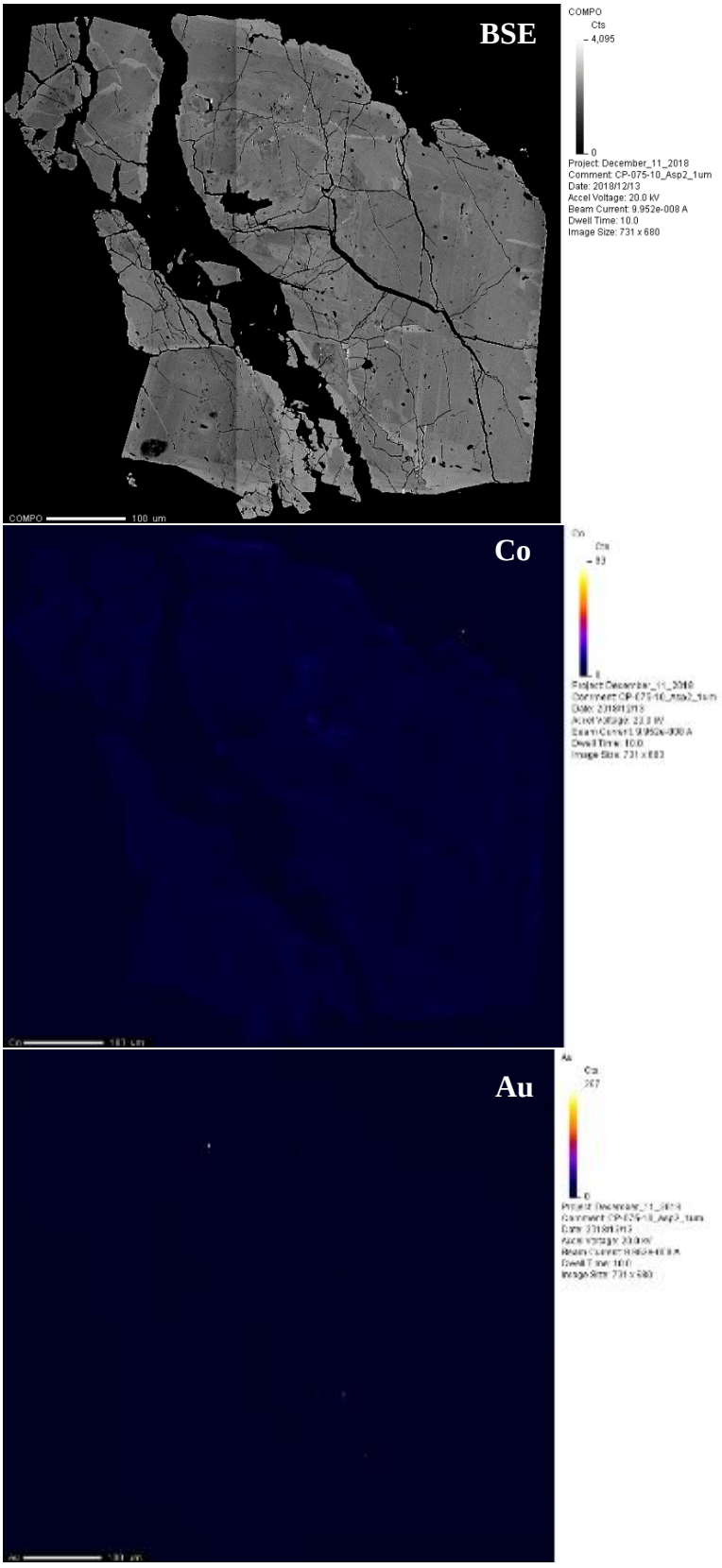
BSE
COMPO
Cts
4,095
0
Project: December_11_2018
Comment: CP-075-10_Asp2_1um
Date: 20181213
Accel Voltage: 20.0 kV
Beam Current: 9.952e-008 A
Dwell Time: 10.0
Image Size: 731 x 680
COMPO
100 um
Co
Au

084-09B Asp03

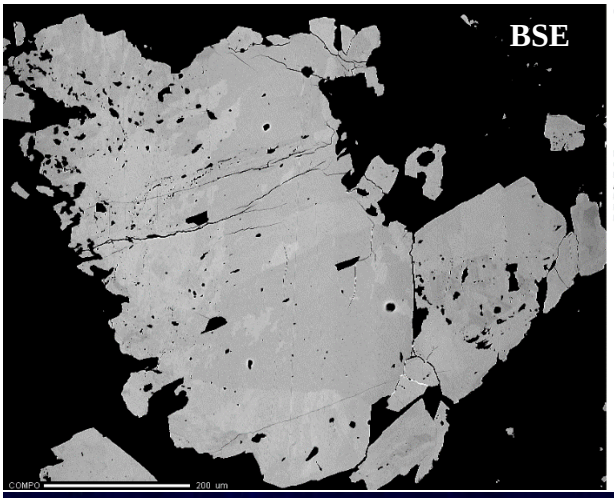

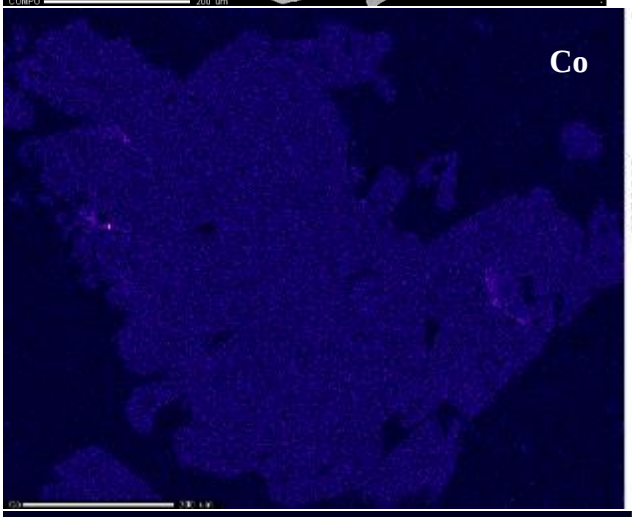

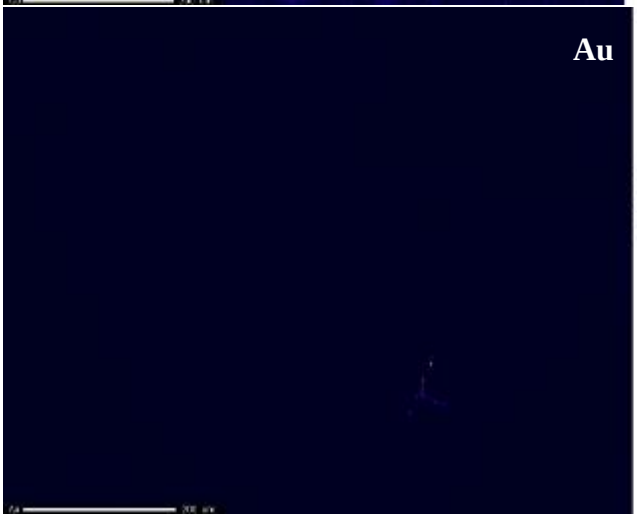

084-07 Asp02

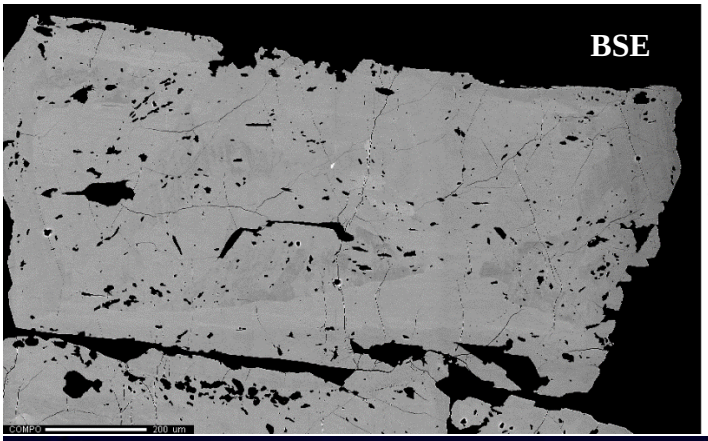
BSE
COMPO
Cts
4,095
0
Project: December_11_2018
Comment: CP-084-07_Asp2_1p5um
Date: 2018/12/13
Accel Voltage: 20.0 kV
Beam Current: 9.960e-008 A
Dwell Time: 10.0
Image Size: 943 x 581
COMPO
200 um

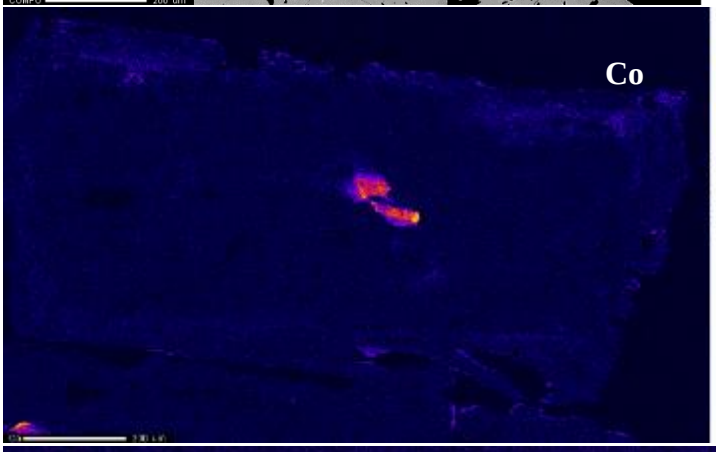
Co

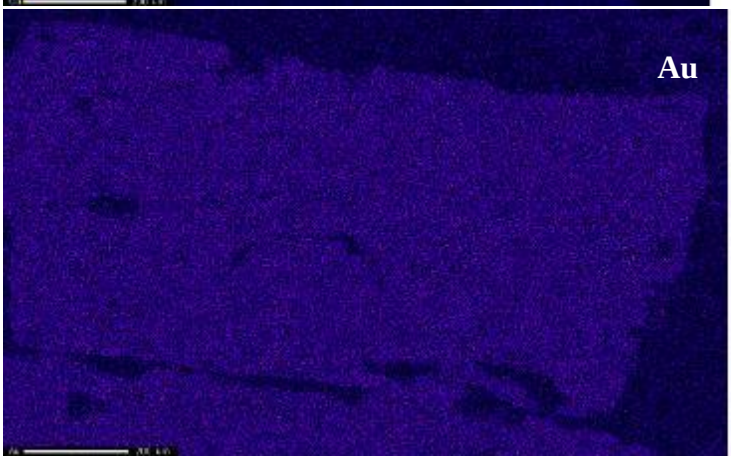
Au

085-08 Asp02

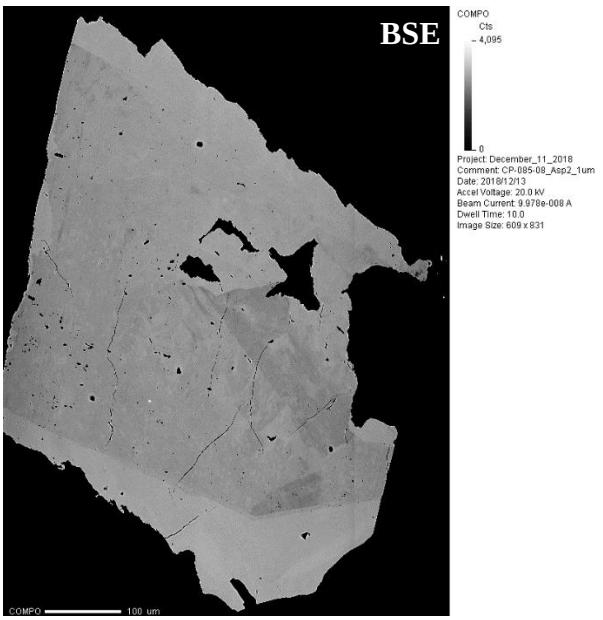
BSE
COMPO
Cts
4,095
0
Project: December_11_2018
Comment: CP-085-08_Asp2_1um
Date: 2018/12/13
Accel Voltage: 20.0 kV
Beam Current: 9.978e-008 A
Dwell Time: 10.0
Image Size: 609 x 831
COMPO
100 um

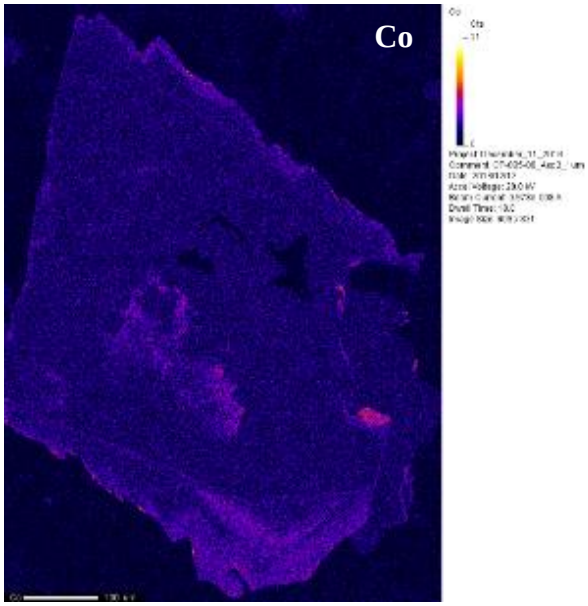
Co

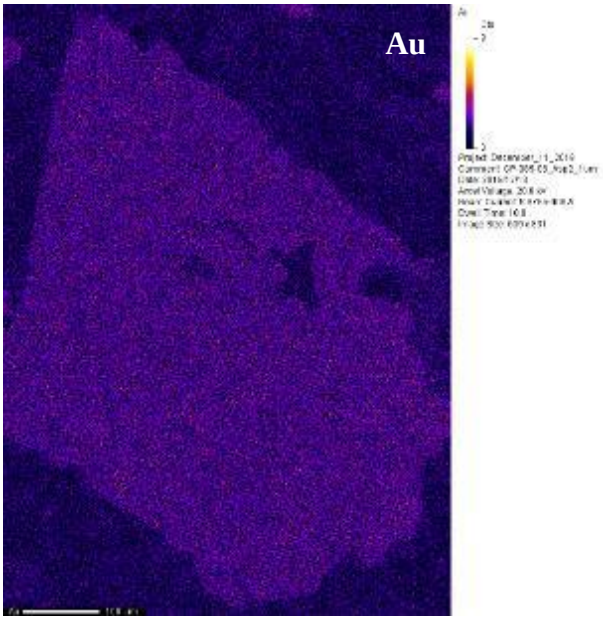
Au

085-08 Asp02

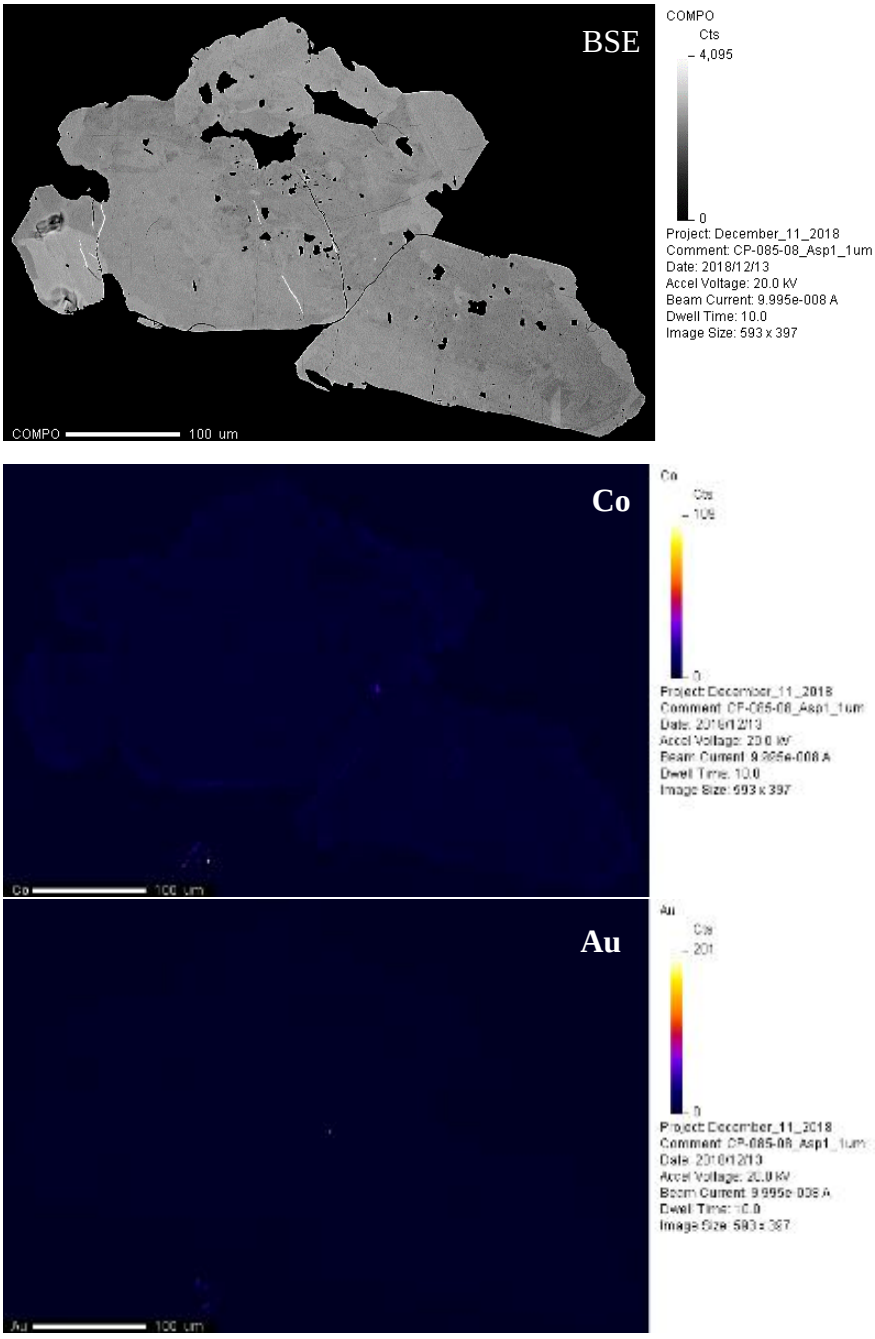
BSE
COMPO
Cts
4,095
0
Project: December_11_2018
Comment: CP-085-08_Asp1_1um
Date: 2018/12/13
Accel Voltage: 20.0 kV
Beam Current: 9.995e-008 A
Dwell Time: 10.0
Image Size: 593 x 397
COMPO
100 um
Co
Cts
109
0
Project: December_11_2018
Comment: CP-085-08_Asp1_1um
Date: 2018/12/13
Accel Voltage: 20.0 kV
Beam Current: 9.995e-008 A
Dwell Time: 10.0
Image Size: 593 x 397
Co
100 um
Au
Cts
201
0
Project: December_11_2018
Comment: CP-085-08_Asp1_1um
Date: 2018/12/13
Accel Voltage: 20.0 kV
Beam Current: 9.995e-008 A
Dwell Time: 10.0
Image Size: 593 x 397
Au
100 um

085-15 Asp01

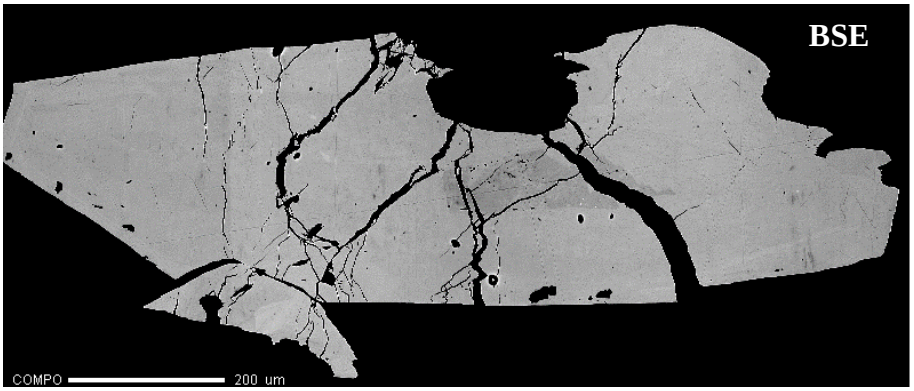
BSE
COMPO
200 um
COMPO
Cts
4,095
0
Project: December_11_2018
Comment: CP-84-15_Asp1_1p5um
Date: 2018/12/12
Accel Voltage: 20.0 kV
Beam Current: 1.009e-007 A
Dwell Time: 10.0
Image Size: 793 x 335

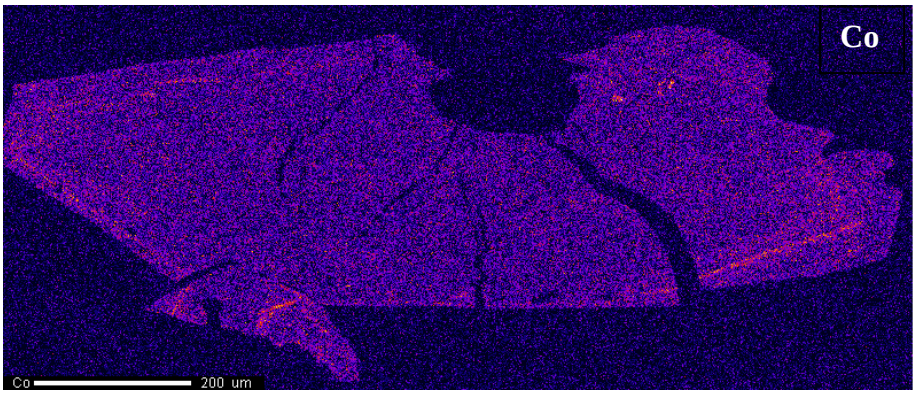
Co
Co
200 um
Co
Cts
12
0
Project: December_11_2018
Comment: CP-84-15_Asp1_1p5um
Date: 2018/12/12
Accel Voltage: 20.0 kV
Beam Current: 1.009e-007 A
Dwell Time: 10.0
Image Size: 793 x 335

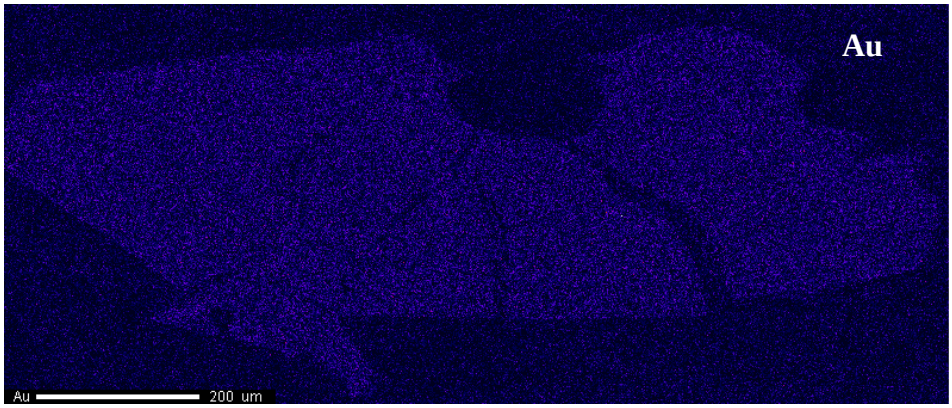
Au
Au
200 um
Au
Cts
21
0
Project: December_11_2018
Comment: CP-84-15_Asp1_1p5um
Date: 2018/12/12
Accel Voltage: 20.0 kV
Beam Current: 1.009e-007 A
Dwell Time: 10.0
Image Size: 793 x 335

084-16 Asp01

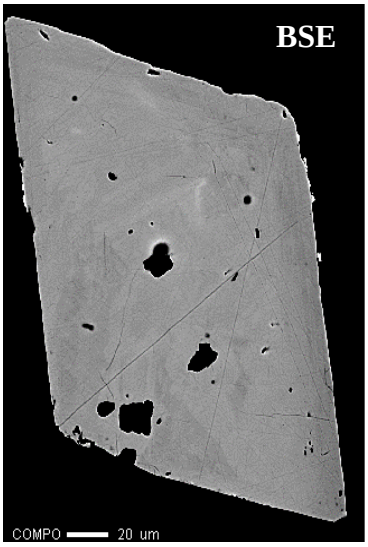

COMPO
Cts
4,095
0
Project: December_11_2018
Comment: CP-084-16_Asp1_0.6um
Date: 2018/12/13
Accel Voltage: 20.0 kV
Beam Current: 1.002e-007 A
Dwell Time: 10.0
Image Size: 323 x 439

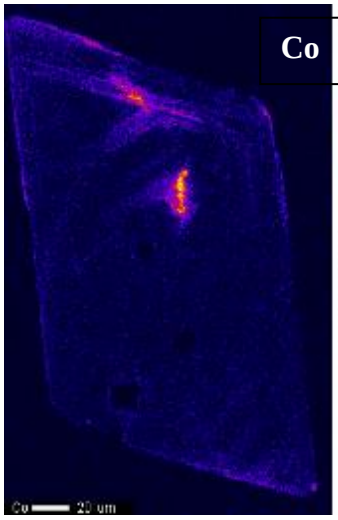

Co
Cts
47
0
Project: December_11_2018
Comment: CP-084-16_Asp1_0.6um
Date: 2018/12/13
Accel Voltage: 20.0 kV
Beam Current: 1.002e-007 A
Dwell Time: 10.0
Image Size: 323 x 439

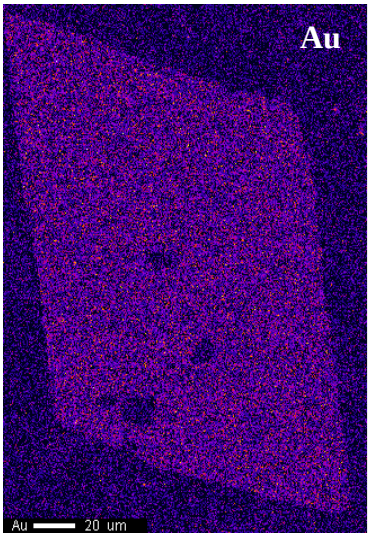

Au
Cts
8
0
Project: December_11_2018
Comment: CP-084-16_Asp1_0.6um
Date: 2018/12/13
Accel Voltage: 20.0 kV
Beam Current: 1.002e-007 A
Dwell Time: 10.0
Image Size: 323 x 439

084-9B Asp01

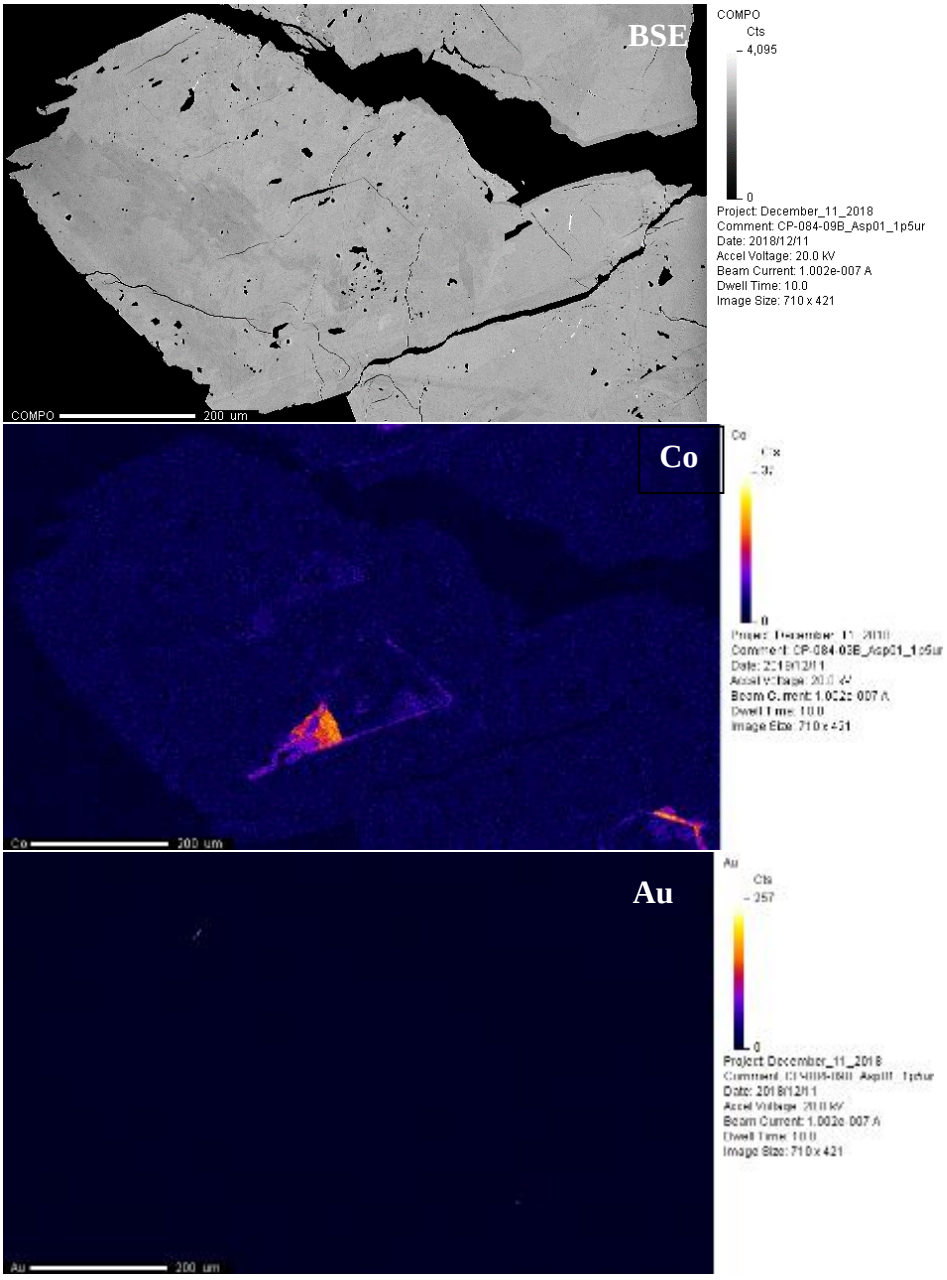
BSE
COMPO
Cts
4,095
0
Project: December_11_2018
Comment: CP-084-09B_Asp01_1p5ur
Date: 2018/12/11
Accel Voltage: 20.0 kV
Beam Current: 1.002e-007 A
Dwell Time: 10.0
Image Size: 710 x 421
COMPO 200 um
Co
Co
200 um
Au
Au
200 um

085-13 Asp02

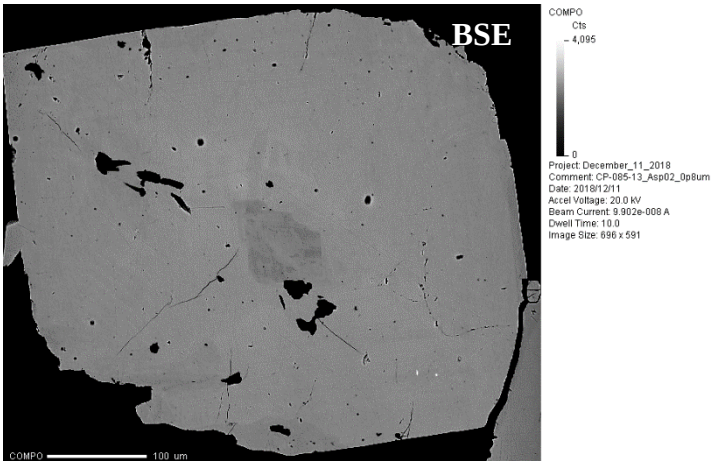
BSE
COMPO
Cts
4,095
0
Project: December_11_2018
Comment: CP-085-13_Asp02_0p8um
Date: 2018/12/11
Accel Voltage: 20.0 kV
Beam Current: 9.902e-008 A
Dwell Time: 10.0
Image Size: 696 x 591
COMPO
100 um

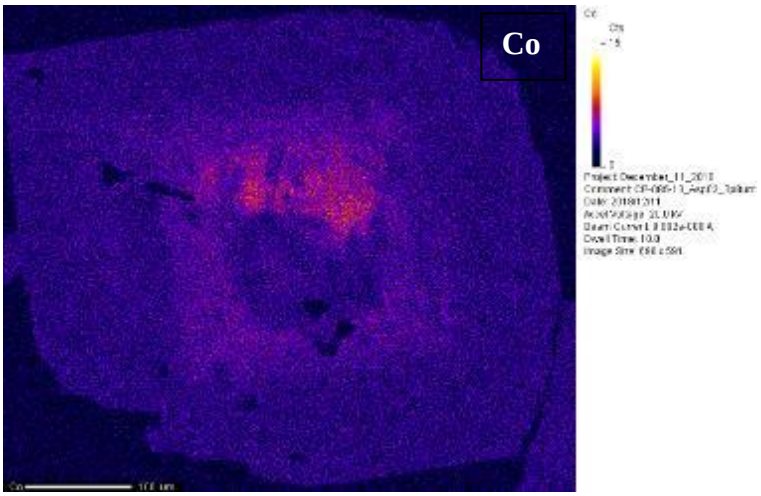
Co

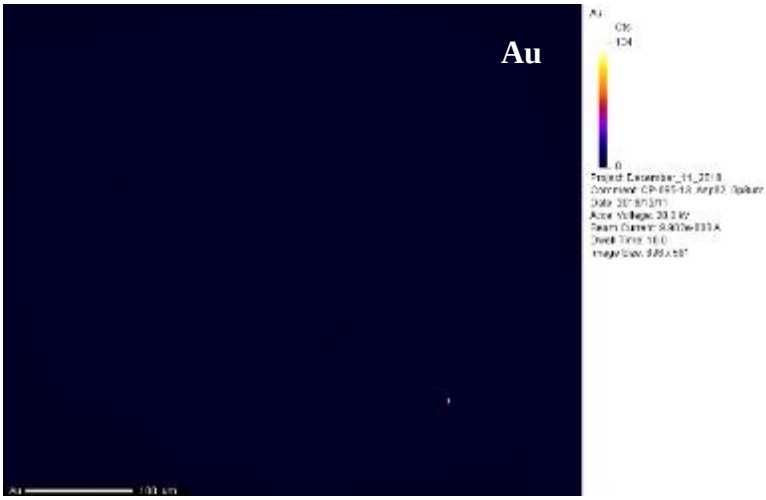
Au

085-13 Asp03

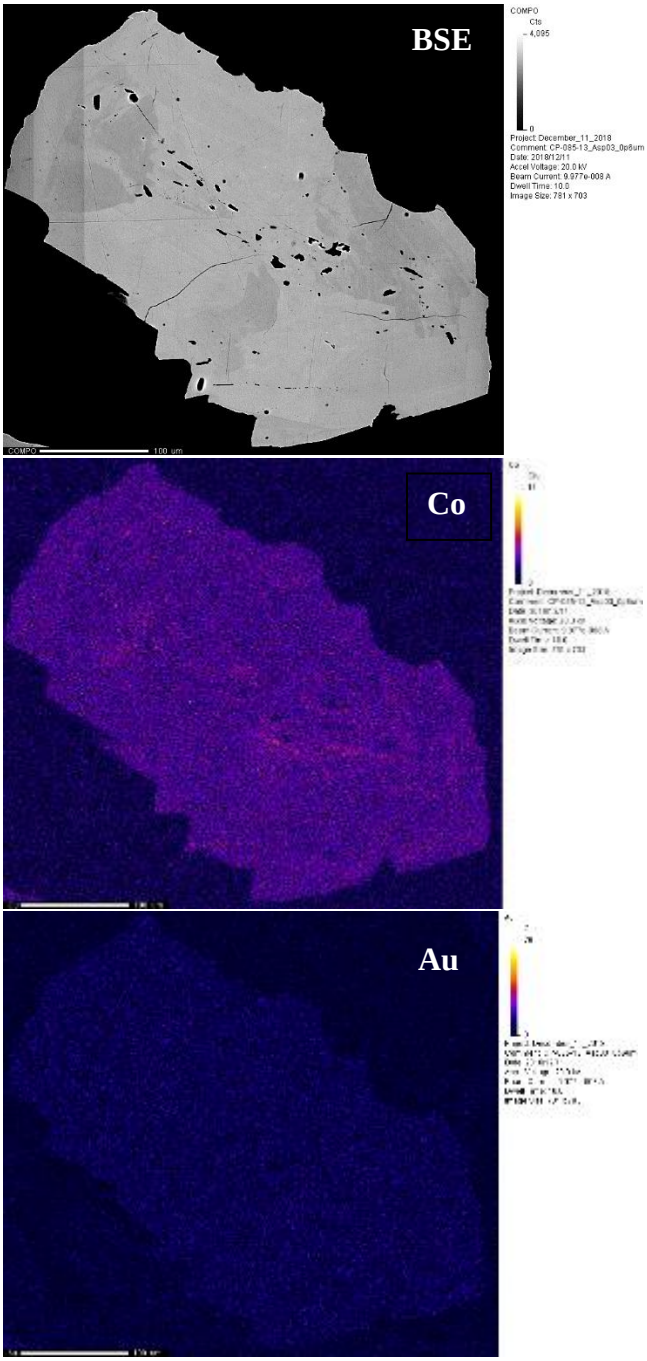
BSE
COMPO
Cts
4,095
0
Project December_11_2018
Comment CP-085-13_Asp03_0p8um
Date 2018/12/11
Accel Voltage 20.0 kV
Beam Current 9.977e-009 A
Dwell Time 10.0
Image Size 781 x 703
COMPO
100 µm
Co
Au

085-13 Asp01

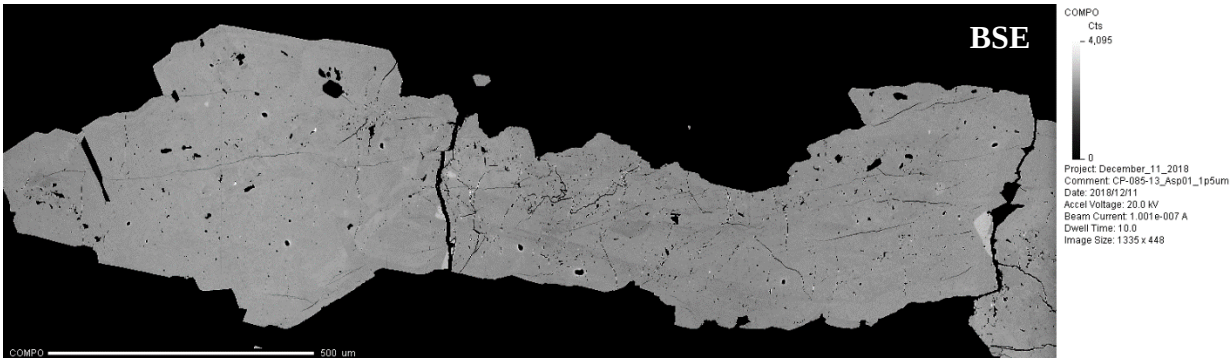
BSE
COMPO
Cts
4,095
0
Project: December_11_2018
Comment: CP-085-13_Asp01_1p5um
Date: 2018/12/11
Accel Voltage: 20.0 kV
Beam Current: 1.001e-007 A
Dwell Time: 10.0
Image Size: 1335 x 448
COMPO
500 um

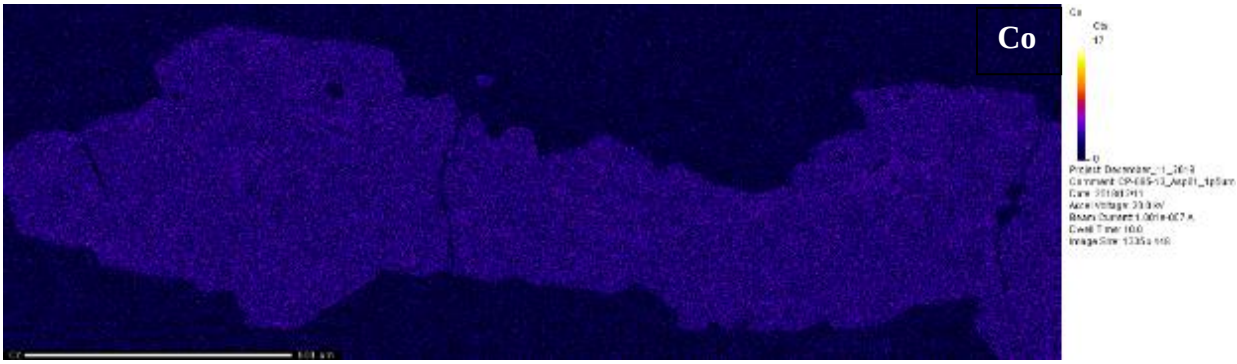
Co

Au

096-08 Asp01

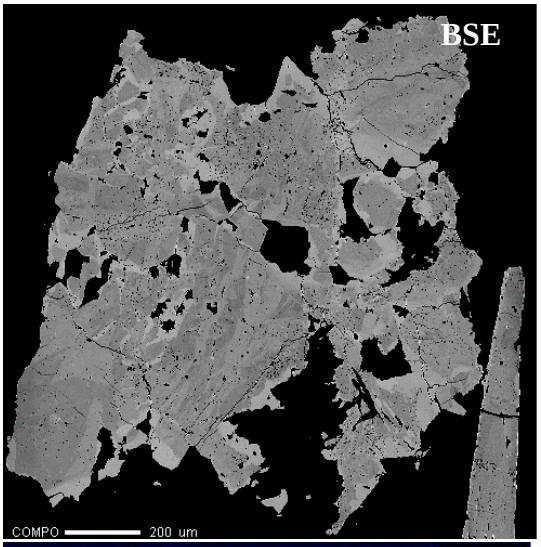
BSE
COMPO
Cts
4,095
0
Project: December_11_2018
Comment: CP-096-08_Asp01_3um
Date: 2018/12/11
Accel Voltage: 20.0 kV
Beam Current: 1.000e-007 A
Dwell Time: 10.0
Image Size: 493 x 494
COMPO
200 um

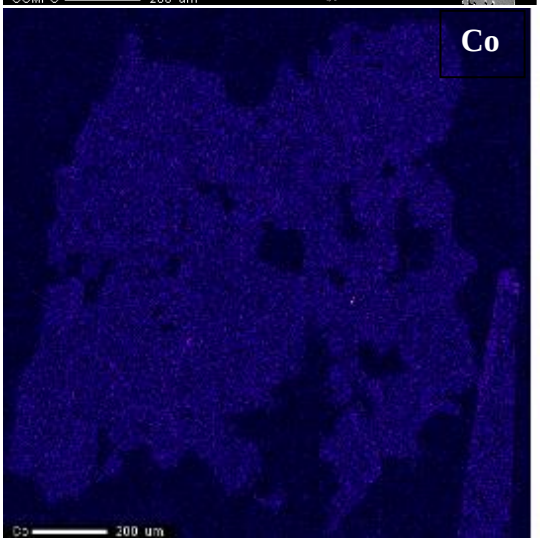
Co
Cts
25
0
Project: December_11_2018
Comment: CP-096-08_Asp01_3um
Date: 2018/12/11
Accel Voltage: 20.0 kV
Beam Current: 1.000e-007 A
Dwell Time: 10.0
Image Size: 493 x 494
Co
200 um

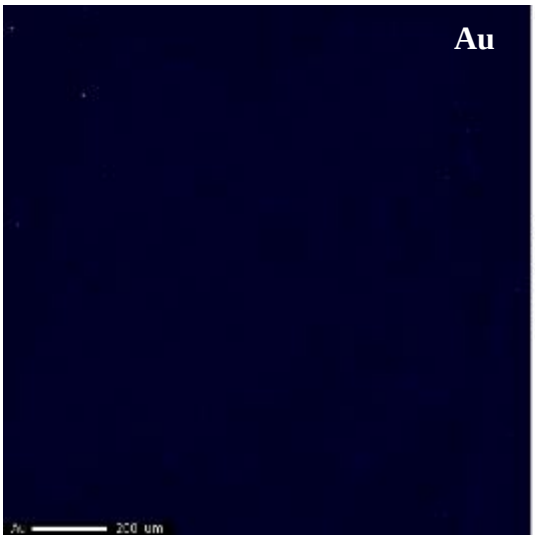
Au
Cts
112
0
Project: December_11_2018
Comment: CP-096-08_Asp01_3um
Date: 2018/12/11
Accel Voltage: 20.0 kV
Beam Current: 1.000e-007 A
Dwell Time: 10.0
Image Size: 493 x 494
Au
200 um

108-03 Asp01

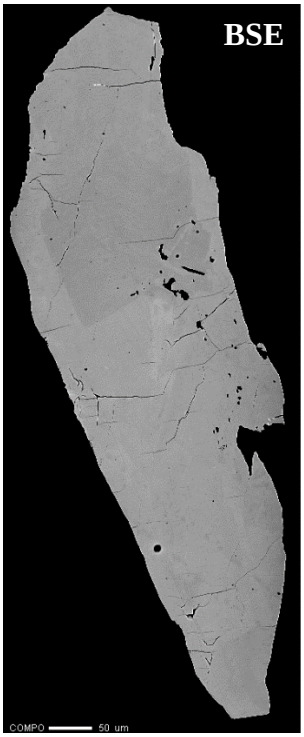
BSE
COMPO
Cts
4,095
0
Project: December_11_2018
Comment: CP-108-03_Asp01_1um
Date: 2018/12/11
Accel Voltage: 20.0 kV
Beam Current: 1.000e-007 A
Dwell Time: 10.0
Image Size: 371 x 908
COMPO
50 um

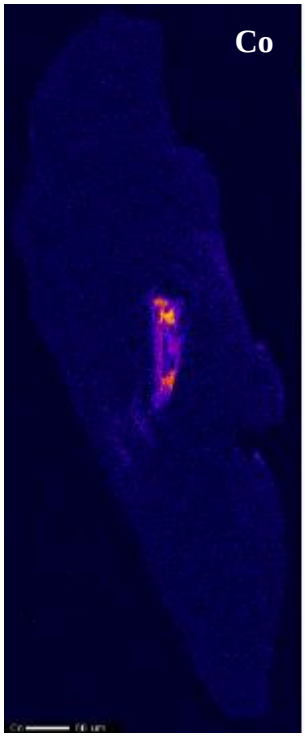
Co

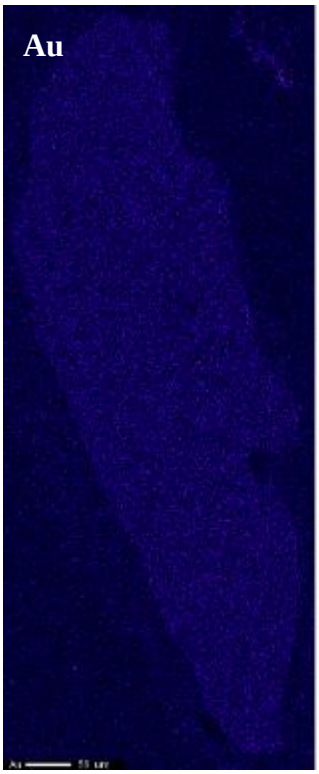
Au

085-2A Asp01

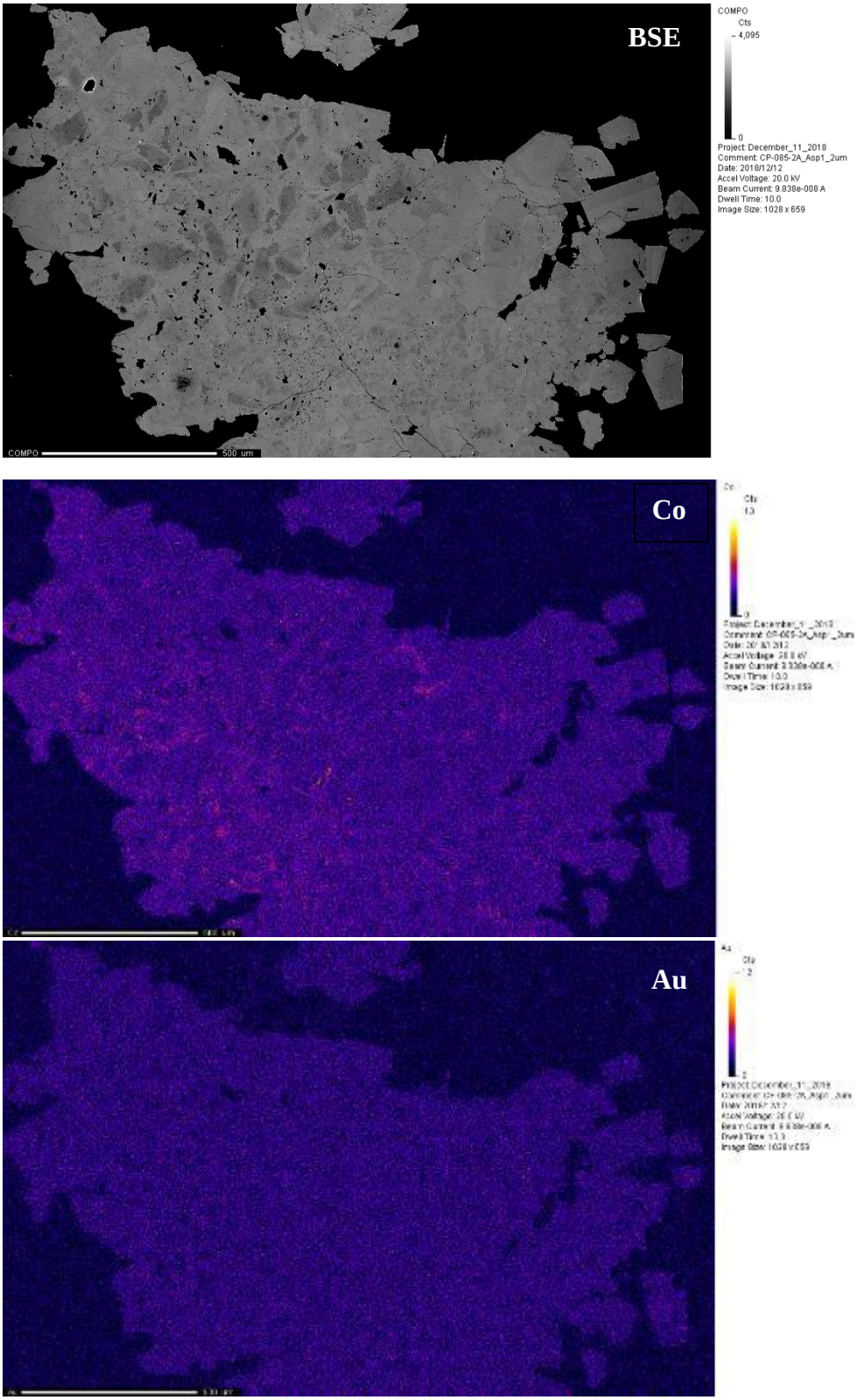
BSE
COMPO
Cts
4,095
0
Project: December_11_2018
Comment: CP-085-2A_Asp1_2um
Date: 2018/12/12
Accel Voltage: 20.0 kV
Beam Current: 9.838e-008 A
Dwell Time: 10.0
Image Size: 1028 x 659
COMPO
500 um
Co
Au

108-03 Asp02

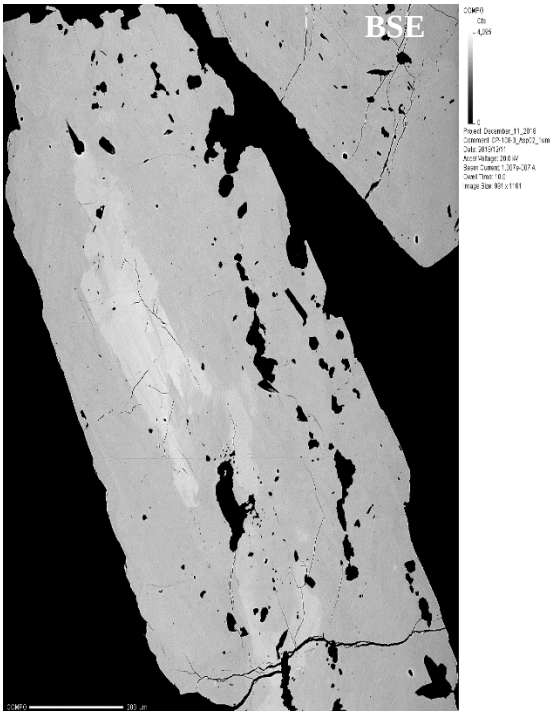

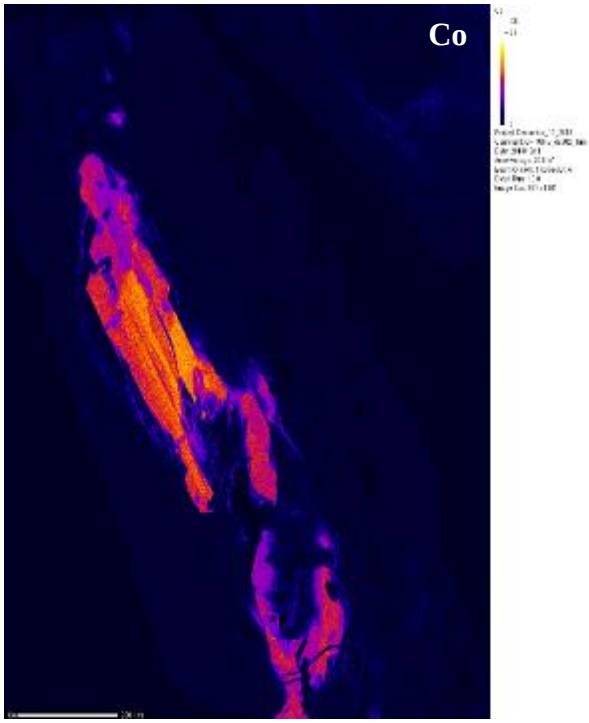

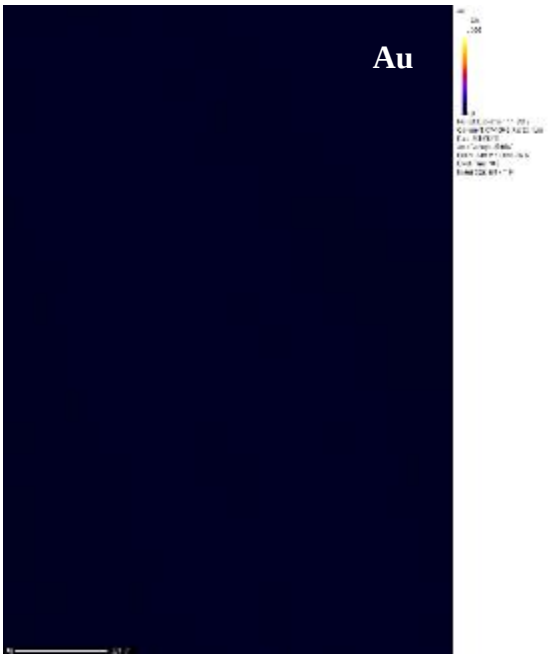

156-02 Asp01

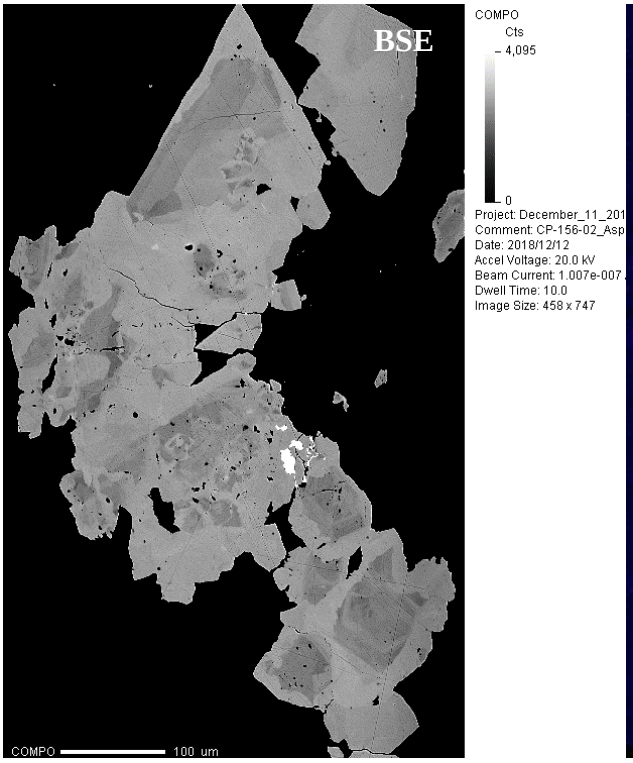
BSE
COMPO
Cts
4,095
0
Project: December_11_201
Comment: CP-156-02_Asp
Date: 2018/12/12
Accel Voltage: 20.0 kV
Beam Current: 1.007e-007
Dwell Time: 10.0
Image Size: 458 x 747
COMPO
100 um

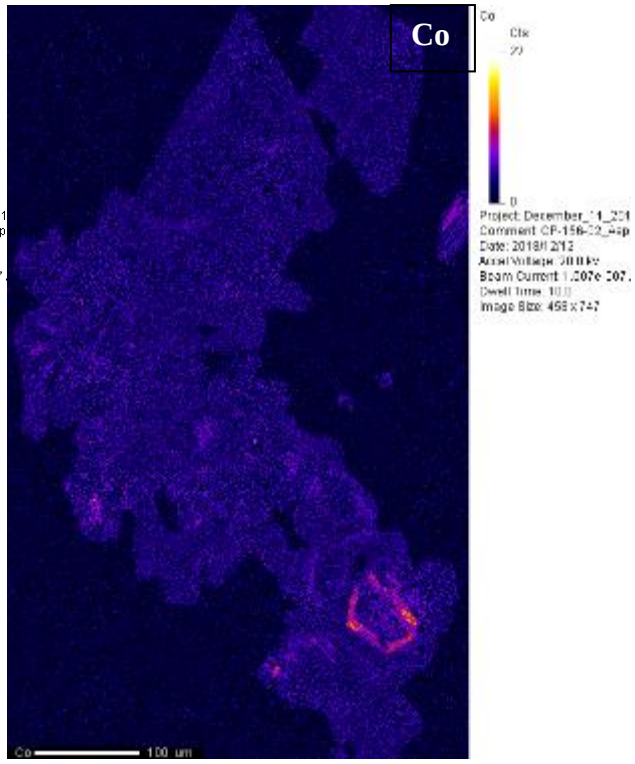
Co
Co
Cts
0
Project: December_11_201
Comment: CP-156-02_Asp
Date: 2018/12/12
Image Size: 458 x 747
Co
100 um

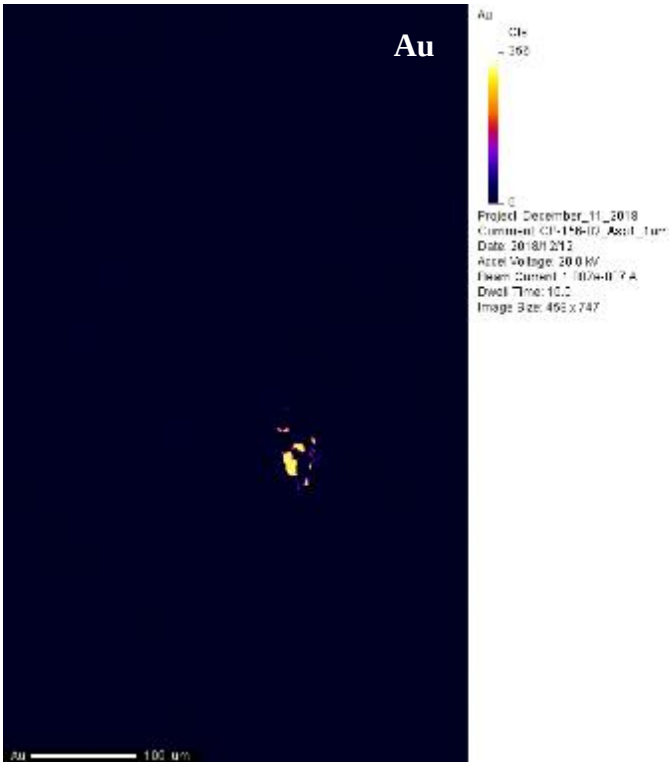
Au
Cts
0
Project: December_11_2018
Date: 2018/12/12
Accel Voltage: 20.0 kV
Dwell Time: 10.0
Image Size: 458 x 747
Au
100 um

156-04 Asp01

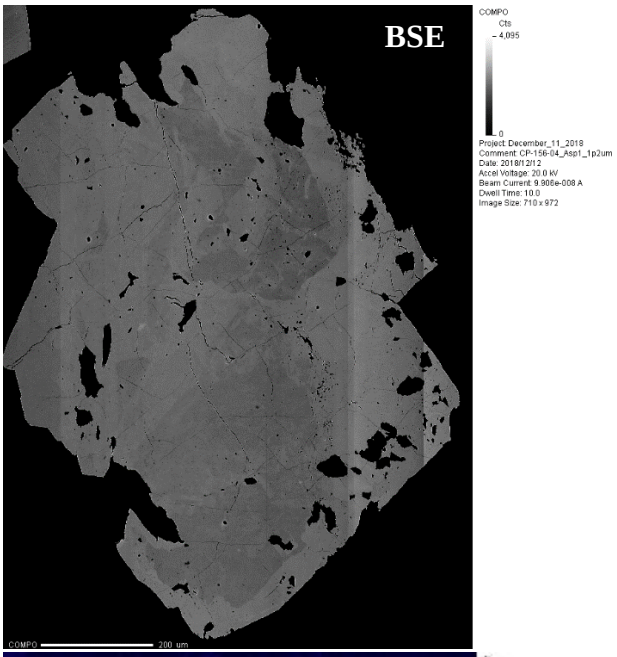
BSE
COMPO
Cts
4,095
0
Project: December_11_2018
Comment: CP-156-04_Asp1_1p2um
Date: 2018/12/12
Accel Voltage: 20.0 kV
Beam Current: 9.985e-008 A
Dwell Time: 10.0
Image Size: 710 x 972
COMPO
200 um

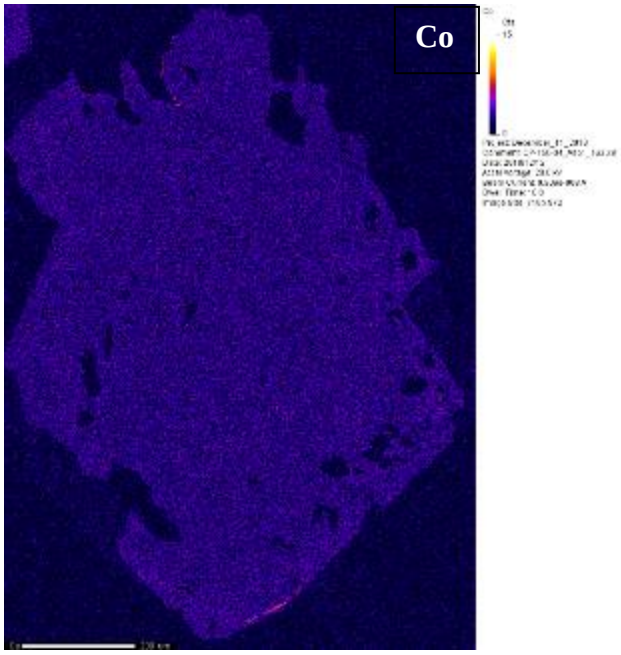
Co

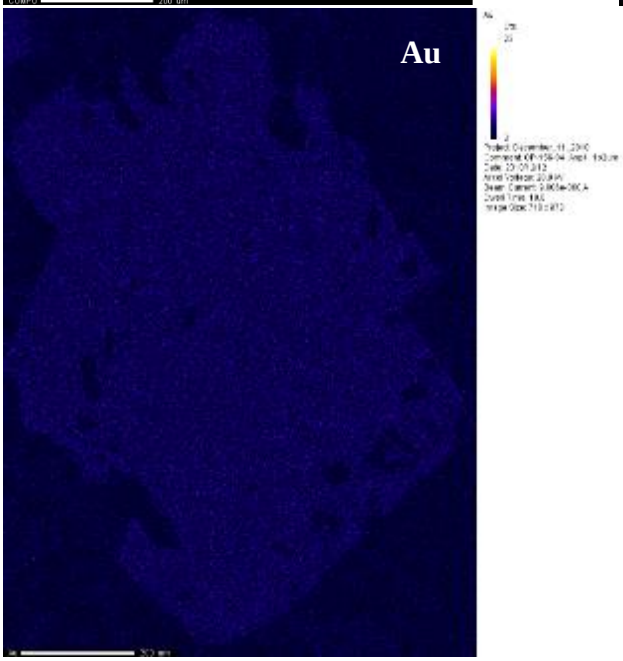
Au

156-05 Asp01

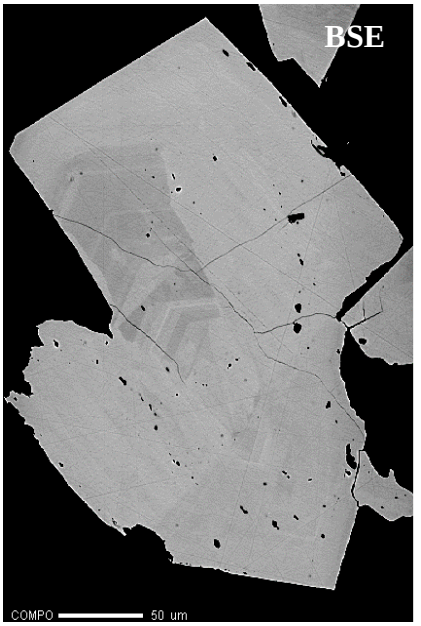
BSE
COMPO
50 um

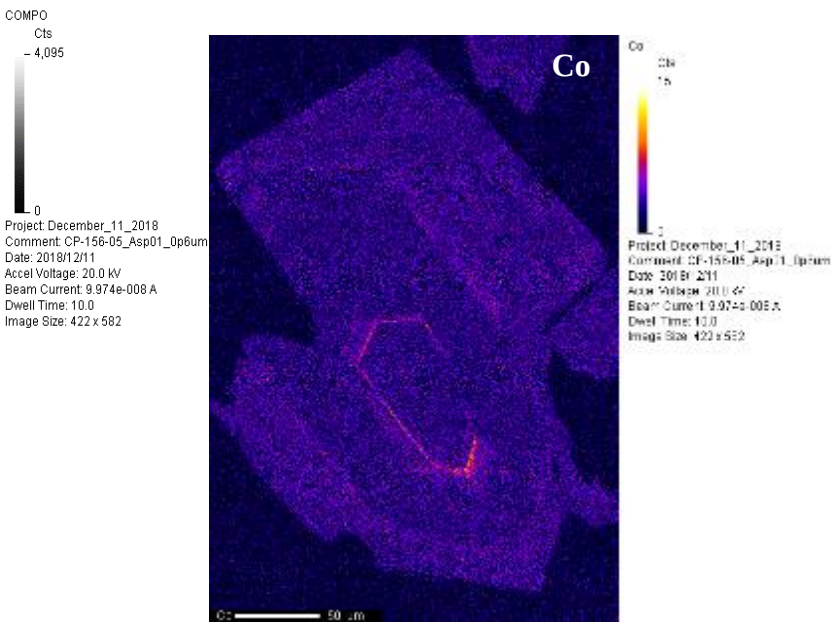
COMPO
Cts
4,095
0
Project: December_11_2018
Comment: CP-156-05_Asp01_0p6um
Date: 2018/12/11
Accel Voltage: 20.0 kV
Beam Current: 9.974e-008 A
Dwell Time: 10.0
Image Size: 422 x 582

Co
50 um

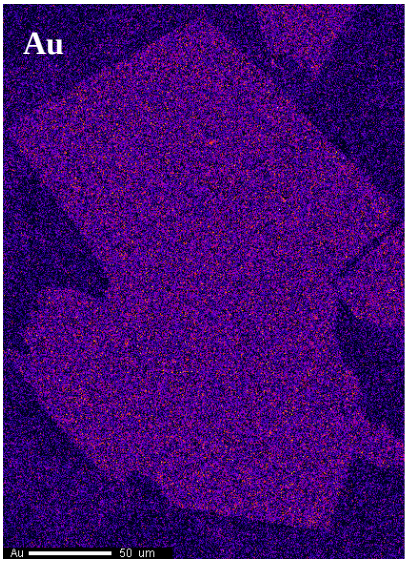
Au
50 um

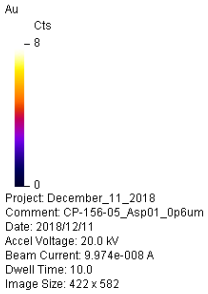
Au
Cts
8
0
Project: December_11_2018
Comment: CP-156-05_Asp01_0p6um
Date: 2018/12/11
Accel Voltage: 20.0 kV
Beam Current: 9.974e-008 A
Dwell Time: 10.0
Image Size: 422 x 582

156-06 Asp01

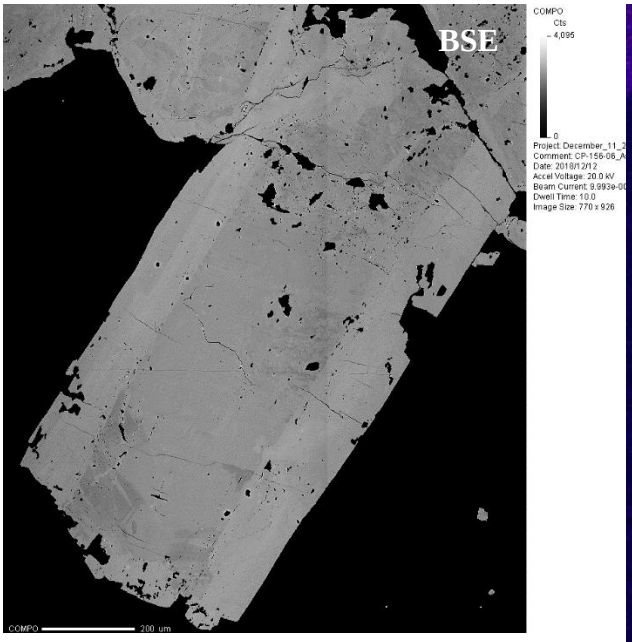

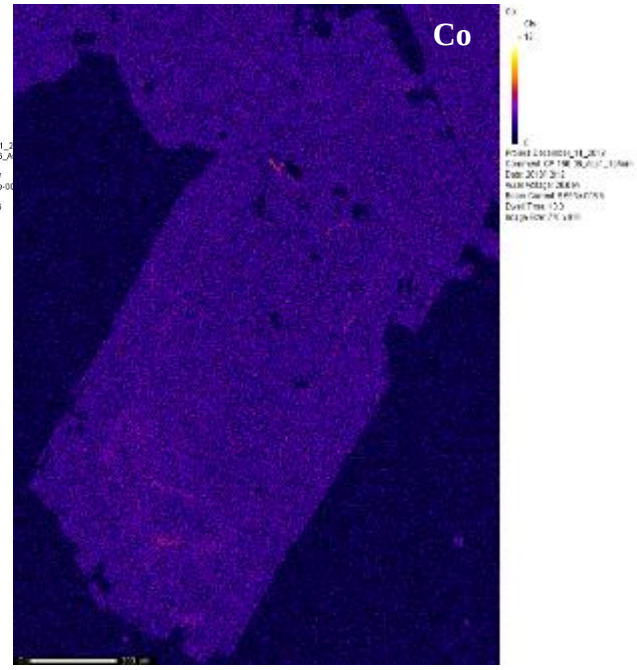

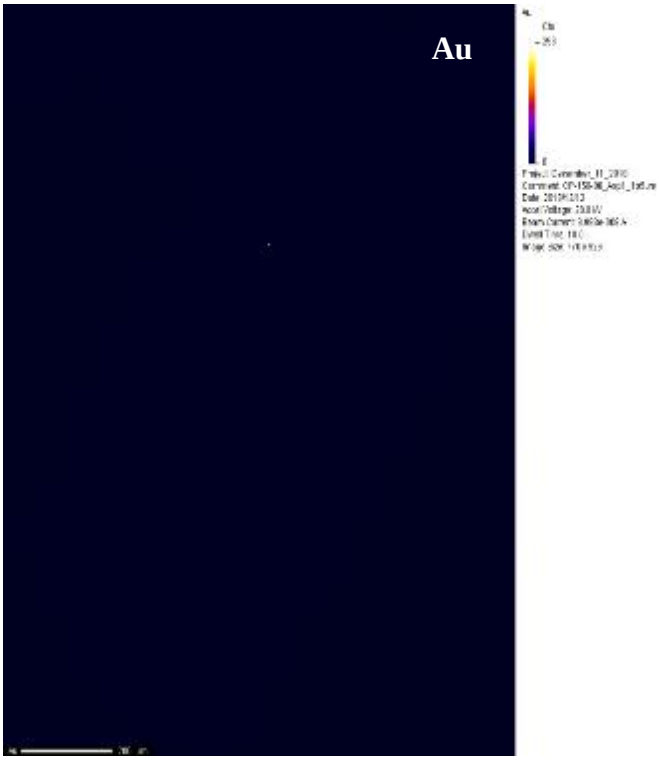

156-04 Asp02

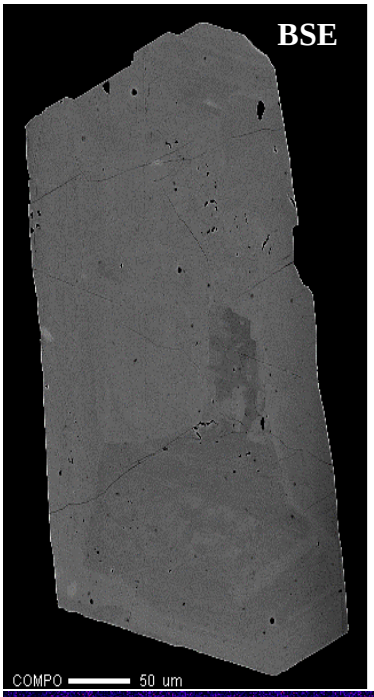

COMPO
Cts
4,095
0
Project: December_11_2018
Comment: CP-156-04_Asp2_1um
Date: 2018/12/12
Accel Voltage: 20.0 kV
Beam Current: 9.820e-008 A
Dwell Time: 10.0
Image Size: 318 x 517

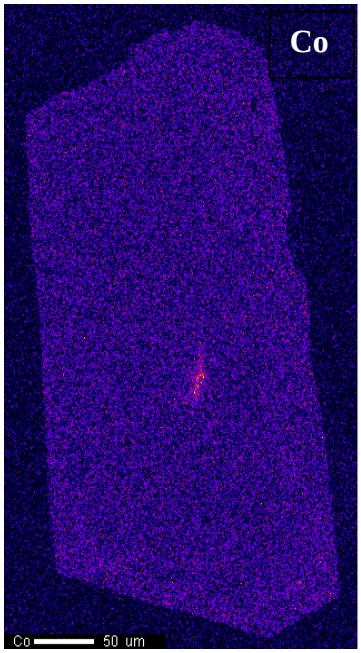

Co
Cts
14
0
Project: December_11_2018
Comment: CP-156-04_Asp2_1um
Date: 2018/12/12
Accel Voltage: 20.0 kV
Beam Current: 9.820e-008 A
Dwell Time: 10.0
Image Size: 318 x 517

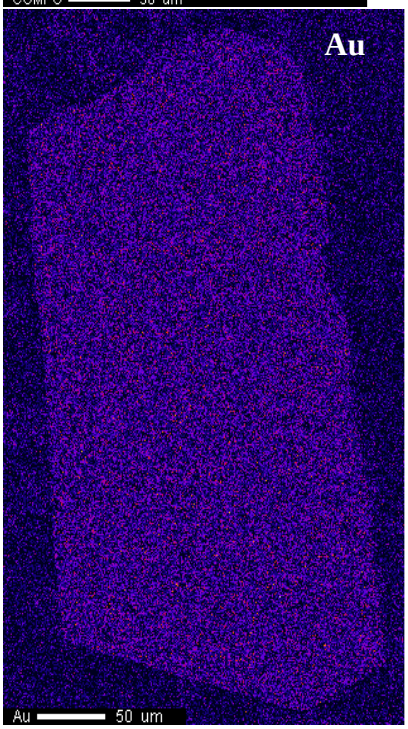

Au
Cts
11
0
Project: December_11_2018
Comment: CP-156-04_Asp2_1um
Date: 2018/12/12
Accel Voltage: 20.0 kV
Beam Current: 9.820e-008 A
Dwell Time: 10.0
Image Size: 318 x 517

156-02 Asp02

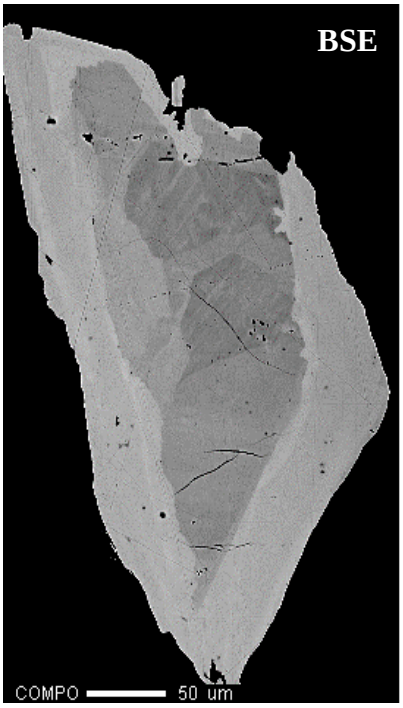

COMPO
Cts
4,095
0
Project: December_11_2018
Comment: CP-156-02_Asp2_1
Date: 2018/12/12
Accel Voltage: 20.0 kV
Beam Current: 1.010e-007 A
Dwell Time: 10.0
Image Size: 270 x 450

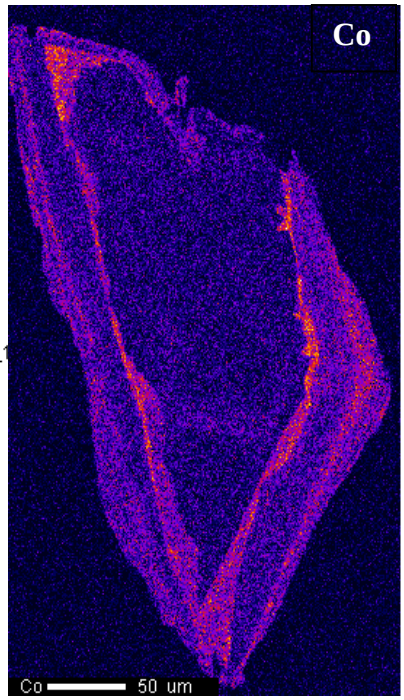

Co
Cts
19
0
Project: December_11_2
Comment: CP-156-02_As
Date: 2018/12/12
Accel Voltage: 20.0 kV
Beam Current: 1.010e-00
Dwell Time: 10.0
Image Size: 270 x 450

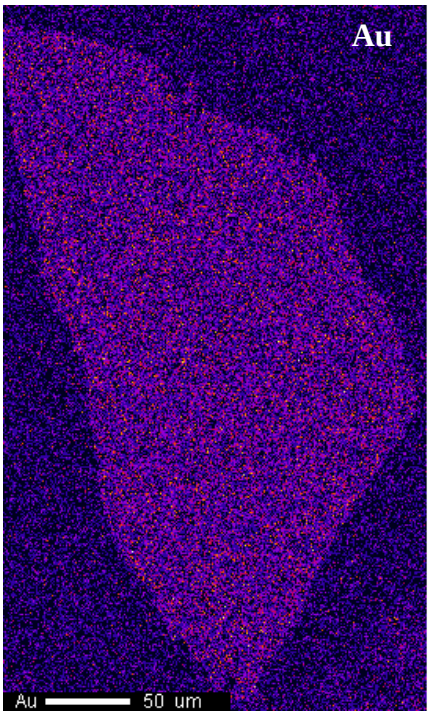

Au
Cts
8
0
Project: December_11_2018
Comment: CP-156-02_Asp2_1um
Date: 2018/12/12
Accel Voltage: 20.0 kV
Beam Current: 1.010e-007 A
Dwell Time: 10.0
Image Size: 270 x 450

156-06 Asp02

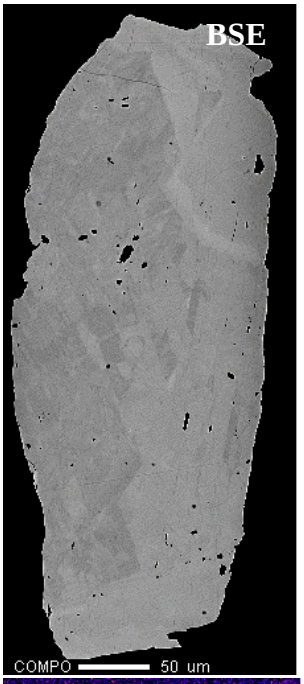

COMPO
Cts
4,095
0
Project: December_11_2018
Comment: CP-156-06_Asp2_1um
Date: 2018/12/12
Accel Voltage: 20.0 kV
Beam Current: 9.987e-008 A
Dwell Time: 10.0
Image Size: 222 x 508

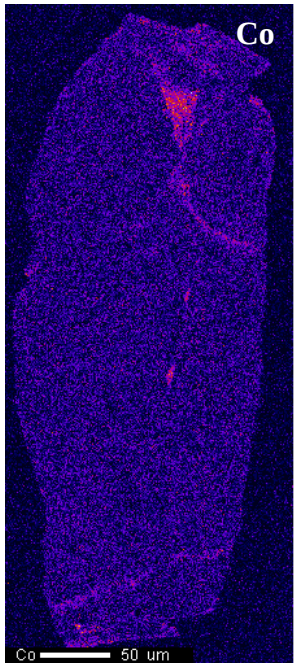

Co
Cts
18
0
Project: December_11_2018
Comment: CP-156-06_Asp2_1um
Date: 2018/12/12
Accel Voltage: 20.0 kV
Beam Current: 9.987e-008 A
Dwell Time: 10.0
Image Size: 222 x 508

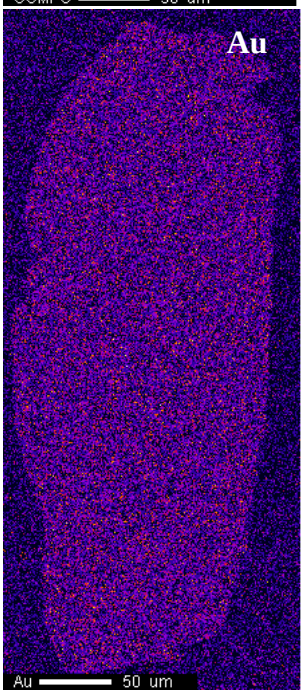

Au
Cts
8
0
Project: December_11_2018
Comment: CP-156-06_Asp2_1um
Date: 2018/12/12
Accel Voltage: 20.0 kV
Beam Current: 9.987e-008 A
Dwell Time: 10.0
Image Size: 222 x 508

Appendix F : LA-ICP-MS

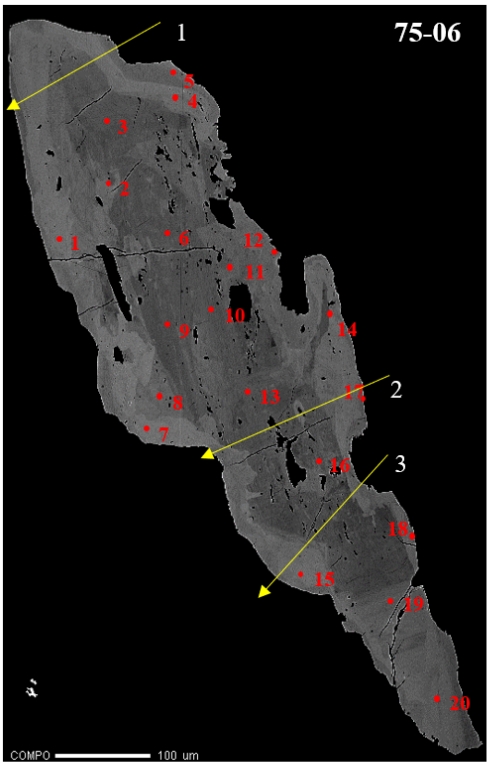

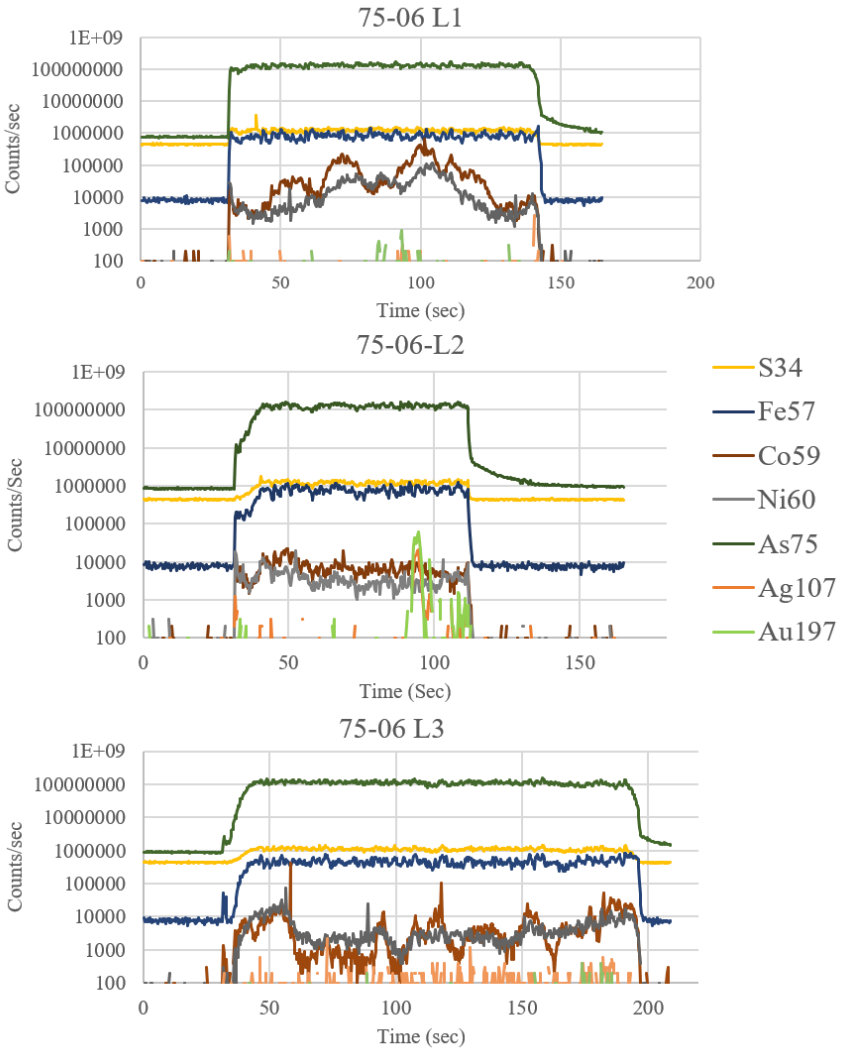

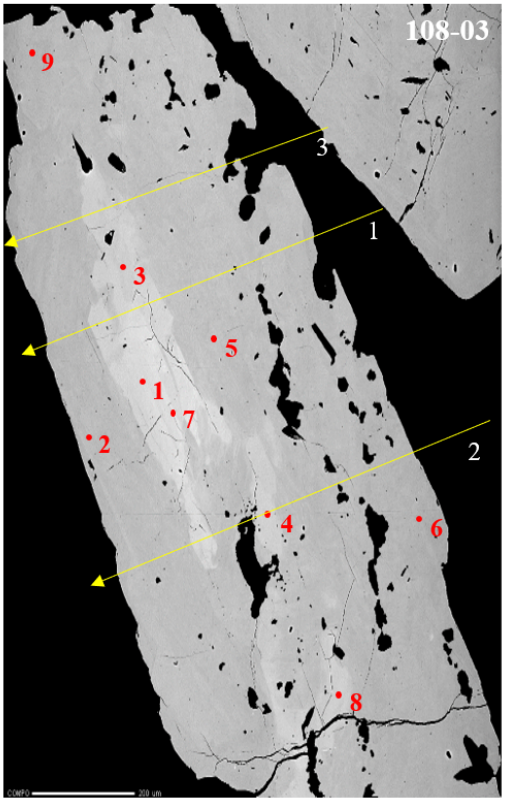
108-03
9
3
1
3
5
1
7
2
2
4
6
8

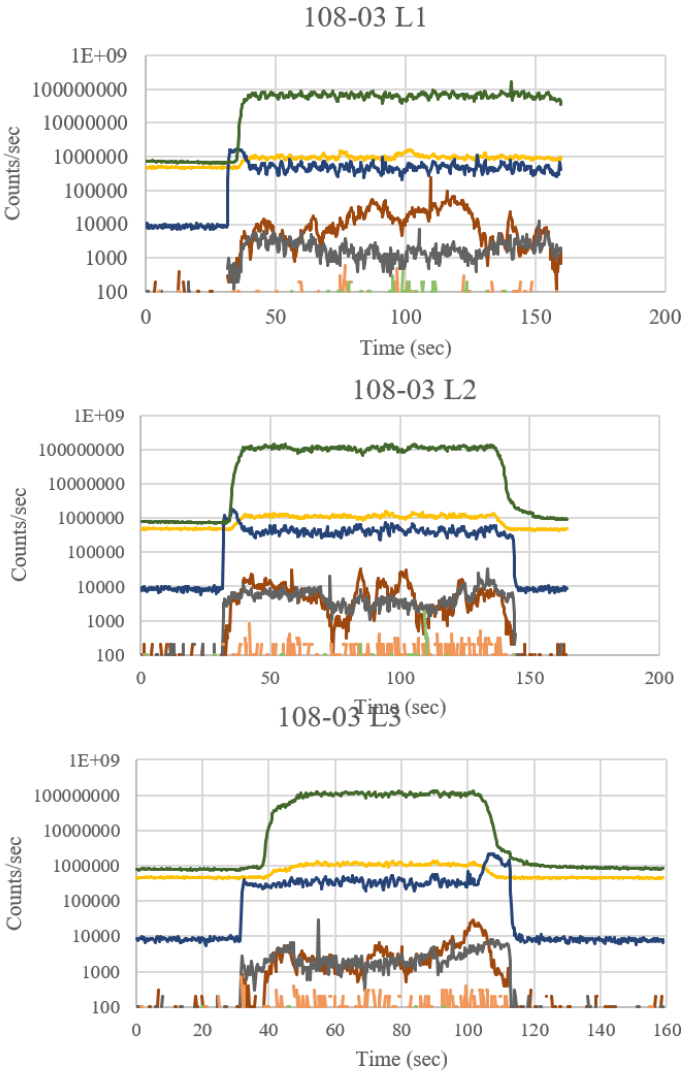
108-03 L1
1E+09
100000000
10000000
1000000
100000
10000
1000
100
Counts/sec
0
50
100
150
200
Time (sec)
108-03 L2
1E+09
100000000
10000000
1000000
100000
10000
1000
100
Counts/sec
0
50
100
150
200
Time (sec)
S34
Fe57
Co59
Ni60
As75
Ag107
Au197
108-03 L3
1E+09
100000000
10000000
1000000
100000
10000
1000
100
Counts/sec
0
20
40
60
80
100
120
140
160
Time (sec)

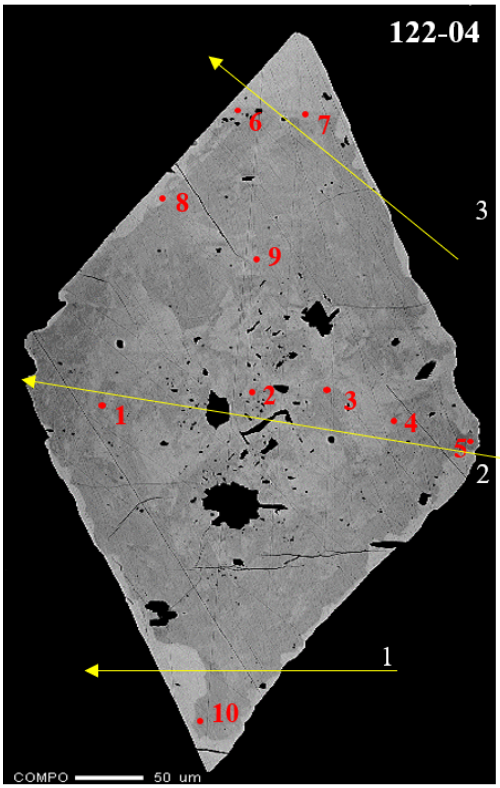
122-04
1
2
3
4
5
6
7
8
9
10
1
2
3
COMPO
50 um

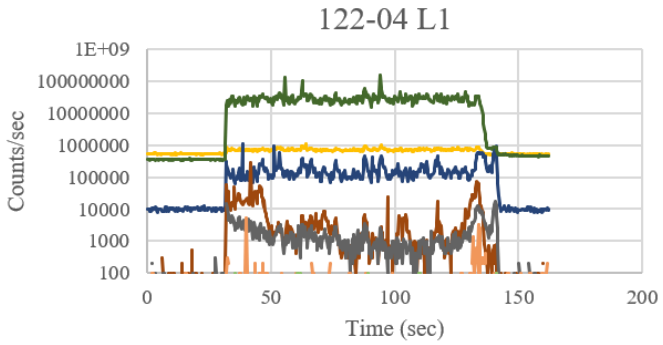
122-04 L1
1E+09
100000000
10000000
1000000
100000
10000
1000
100
Counts/sec
0
50
100
150
200
Time (sec)

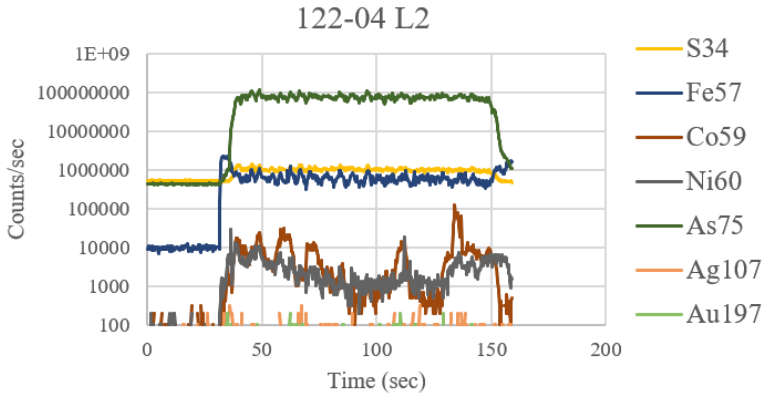
122-04 L2
1E+09
100000000
10000000
1000000
100000
10000
1000
100
Counts/sec
0
50
100
150
200
Time (sec)
S34
Fe57
Co59
Ni60
As75
Ag107
Au197

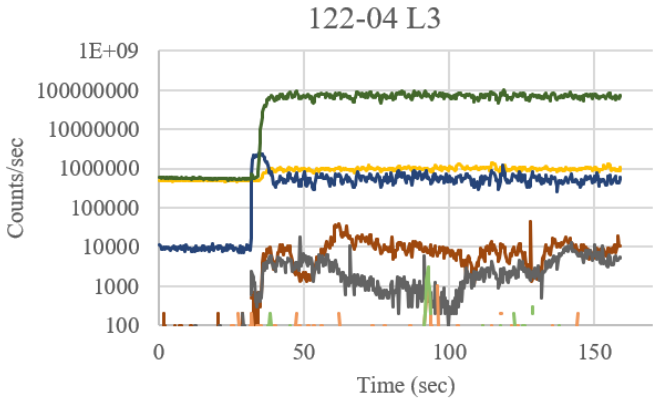
122-04 L3
1E+09
100000000
10000000
1000000
100000
10000
1000
100
Counts/sec
0
50
100
150
Time (sec)

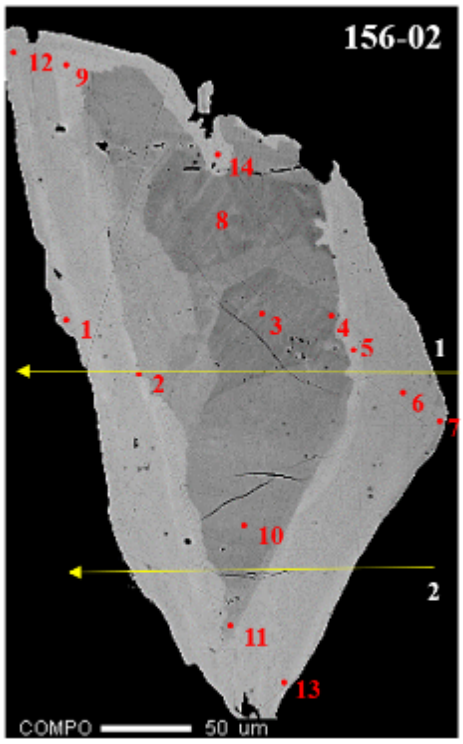
156-02
12
9
14
8
1
3
4
5
1
2
6
7
10
2
11
13
COMPO
50 um

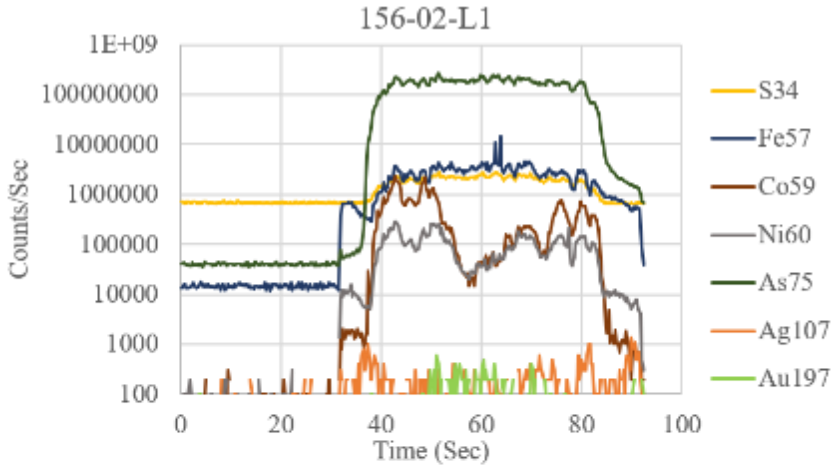
156-02-L1
1E+09
100000000
10000000
1000000
100000
10000
1000
100
Counts/Sec
0
20
40
60
80
100
Time (Sec)
S34
Fe57
Co59
Ni60
As75
Ag107
Au197

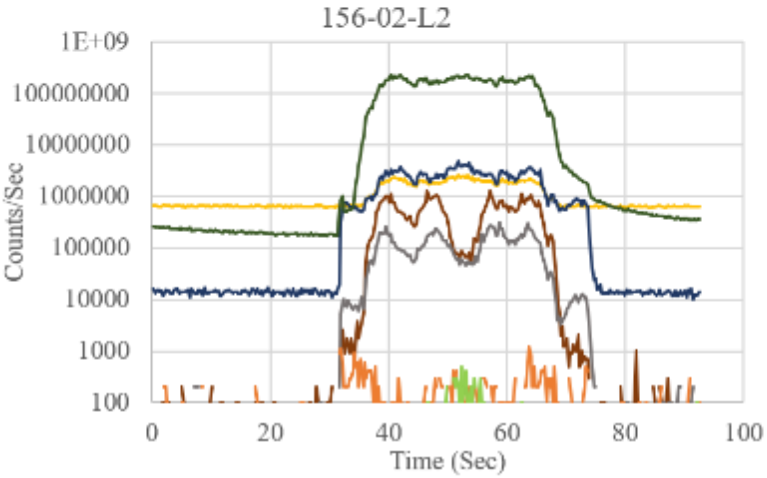
156-02-L2
1E+09
100000000
10000000
1000000
100000
10000
1000
100
Counts/Sec
0
20
40
60
80
100
Time (Sec)

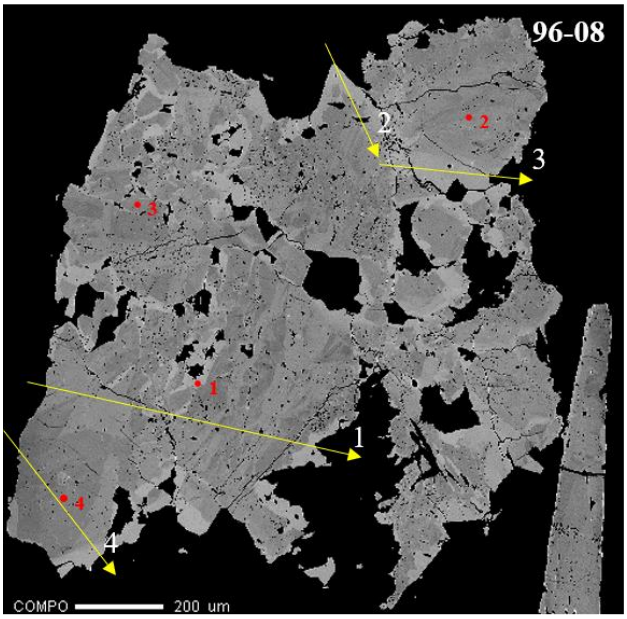
96-08
1
2
3
4
COMPO
200 um

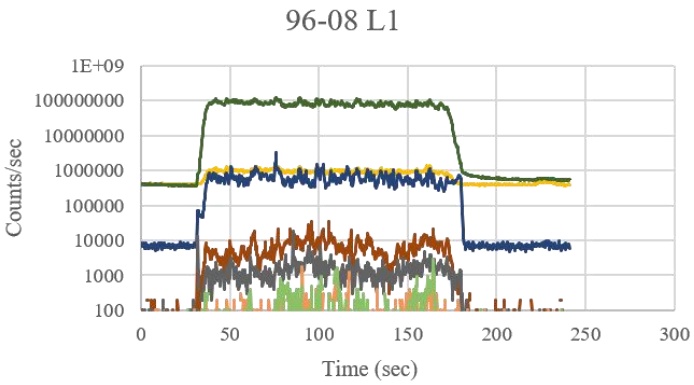
96-08 L1
Counts/sec
Time (sec)

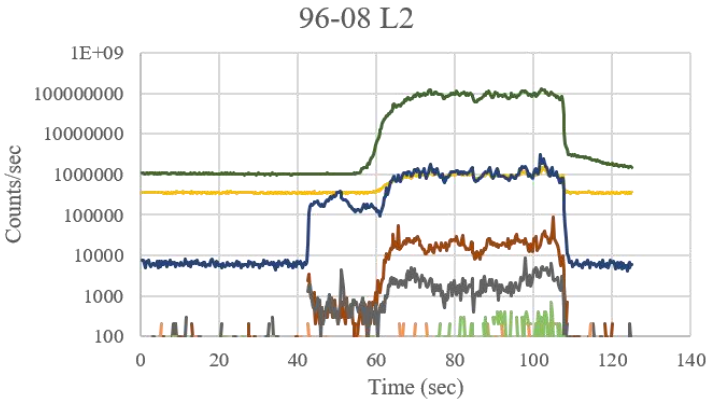
96-08 L2
Counts/sec
Time (sec)

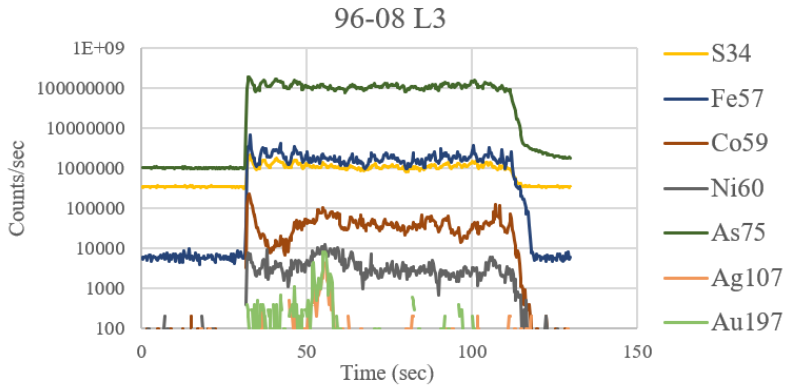
96-08 L3
Counts/sec
Time (sec)
S34
Fe57
Co59
Ni60
As75
Ag107
Au197

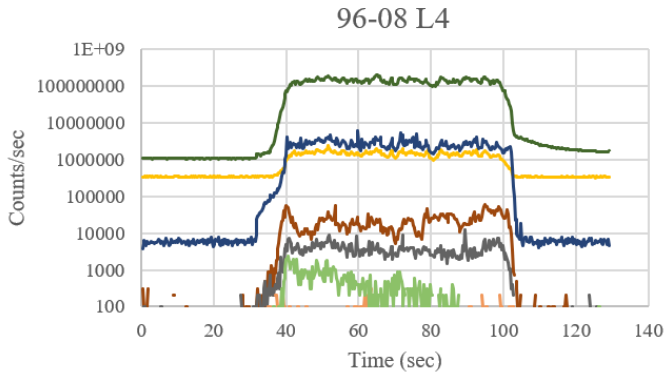
96-08 L4
Counts/sec
Time (sec)

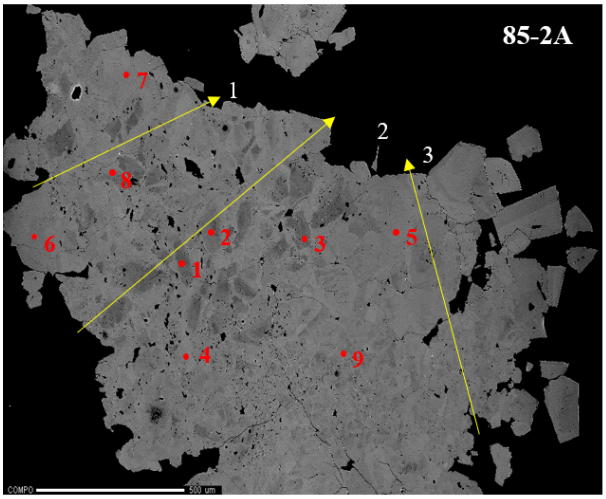
85-2A
1
2
3
7
8
6
2
3
5
1
4
9

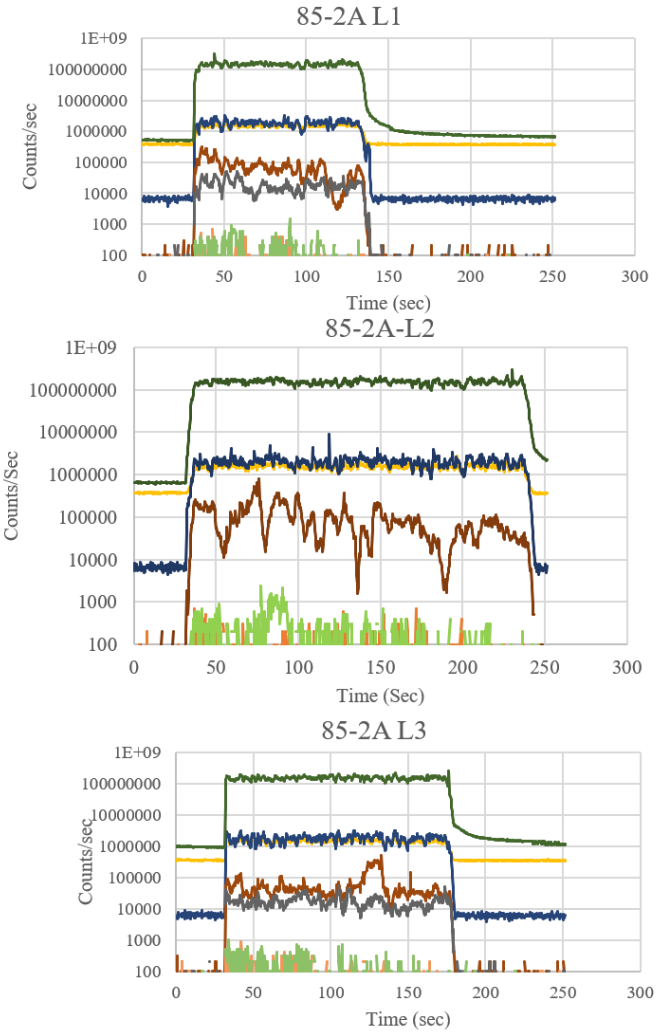
85-2A L1
Counts/sec
Time (sec)
85-2A-L2
Counts/Sec
Time (Sec)
85-2A L3
Counts/sec
Time (sec)
S34
Fe57
Co59
As75
Ag107
Au197

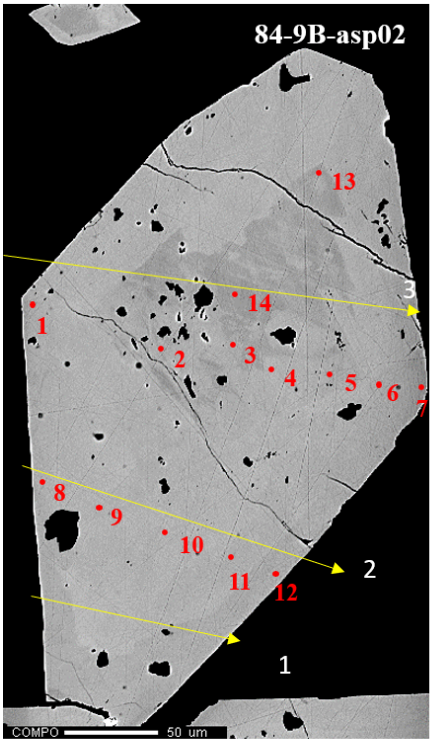
84-9B-asp02
13
14
1
2
3
4
5
6
7
8
9
10
11
12
2
1
COMPO
50 um

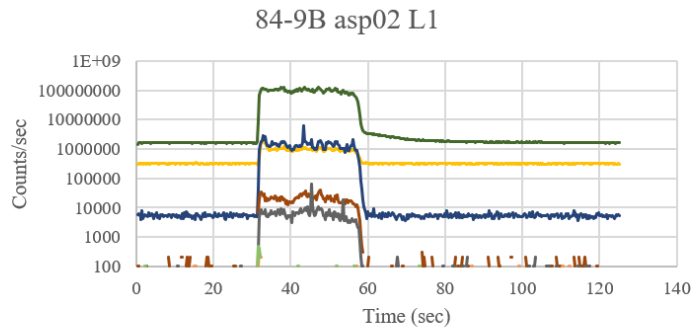
84-9B asp02 L1
Counts/sec
1E+09
100000000
10000000
1000000
100000
10000
1000
100
0
20
40
60
80
100
120
140
Time (sec)

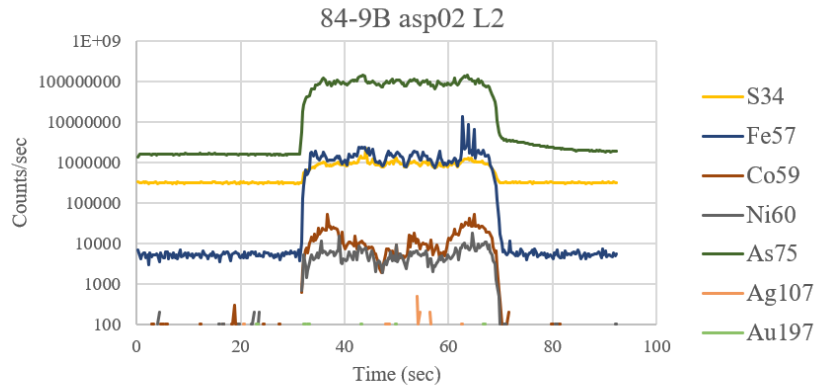
84-9B asp02 L2
Counts/sec
1E+09
100000000
10000000
1000000
100000
10000
1000
100
0
20
40
60
80
100
Time (sec)
S34
Fe57
Co59
Ni60
As75
Ag107
Au197

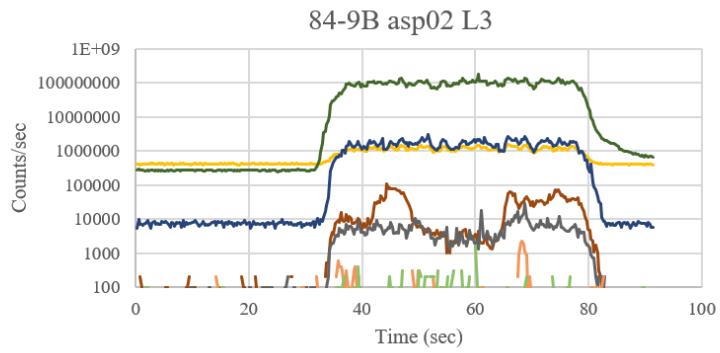
84-9B asp02 L3
Counts/sec
1E+09
100000000
10000000
1000000
100000
10000
1000
100
0
20
40
60
80
100
Time (sec)

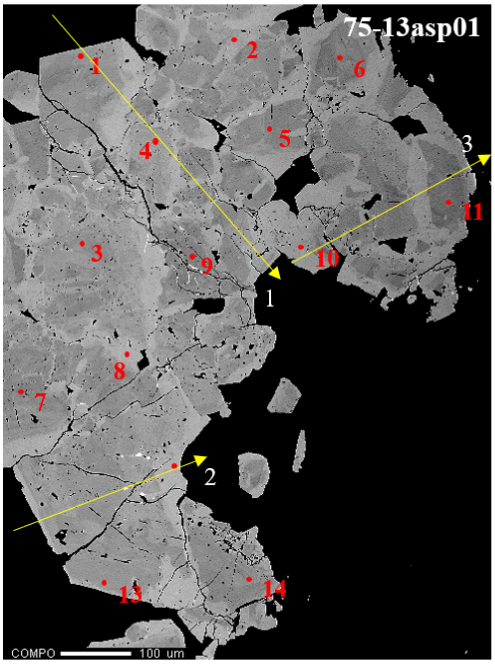
75-13asp01
1
2
3
4
5
6
7
8
9
10
11
12
13
14
COMPO
100 um

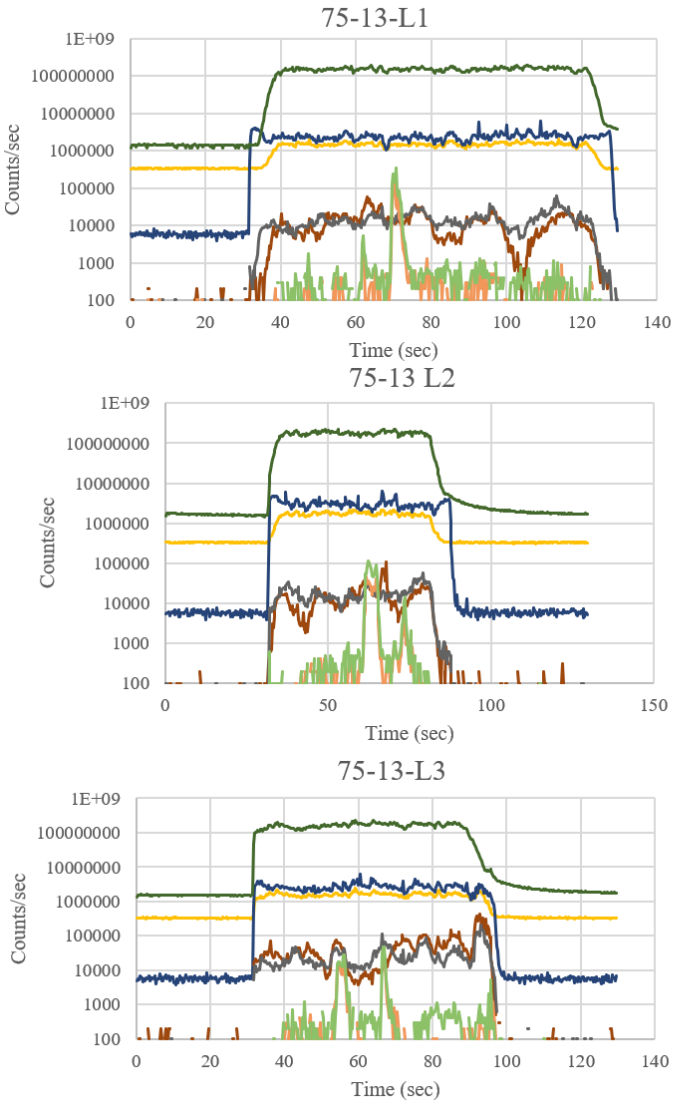
75-13-L1
75-13 L2
75-13-L3
Counts/sec
Time (sec)
1E+09
100000000
10000000
1000000
100000
10000
1000
100
S34
Fe57
Co59
Ni60
As75
Ag107
Au197

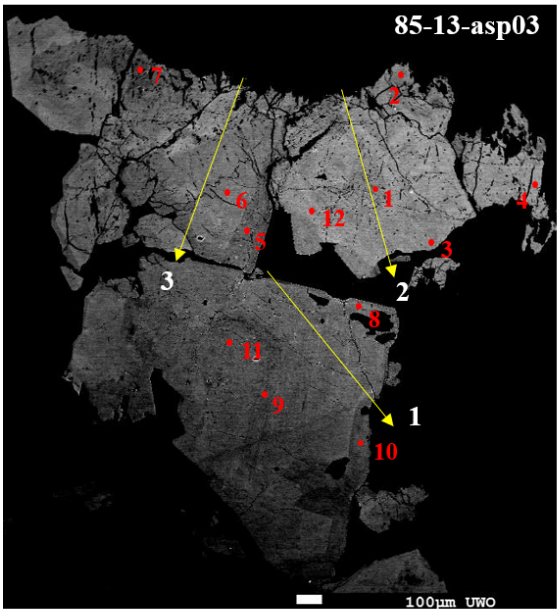
85-13-asp03
7
2
6
1
12
4
5
3
3
2
8
11
9
1
10
100µm UWO

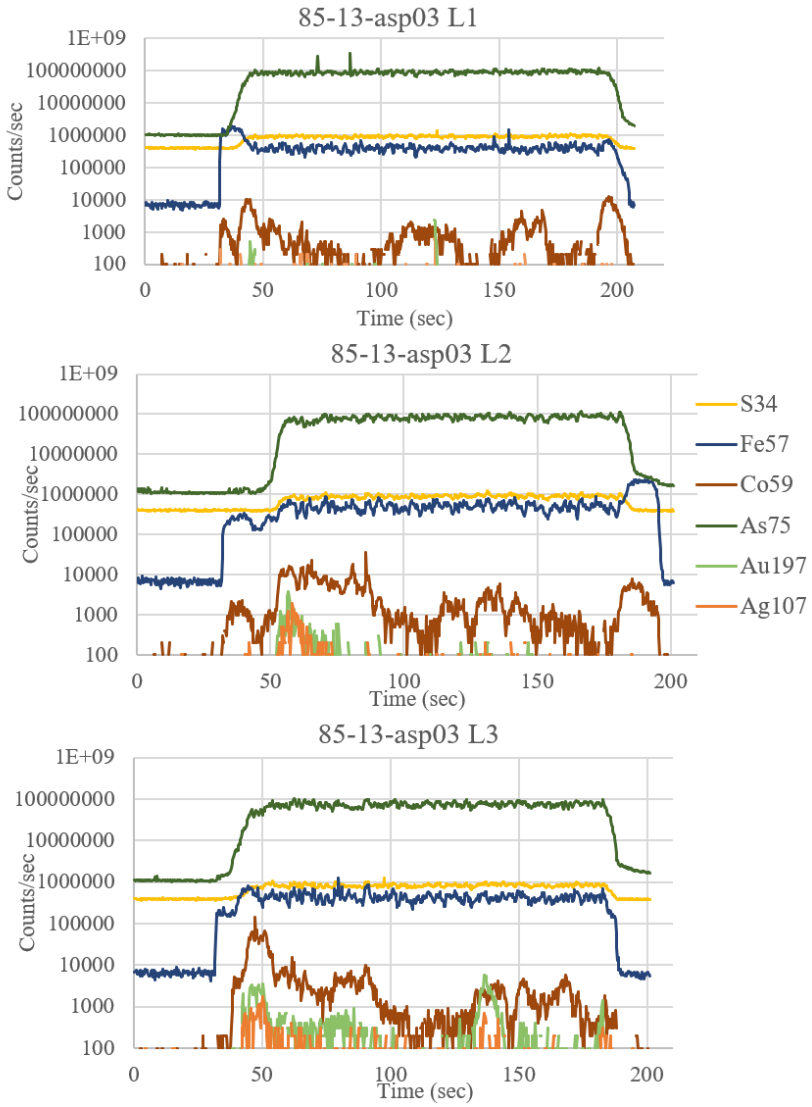
85-13-asp03 L1
1E+09
100000000
10000000
1000000
100000
10000
1000
100
Counts/sec
0
50
100
150
200
Time (sec)
85-13-asp03 L2
1E+09
100000000
10000000
1000000
100000
10000
1000
100
Counts/sec
0
50
100
150
200
Time (sec)
S34
Fe57
Co59
As75
Au197
Ag107
85-13-asp03 L3
1E+09
100000000
10000000
1000000
100000
10000
1000
100
Counts/sec
0
50
100
150
200
Time (sec)

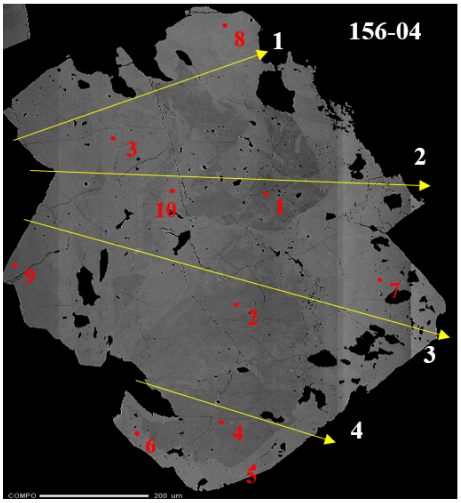
156-04
1
2
3
4
5
6
7
8
9
10

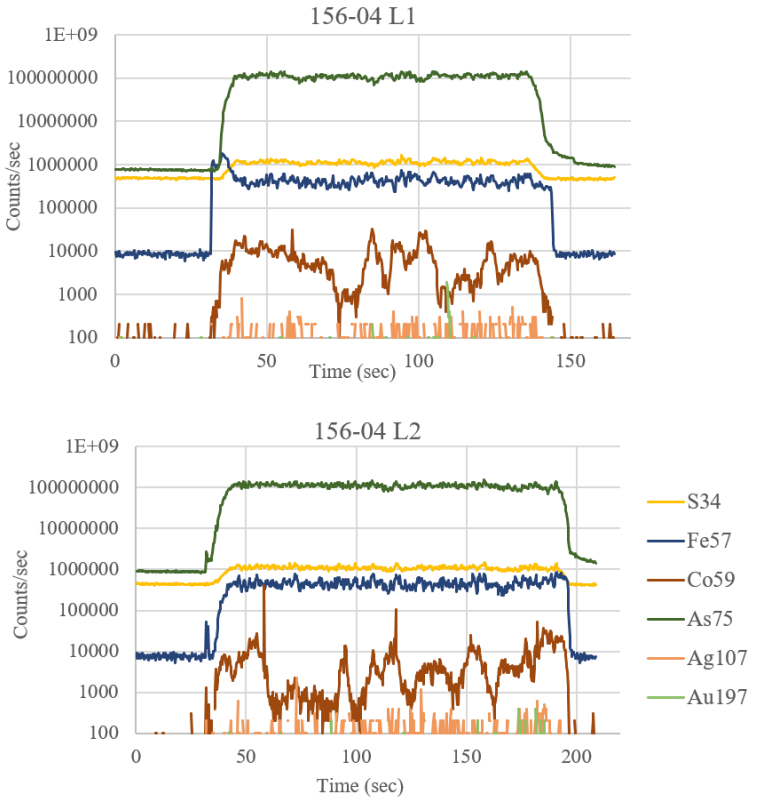
156-04 L1
156-04 L2
Counts/sec
Time (sec)
1E+09
100000000
10000000
1000000
100000
10000
1000
100
0
50
100
150
200
S34
Fe57
Co59
As75
Ag107
Au197

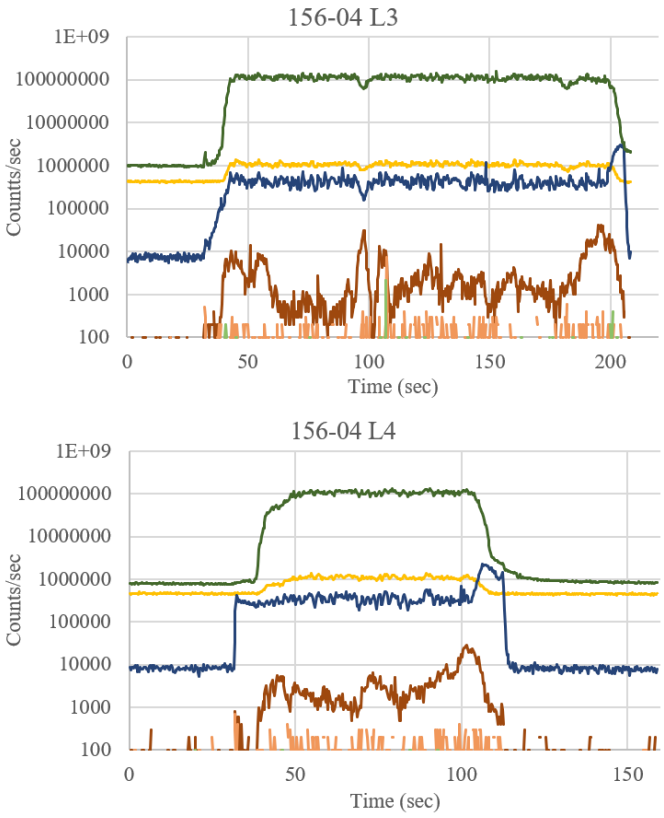
156-04 L3
156-04 L4
Counts/sec
Time (sec)
1E+09
100000000
10000000
1000000
100000
10000
1000
100
0
50
100
150
200

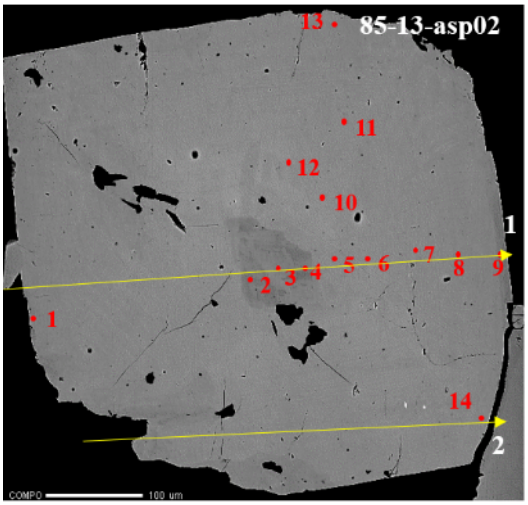
85-13-asp02
13
11
12
10
1
2
3
4
5
6
7
8
9
1
14
2
COMPO
100 um

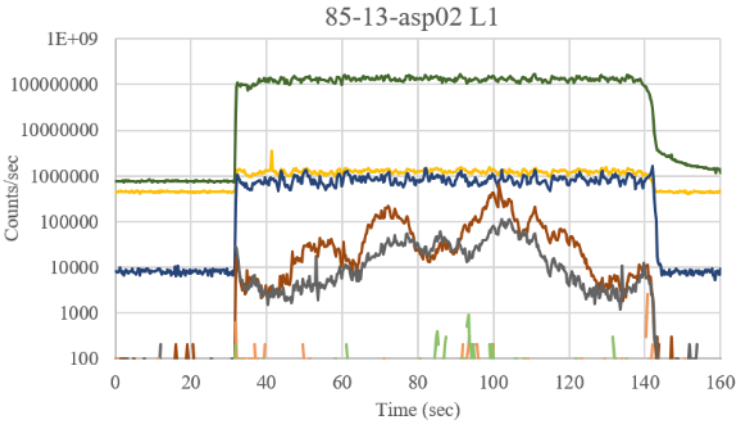
85-13-asp02 L1
1E+09
100000000
10000000
1000000
100000
10000
1000
100
Counts/sec
0
20
40
60
80
100
120
140
160
Time (sec)

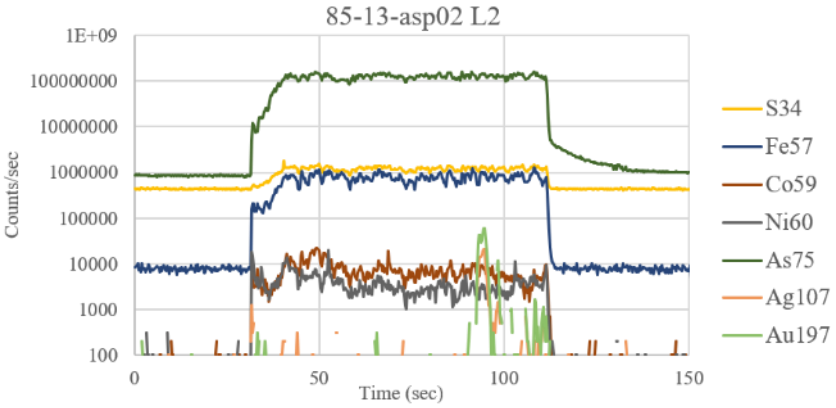
85-13-asp02 L2
1E+09
100000000
10000000
1000000
100000
10000
1000
100
Counts/sec
0
50
100
150
Time (sec)
S34
Fe57
Co59
Ni60
As75
Ag107
Au197

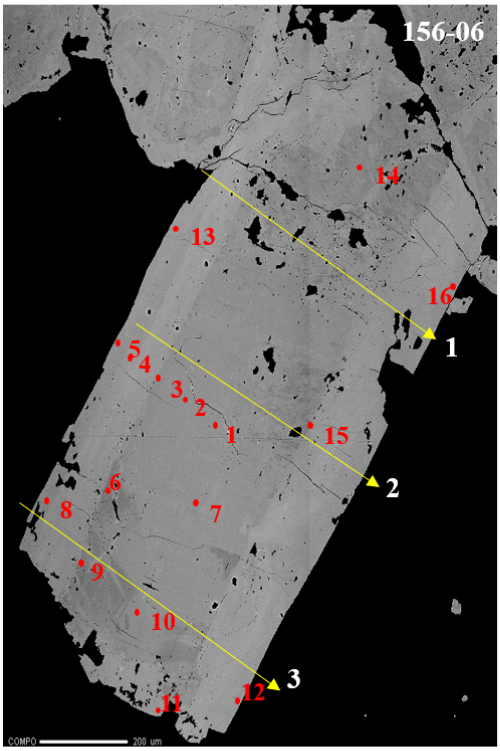
156-06
14
13
16
1
5
4
3
2
1
15
2
6
8
7
9
10
3
11
12
COMPO
200 um

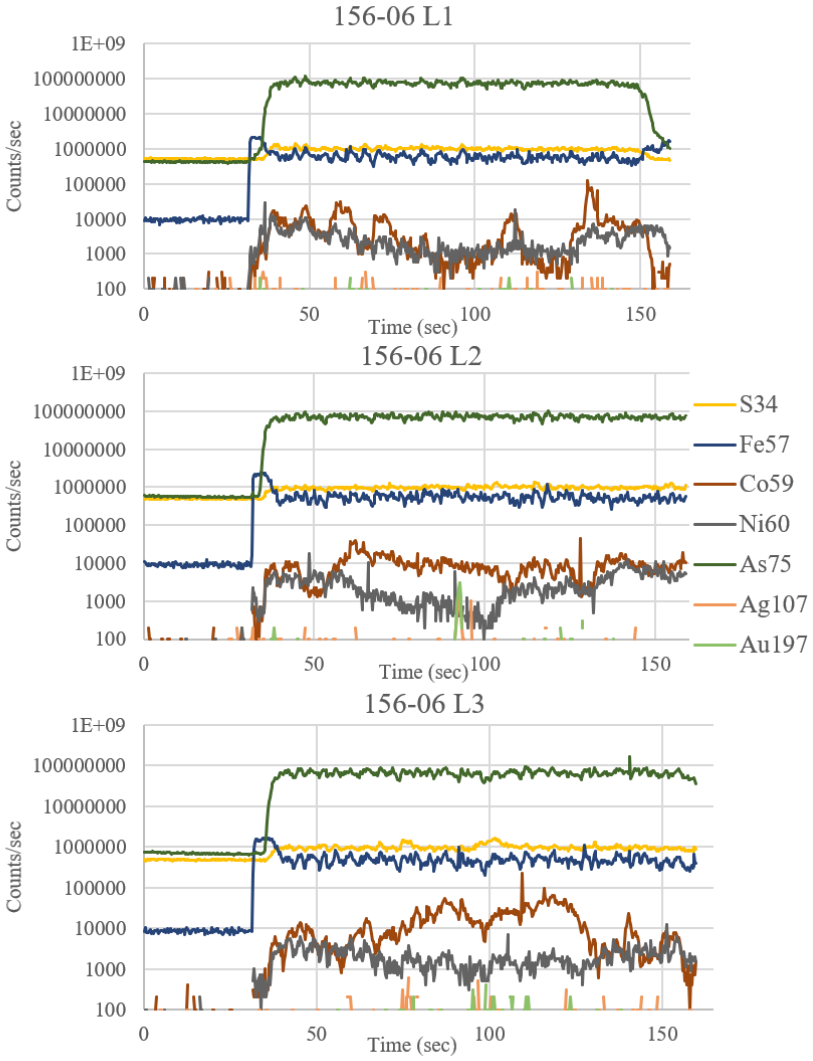
156-06 L1
1E+09
100000000
10000000
1000000
100000
10000
1000
100
Counts/sec
0
50
100
150
Time (sec)
156-06 L2
1E+09
100000000
10000000
1000000
100000
10000
1000
100
Counts/sec
0
50
100
150
Time (sec)
S34
Fe57
Co59
Ni60
As75
Ag107
Au197
156-06 L3
1E+09
100000000
10000000
1000000
100000
10000
1000
100
Counts/sec
0
50
100
150
Time (sec)

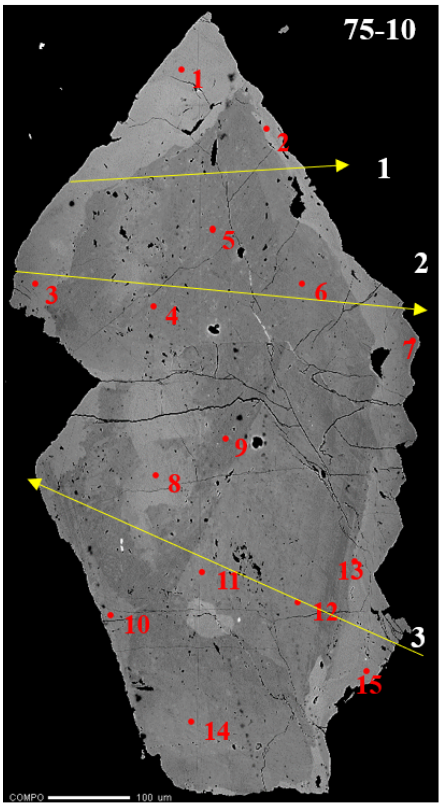
75-10
1
2
3
1
2
3
4
5
6
7
8
9
10
11
12
13
14
15
COMPO
100 um

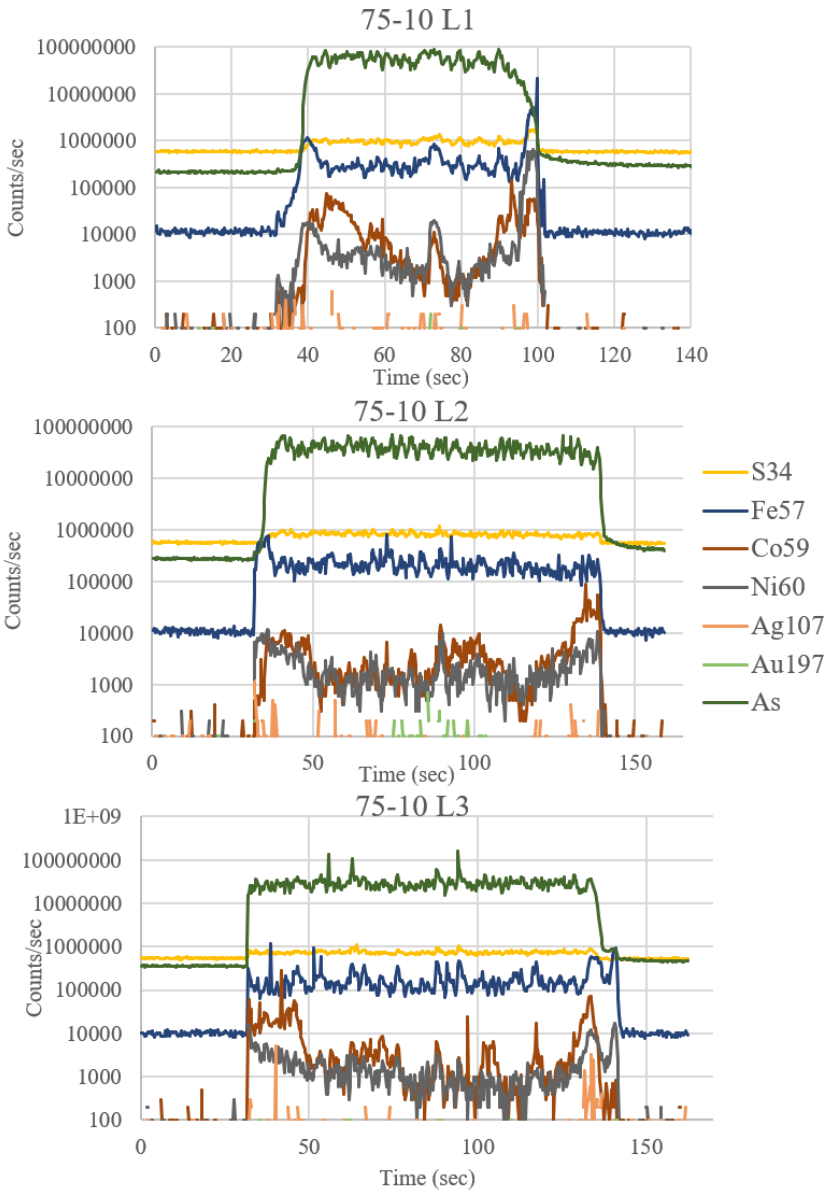
75-10 L1
Counts/sec
Time (sec)
75-10 L2
Counts/sec
Time (sec)
S34
Fe57
Co59
Ni60
Ag107
Au197
As
75-10 L3
Counts/sec
Time (sec)

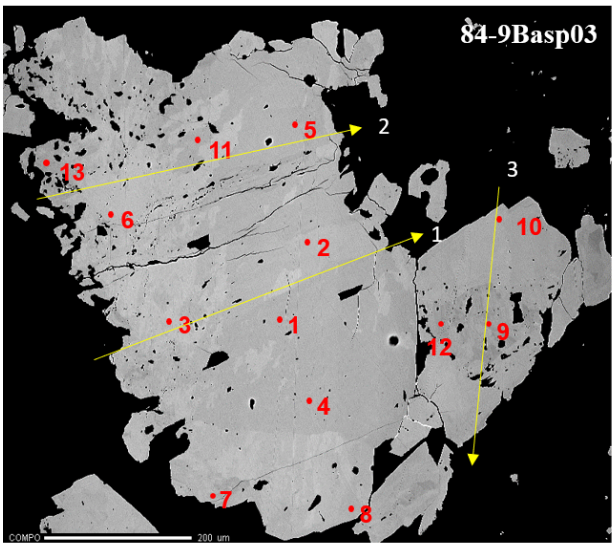
84-9Basp03
13
11
5
2
6
2
1
3
10
3
1
12
9
4
7
8
COMPO
200 um

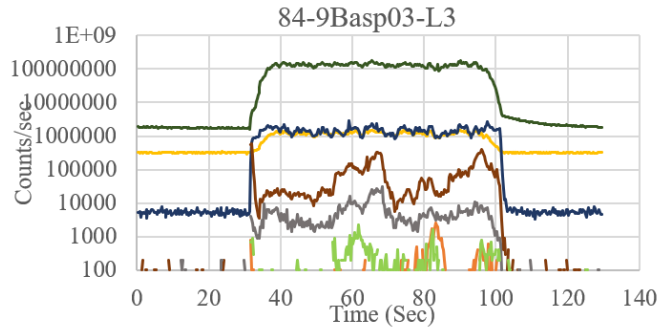
84-9Basp03-L3
Counts/sec
1E+09
100000000
10000000
1000000
100000
10000
1000
100
0
20
40
60
80
100
120
140
Time (Sec)

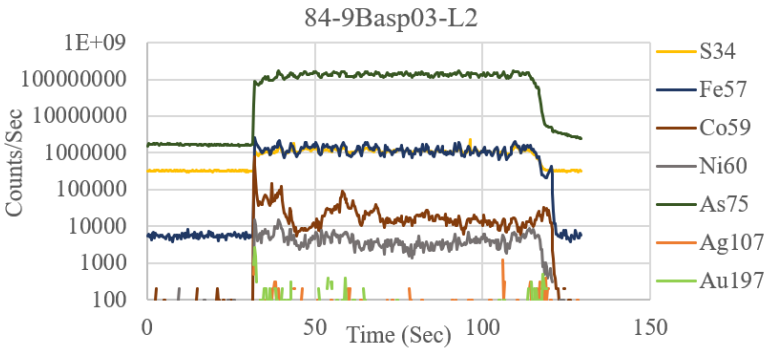
84-9Basp03-L2
Counts/Sec
1E+09
100000000
10000000
1000000
100000
10000
1000
100
0
50
100
150
Time (Sec)
S34
Fe57
Co59
Ni60
As75
Ag107
Au197

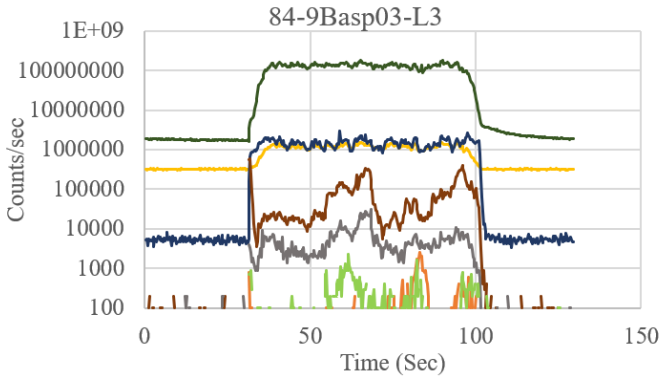
84-9Basp03-L3
Counts/sec
1E+09
100000000
10000000
1000000
100000
10000
1000
100
0
50
100
150
Time (Sec)

Curriculum Vitae

Name: Cassandra Powell

Post-secondary Education and Degrees:

Western University
London, Ontario, Canada
2017-Present M.Sc.

University of Ottawa
Ottawa, Ontario, Canada
2014-2017, HB.Sc.

CEGEP John Abbott College
Sainte-Anne-de-Bellevue, Quebec
2011-2013, Diplôme D'études Collégiales (DEC)

Related Work Experience:

Senior Filed Assistant
Ontario Geological Survey
May-August 2018

Student Geologist
Alexandria Minerals Corp.
May-September 2017

Graduate Teaching Assistant
Western University
2017-2019

Publications:

Powell, C., and Linnen, R.L. 2020. Western University Earth Sciences Deans Advisory Council (Oral) 2020

Powell, C., and Linnen, R.L. 2020. Gold-Arsenopyrite-Tourmaline relationships at the Orenada Zone 4 Deposit, Val d'Or, Québec. AME Roundup 2020. (Poster)

Powell, C., and Linnen, R.L. 2019. The controls of Gold Mineralization at The Orenada Zone 4 Deposit, Val d'Or, Québec. PDAC 2019. (Poster)

Powell, C., Schneider, D.A., Grasemann, B., Soukis, K., and Camacho, A. 2017. Identifying the hanging-wall of the West Cycladic Detachment System, Aegean Region, Greece, through geochronology and thermochronology. GAC-MAC 2017. (Poster)